LBNL-41865

ERNEST ORLANDO LAWRENCE BERKELEY NATIONAL LABORATORY

Microdefects and Self-Interstitial Diffusion in Crystalline Silicon

William Barthélémy Knowlton

Engineering Division

May 1998

Ph.D. Thesis

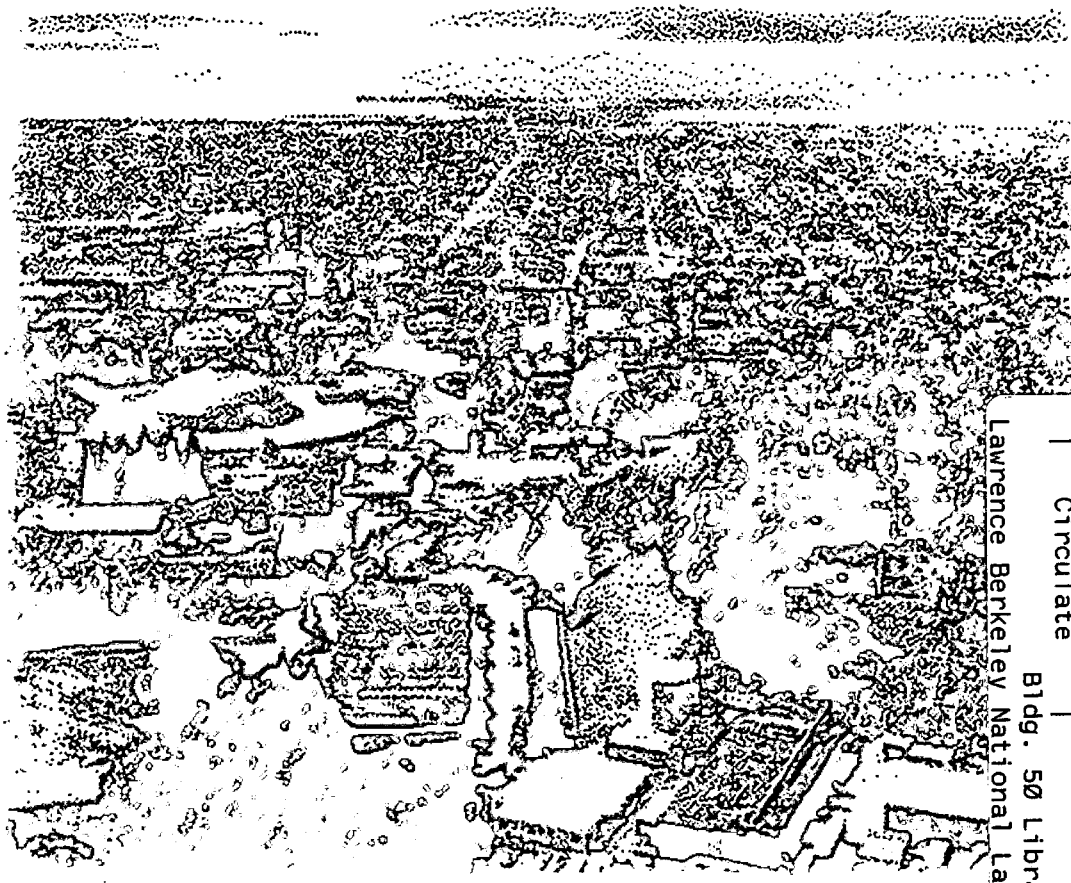

REFERENCE COPY
Does Not
Circulate
Bldg. 50 Library - Ref.
Lawrence Berkeley National Laboratory
LBNL-41865
Copy 1

DISCLAIMER

This document was prepared as an account of work sponsored by the United States Government. While this document is believed to contain correct information, neither the United States Government nor any agency thereof, nor the Regents of the University of California, nor any of their employees, makes any warranty, express or implied, or assumes any legal responsibility for the accuracy, completeness, or usefulness of any information, apparatus, product, or process disclosed, or represents that its use would not infringe privately owned rights. Reference herein to any specific commercial product, process, or service by its trade name, trademark, manufacturer, or otherwise, does not necessarily constitute or imply its endorsement, recommendation, or favoring by the United States Government or any agency thereof, or the Regents of the University of California. The views and opinions of authors expressed herein do not necessarily state or reflect those of the United States Government or any agency thereof or the Regents of the University of California.

LBNL-41865

Microdefects and Self-Interstitial Diffusion in Crystalline Silicon

William Barthélémy Knowlton

Engineering Division
Ernest Orlando Lawrence Berkeley National Laboratory
1 Cyclotron Road
Berkeley, California 94720

and

Materials Science and Mineral Engineering Department
University of California
Berkeley, California 94720

Ph.D. Thesis

May 1998

This work was supported by the Director, Office of Energy Research, Office of Basic Energy Sciences, Materials Sciences Division, of the U.S. Department of Energy under Contract No. DE-AC03-76SF00098.

Microdefects and Self-Interstitial Diffusion in Crystalline Silicon

by

William Barthélémy Knowlton

B. S. (University of California at Berkeley) 1992
M. S. (University of California at Berkeley) 1995

A thesis submitted in partial satisfaction of the

requirements for the degree of

Doctor of Philosophy
in

Engineering-Materials Science and Mineral Engineering

in the

GRADUATE DIVISION

of the

UNIVERSITY OF CALIFORNIA, BERKELEY

Committee in charge:

Professor Eugene E. Haller, Chair
Professor Timothy Sands
Professor Chenming Hu

Spring 1998

Abstract

Microdefects and Self-Interstitial Diffusion in Crystalline Silicon

By

William Barthélémy Knowlton

Doctor of Philosophy in Engineering-
Materials Science and Mineral Engineering

University of California, Berkeley

Professor Eugene E. Haller, Chair

In this thesis, a study is presented of D-defects and self-interstitial diffusion in silicon using Li ion (Li^+) drifting in an electric field and transmission electron microscopy (TEM). Obstruction of Li^+ drifting has been found in wafers from certain but not all FZ *p*-type Si. Incomplete Li^+ drifting always occurs in the central region of the wafers.

This work established that interstitial oxygen is not responsible for hindering Li^+ drifting. The O_i concentration was measured (~$2x10^{15}$ cm^{-3}) by local vibrational mode Fourier transform infrared spectroscopy and did not vary radially across the wafer.

TEM was performed on a samples from the partially Li^+ drifted area and compared to regions without D-defects. Precipitates were found only in the region containing D-defects that had partially Li^+ drifted. This result indicates D-defects are responsible for the precipitation that halts the Li^+ drift process. The precipitates were characterized using selected area diffraction (SAD) and image contrast analysis. The results suggested that the precipitates may cause stacking faults and their identity may be lithium silicides such as $Li_{21}Si_5$ and $Li_{13}Si_4$. TEM revealed a decreasing distribution of Li

precipitates as a function of Li^+ drift depth along the growth direction. A preliminary model is presented that simulates Li^+ drifting. The objective of the model is to incorporate the Li precipitate density distribution and Li^+ drift depth to extract the size and capture cross-section of the D-defects.

Nitrogen (N) doping has been shown to eliminate D-defects as measured by conventional techniques. However, Li^+ drifting has shown that D-defects are indeed still present. Li^+ drifting is able to detect D-defects at concentrations lower than conventional techniques.

Li^+ drifting and D-defects provide a useful means to study Si self-interstitial diffusion. The process modeling program SUPREM-IV was used to simulate the results of Si self-interstitial diffusion obtained from Li^+ drifting experiments. Anomalous results from the Si self-interstitial diffusion experiments forced a re-examination of the possibility of thermal dissociation of D-defects. Thermal annealing experiments that were performed support this possibility. A review of the current literature illustrates the need for more research on the effects of thermal processing on FZ Si to understand the dissolution kinetics of D-defects.

Table of Contents

1. D-defects as Studied by Li Ion Drifting and Transmission Electron Microscopy 1

1.1 Introduction 1
1.1.1 Li ion drifting and compensation in silicon 3
1.1.2 D-defects in crystalline silicon 7

1.2 Experiment and Results 14
1.2.1 Si self-interstitial injection by diffusion of phosphorus at high concentrations 19
1.2.2 The effect of oxygen on Li^+ drifting 22
1.2.3 The effect of nitrogen doping on D-defects 26

1.3 Preliminary TEM Study of the Partially Li^+ Drifted D-defect Region 33
1.3.1 General TEM background 33
1.3.2 Experimental procedure, results and discussion 35

1.4 Selected Area Diffraction and Contrast Analysis of Precipitate-Like Defects 39
1.41 Experimental procedure 39
1.42 Results and discussion 40

1.5 Precipitate Density Study Using TEM and Process Modeling 73
1.5.1 TEM precipitate density study 73
1.5.2 Preliminary process modeling of precipitation density results 87

2. Self-Interstitial Diffusion in Crystalline Silicon 91

2.1 Introduction 91

2.2 Background 93
2.2.1 The basics of diffusion 93
2.2.2 Diffusion in silicon – the role of point defects 100
2.2.3 Experiments used to determine D_I 108

2.3 Modeling D_I 113
2.3.1 Simulation of D_I using SUPREM-IV 113
2.3.2 The Bracht-Knowlton Si self-interstitial diffusion model 116

2.4 D_I as Revealed by Li^+ Drifting 125
2.4.1 Experiment 1: D-defect study yielding D_I 125
2.4.2 Experiment 2: Possibility of Li^+ drifting assisting the transport of Si self-interstitials 135

2.4.3 Experiment 3: The $POCl_3$ process of 2 cm thick wafers 136
2.4.4 Experiment 4: A time reduction in the $POCl_3$ process of 2 cm thick wafers 148
2.4.5 Nitridation 156
2.4.6 Experiment 5: Thermal annealing of 3 mm thick Si crystals 162
2.4.7 Re-evaluation of the thermal dissolution of D-defects 163

3. Conclusion 167

4. Appendices 170

4.1 Oxidation of Silicon 170

4.2 Local Vibrational Mode Fourier Transform Infrared (FTIR) Spectroscopy 171

4.3 TEM Calibrations 173

4.4 Background for Selected Area Diffraction and Contrast Analysis 179
4.4.1 The basis for contrast analysis 179
4.4.2 Types of contrast caused by precipitates 183
4.4.3 Two beam condition 187
4.4.4 Effects of precipitate-matrix coherency on electron diffraction 188
4.4.5 Diffraction analysis using selected area diffraction 192
4.4.6 Double diffraction 196

4.5 The Bracht-Knowlton Si Self-Interstitial Diffusion Model 197

5. References 205

Acknowledgments

I could not have written this thesis without the help of many people, both in the past and in the present. Many of those whom I acknowledged in my Master's thesis have contributed both directly and indirectly to this thesis. I thank my advisor, Eugene Haller, who has given me the opportunity to pursue graduate school and aspire to the goals necessary for attaining a Ph.D. He has provided guidance and mentorship that aided in my success thus far. I also thank Jack Walton for allowing me to work with he and his staff on microdefects and diffusion in Si using Li^+ drifting. His story telling has added a degree of mirth to our research. Both Yu Wong and Julie Lee have been instrumental in schooling me on the finer points of processing and fabrication of Li^+ compensated (i.e., passivated) diodes. Jack, Yu and Julie have contributed immensely to this thesis work. So have Dave Lewak, Amy Barnes, Isaac Mason, Carolyn Rossington, and Donny Suhartono. I'm grateful to Jeff Beeman for being such a great source of information and humor. I am very appreciative of Kohei Itoh who first employed me at LBNL to aid him in several projects. He gave me the opportunity to prove my worth at LBNL. David Hom has been very helpful with LBNL protocol for travel to conferences, paper and abstract submission and the multitude of other administrative obligations with which we are faced. Oscar Dubon, Kristin Duxstad, Chris Olsen, Marlene Almonte, Dawnelle Wynne, Matthew McCluskey and the rest of the Haller group have been a tremendous wealth of information and assistance. I am indebted to Harmut Bracht who is one of the most knowledgeable diffusion experts in the world and I have greatly benefited from his presence at LBNL.

I have benefited from the generosity of Jeff Rosner for allowing me to use his group's TEM facilities at Hewlett Packard Laboratories on Deer Creek Road in Palo Alto. While using the facilities, Grant Girolomi, Mark Juanitas, and Margaret Wong have provided a wealth of knowledge and immeasurable patience when teaching me the techniques of TEM sample preparation and the operation of the JEOL 200CX TEM.

With warm regards, I thank my chemistry instructor at Sacramento City College, Joe Grim, whom more than any other teacher allowed me to see beyond my envisioned limits in striving for success. Jay Seibens, the friend I met in the oil fields, instilled the intellectual confidence I lacked which opened the academic door for me.

My immediate family has given me much during my academic trek. Without them, I would not be here writing this today. My mother, Simone, has given me love and sustenance. She has been very instrumental in my academic success. My sister, Lorraine Lyvia, has always provided her love and support, but she especially shined during the difficult times following our father's death. With warm gratitude, I thank her husband, Les, who gave so much of himself during those difficult times. My nephew, Tyler, has provided us with much joyful delight. My father (a.k.a. "Pa") was very supportive in my endeavors – whether in the oil fields or academically. Although he is not here in the physical sense, he is here in the spiritual sense. With fond gratitude, I thank Timothy Rogers, the big brother I never had, who has provided support during times when I needed it most.

Amy, who has read and edited both my theses, now gets the break from reading she most assuredly deserves. I am very grateful for her love and support – completing graduate school was made much easier with the aid of my pack: Amy, Bica, Duke, and

Selway and Murfee. To those I have forgotten, I apologize – time, not disregard, was the limiting factor.

I am very grateful for the two University Fellowships that I received through the Department of Materials Science and Mineral Engineering. I thank the professors that thought enough of me to grant me the fellowships, and in addition, the funds and academic praise that come with them.

This work has been supported by the Director, Office of Energy Research, Office of Energy Sciences, Materials Sciences Division of the U.S. Department of Energy under contract No. DE-AC03-76SF00098.

1. D-defects as Studied by Li Ion Drifting and Transmission Electron Microscopy

1.1 Introduction

Ultra large scale integration (ULSI) technology requires ultra-thin device oxides with excellent breakdown integrity. Incorporation of native defects from the Si substrate during oxide growth has been shown to affect the integrity of the oxide [Abe and Kato, 1992, 4; Ammon, et al., 1994, 10; Suga, et al., 1993, 102] Deterioration of the gate oxide due to defects in the Si substrate has been presented by Itsumi and Kiyosumi.[Itsumi and Kiyosumi, 1982, 58] Recent studies of DRAM devices have indicated degradation of the dielectric breakdown voltage of thermally grown ultra-thin oxides.[DiMaria, et al., 1993, 26; Dumin, 1995, 28; Ling, 1994, 67; Triplett, 1994, 106]

Several studies have correlated D-defects, believed to be vacancy clusters, with poor gate oxide integrity. D-defects exist mostly in the central region of some floating zone (FZ) and Czochralski (CZ) grown Si crystals.[Abe, et al., 1982, 1; Roksnoer and van den Boom, 1981, 91] Abe and Kato as well as others have shown a relationship between the presence of D-defects and the degradation of the dielectric breakdown voltage of gate oxides.[Abe and Kato, 1992, 4; Ammon, et al., 1994, 10; Suga, et al., 1993, 102] Furthermore, the crystal originated particle (COP) technique was used to show that poor gate oxide integrity is indeed related to D-defects.[Ravi and Wijaranakula, 1996, 88; Suga, et al., 1993, 102; Yamagishi, et al., 1992, 114] Detected by laser scattering tomography (LST), COPs are D-defects which evolve into etch pits created during cleaning in the standard cleaning solution $NH_4OH:H_2O_2:H_2O$ (i.e., the *SC1*

clean).[Ravi and Wijaranakula, 1996, 88; Ryuta, et al., 1990, 92; Suga, et al., 1993, 102; Yamagishi, et al., 1992, 114] Park *et al.* and others have found D-defects incorporated into thermally grown gate oxides using transmission electron microscopy (TEM) studies.[Itsumi, et al., 1995a, 57; Itsumi, et al., 1995b, 59; Park, et al., 1995, 79; Park, et al., 1994, 80] Most recently, Ueki, Itsumi and Takeda [Ueki, et al., 1997, 107] have found D-defects in untreated (i.e., neither oxidized or annealed) bulk CZ Si. In all cases in which D-defects have been found in CZ Si, either in the bulk or at the Si/SiO_2 interface, they consist of octahedral voids of 100 to 300 nm in diameter with their walls coated with SiO_2.

The Li ion (Li^+) drift process is sensitive to D-defects.[Walton, et al., 1993, 109; Walton, et al., 1994, 110] In the first part of this thesis, a study is presented of D-defects in floating zone (FZ) Si with many of the same characteristics described above. The D-defects are studied using Li ion (Li^+) drifting, transmission electron microscopy (TEM) and process modeling. In the first section, a general background on D-defects is presented. This is followed by a description of Li^+ drifting. The following three sections encompass the experimental procedures, results and discussion. First, the delineation of the D-defects by Li^+ drifting is described. Then, D-defect reduction by silicon self-interstitial injection into the bulk and nitrogen (N) doping is discussed, and finally a TEM study of the delineated D-defects is presented. The experimental results show that D-defects can be reduced by Si self-interstitial injection. Furthermore, they indicate that N-doping does not completely eliminate D-defects and that Li^+ drifting is a sensitive means to delineate D-defects in N-doped Si crystals. TEM results show that Li precipitation is

caused by D-defects and that precipitation halts the Li^+ drift process. Also, the TEM results show that a precipitate density distribution exists.

1.1.1 Li ion drifting and compensation in silicon

Background

When acceptor or donor elements diffuse into *n*-type or *p*-type Si, respectively, *p-n* (or *n-p*) junctions are formed. Knowing the doping concentration in the Si and the distance of the junction from the surface, the diffusivities and concentrations of the diffusing dopant species can be determined.[Fuller, 1952, 35] Severiens and Fuller [Severiens and Fuller, 1953, 93] found diffusivities of certain ions can be determined when applying an electric field (i.e., ion drifting). Ion drifting is limited to species that are fast diffusers in the given matrix. Ion drifting experiments have been reported for Li in Si or Ge and Cu in Ge. The diffusivities (i.e., drift mobilities) are a function of temperature, *p-n* junction distance from the surface, electric field, and time. Each of these parameters is easily measured to within a few percent. Since interstitial Li^+ is a donor in Si, Li^+ drifting is used in *p*-type Si to compensate acceptors and form intrinsic regions. Furthermore, Li^+ diffuses rapidly in *p*-type Si and Ge which allows a good diode to be formed at relatively low diffusion temperatures and in short times.[Pell, 1961, 84; Walton, et al., 1993, 109]

Li^+ drifting has since been used extensively as a sensitive probe to determine the diffusivity of Li^+ and to understand Li^+ pairing interactions with various impurities including the acceptors (i.e., acceptor passivation) B, Al, Ga, and In and O.[Pell, 1960b,

82; Pell, 1961, 84; Pell and Ham, 1961, 85; Reiss, et al., 1956, 89] Li^+ also interacts with interstitial O (O_i) forming immobile LiO^+ donor complexes. Therefore, only floating zone (FZ) Si crystals can be used for the Li^+ compensation process because the O_i concentration in the crystals is relatively low (10^{15} to 10^{16} cm^{-3}). CZ Si crystals are grown in SiO_2 crucible causing an O_i concentration to be at least two orders of magnitude higher than in FZ Si crystals. With the subsequent realization that thick semiconductor (both Si and Ge) regions could be made nearly intrinsic by acceptor compensation or passivation by interstitial Li^+, a variety of wide depletion layer semiconductor devices, Si:Li and Ge:Li, were developed for the detection of energetic radiation (X- and γ-rays) and particles. Currently, the principal application of the Li^+ compensation technique is the fabrication of Si:Li X-ray detectors. Throughout this thesis, Li^+ drifting implies Li^+ compensation, which is a misnomer since it is passivation that is occurring.

Si:Li device fabrication and Li^+ drift process

The Li^+ drifting process begins with the thermal evaporation of Li metal onto a lapped surface and subsequent diffusion forming a n^+ region. A *p-n* junction is formed within the bulk where the Li^+ concentration is equal to that of the original net acceptor concentration. On the opposite side of the Si wafer, the surface is etched and a thin film of Au is thermally evaporated forming a Schottky barrier. A reverse bias is applied to this *p-n* structure which induces an electric field across the *p-n* junction forcing the Li^+ to drift from the Li^+ rich n^+ layer to the Li poor p^- region. The optimal temperature for Li^+ drifting is approximately 100°C. At this temperature, the *p-n* Si diodes still exhibit good

current voltage characteristics. The drifting Li^+ passivate shallow acceptors producing an intrinsic region of width W. The Li^+ drifting process is shown in figure 1.1.

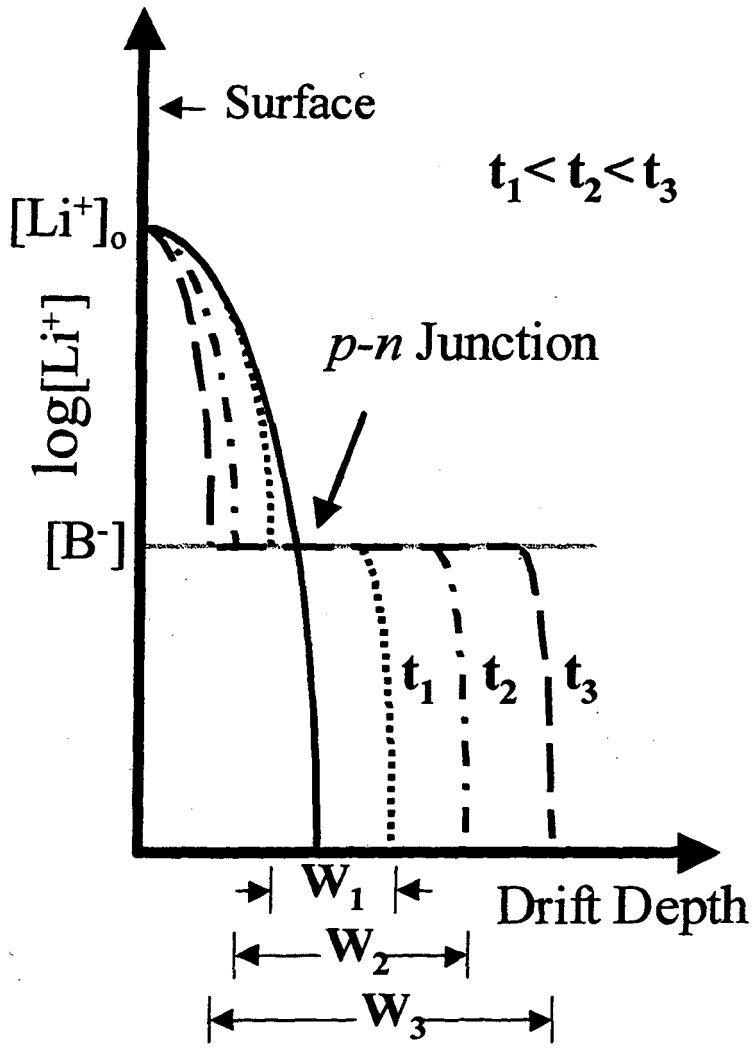

Figure 1.1: This plot shows the Li concentration profile versus the drift depth from the surface into the bulk. The initial Li diffusion profile is shown by the solid curve and the solid gray line of constant concentration denotes the acceptor concentration represented by boron. As the drift time, *t*, increases the intrinsic region, *W*, increases in width. After a long enough time, the intrinsic region extends across the entire wafer thickness.

Li^+ drift theory

The intrinsic region growth rate is described by:

$$\frac{dW}{dt} = \frac{\mu V}{W} - \frac{W}{\tau_L} \tag{1.1}$$

where μ, τ_L, and V are the Li^+ mobility, the Li^+ lifetime, and the applied bias, respectively.[Sher and Coleman, 1970, 94] The last term, which includes the Li^+ lifetime, is a "loss term" to account for Li^+ precipitation. The solution to equation 1.1 for constant V, τ_L, and μ is given by:

$$W = W_{\max}\left(1 - e^{-2t/\tau_L}\right)^{1/2} \tag{1.2}$$

where

$$W_{max} = (\mu V \tau_L)^{1/2} \tag{1.3}$$

is the maximum width of the intrinsic region reached for t approaching infinity. For $t \ll \tau$, equation 1.3 simply becomes a function of the drift time. The Li^+ mean free drift time is on the order of 300 hours. This is typical for most FZ Si with acceptor concentrations of about 10^{13} cm^{-3}. For drift times of about 100 hours at 1 kV potential, intrinsic regions of several millimeters can be obtained.

For the case of small τ_L, W_{max} may be smaller than the physical thickness of the Si wafer resulting in incomplete Li^+ drifting. Li^+ drifting ceases before the full width of the wafer is passivated. This result is typical of CZ Si or FZ Si doped with large oxygen concentrations.[Pell, 1961, 84] However, this can also be the case due to microdefects as

Walton *et al.* have found.[Walton, et al., 1993, 109] The following section discusses this in detail.

1.1.2 D-defects in crystalline silicon

During the growth of bulk single crystal silicon intrinsic point defects are created. The point defects can agglomerate during growth into microdefects. Such microdefects present in Si include the A-defect, the B-defect, and the D-defect. The A-defect and B-defects are also referred to as "swirl" defects because of their striated distribution. The A-defects were identified by Bernewitz *et al.* [Bernewitz, et al., 1974, 14] and Föll and Kolbesen [Föll and Kolbesen, 1975, 33] using TEM analysis and found to be extrinsic dislocations surrounding an extrinsic stacking fault formed by the agglomeration of silicon self-interstitials. The B-defects have not been identified but they are generally believed to be the embryonic nuclei of A-defects.[Chikawa, et al., 1986, 23]

D-defects were first discovered by Roksnoer and van den Boom [Roksnoer and van den Boom, 1981, 91] using X-ray topography on FZ Si which had been decorated with Li or Cu. By performing X-ray topography on the decorated wafers cut from a FZ grown Si ingot, they found that D-defects were homogeneously distributed within the inner two-thirds of the crystal diameter. Swirl defects were distributed in the area near the periphery as shown in figure 1.2. They found that the formation of swirl and D-defects strongly depends on the growth rate and the diameter of the Si ingot. They determined that the swirl defect formation is enhanced at low growth rates and is suppressed at high growth rates. However, when they grew crystals with higher growth rates to suppress swirl defect

formation, they found that D-defect formation occurred. The results of this experiment are shown in figure 1.3.

Roksnoer and van den Boom [Roksnoer and van den Boom, 1981, 91] also performed in situ annealing by halting the pulling of the crystal during growth. They found that D-defect dissolution occurred at the liquid/solid interface at 1140°C. Furthermore, A-defects formed in the former D-defect region. TEM of the D-defect region revealed a strain-free environment without strain-induced defects (e.g., extrinsic stacking faults). Electrical characterization of the same region showed that deep level states in the band gap did not exist. Roksnoer and van den Boom postulated that dopant atoms did not initiate D-defects, since D-defects are homogeneously distributed. Doping with impurity atoms during FZ crystal growth causes the dopants to be distributed in a striated pattern due to heat convection currents apparent during crystal growth. Based on their results, they concluded that the most likely microdefect candidate is the vacancy cluster.

Following Roksnoer and van den Boom's discovery, other investigators have provided further evidence that D-defects are vacancy agglomerates. Chikawa *et al.* [Chikawa, et al., 1986, 23] found that the D-defect region decreased when certain substitutional shallow dopants, that are assisted by Si self-interstitials during diffusion, were introduced into the crystal (see chapter 2). This result was attributed to Si self-interstitials recombining with vacancy clusters thereby reducing their concentration. Also, when doping with antimony, which diffuses via the vacancy assisted mechanism, the D-defect density increased. Chikawa *et al.* proposed that supersaturation of vacancies resulted in an increase in D-defect density.

Correlating with the aforementioned findings, Abe *et al.* [Abe and Kimura, 1990, 5] found that oxidation of FZ Si, which leads to Si interstitial injection (see appendix 4.1) into the Si lattice, decreases the D-defect region. Conversely, the nitridation of FZ Si, which causes the injection of vacancies into the Si lattice, increases the extent of the D-defect region.

D-defects have been delineated by Li^+ drifting in some FZ Si crystals. This effect has been seen by Walton *et al.*[Walton, et al., 1993, 109; Walton, et al., 1994, 110] They found that in certain FZ Si crystals, the Li^+ drifting would cease after the Li^+ drifted approximately 1 mm in a 3 mm thick FZ Si wafer. That is, the Li^+ did not fully or completely drift through the wafer. Although Li^+ drifting ceased in the inner two-thirds of the Si wafer, the outer one-third of the wafer, near the periphery, Li^+ drifted as normally occurs in the entire wafer. They found that Li^+ drifting for drift times longer than the standard Li^+ drift time (i.e., ~100 hrs at 1kV) did not increase the Li^+ drift depth in the central region of the wafer. This indicates the Li^+ mean free drift time, τ, is less than the drift time, t, which would lead to a W_{max} (equation 1.3) less than the thickness of the wafer.

Walton *et al.* have shown that wet oxidation (see appendix 4.1) eliminates the D-defect region in *p*-type FZ Si. In their experiment, they performed Li^+ drifting before and after oxidation. The wet oxidation was performed at 950°C for about 100 min. The wafers that were Li^+ drifted prior to oxidation did not fully Li^+ drift, indicating the presence of D-defects. The thermally oxidized wafers fully Li^+ drifted indicating that the D-defects were eliminated.

Walton *et al.* [Walton, et al., 1993, 109; Walton, et al., 1994, 110] have used the $POCl_3$ process on FZ Si crystals that contain D-defects which hinder Li^+ drifting. Analogous to thermal oxidation, the $POCl_3$ process injects Si self-interstitials into the Si bulk. They found that the defective FZ Si completely Li^+ drifted following the $POCl_3$ process. They concluded that the Si self-interstitials injected during the $POCl_3$ process recombined with vacancies forming the D-defects. The D-defects were eliminated and the Li^+ drifted completely through the entire bulk.

The results presented above suggest that D-defects are vacancy agglomerations. In order for D-defects to form in Si, experiments have shown that the growth rate has to be high, suggesting that D-defects are quenched or frozen into the lattice. Vacancies have a higher concentration at high growth rates and are in quasi-equilibrium. Studies have shown that the D-defect region in both FZ and CZ Si wafers can be reduced or eliminated by both in situ and ex situ thermal annealing. In situ annealing ($T>1000^oC$) decreases the D-defect region indicating that the defects are frozen in the lattice and thus are in a state of quasi-equilibrium analogous to vacancies.

Abe *et al.* [Abe, et al., 1982, 1] have shown that in situ annealing during crystal growth eliminates the D-defect region. Gräf *et al.* [Gräf, et al., 1996, 45] indicated that annealing CZ wafers in Ar, grown using a fast cooling rate typical of a high D-defect density, decreased the COP density. The annealing also improved the gate oxide integrity (GOI) in that the time zero (i.e., time independent) dielectric breakdown voltage of gate oxides increased.[Dumin, 1995, 28] However, since the O_i concentration is at least two orders of magnitude greater in CZ than FZ silicon, the authors believe oxygen plays a role in COP formation. Moreover, the temperature at which annealing was performed was

not reported. Several groups have shown that a 1200°C anneal for two hours removes D-defects.[Park, et al., 1995, 79; Ravi and Wijaranakula, 1996, 88] However, annealing was performed in a dry oxygen ambient, so Si self-interstitial injection is most likely reducing the D-defect concentration rather than thermal dissolution. Walton *et al.* [Walton, et al., 1994, 110] have shown that thermal annealing at 950°C for 100 minutes without oxidation or P diffusion does not reduce the D-defect concentration. Since 950°C is much lower than 1200°C, thermal dissolution of vacancy clusters at 950°C temperature is improbable.

Striations, usually caused by dopant atoms, are not apparent in the D-defect region providing further evidence that D-defects are not related to dopant impurities but are vacancy clusters. Also, vacancies produce minimal lattice distortion and TEM studies of the D-defect region show no lattice distortion in FZ Si. The introduction of dopants which diffuse via the interstitialcy mechanism (see chapter 2) shrinks the D-defect region indicating that Si self-interstitials annihilate vacancies and reduces the vacancy cluster concentration. Similarly, doping with antimony, which is vacancy assisted while diffusing, gives rise to an increase in the D-defect region supporting the theory that the vacancies, assisting in the diffusion process, combine with the vacancy clusters thus increasing the D-defect region. Lastly, the effect of oxidation and nitridation, respectively, shrinking and expanding the D-defect region, substantiates the vacancy cluster theory since oxidation injects Si self-interstitials and nitridation injects vacancies.

Although the aforementioned experiments were performed using floating zone (FZ) silicon, the same defects and growth rate-effects occur in Czochralski (CZ) grown silicon.[Abe, et al., 1982, 1; Abe and Takeno, 1992, 6] D-defects have recently been

detected with TEM in CZ Si after nearly 20 years of searching. Since they have not been observed by TEM in FZ Si, it is postulated that D-defects in CZ Si are larger.[Ueki, et al., 1997, 107] Furthermore, the walls of D-defects are coated with SiO_2 in CZ Si inducing strain into the lattice resulting in strain contrast. Strain contrast is readily observed by TEM. This is most likely not the case in FZ Si since the oxygen concentration is two to three orders of magnitude less than in CZ Si.

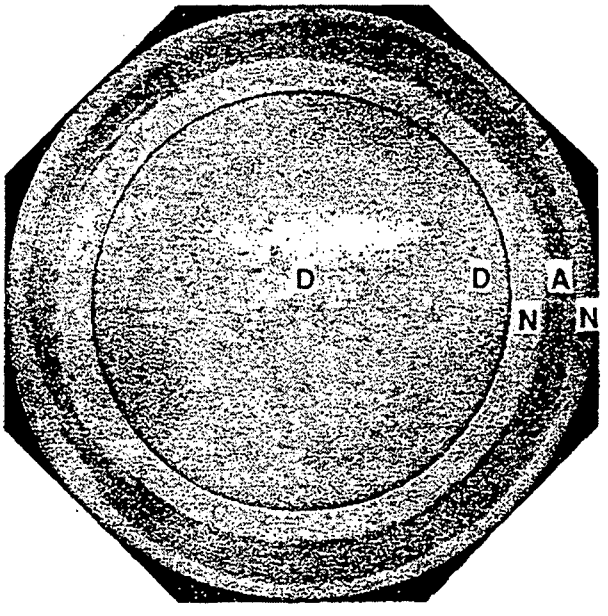

Figure 1.2: X-ray topograph after Cu decoration of a FZ Si wafer containing both swirl (region marked "A") and D (region marked "D") defects. The "N" region is defect-free.[Abe and Kimura, 1990, 5]

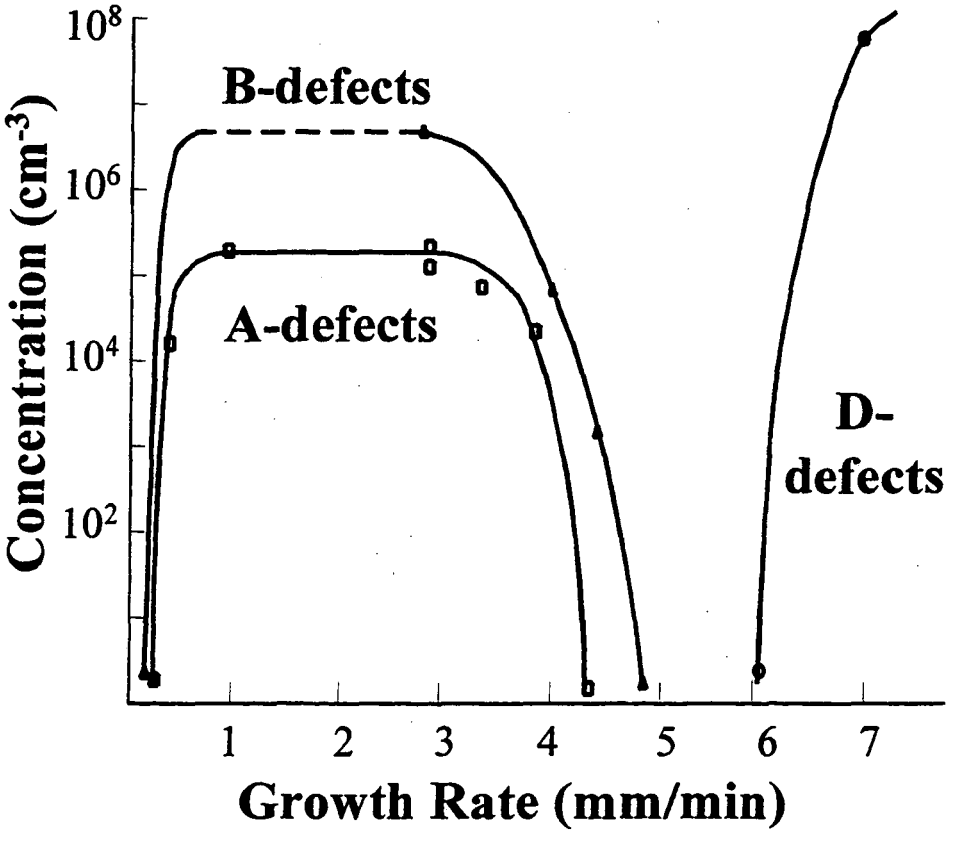

Figure 1.3: The concentration of growth-induced defects as a function of FZ Si ingot growth rate for a 23 mm diameter Si ingot. The nucleation and growth of D-defects occurs at a higher growth rate than for swirl defects. As the diameter increases, the growth rate for defect formation decreases.[Roksnoer and van den Boom, 1981, 91]

1.2 Experiment and Results

Using Li^+ drifting and FZ Si for the study of D-defects has several distinct benefits. The Li^+ drifting process is a low temperature process, thus contamination by impurity diffusion is negligible. Furthermore, Li^+ drifting can be performed in *p*-type Si doped as low as 10^{12} cm^{-3}. Therefore, D-defect formation or decoration with dopant atoms is limited. Lastly, FZ Si has a low concentration of oxygen relative to CZ Si, and oxygen has been shown to pair with Li^+ [Watkins, 1991, 111] and hinder Li^+ drifting.[Pell, 1961, 84; Young, et al., 1969, 116] Hence, D-defects can be studied in a relatively clean environment with minimal interference or interaction from impurity or dopant atoms.

Li^+ drifting is a very sensitive technique for delineating D-defects.[Knowlton, et al., 1995, 65] The Li^+ flux and concentration in the intrinsic region are directly proportional to the acceptor concentration, N_A.[Pell, 1960c, 83] Since such a low flux of Li drifts within the intrinsic region, low concentrations of defects can have a profound effect on the Li^+ drift process.

For this study, a number of FZ *p*-type Si (<100> and <111> orientation) ingots were chosen based on previous work in which Li^+ drifting was shown to be incomplete in the central region of wafers indicating the presence of D-defects. [Walton, et al., 1993, 109; Walton, et al., 1994, 110] The ingots used in this study are listed in table 1.1.

Wafers are cut from the ingots and processed into 3 mm thick wafers. After lapping with 1900 mesh alumina grit Li is evaporated on one side. The Li is diffused at 400°C for 15 minutes into the *p*-type wafers. After diffusion, a n^+p junction has formed. A Schottky barrier is created on the opposite side by evaporating Au on a polish etched

surface. The Li^+ ions are drifted under a reverse bias at a temperature of ~110°C. Following Li^+ drifting, the wafers are cross-sectioned and copper stained to delineate the extent of the Li^+ drifted region. The copper plates out onto surfaces of regions that have been Li^+ drifted. That is, the copper precipitates in the intrinsic region. The reaction is given by:

$$Cu^+ + 1e^- \rightarrow Cu_s \tag{1.4}$$

where the subscript *s* denotes a solid. As seen from equation 1.4, the copper plates out in regions that provide electrons. Since the Li^+ drifted region (i.e., intrinsic region) has a larger concentration of electrons than the undrifted p-type region, then the copper plates out onto the Li^+ drifted region. A schematic of the copper staining method is shown in figure 1.4.

A Li^+ drift profile characteristic of D-defect free wafers is shown in figure 1.5. The Li^+ drift profile for the wafers containing D-defects indicates that Li^+ drifting ceases approximately 1 mm from the lithiated surface. Only the central region of the wafer does not Li^+ drift. Near the periphery of the wafer Li^+ can be drifted through the full thickness of the wafer. This result is typical of the effect that D-defects have on Li^+ drifting. It is interesting to note the similarity in the radial distribution of D-defects when comparing figure 1.5 to figure 1.2.

Table 1.1: Ingot and wafer properties of Si crystals that could not be fully Li^+ drifted.

wafer properties	ingot number					
	42115/30	42115/30	41575/03	75556/01	40541/0931	39614/0770
wafer position*	9 mm	41 mm	unknown	unknown	unknown	unknown
crystal growth direction	<100>	<100>	<111>	<111>	<111>	<111>
Li^+ drift direction	<100>	<100>	<111>	<111>	<111>	<110>
diameter (mm)	103	103	103	125	78.74	100.4
thickness (mm)	3	3	3	3	3	10
growth rate (mm/min)	2.5	2.5	2.5	unknown	unknown	unknown
τ (μs)	900	900	unknown	unknown	1200	1900
ρ (Ω*cm)	660	1060	1250	1500	1100	1700
[B] cm^{-3}	$\sim 2x10^{13}$	$\sim 1.5x10^{13}$	$\sim 1x10^{13}$	$\sim 1x10^{13}$	$\sim 1.5x10^{13}$	$\sim 7x10^{12}$
[C] cm^{-3}	$<2x10^{15}$	$<3x10^{15}$	$\leq 5x10^{15}$	$\leq 5x10^{15}$	$\leq 5x10^{15}$	$\leq 5x10^{15}$
[N] cm^{-3}	$1x10^{14}$	$1x10^{14}$	$3x10^{14}$	unknown	unknown	unknown
[O] cm^{-3}	$2.2x10^{15}$	$1.5x10^{15}$	$2x10^{15}$	unknown	unknown	unknown

*from seed end of ingot

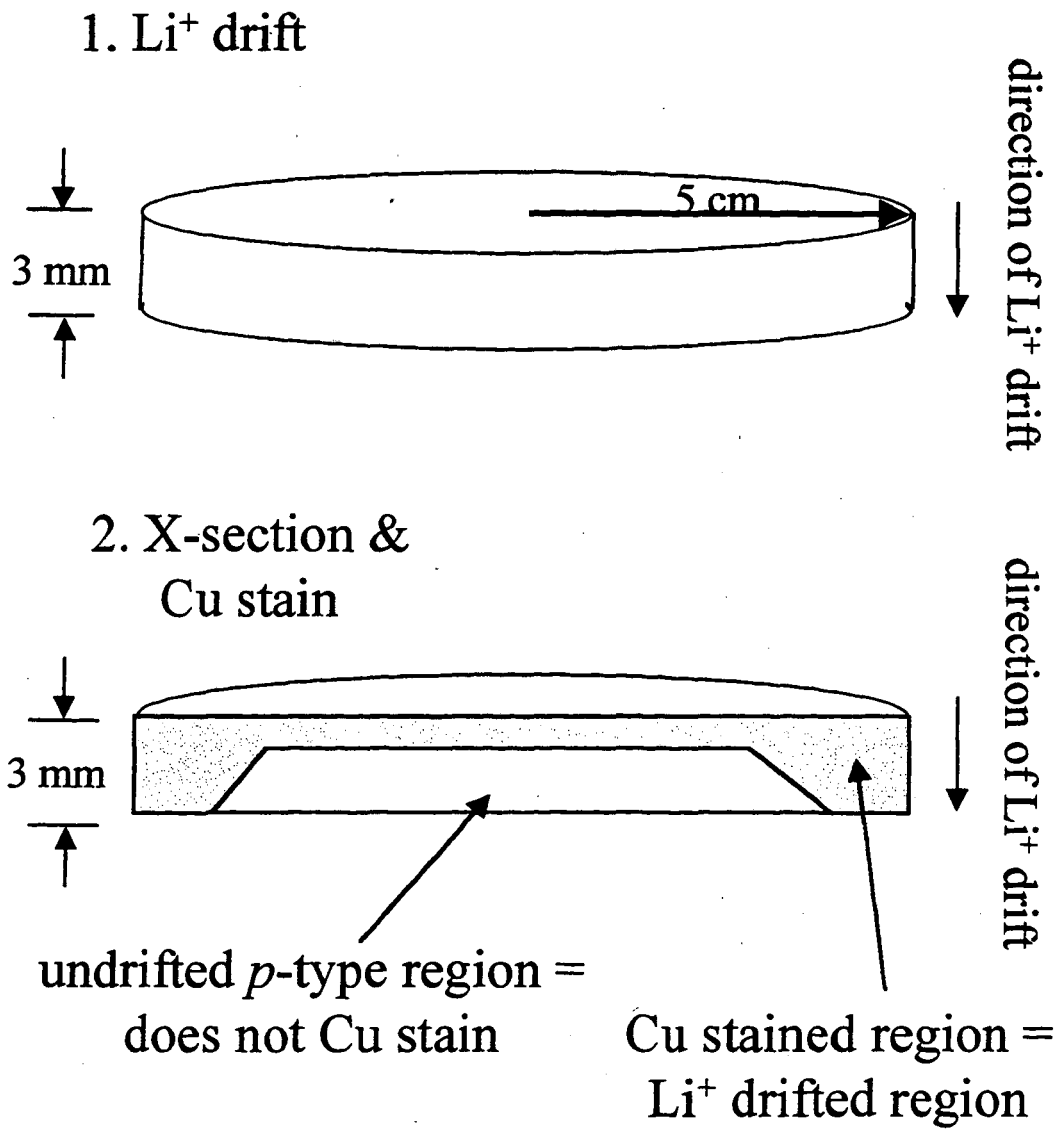

Figure 1.4: A schematic illustration of the process of cross sectioning and copper staining of the cut face of a partially Li^+ drifted wafer. The copper plates out on the Li^+ drifted region leaving the undrifted regions stain-free. As can be seen, the central region does not copper stain indicating the presence of D-defects.

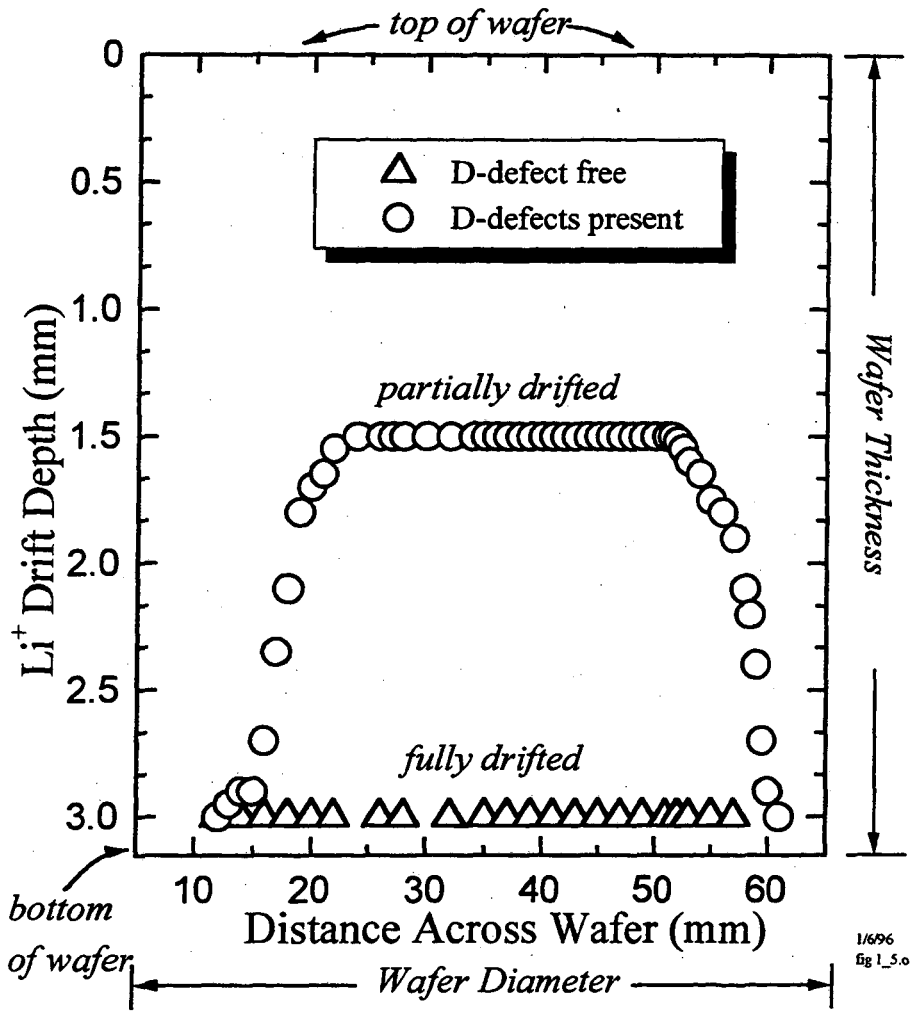

Figure 1.5: Li^+ drift profile showing the Li^+ drift depth as a function of distance across the 3 mm thick wafer, from the left to right wafer edge. The wafer contained D-defects and only partial Li^+ drifting occurred within the central region of the wafer. This is shown by the circles (O). This indicates that D-defects are present in the central region of the crystal, which is similar to figure 1.1. Li^+ drifted all the way (fully) through the peripheral region of the wafer, which indicates that D-defects are not present in this region of the crystal. In FZ *p*-type Si that does not contain D-defects, Li^+ drifting occurred completely through the 3 mm thick wafer as indicated by the triangles (Δ).

1.2.1 Si self-interstitial injection by diffusion of phosphorus at high concentrations

Another method of Si self-interstitial injection is phosphorus (P) doping via diffusion from a phosphorosilicate glass formed by oxidation using the $POCl_3$ process. The $POCl_3$ process involves bubbling N_2 and O_2 gas through a liquid $POCl_3$ source. The $POCl_3$ vapor is carried into the furnace by the N_2 gas and reacts with O_2 forming phosphorus pentoxide ($P_2O_{5(g)}$) in the vapor phase as shown in the following reaction:

$$4POCl_{3(l)} + 3O_{2(g)} \rightarrow 2P_2O_{5(g)} + 6Cl_{2(g)} \qquad (1.5)$$

where (l) and (g) denote the liquid and gas phase, respectively. The $P_2O_{5(g)}$ reacts with Si which oxidizes and introduces P into the Si. This reaction is given by:

$$2P_2O_{5(g)} + 5Si \rightarrow 4P + 5SiO_2 \qquad (1.6).$$

The wafer is then annealed at a temperature of 950°C for 100 min to diffuse the P from both wafer faces and into the bulk (~1 μm).

Several groups have firmly established that this process injects Si self-interstitials.[Ourmazd and Schröter, 1984, 75; Strunk, et al., 1979, 101] The reason for injection has been explained by Hu. [Hu, 1991, 53; Hu, 1994, 54] It involves the diffusivity of P and its solid solubility (i.e., the thermal equilibrium concentration of P). Hu has shown that during impurity diffusion at high concentrations, the fraction of concentration above the saturation concentration of Si self-interstitials is given by:

$$\frac{C_I(x)}{C_I^{eq}} = \frac{\frac{D_s C_s}{D_A} f_I^s + C_A(0)}{\frac{D_s C_s}{D_A} f_I^s + C_A(x)} \qquad (1.7)$$

where C_I^{eq} is the thermal equilibrium concentration of Si self-interstitials, D_s is the Si self-diffusion coefficient, f_I^s is its fractional interstitialcy component, D_A is the effective

diffusivity of dopant atoms, C_s is the concentration of Si atoms, and C_A is the concentration of dopant atoms. Inspection of equation 1.9 reveals that as C_A and $C_A(0)$ increase the Si self-interstitial supersaturation increases. At $POCl_3$ process temperatures (~950°C), the diffusivity of P is greater than the diffusivity of B, Ga, Sb and As, respectively and nearly that of Al. The solid solubility of P is greater than that of As, B, Sb, Ga, and Al (see for instance [Muller and Kamins, 1986, 72]). Indeed, Hu [Hu, 1994, 54] has pointed out that the number of Si self-interstitials injected during the $POCl_3$ process is an order of magnitude larger than the number injected during the thermal oxidation process.

Using the procedure outlined above, the $POCl_3$ process was performed on all crystals shown in table 1.1. After the $POCl_3$ process, the P doping layer (> 1 um) was removed from the 3 mm thick FZ *p*-type Si wafers. The wafers were processed for Li^+ drifting and Li^+ drifted. Another set of control wafers was cut from the same ingots and was Li^+ drifted but was not $POCl_3$ processed. The wafers were cross-sectioned and Cu stained. Typical results for the $POCl_3$ processed wafers and the control wafers are illustrated in figure 1.6. In the control wafers, only partial Li^+ drifting occurred within the central region verifying the presence of D-defects. In the region at the periphery of the wafer, the Li^+ drifts fully through the wafer thickness indicating that D-defects are not present in this region. In the wafers on which the $POCl_3$ process was performed, Li^+ drifting occurred completely through the 3 mm thick wafer. This result indicates that the D-defects were eliminated throughout the wafer thickness. These results have been reproduced repeatedly (see chapter 2).

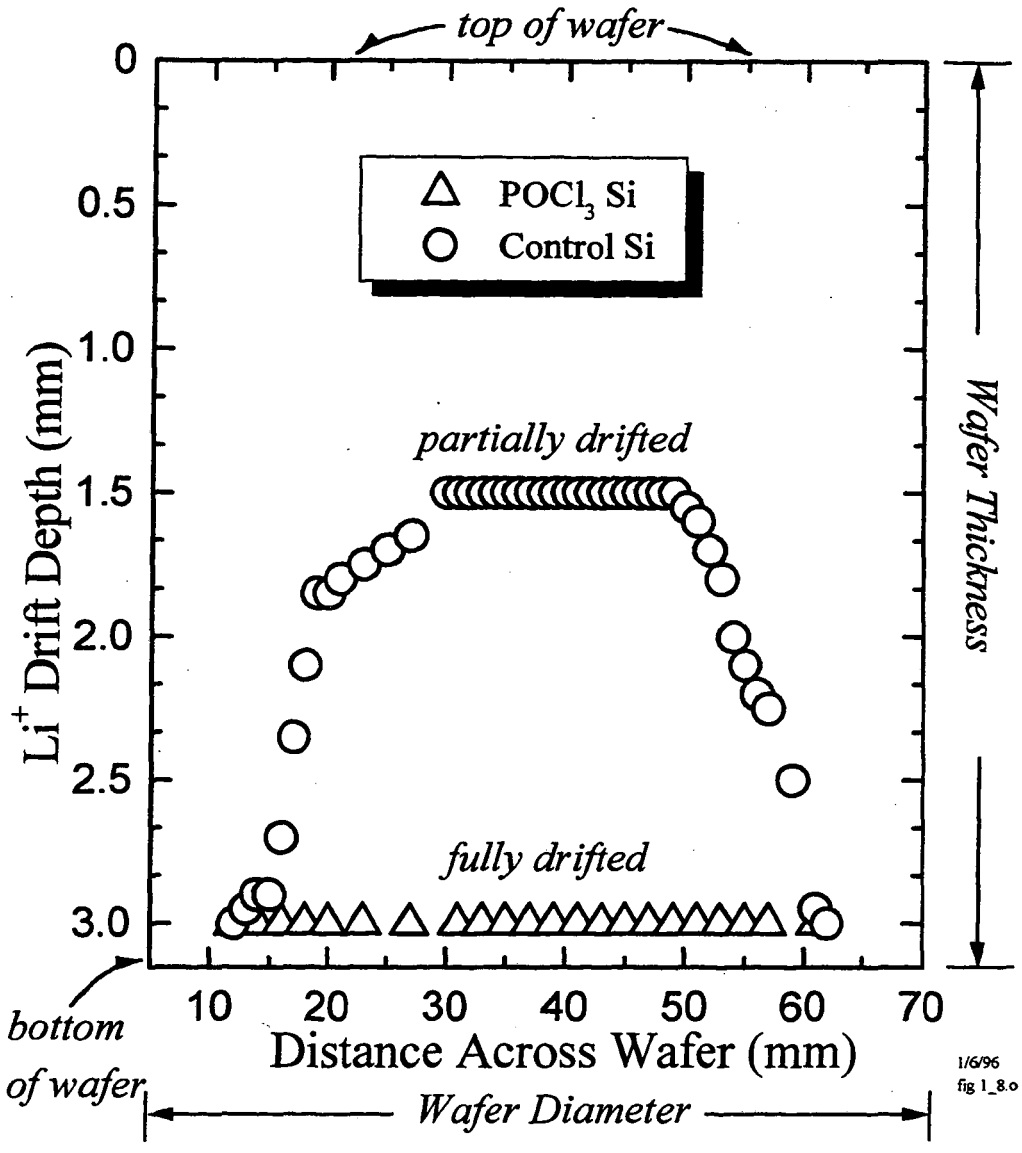

Figure 1.6: A Li^+ drift profile of a cross-sectioned and copper stained 3mm thick wafer showing the Li^+ drift depth as a function of distance across the wafer, from the left to right wafer edge. The control wafers did not completely Li^+ drift as shown by the circles (O). However, for the $POCl_3$ processed wafers, Li^+ drifted completely through the wafer as depicted by the triangles (Δ). Hence, the D-defects have been eliminated such that Li^+ drifting is unhindered.

1.2.2 The effect of oxygen on Li^+ drifting

To ensure that no defects except D-defects are responsible for impeding Li^+ drifting, the effect of oxygen on Li^+ drifting is explored. In principle, the results mentioned above may be explained if the oxygen concentration in the central region of the wafers is sufficiently large to hinder Li^+ drifting. Interstitial oxygen (O_i) and lithium form immobile LiO^+ donor complexes.[Pell, 1961, 84; Watkins, 1991, 111] Local vibrational mode spectroscopy (LVM) has been used to measure the oxygen concentration across the wafers before Li^+ drifting.

Wafers, 3 mm thick, were cut from several ingots and were lapped with 1900 grit alumina. A 2 mm wide strip was cut from central region of the wafer across the diameter. The 2 mm wide, 3 mm thick, diameter long strip was cut into approximately 2 mm long sections. These quadratic samples were chemomechanically polished. The O_i concentrations was assumed to exhibit a radial dependence.[Ammon, et al., 1994, 10; Ono, et al., 1995, 73] The LVM measurements were performed at low temperatures (~10 K) using a high resolution (~0.2 cm^{-1}) Bomem or Digilab FTIR instrument and a liquid He cooled cryostat. The O_i concentration was determined from the calculated absorption line area and the temperature dependent calibration constant.[Pajot, 1977, 76; Pajot, 1995, 77]

The results showed that the O_i concentration did not vary measurably across the wafer. A typical transmittance spectrum is shown in figure 1.7. The arrow points to the vibrational mode line of O_i. The inset shows an enlarged view of the vibrational spectrum. This spectrum is representative of all the samples measured. The O_i concentration was calculated for each sample using the method outlined in appendix 4.1.

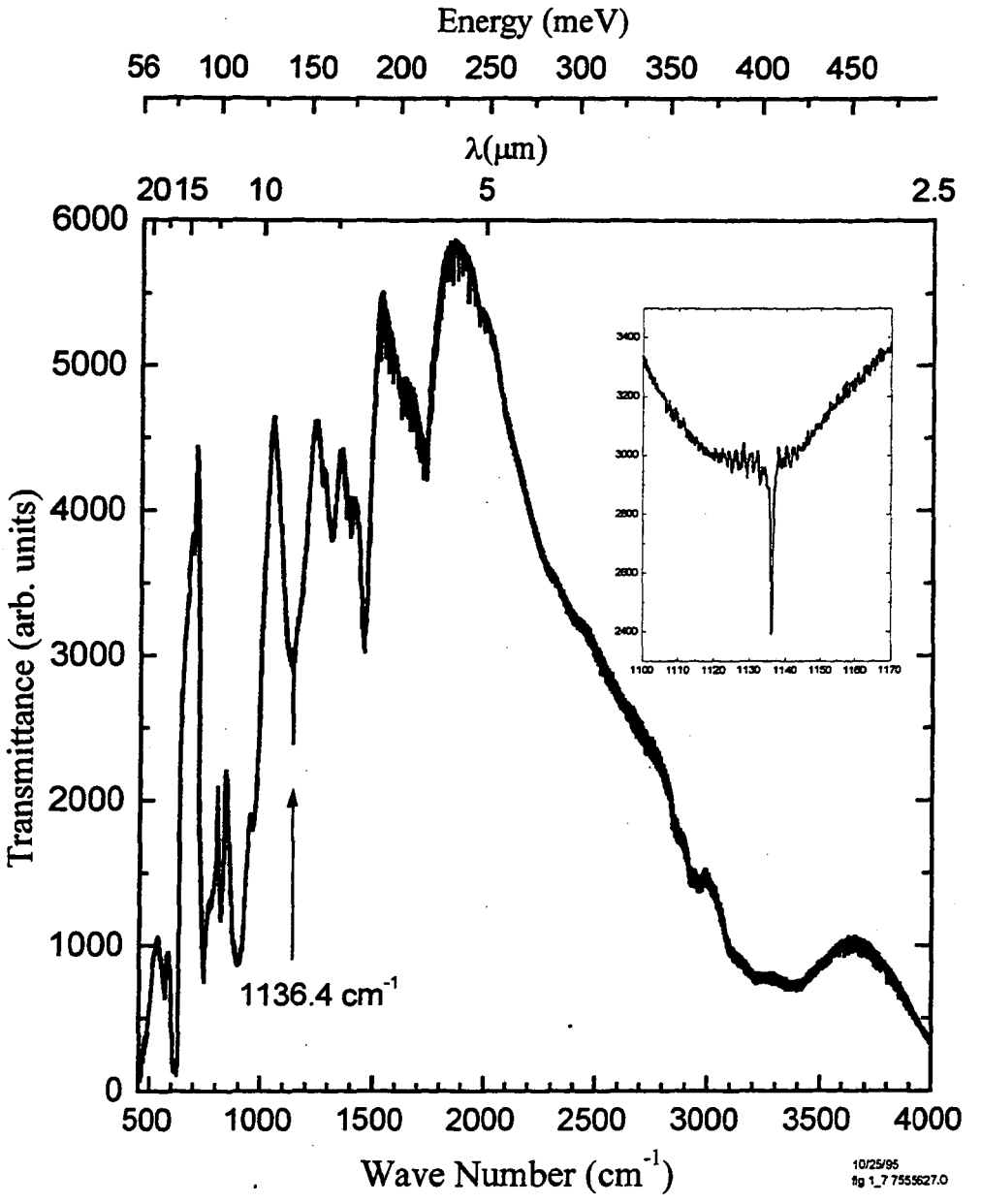

Figure 1.7: The transmittance spectrum of a FZ Si sample is plotted as a function of wavenumber (proportional to photon energy, $h\nu$). The arrow indicates the position of the local vibrational mode of interstitial oxygen. The inset plot shows the spectrum magnified over a narrower frequency range. The temperature of the sample at which the measurements were taken was about 9.5 K. The resolution of the spectrometer used in this experiment was 0.2 cm^{-1}. (8.06 cm^{-1} = 1 meV; 1 cm^{-1} = $10^4/\lambda(\mu m)$)

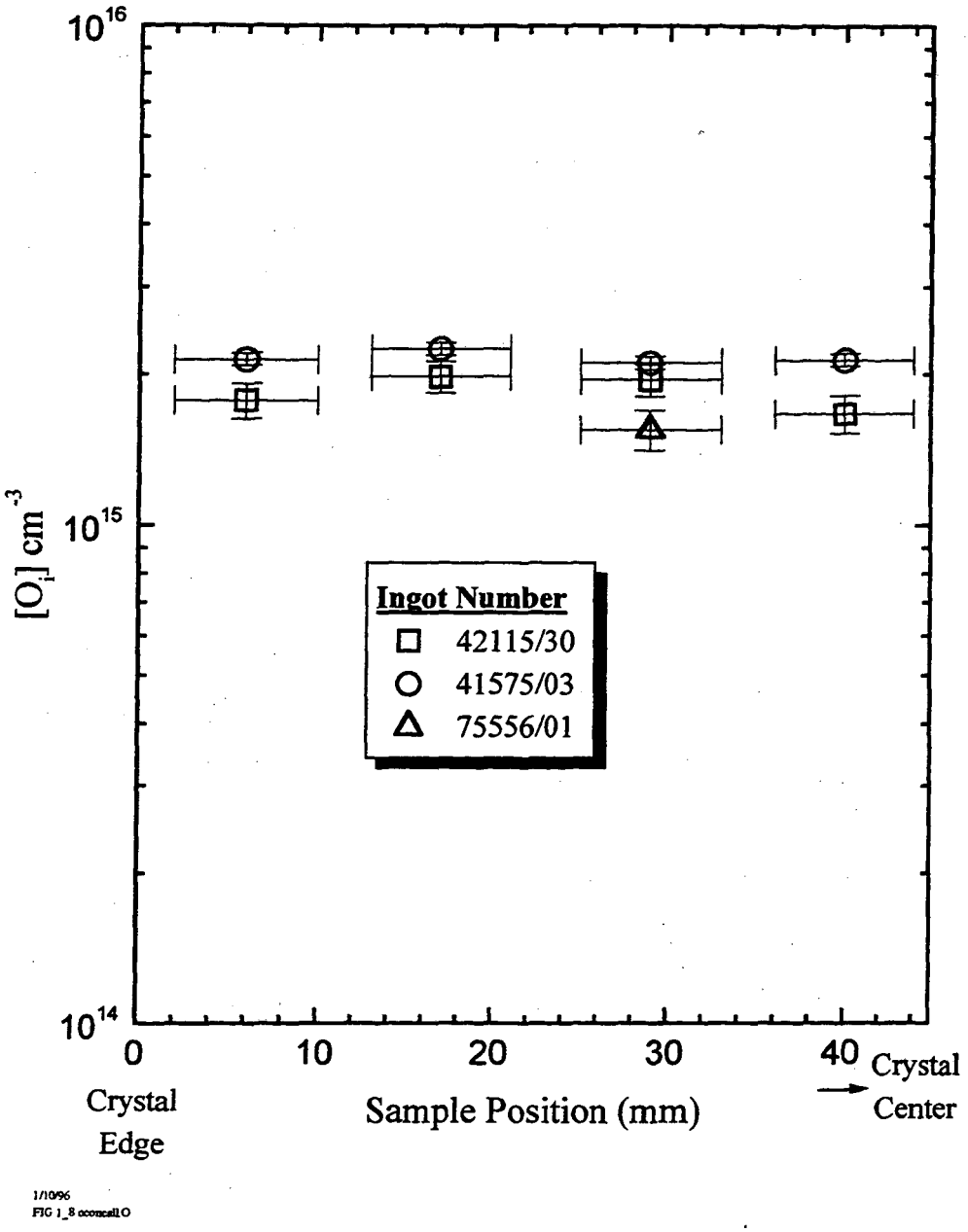

Figure 1.8: The oxygen interstitial concentration is shown as a function of radial position across several 100 mm in diameter FZ Si wafers. The concentrations were calculated from the measured vibrational spectra of samples taken from the wafers. The same temperature and resolution were used as stated in figure 1.7. For information concerning the Si crystals listed in the legend, refer to table 1.1.

Figure 1.8 is a plot of the O_i concentration with respect to the radial position of each sample. The results for several wafers are included on the plot. As can be seen, the O_i concentration is about $2x10^{15}$ cm^{-3} and does not vary radially.

Since the O_i concentration in the central region of the wafers is the same as in the wafer periphery as shown in figure 1.8, then oxygen is not responsible for hindering Li^+ drifting. Hence, the only currently viable explanation for hindering Li^+ drifting in the central region of the wafers is the presence of D-defects. In fact, many researchers have reported an accumulation of D-defects in the central region of Si crystals.[Abe and Kimura, 1990, 5; Abe and Takeno, 1992, 6; Ammon, et al., 1996, 9; Chikawa, et al., 1986, 23; Kitano, 1991, 63; Roksnoer, 1984, 90; Takeno, et al., 1992, 104; Yamagishi, et al., 1992, 114] In summary, this result indicates that the defects responsible for hindering Li^+ drifting are most likely D-defects.

1.2.3 The effect of nitrogen doping on D-defects

Several authors have suggested that nitrogen (N) doping of Si during crystal growth inhibits the formation of D-defects. [Abe, et al., 1986, 2; Ammon, et al., 1994, 10; Yamagishi, et al., 1992, 114] In this section, results are presented from a study using Li^+ drifting to test this hypothesis.

Background

In N-doped Si in which N – O interaction is minimal, N interstitial pairs (N_2^I) having C_{2h} symmetry are the dominant defect.[Jones, et al., 1994, 60; Rasmussen, et al., 1995, 87; Stein, 1985, 97]] In the D-defect rich region, N pairs are thought to be incorporated into vacancies forming complexes.[Abe, et al., 1986, 2] It has been suggested that the apparent disappearance of the D-defect region in N doped Si is attributed to the interaction between Si self-interstitials with the N-vacancy (N-V) complexes forming N_i pairs and annihilating vacancies.[Abe and Kimura, 1990, 5; Ammon, et al., 1994, 10]. The reactions are given by:

$$N_2^I + V \rightarrow N_2^{subst} \tag{1.8}$$

and

$$N_2^{subst} + I \rightarrow N_2^I \tag{1.9}$$

where N_2^I and N_2^{subst} are the interstitial and substitutional nitrogen pairs, respectively. From the overall reaction, it can be seen that the vacancy is annihilated by a Si self-interstitial.

To better understand the results of the various authors, it is important to understand the methods used to detect D-defects and their limitations. Cu decoration in conjunction with X-ray topography and X-ray absorption fine structure (XAFS) of FZ Si wafers has been successfully used to reveal a region of A-defects near the wafer periphery and D-defects in the central region of the wafer.[Kitano, 1991, 63; Roksnoer and van den Boom, 1981, 91] However, Cu decoration requires high temperature processing (~1000°C), potentially giving rise to unwanted thermally activated processes.

For this reason, other techniques, not requiring high temperature cycles, have been developed to identify the distribution of point defect agglomerates in Si wafers.

Yamagishi *et al.* have demonstrated that clusters of point defects can be revealed in Si wafers by using a Secco etch and examining the surface morphology of the resultant patterns with optical microscopy.[d'Aragona, 1972, 25; Yamagishi, et al., 1992, 114] The surface morphology of the A-defect region is striated while the D-defect region shows flow-like patterns called flow pattern defects (FPDs). The FPD region has been shown to correlate well with the D-defect regions revealed by the Cu decoration technique. The Secco etch technique depends on careful etching of the wafer and some interpretation of the observed FPDs.

Regions with a high concentration of crystal originated particles (COPS) have been well correlated with the D-defect regions revealed by Cu decoration. The COPS test originated from the observation that extended cleaning of Si wafers in the SC1 solution (section 1.1) led to an increased particle count as detected by laser particle counting (LPC). The use of the COPS test for detecting D-defects is dependent on the etching process, wafer cleanliness, and a well calibrated LPC system.[Ryuta, et al., 1990, 92]

The three diagnostic techniques described above give indirect evidence of the poor gate oxide integrity (GOI) of devices, indicating poor device yield, noted earlier. A direct approach to the question of device yield is to actually fabricate and test simple MOS devices. The GOI test does this by determining the dielectric breakdown voltage (DBV) of simple MOS diodes (e.g., [Triplett, 1994, 106]). Abe and Kimura [Abe and Kimura, 1990, 5] have shown that a possible correlation exists between FPDs and poor GOI. They postulated that a low DBV in SiO_2 was caused by D-defects. This result was

collaborated by other researchers.[Ammon, et al., 1994, 10; Yamagishi, et al., 1992, 114; Yamagishi, et al., 1994, 115] A correlation between COPS and poor GOI was found to support the suggestion that D-defects cause poor gate oxide integrity.[Abe and Takeno, 1992, 6; Yamagishi, et al., 1992, 114] Finally, the GOI procedure also requires high thermal processing and therefore suffers from the same difficulty as the Cu decoration technique.

Experimental procedure, results and discussion

To explore the effects of N used during crystal grown on Li^+ drifting several 3 mm thick, 103 mm diameter, B and N doped <111> p-type FZ Si wafers were cut from an ingot grown by Wacker-Chemitronic which successfully passed their GOI tests. To test GOI, the time zero dielectric breakdown voltage (DBV) of MOS devices is measured. A range of time zero DBVs exist which corresponds to various mode failures. For instance, a DBV of greater than 8MV/cm corresponds to a C mode failure. Table 1.2 lists the failure modes coinciding with DBVs.

In the wafers used in this experiment, the concentration of N, C, and O was $3x10^{14}$ cm^{-3}, $\leq 5x10^{15} cm^{-3}$, $2x10^{15}$ cm^{-3}, respectively (see table 1.1). Furthermore, the resistivity was 1250 Ω cm, the lifetime was 900 μs, and the growth rate was 2.5 mm/min. Each wafer was cut radially through the center into several 11 mm^2 square samples. To determine the radial driftability of the wafer, four pairs of samples, with each pair spatially equivalent, were taken starting at the center and moving to the wafer edge as shown in figure 1.9. Sample pairs were used to assess reproducibility. Following the

thermal evaporation of a Li metal film, diffusion of Li was performed. Each sample was Li^+ drifted. The regions in which Li drifting was performed in the cut samples are shown as shaded squares in figure 1.9. The samples were cut in half and copper stained to measure the Li^+ drift depth profile (i.e., drift depth with respect to the radial distance from the wafer center).

Table 1.2: Types of time zero DBV failures [Ammon, et al., 1994, 10]

Failure Mode	A mode	B^- mode	B^+ mode	C mode*
***E* (MV/cm)**	<1	1-5	5-8	>8

***Note:** C^- and C^+ mode failures exist with the range of *E* that C has, but their hold times differ.

The results of copper staining of the cut samples are shown in figure 1.10. The Li^+ drift depth is given as a function of radial distance across the wafer. For the sample pairs from the central region, the Li^+ drifts less than half of the way through the sample. Approximately 22 mm from the wafer edge, the Li^+ drift depth increases significantly. Li^+ drifting is complete about 12 mm from the edge. Reproducibility is apparent between sample pairs.

From figure 1.10, a correlation between Li^+ drift depth and radial distance from the wafer center becomes evident. The abrupt increase in Li^+ drift depth 12 mm from the wafer edge indicates a circular border separating an outer driftable from an inner predominantly undriftable region. This same pattern was seen in wafers containing D-defects as described in the preceding section. Comparing the results in the preceding section to those reported here, good agreement exists between the undrifted region in figure 1.10 relative to figures 1.5 and 1.6. The undrifted regions of both the N doped and

undoped FZ Si are similar indicating that the N doping has not completely removed the D-defects. Furthermore, these results correlate well with the poor GOI regions reported by von Ammon et al. on similar non-N doped FZ Si wafers.[Ammon, et al., 1994, 10]

The results indicate that, although N reactions following equations 1.8 and 1.9 may take place, the D-defect regions are still present. In other words, the concentration of D-defects has been reduced below the detection limits of typical detection techniques used to determine the presence of D-defects. These techniques include X-ray topography or XAFS of Cu decorated Si wafers, optical microscopy of a Secco etched Si surface, LPC of a Si surface after an extended SC1 clean, and voltage stressing of patterned oxidized Si wafers. Although X-ray topography of Cu decorated crystals and GOI tests are more sensitive than the etching techniques that reveal D-defects via the creation of FPD and COPS, they are not nearly as sensitive as the Li^+ drifting method.

Subsequent to the results reported here, several companion samples from this N doped crystal were subjected to the $POCl_3$ procedure discussed in the previous section. These samples could be Li^+ drifted through the entire wafer with the results similar to those obtained in the section on the $POCl_3$ process. Two points can be made in response to the cessation of Li^+ drifting in the central region of N doped FZ Si and the success of the $POCl_3$ process of N doped FZ Si. First, Li^+ drifting is a more sensitive means to detect D-defects than other techniques used to delineate D-defects, and second, a very likely cause for the undriftability of the central region in the N doped FZ Si are D-defects. Transmission electron microscopy results of Li^+ drifted N doped samples are presented in section 1.3.2.

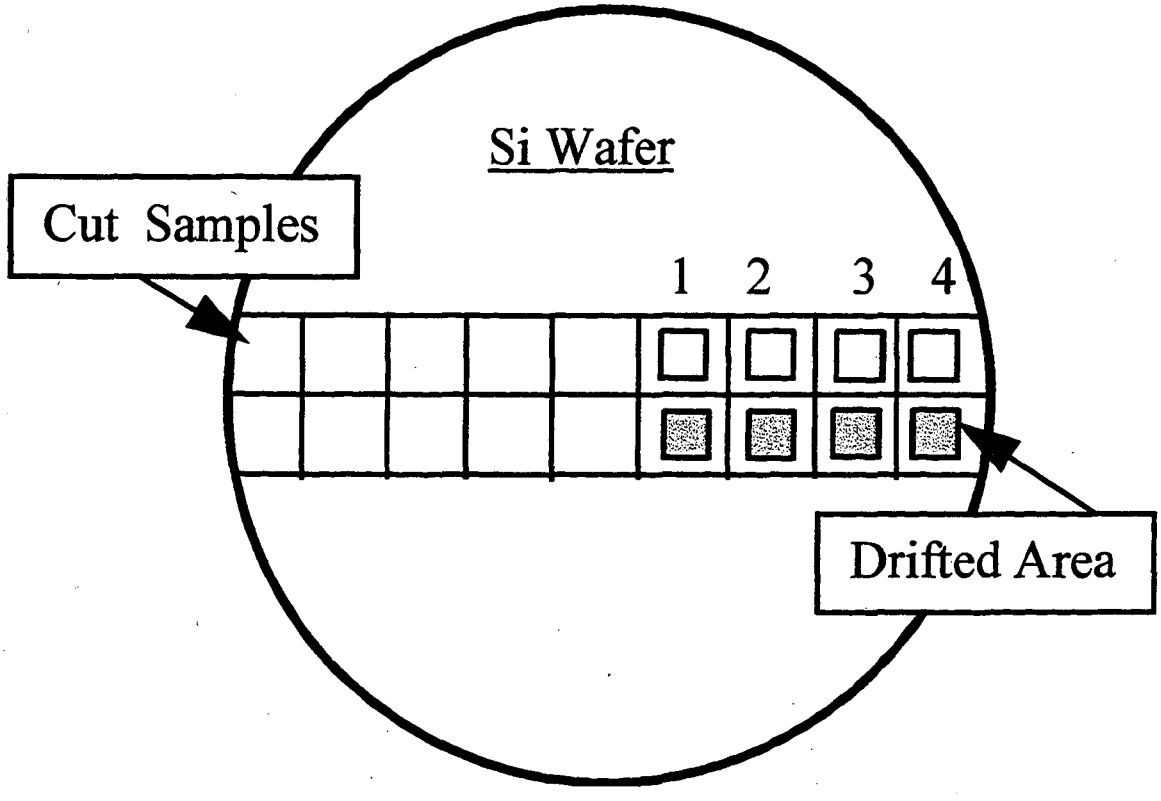

Figure 1.9: The pairs of samples which were drifted are labeled 1 through 4. Due to detector fabrication restraints, the shaded areas are the regions that are Li^+ drifted.

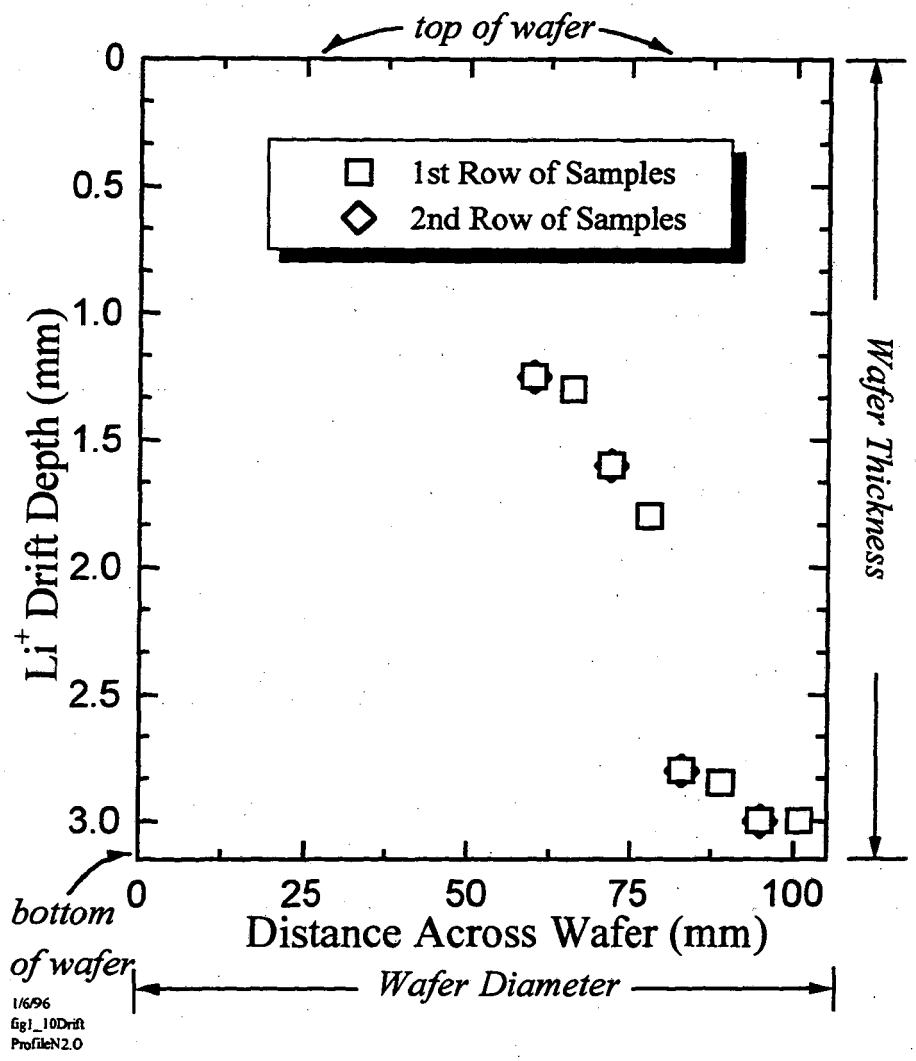

Figure 1.10: Li^+ drift depths shown for samples pairs 1-4 as illustrated in figure 1.9. The results are analogous to figure 1.5 and 1.6.

1.3 Preliminary TEM Study of the Partially Li^+ Drifted D-defect Region

Although D-defects are known to impede Li^+ drifting, it is not known how or why they hinder the Li^+ drifting process. Precipitation of Li^+ is a reasonable hypothesis since vacancy clusters provide a suitable site for precipitates to form. To examine this hypothesis, an exploratory TEM study was conducted. In this section, general background information on TEM is given first. Next, the experimental procedure, results and discussion are presented.

1.3.1 General TEM background

TEM is a powerful analytical tool used in the characterization of a wide variety of materials. The great strength of TEM is that it provides access to information down to the atomic level in real and reciprocal space using the same instrument. Furthermore, it offers the ability to filter the information in one space and observe the effect in the other space.

In TEM, electrons are accelerated to an energy between a few tens of keV to over 1 MeV and pass through the thin sample (~ 100 Å to 10 μm thick) to be investigated. The electrons are focused electromagnetically. The electron image is filtered in real and reciprocal space with apertures placed in the electron beam at appropriate foci. The wave-like nature of the incident electrons (and all electrons) gives rise to diffraction effects from periodic potentials in the material. A crystal will therefore act like a diffraction grating resulting in well defined maxima in reciprocal space. The transmitted beam and diffracted beams can be used to form an image in several ways.

The two types of imaging that can be used are *low magnification* (< x100,000) *diffraction contrast* and *high magnification* (≥ x100,000) *phase contrast.* In low magnification diffraction contrast, usually either the transmitted or a single diffracted beam is used to form the image. *Bright field* (BF) images are formed using the transmitted beam while *dark field* (DF) images are formed with the diffracted beam. These images contain information about crystal orientation and perfection, and they are commonly used to investigate the structure of extended crystal defects (e.g., dislocations, stacking faults, precipitates, etc.). Diffraction contrast images are obtained from crystals as thick as several micrometers.

In phase contrast, many diffracted beams are used together with the transmitted beam to generate an image. The image contains periodic fringes corresponding to the projected planar spacings of the crystal. Phase contrast images are usually taken along high symmetry directions containing several low index planes. Phase contrast is applicable only to very thin (~ 100 Å) specimens. For a full discussion of phase contrast imaging, refer to the references of Loretto and Thomas.[Loretto, 1984, 68; Thomas and Goringe, 1979, 105]

Understanding image contrast requires knowledge of diffraction theories. If multiple scattering of a diffracted electron beam occurs, then *dynamical theory* must be used. The much simpler *kinematic theory* is used if single scattering of an electron beam can be assumed. Kinematic theory is valid for thin specimens and weak scattering (diffraction) of electrons. If the crystal is oriented with respect to the incident electron beam such that only one diffracted beam is excited, then the *two beam approximation* (two beam condition) is presumed.[Hull and Bacon, 1984, 55] This further simplifies the

analysis of diffraction contrast images. A full discussion of diffraction contrast is beyond the scope of this thesis.

1.3.2 Experimental procedure, results and discussion

TEM was performed on samples taken from the region in which Li^+ drifting was hindered. These results were compared to TEM results obtained from wafers that are D-defect free that have and have not been Li^+ drifted. Furthermore, comparisons were made to TEM results acquired from samples taken from the Li^+ drifted near periphery region of wafers containing D-defects. Recall that the near periphery region of D-defect containing wafers fully Li^+ drift indicating that D-defects do not exist near the crystal periphery (see figure 1.5).

Sections were cut from a wafer in the partially Li^+ drifted region caused by D-defects and also the near periphery fully Li^+ drifted region. Sections were also cut from both undrifted and Li^+ drifted wafers that did not contain D-defects. Samples, 3 mm in diameter, were cored with an ultrasonic cutting tool from the sections. TEM samples were prepared from the cores by etching with a $HF:HNO_3:H_2O$ solution until they were electron transparent. TEM was performed on samples from each region using bright field (BF) imaging conditions. The results from each region were compared.

The TEM results from the samples taken from the region in which Li^+ drifting was impeded show the presence of precipitates. The precipitates are readily discernable in the BF micrograph in figure 1.11. This is not the case for the samples taken from the Li^+ drifted near periphery region of wafers containing D-defects. TEM results on these

samples do not show precipitates. The BF micrograph (figure 1.12) is typical of the TEM results obtained from Li^+ drifted, as well as undrifted, wafers that are D-defect free. Precipitates were not observed in these samples either.

The results indicate that D-defects inhibit the Li^+ drifting process by Li precipitation. The flux of Li^+ is proportional to the acceptor concentration ($\sim 5 \times 10^{12}$ cm^{-3}) and thus is very small. Therefore, the halting of drifting Li^+ at such small concentration by precipitation is indeed plausible.

Nitrogen (N) doping of single crystalline Si is a technique that has been shown and utilized to suppress the D-defects in the central region of the Si ingot. Experiments were previously described in which the Li^+ drifting process on N doped FZ Si was carried out. The results indicated that D-defects were present, but perhaps at concentrations below the sensitivity of the other techniques used to determine their existence. TEM was subsequently performed on N doped FZ Si using the same experimental procedure described above. Again, precipitates were seen in the central region after Li^+ drifting but were not found in the peripheral regions of the wafers. This further establishes the presence of D-defects in N doped FZ Si and that D-defects hinder the Li^+ process via precipitation.

Further TEM studies are needed to determine the structure of the precipitate through contrast and diffraction analysis. Moreover, a TEM study of precipitation density distribution may provide information on D-defects.

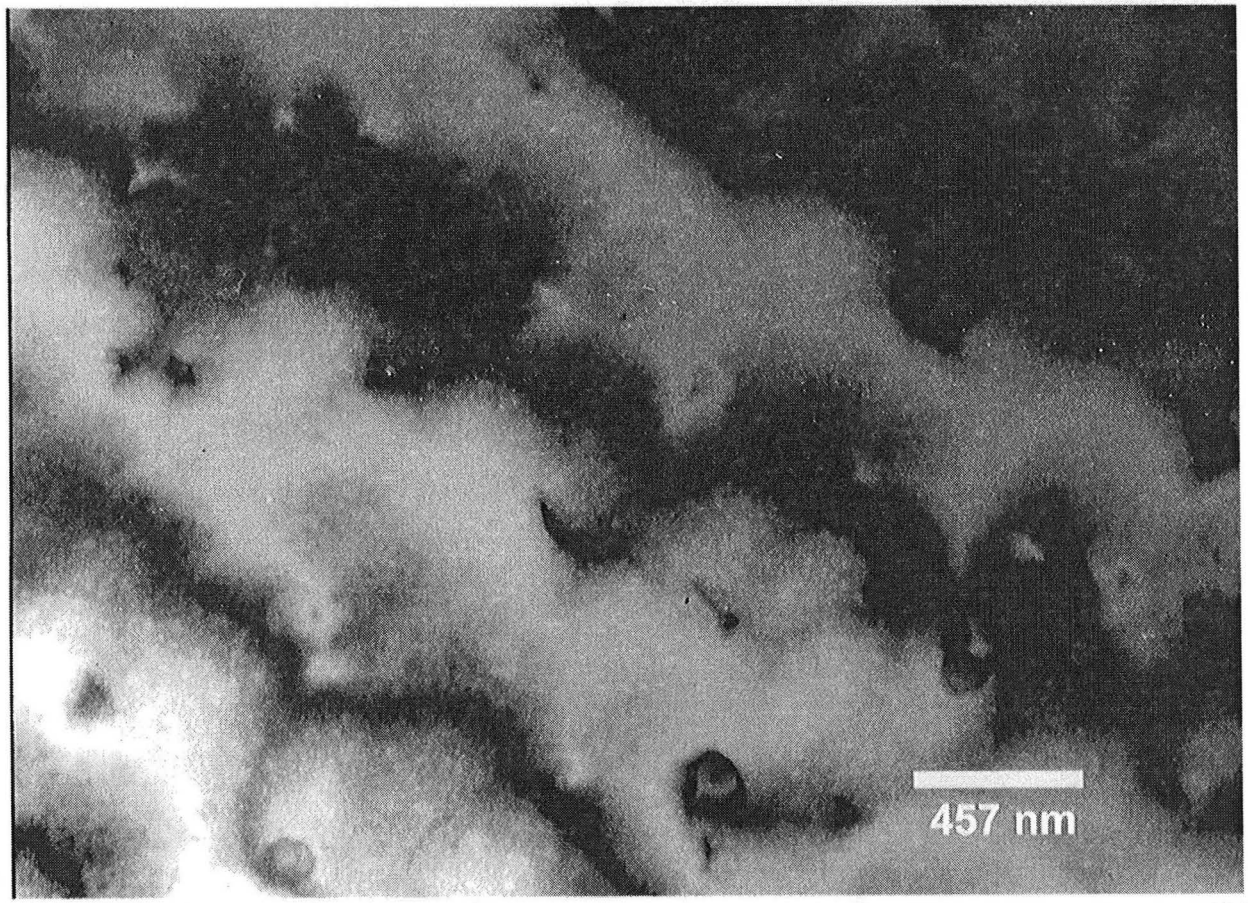

Figure 1.11: A bright field TEM micrograph of the samples taken from the region in which Li^+ drifting was hindered. Note the presence of precipitates. The alternating dark and bright bands, called thickness fringes, are due to the change in thickness brought about by the wedge-like shape of the sample. The change in the thickness fringes by the precipitates is caused by strain.

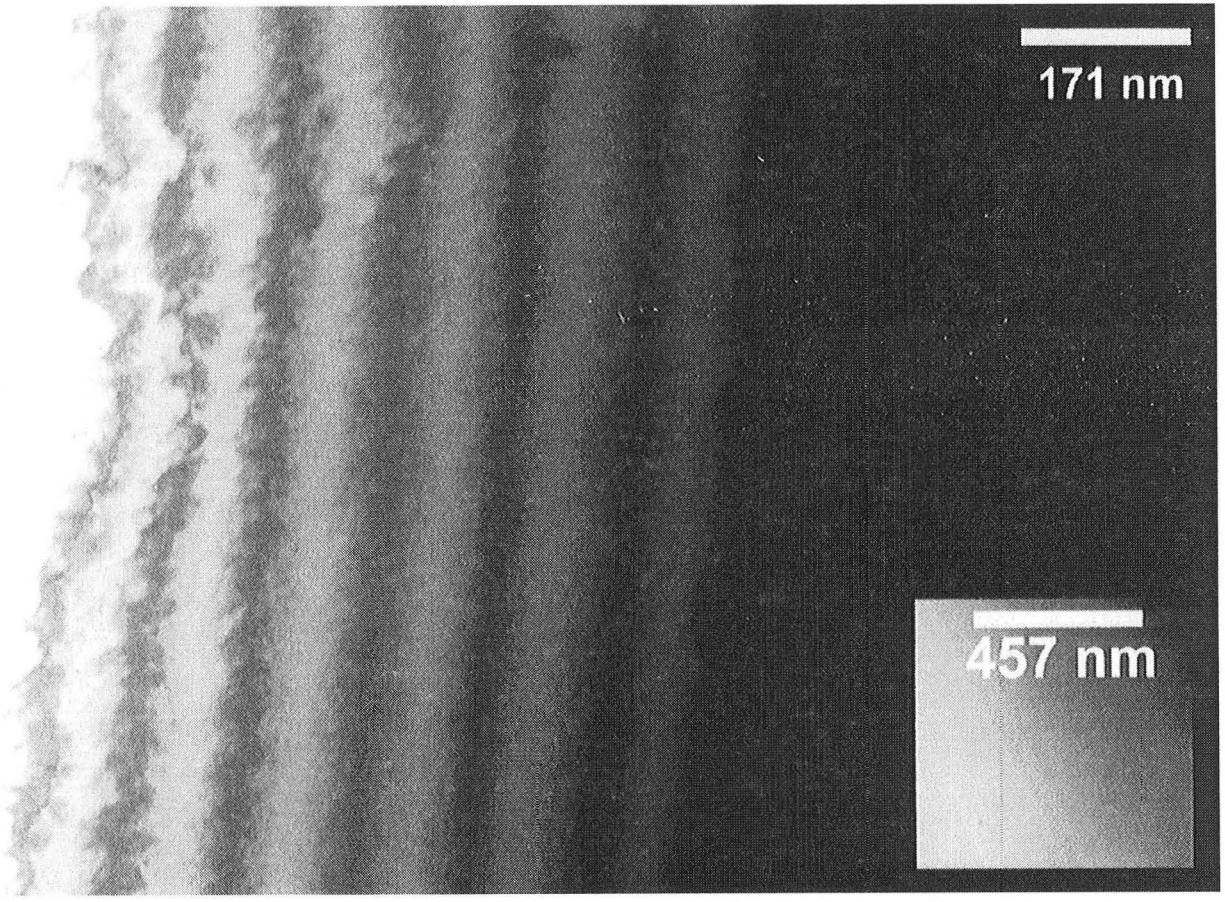

Figure 1.12: The bright field TEM micrograph represents results obtained from wafers that are D-defects free and that both have and have not been Li^+ drifted. The micrograph is also represtative of results obtained from samples taken out of the Li^+ drifted periphery region of wafers containing D-defects. For comparison, the inset shows a micrograph taken at the same magnification as figure 1.11 since the micrograph above was taken at a higher magnification.

1.4 Selected Area Diffraction and Contrast Analysis of Precipitate-Like Defects

As described in the previous section, Li^+ drifting is impeded by D-defects via precipitation. In this section, a study of the precipitates is conducted using selected area diffraction (SAD) and contrast analysis. The TEM techniques required for this study, such as selected area diffraction, the two-beam condition, and double diffraction effects, are described in appendix 4.4. In this section, the experimental procedure and results are presented and discussed and conclusions are formulated.

1.41 Experimental procedure

Samples were taken from various regions of wafers containing D-defects following Li^+ drifting. Most of the samples examined came from regions where Li^+ drifting was incomplete. Thin and thick regions with a particularly high concentration of precipitates were chosen for analysis. SAD was performed on both regions. However, emphasis for the analysis was placed on the thin region. SAD was done in three zone axes orientations: [111], [110], and [322], and micrographs were taken for each zone axis. Additionally, image contrast analysis was performed in the thin region for the three zone axes orientations. For these zone axes orientations, the two-beam condition was met for several reciprocal lattice vectors (***g***'s). Both BF and DF image micrographs were taken for the selected ***g***'s. On only a few occasions were -***g*** two-beam conditions performed and recorded on film. Finally, TEM calibrations were performed to properly interpret the data. The background and results of the calibrations are presented in appendix 4.3.

1.42 Results and discussion

The results of the TEM indicate the presence of precipitates within the matrix and are shown in figure 1.13. Non-matrix reflections were obtained for the [-233] (figures 1.14 and 1.15) and [111] (figures 1.16 and 1.17) matrix zone axes when performing SAD but no new reflections were seen for the [110] zone axis (figures 1.18 and 1.19). The new reflections for the [111] zone axis have three-fold symmetry (figures 1.16 and 1.17). The new reflections for the [-233] zone axis (figure 1.15) have two-fold symmetry. Streaks were not seen in the DPs indicating that microtwinning or thin platelet precipitates were not present.

Image contrast results show symmetric reversal of contrast and the absence of fringes and lines of no contrast when going from BF to DF for several ***g***'s of several zone axes. For the [111] zone axis, two-beam conditions were set for the (20-2), (-202), (2-20), and (02-2) reciprocal lattice vectors as shown in figures 1.20-1.21, 1.22-1.23, 1.29-1.30, and 1.31-1.32, respectively. Image contrast was sharp and contrast reversal was complimentary. Also for the [111] zone axis, a *2**g*** was accomplished for the (2-20) giving a (4-40) ***g***. In the BF case, contrast was poor for this ***g*** and the DF could not be recorded due to long exposure times and sample drift.

For the [-233] zone axis, two-beam conditions were chosen for contrast analysis of the (-3-31), (33-1), and (3-13) reciprocal lattice vectors. When comparing (-3-31) ***g*** to (33-1) ***g*** (i.e., figures 1.24-1.25), no differences in contrast could be seen. A symmetric reversal of contrast was seen between the BF and DF (33-1) ***g*** as shown in figures 1.25 and 1.26. The sharpness of the image contrast was reduced for both the BF and DF of the (3-13) ***g***; however, a contrast reversal was seen between the two in figures 1.27 and 1.28.

Contrast analysis was performed for several ***g***'s of the [110] zone axis including (111) and (2-20). In general for the [110] ***g***'s, the contrast was diminished, relative to ***g***'s of other zone axes. Contrast reversal occurred between the BF and DF with (111) ***g*** as shown in figures 1.33 and 1.34. Although a reduction in contrast occurred for the *2**g*** (222), contrast reversal did occur between BF and DF which is exhibited in figures 1.35 and 1.36. This was also the case for 3***g*** and 4***g*** (444). This is illustrated for the 4***g*** in figure 1.37 and 1.38 where the two-beam condition in the inset of both figures is the DF 4***g***. For the (2-20) ***g***, reversal of the contrast was apparent between the BF and DF images as depicted in figures 1.39 and 1.40, respectively.

Because the drifting of Li^+ in certain types of FZ *p*-type Si is inhibited Li^+ only partially drifts through these types of Si samples. Li^+ precipitation at grown-in defects was thought to be one explanation of partial drifting. The presence of precipitates in figure 1.13 supports this conclusion. However, the chemical identity of the precipitates has not been absolutely determined.

The extra reflections in the selected area diffraction pattern along the Si [-233] and [111] zone axes can provide information on the identity of the precipitates. Diffraction pattern reflections may be indexed by using vector addition. In figures 1.15 and 1.17 the Si reflections nearest the incident beam are {022} reflections. By vector addition, the extra reflections (indicated by the arrows) must be assigned to the {111} type. The lattice constant of Si is 5.431Å and the crystal structure is diamond cubic (dc). In Si, the $\boldsymbol{g}_{111}$ magnitude is ~0.32 $Å^{-1}$. The distance from the incident reflection to the nearest extra reflection in figure 1.15 is measured using the camera constant calibration (see appendix). The calculated magnitude of the reciprocal lattice vector representing the

extra reflection is 0.28 $Å^{-1}$. Although the magnitude of the reciprocal lattice vectors is very similar to the g_{111} magnitude, reflections from {111} are forbidden along the [-233] and [111] zone axes.[Edington, 1976, 30] The allowed reflections of Si cannot account for the new reflections, therefore they cannot be formed by double diffraction due to the Si.

In certain orientations, the {110} planes in cubic and hexagonal crystal structures produce reflections with three-fold symmetry. The three-fold symmetry of the extra reflections in figure 1.17 suggests indexing these reflections as {110} type planes. The magnitude of the g for the extra reflections nearest the incident reflection in figure 1.17 is 0.29 $Å^{-1}$, which is nearly the same as the magnitude of the g measured in figure 1.15. Therefore, it is probable that the extra reflections in both SAD patterns are created by the same type of planes. Metallic Li has a body centered cubic (bcc) structure and a lattice constant of 3.5101Å. In the bcc structure, the {111} reflections are forbidden but {110} reflections are allowed. In Li, the g_{110} has a magnitude of ~0.4 $Å^{-1}$. A metallic Li precipitate would have reflections beyond the {220} reflections in figure 1.17. Thus, the extra reflections are not from metallic Li.

Another explanation for the extra reflections is that the precipitates may be a lithium silicide. $Li_{21}Si_5$ is listed in the powder diffraction file as having a cubic crystal structure. The Bragg angle (actually $2\theta_B$) for the {440} is 26.83° resulting in a magnitude of g_{440} of 0.30 $Å^{-1}$ which is nearly the same magnitude of g for the extra reflections in figure 1.17. However, the relative intensity of the {440} is only 6%. Another possibility is $Li_{13}Si_4$, which has an orthorhombic crystal structure. The planes and lattice constants of an orthorhombic crystal system can be transformed into the hexagonal system. The

magnitude of g_{220} in $Li_{13}Si_4$, is 0.28 $Å^{-1}$, is approximately the same magnitude of g for the extra reflections in figure 1.17. Again, the {220} has a low relative intensity of 1%.

The extra reflections seen for the SADP along the Si [111] zone axis in figure 1.17 may be explained in another way. The extra reflections can be indexed as 1/3{-422} Si type reflections. The magnitude for $g_{1/3(422)}$ for Si is ~0.3$Å^{-1}$ which is close to that of the extra reflections. John Spence [Spence, 1996, 96] explained that they may be due to stacking faults. Along the [111], introduction or elimination of a half-plane would create a stacking fault. In a thin crystal, stacking faults normal to the electron beam produce forbidden 1/3{-422} Bragg reflections.[Alexander, et al., 1986, 8] This may allow for new reflections to be formed of the type seen in figure 1.17.

Extra reflections are not seen for the SADP along the Si [110] zone axis in figure 1.19. Also, displacement of the reflections is not occurring for each of the zone axis orientations examined. However, streaking of the diffraction spots is apparent which suggests that the precipitate-like defects may induce strain into the crystal.

The contrast analysis of the precipitate-like defects does not reveal any indication of Moiré patterns. Furthermore, displacement fringes are absent as is interface contrast. Although small misfit precipitates creating strain fields may produce images consisting of lobes of contrast, this effect is not seen. This indicates that the defects may not be misfit precipitates. Additionally, lines of no contrast are not seen within the defect suggesting the absence of spherical coherency of the precipitate-like defect with the matrix.

Contrast analysis shows, in all cases, that contrast reversal occurs when changing from BF to DF. Using a matrix two-beam condition, DF imaging shows a sharp reversal of contrast. This indicates that the primary contrast occurring is structure factor contrast.

Precipitate-like defects in Si:Li were seen by TEM. The extra reflections observed in the SADP taken along the Si [-233] zone axis are not produced by Si nor by metallic Li. Furthermore, the extra reflections are most likely produced by a material with a lattice constant greater than that of metallic Li. The presence of extra reflections in the SADP taken along the Si [111] zone axis may be from stacking faults produced by the precipitates. They may also be due to lithium silicides such as $Li_{21}Si_5$ and $Li_{13}Si_4$, which produce g_{220} and g_{440}, respectively, of similar magnitudes. Contrast analysis shows only that structure factor contrast dominates indicating that the predominant contrast type is precipitate rather than matrix type contrast. This suggests that the precipitate-like defects are precipitates.

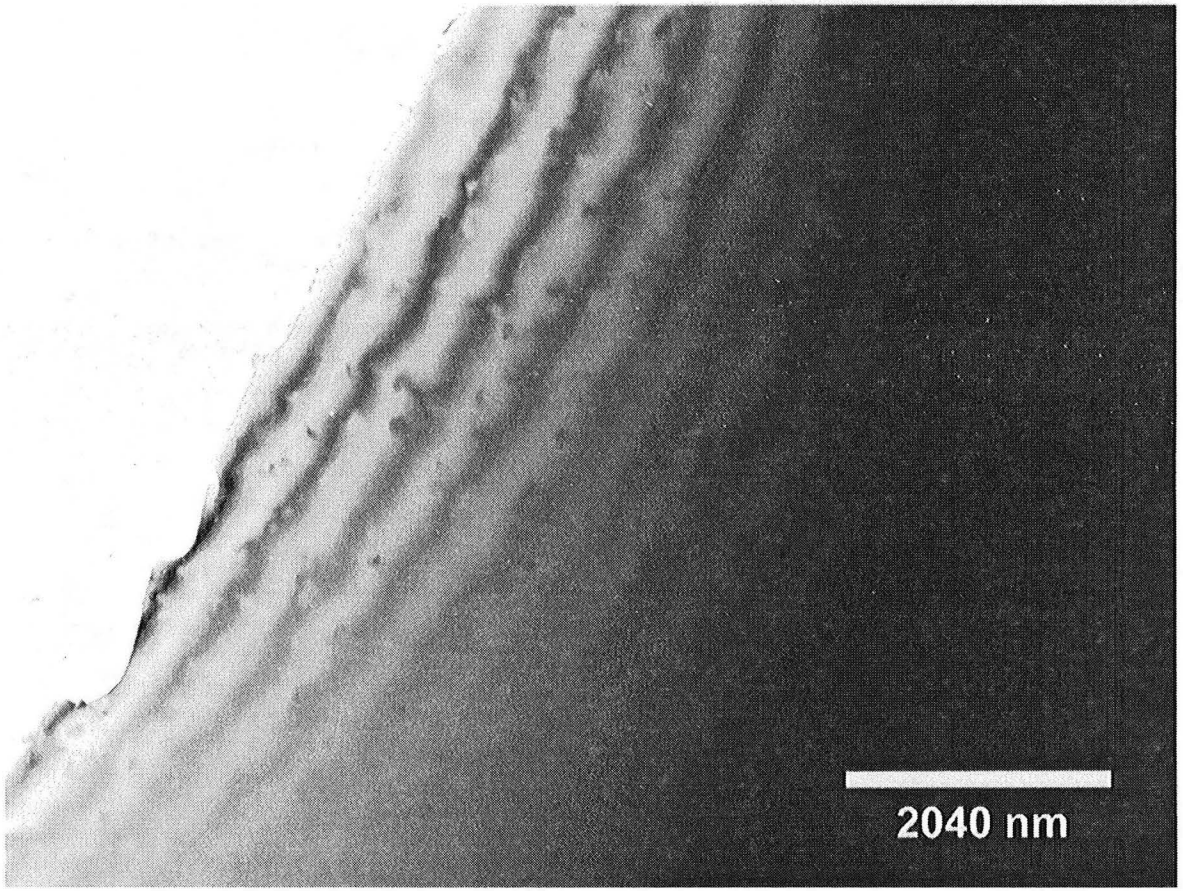

Figure 1.13: The presence of precipitates are apparent in this bright field micrograph taken along the [111] zone axis.

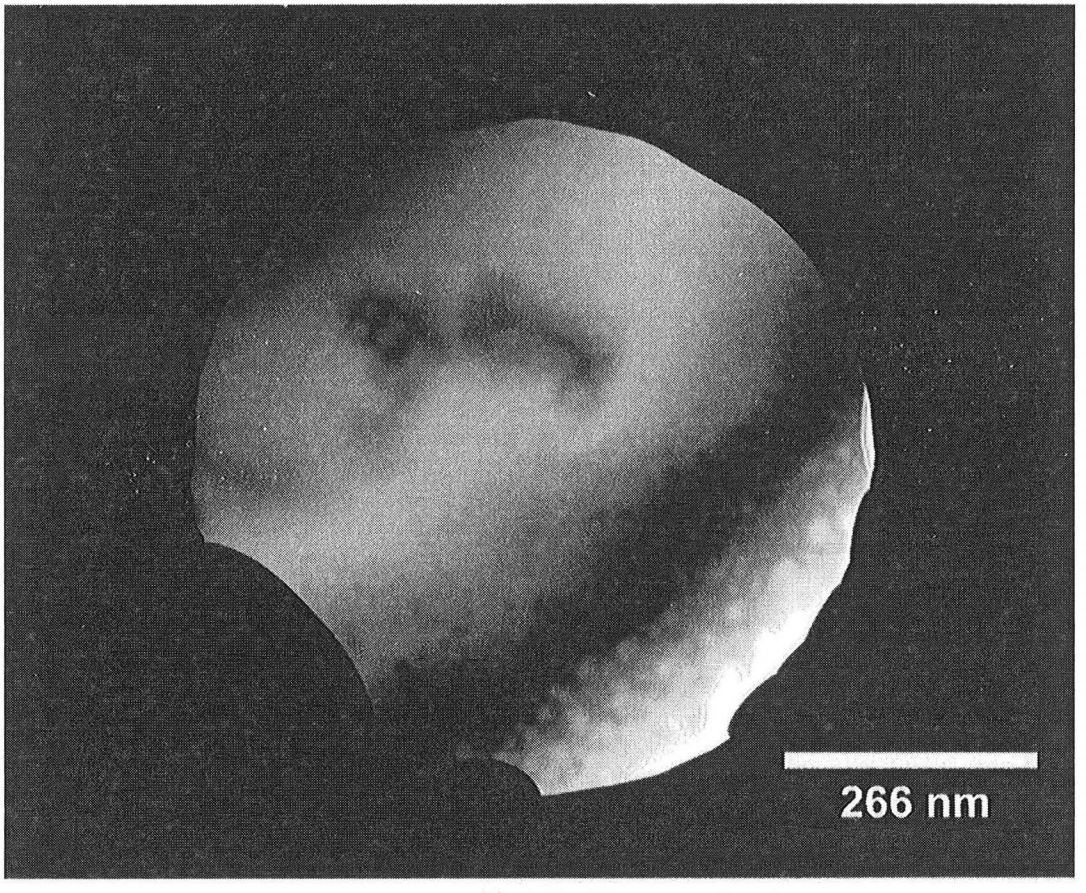

Figure 1.14: The selected area diffraction aperture is shown placed around several precipitates. The bright field image is taken along the [-233] zone axis. The diffraction pattern of figure 1.15 corresponds to this image and aperture.

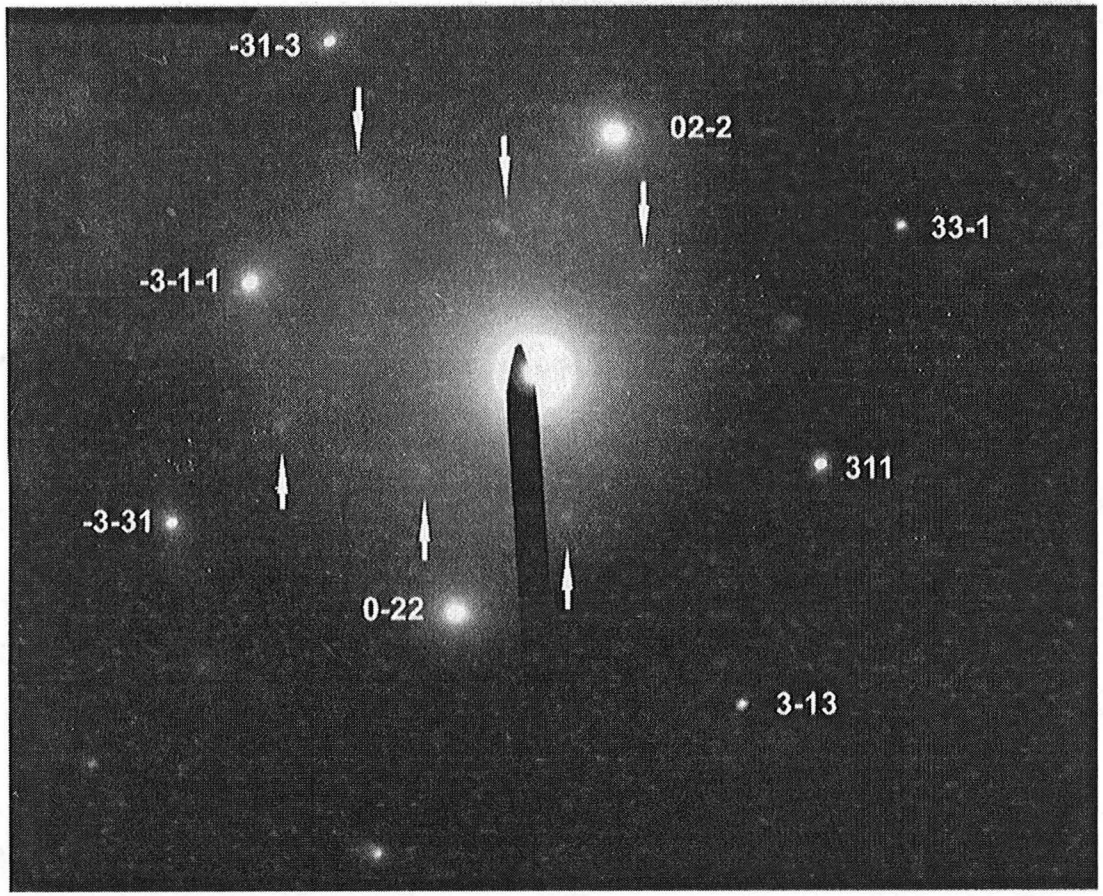

Figure 1.15: SAD pattern of precipitates along the[-233] zone axis of Si. The main reflections of the two-fold symmetric diffraction pattern are labeled. The dark pointer is masking the brightest reflection, which is caused by the incident beam. Notice the dimmer reflections closer to the incident reflection, which are indicated by the arrows. They are not allowed for the diamond cubic crystal structure.

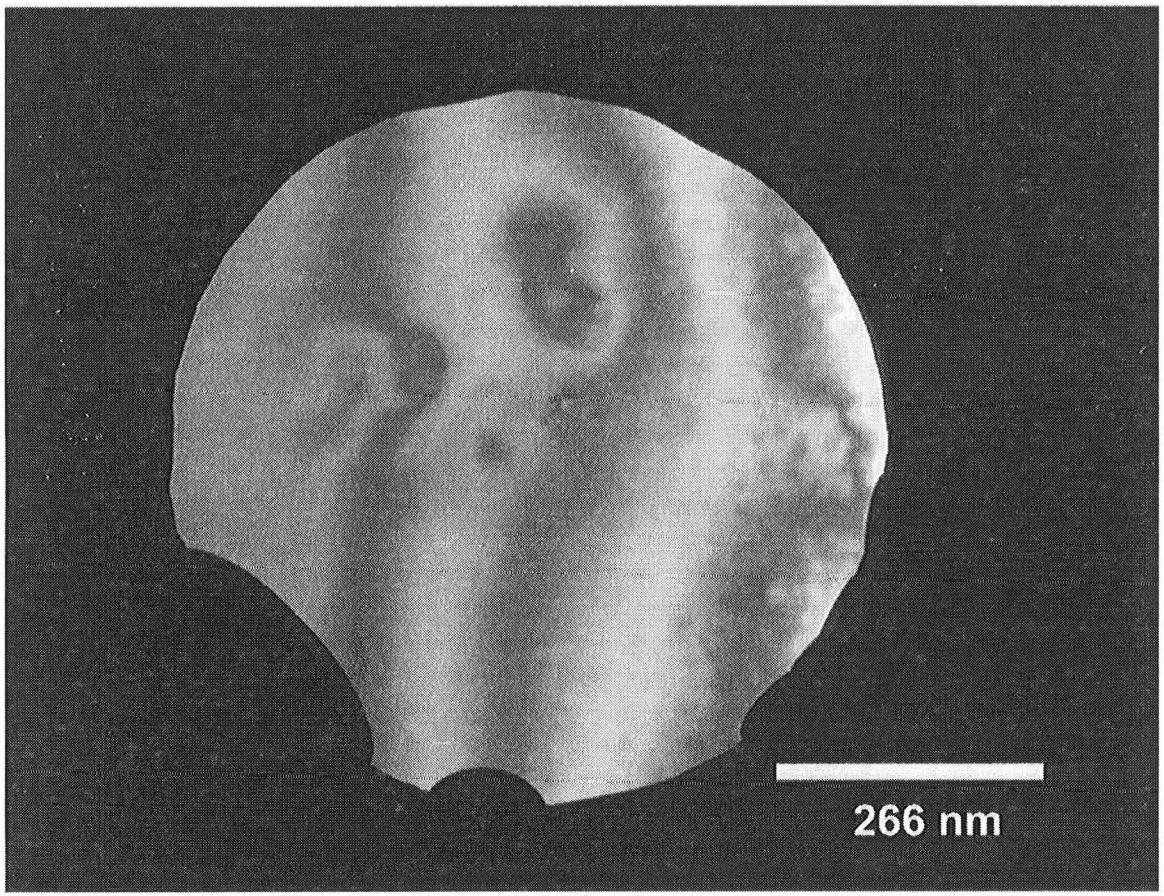

Figure 1.16: The selected area diffraction aperture is shown placed around several precipitates. The bright field image is taken along the [111] zone axis. The diffraction pattern of figure 1.17 corresponds to this image and aperture.

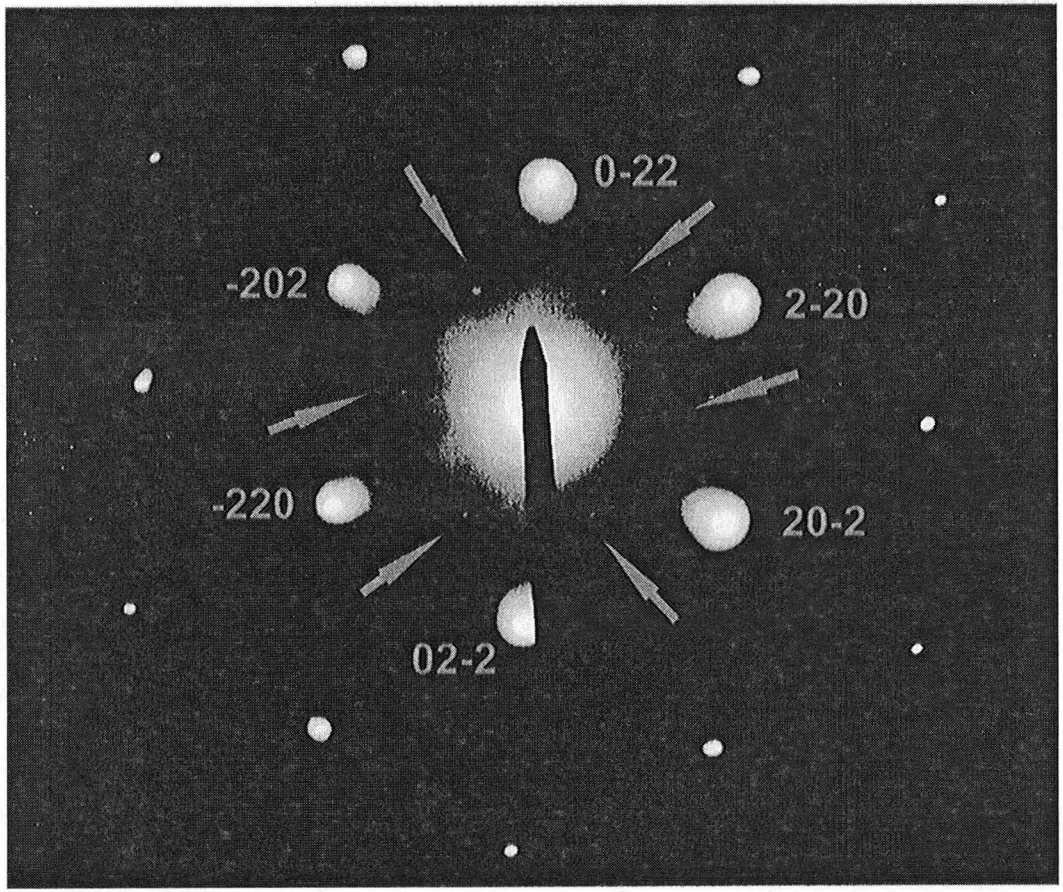

Figure 1.17: A selected area diffraction pattern from the region shown in figure 1.16. As in figure 1.15, reflections not allowed for diamond cubic lattice are seen near the incident beam as indicated by the arrows. These extra forbidden reflections cannot be described by double diffraction. .

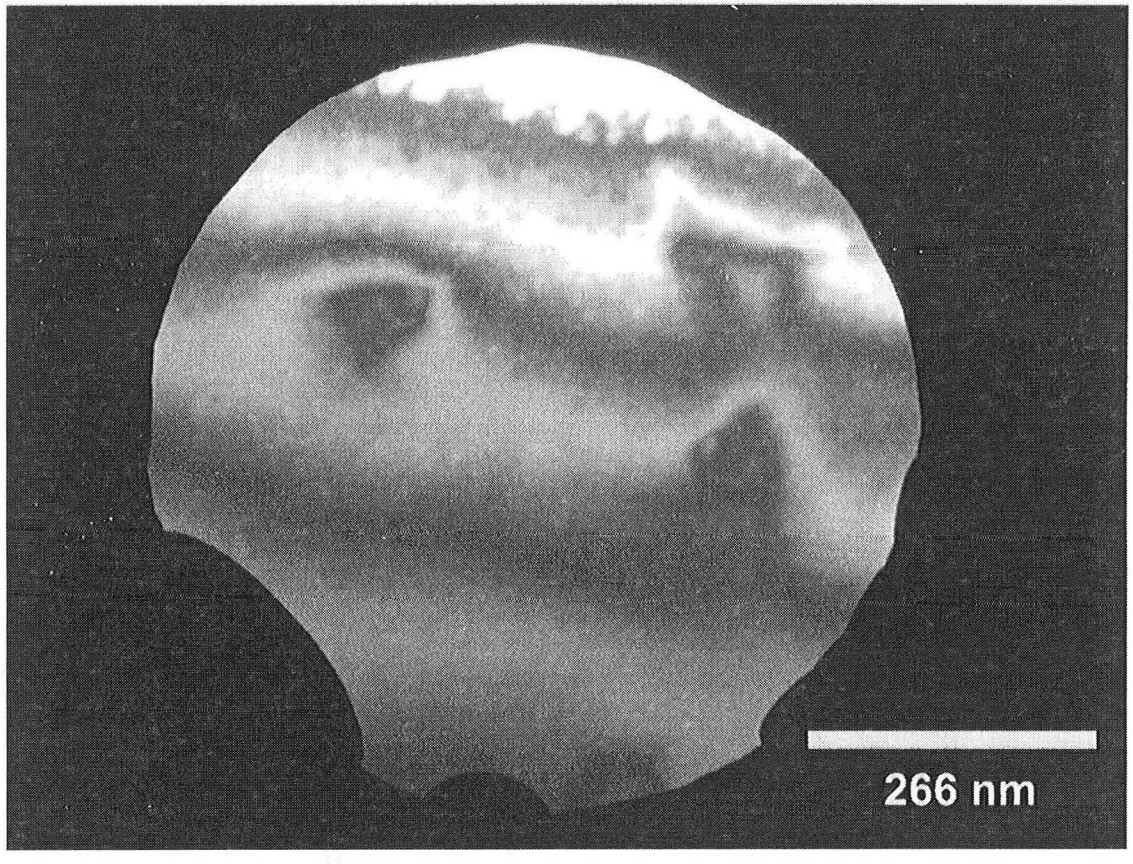

Figure 1.18: The selected area diffraction aperture is shown placed around several precipitates. The bright field image is taken along the [110] zone axis. The diffraction pattern produced from this image is shown in figure 1.19.

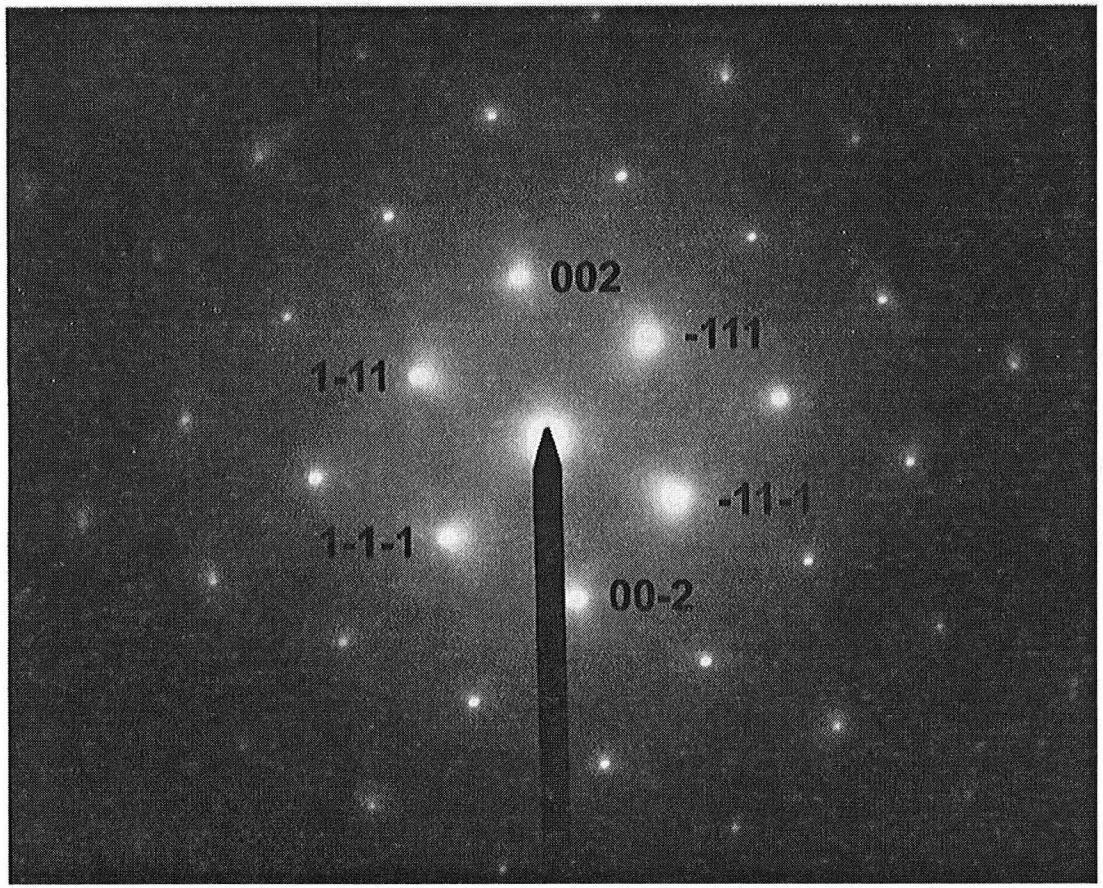

Figure 1.19: A selected area diffraction pattern along the [110] zone axis from the region shown in figure 1.18. Note that extra reflections are not are not present in this [110] zone axis orientation.

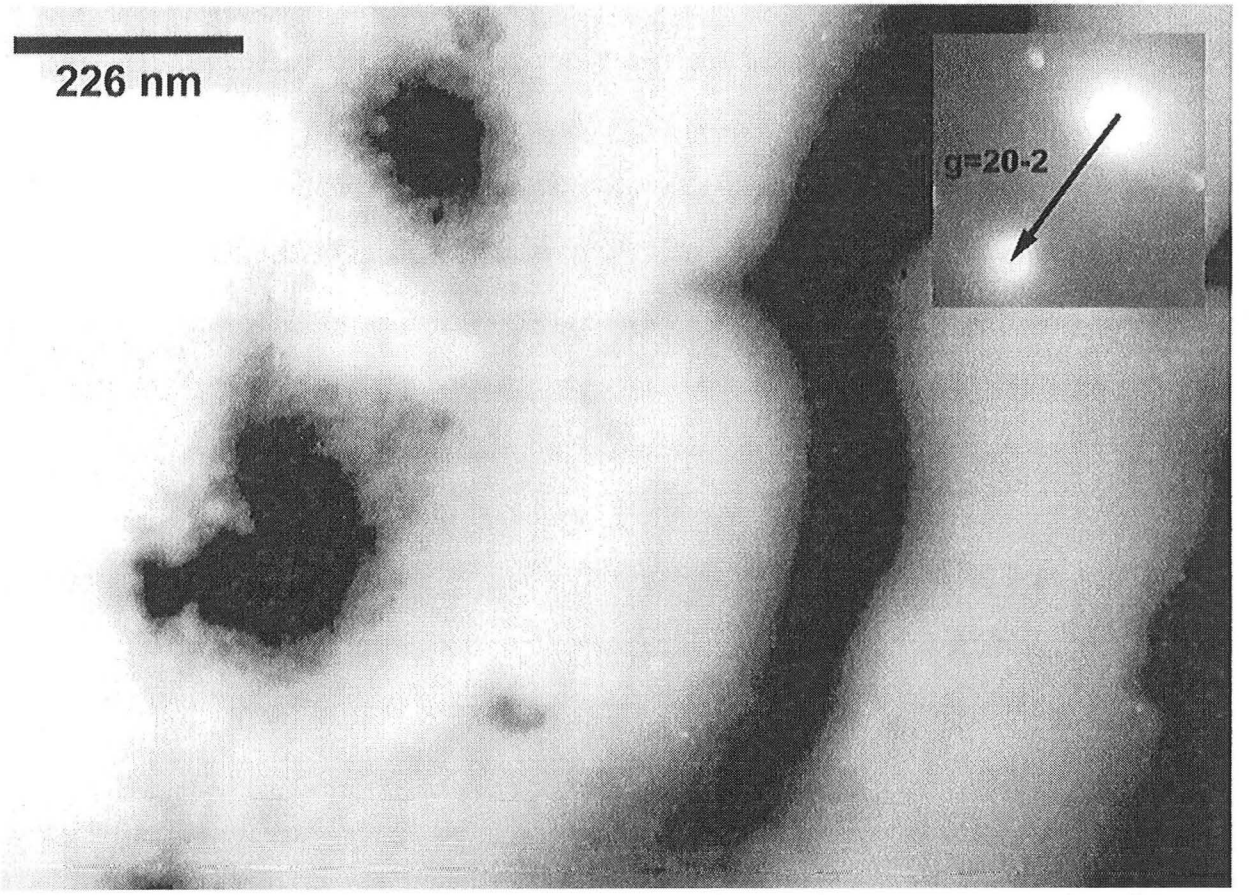

Figure 1.20: A bright field image for the two beam condition, g=20-2. The inset is the two beam condition for the ***g*** shown in figure 1.21. Th two beam condition was achieved with a slight tilt from the [110] zone axis.

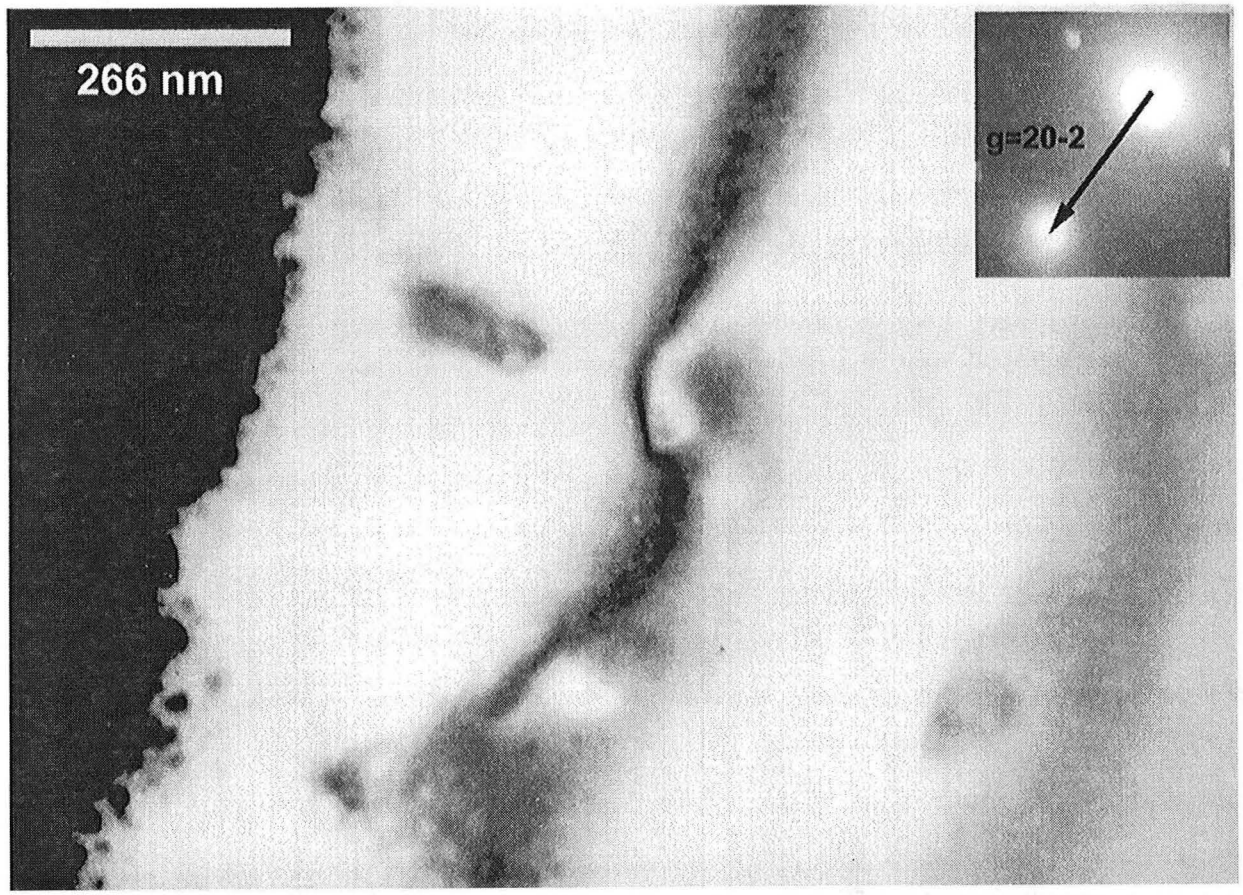

Figure 1.21: A dark field image of the same region, ***g***, and magnification as in figure 1.20. Note that the precipitates have opposite or reversed contrast as compared to figure 1.20. The tail of the arrow in the inset is the reflection from the diffracted beam rather than the incident beam as it is for bright field conditions.

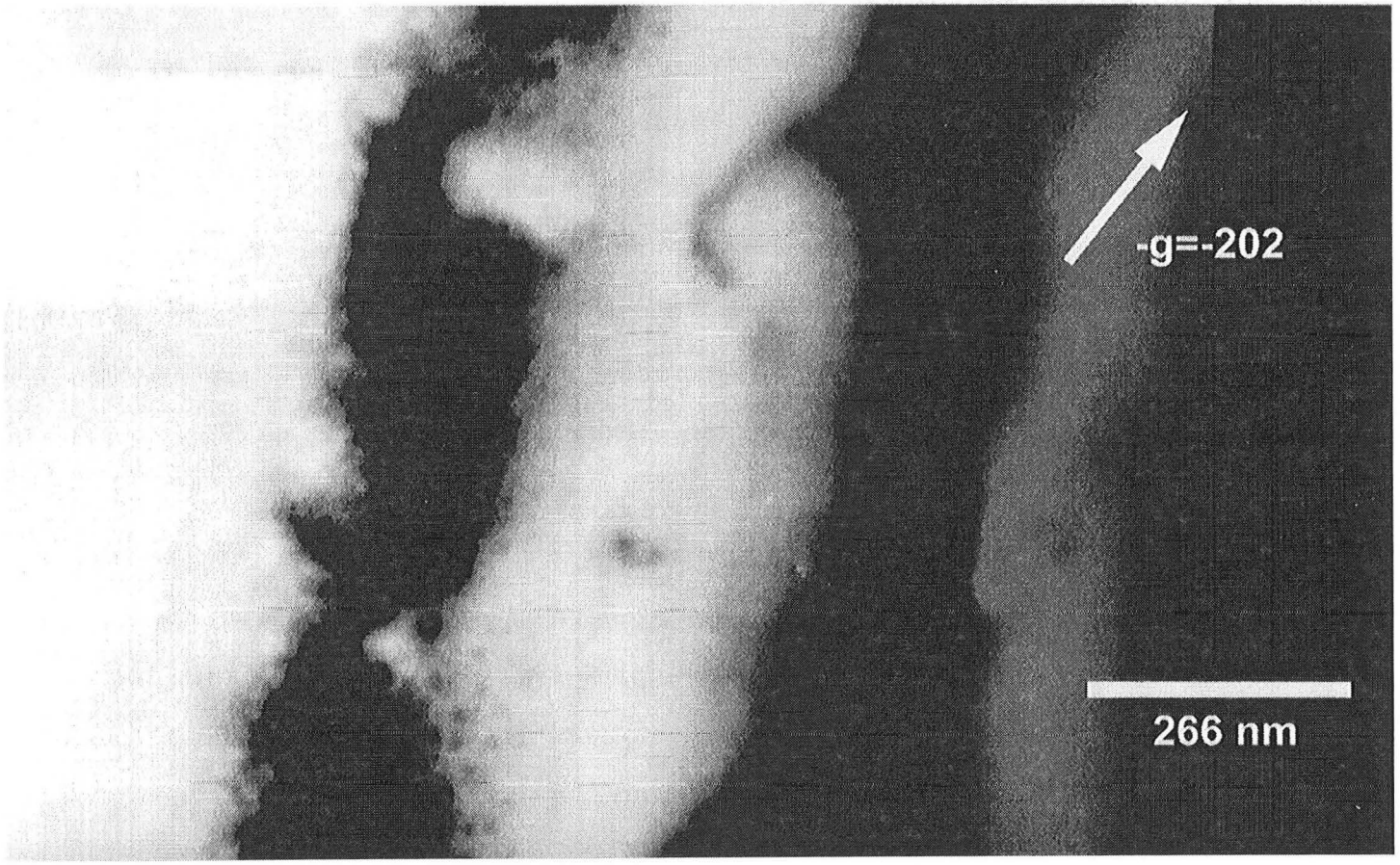

Figure 1.22: A bright field image for the two beam condition, -*g*=-202. A Tilt in the opposite direction from the ***g*** in figure. 1.20 was performed. Note the change in contrast in the precipitates when compared to figure 1.21.

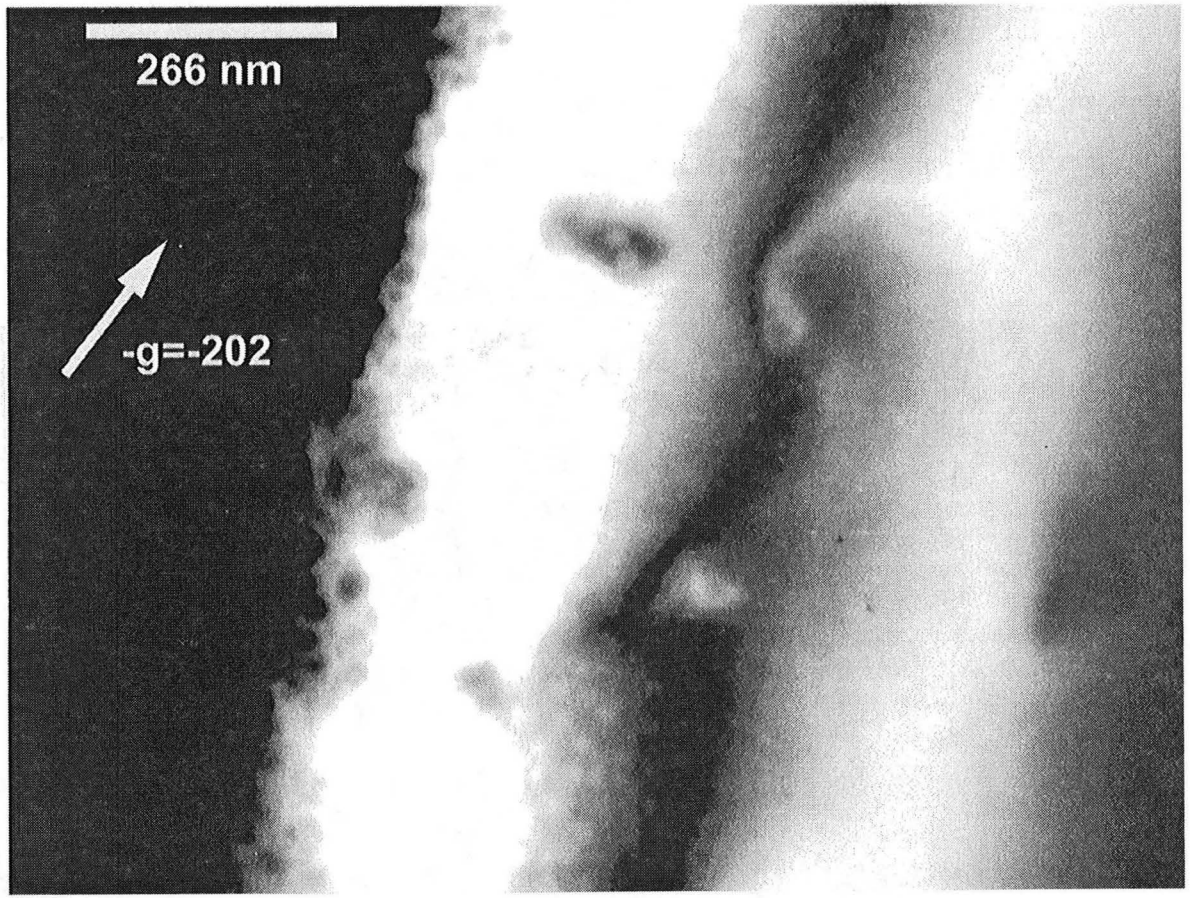

Figure 1.23: A dark field image for the two beam condition, -***g***=-202. A tilt in the opposite direction from the ***g*** in figure. 1.21 was performed. Note the change in contrast in the precipitates when compared to figure 1.22.

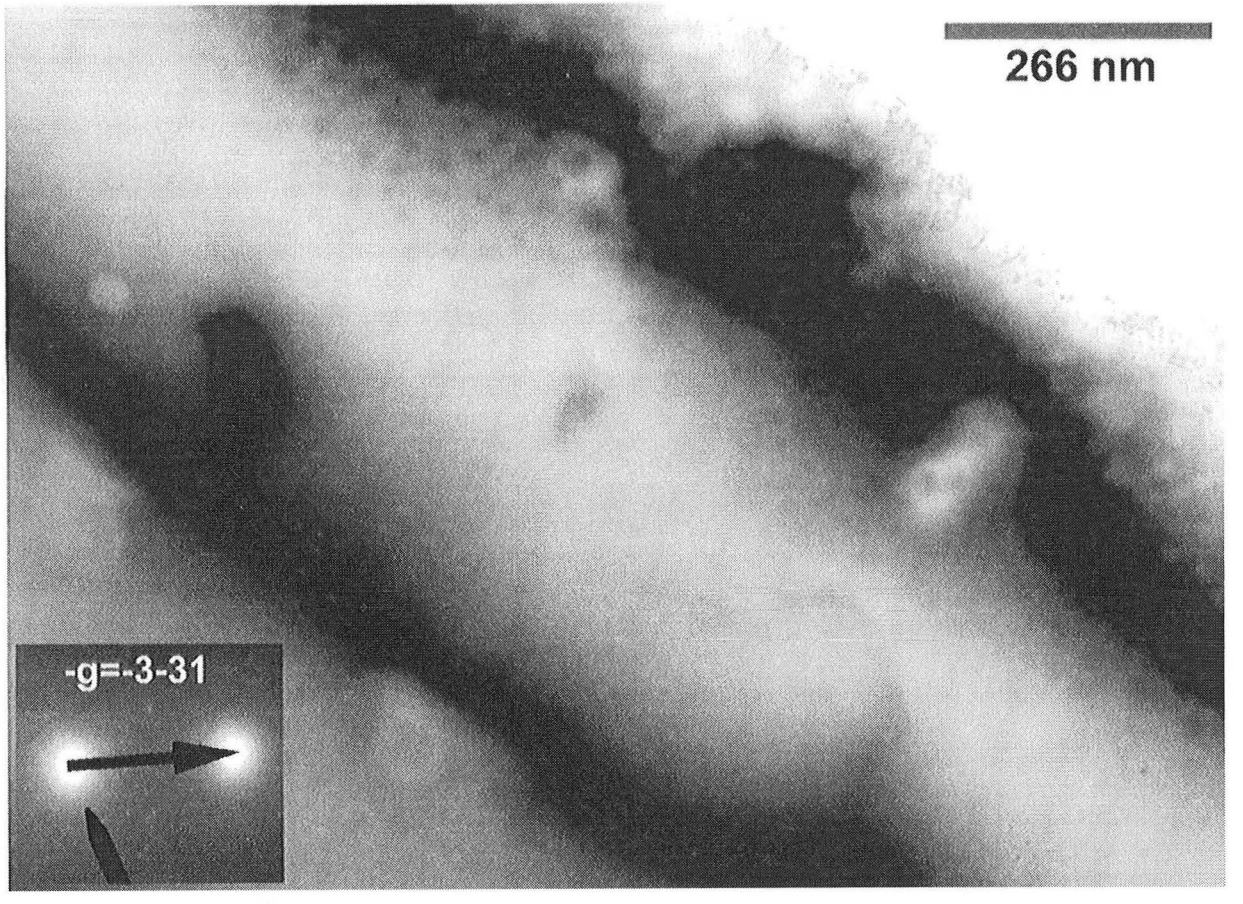

Figure 1.24: A bright field image for the two beam condition, ***-g***=-3-31, shown in the inset. The contrast does not change relative to ***g***=33-1 depicted in figure 1.25. The two beam condition was performed with a slight tilt from the [-233] zone axis.

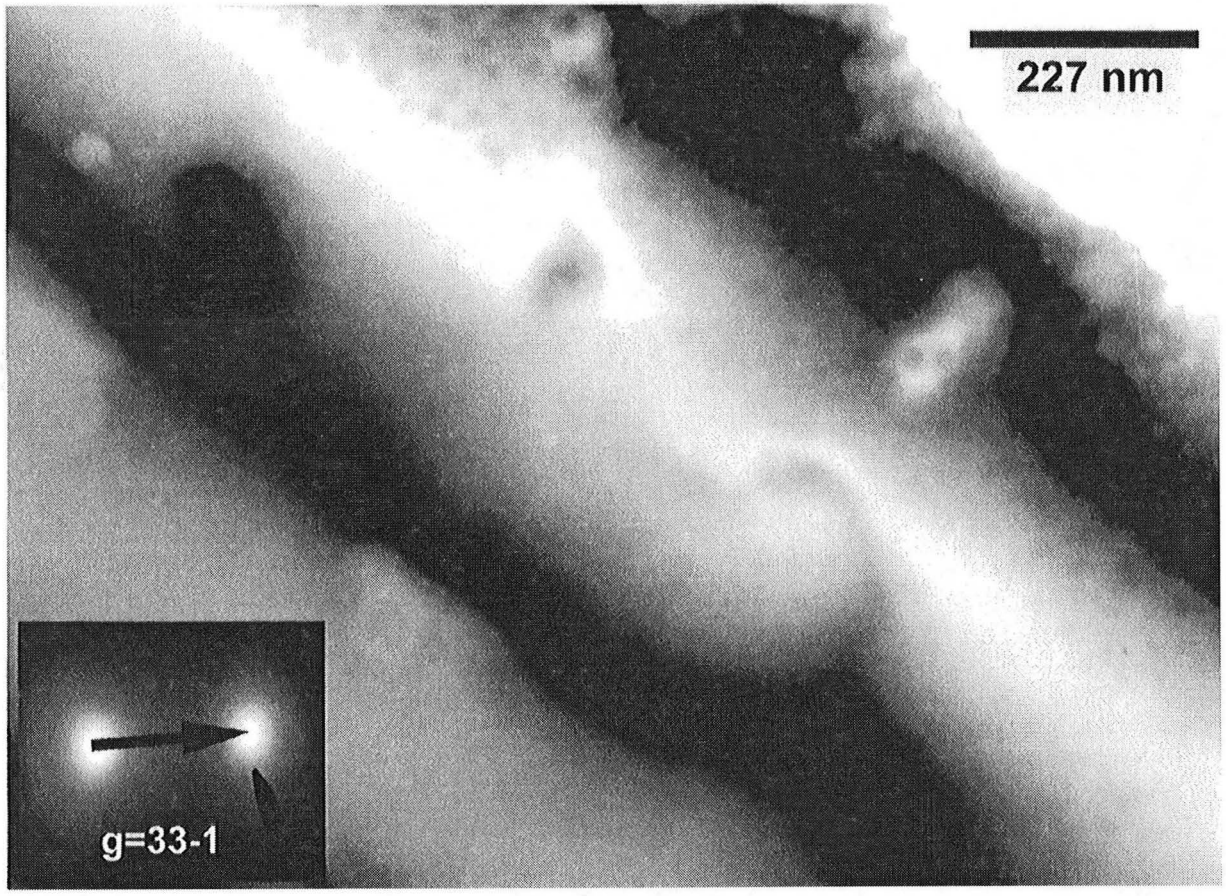

Figure 1.25: A bright field image for the two beam condition, ***g***=33-1, shown in the inset illustrates a change in contrast for the precipitates relative to figure 1.26. The two-beam condition in the inset is the dark field diffraction condition for figure 1.26. However, the magnitude of ***g*** is the same as the bright field ***g***.

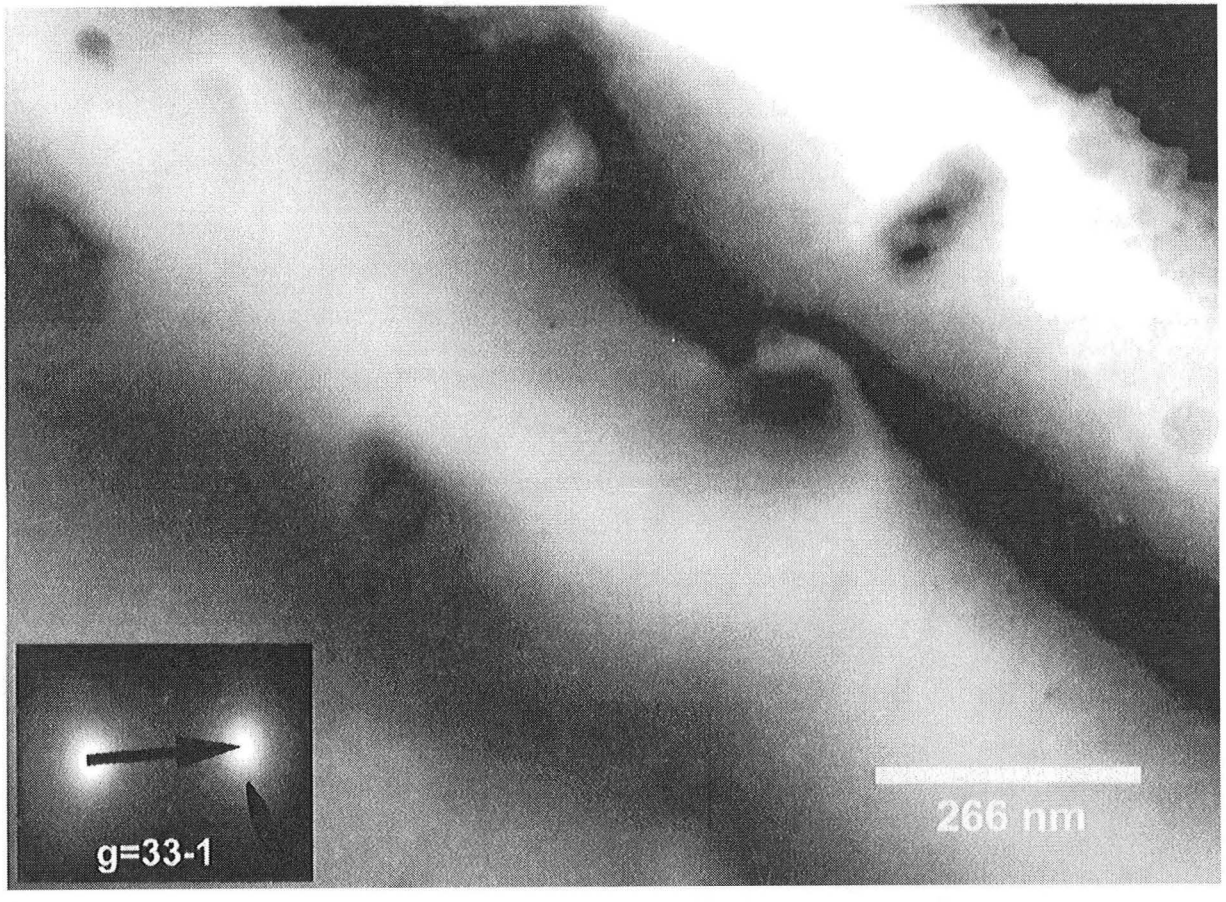

Figure 1.26: A dark field image for the two beam condition, ***g***=33-1, shown in the inset. A change in contrast occurs for the precipitates relative to figure 1.25.

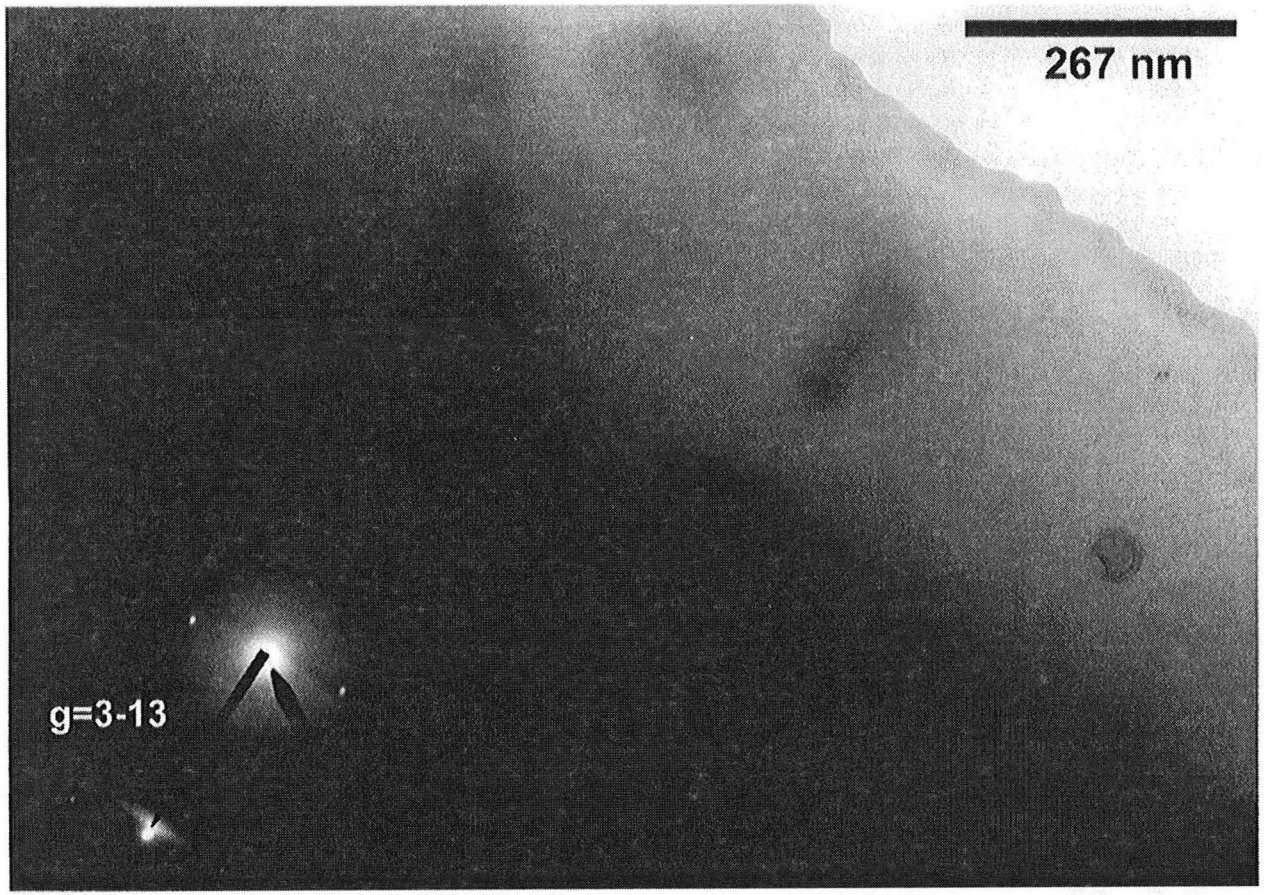

Figure 1.27: A bright field image for the two-beam condition, ***g***=3-13, shown in the inset. A change in contrast occurs for the precipitates relative to figure 1.28. The two-beam condition was obtained by tilting from the [-233] zone axis. Note that ***s*** is slightly negative.

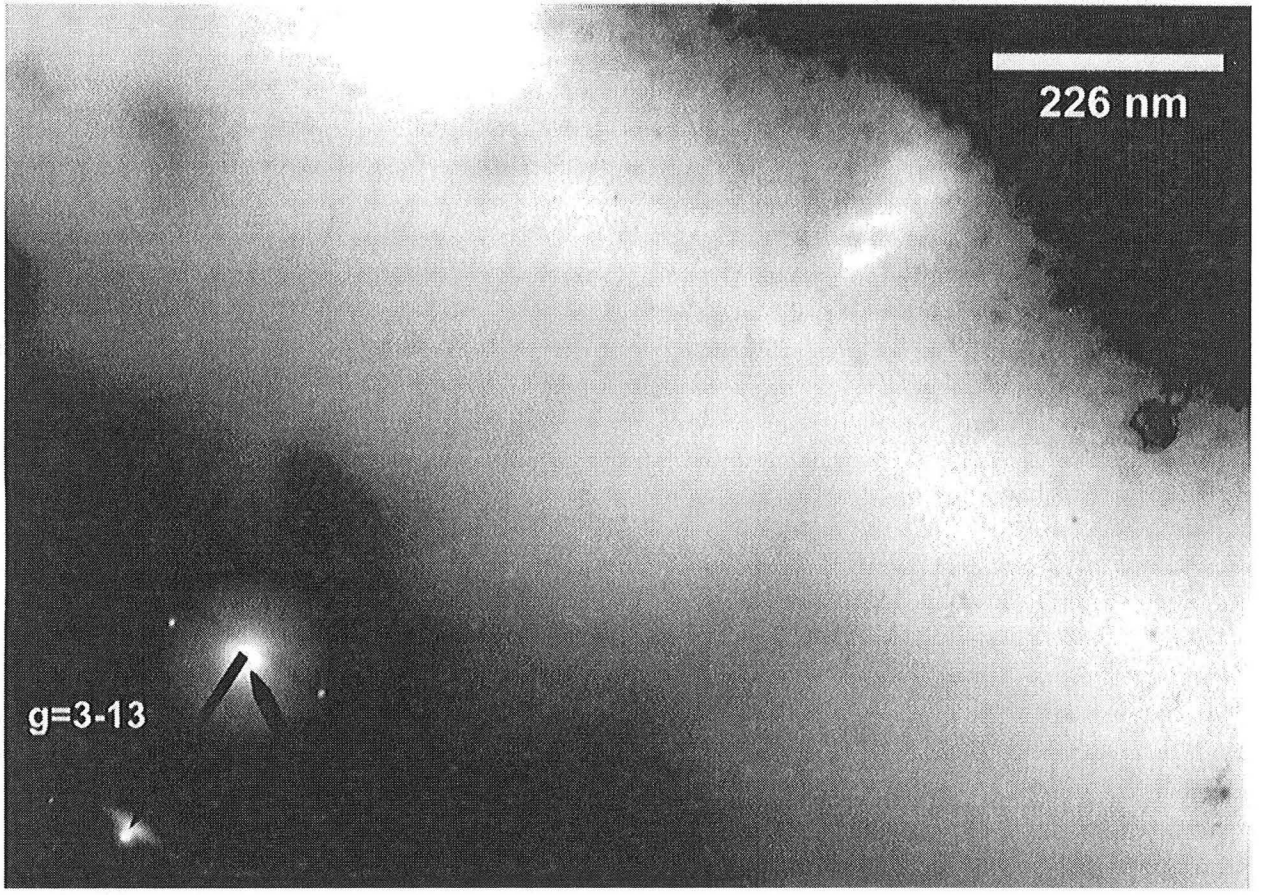

Figure 1.28: A dark field image for the two beam condition, ***g***=3-13, shown in the inset. A change in contrast occurs for the precipitates relative to figure 1.27.

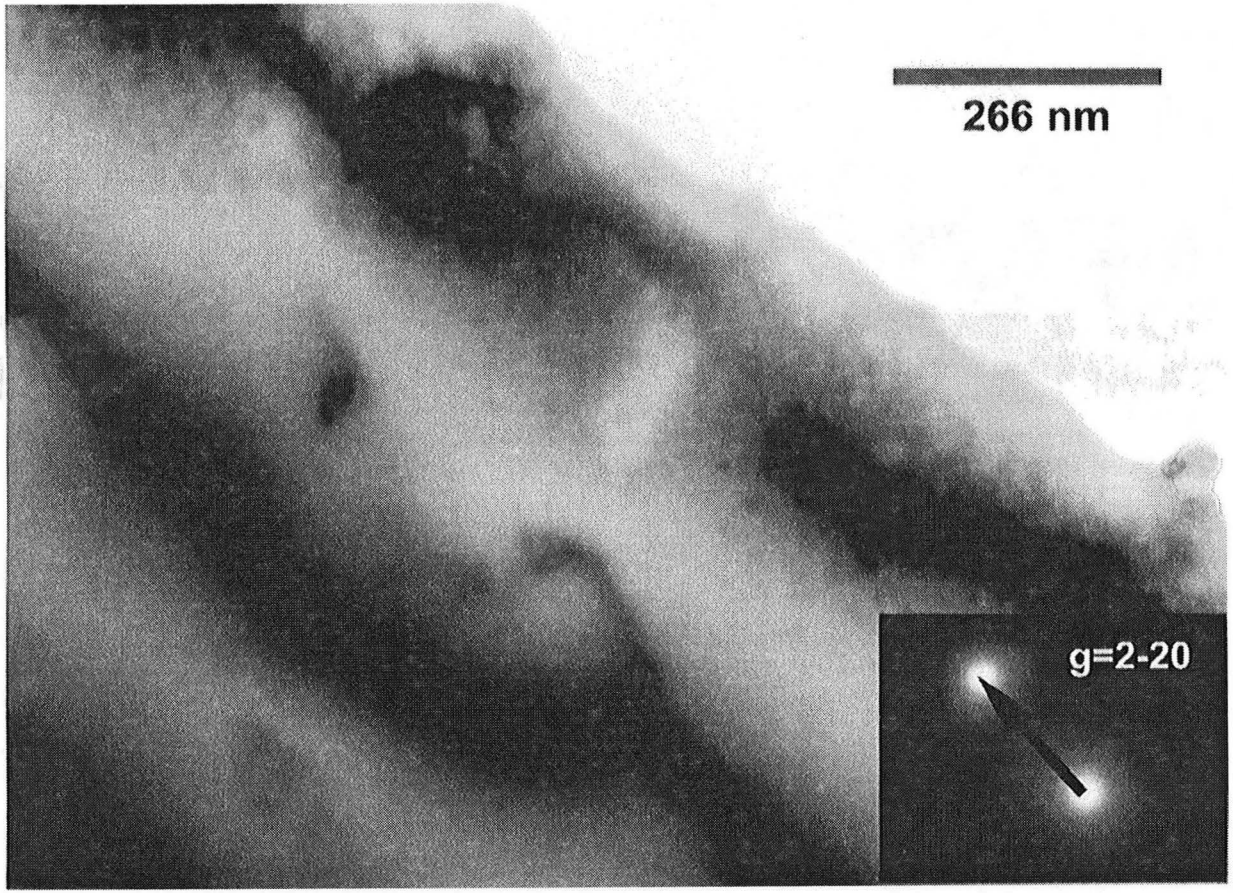

Figure 1.29: A change in precipitate contrast, relative to figure 1.30, can be seen in this bright field image. The reciprocal lattice vector for the two-beam condition is ***g***=2-20 which was obtained by tilting from the [111] zone axis.

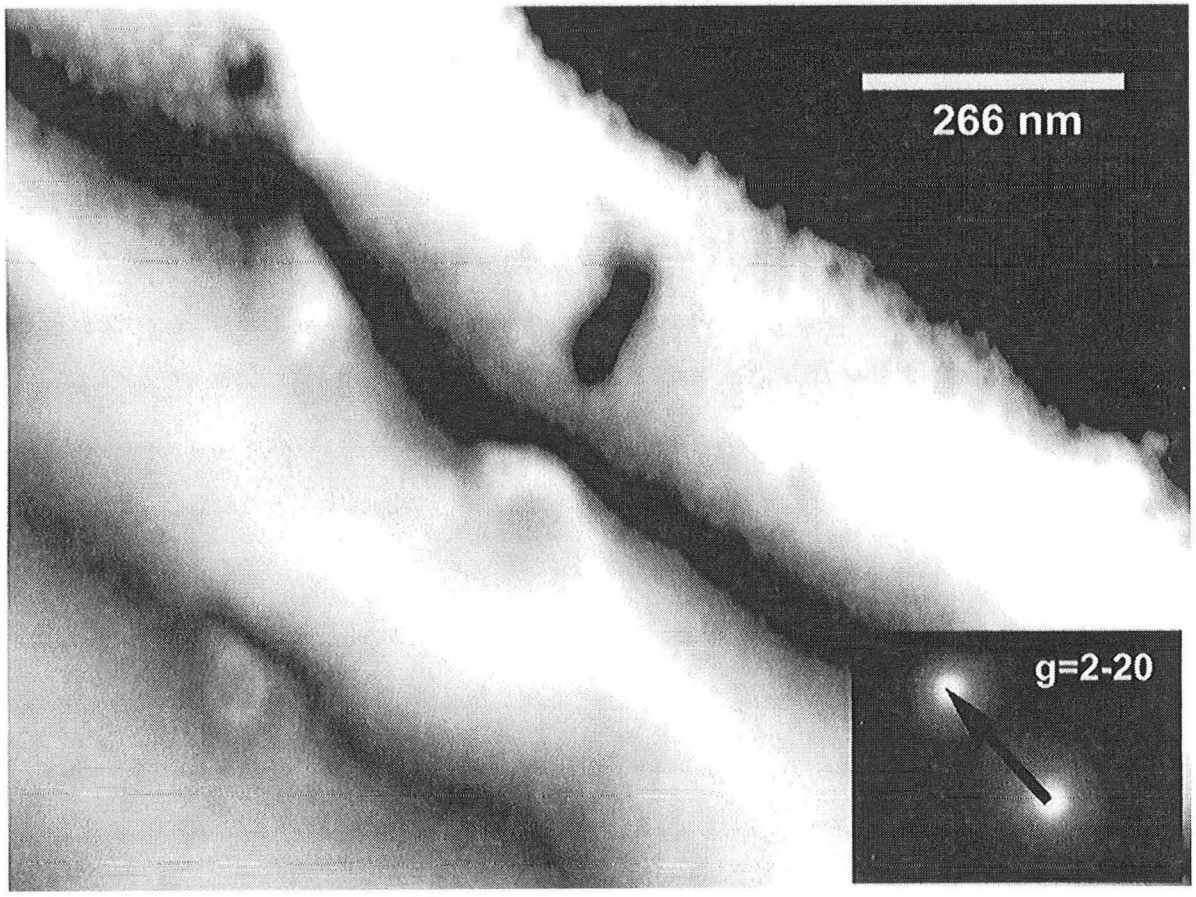

Figure 1.30: The precipitate contrast changes relative to figure 1.29 in this dark field image. The reciprocal lattice vector for the two-beam condition is ***g***=2-20.

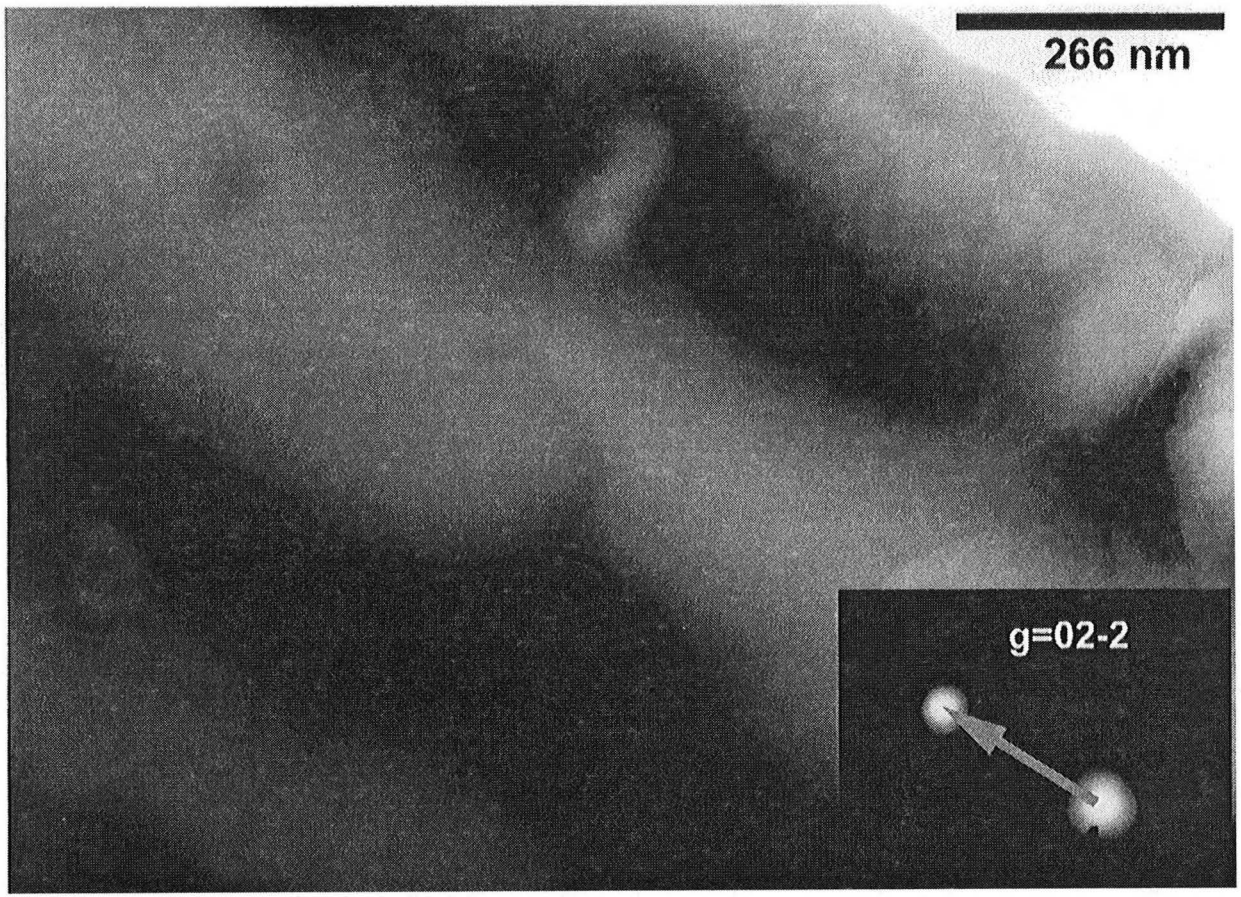

Figure 1.31: The bright field image was obtained for the two-beam condition, ***g***=02-2, shown in the inset. A change in contrast occurs for the precipitates relative to figure 1.32. The two-beam condition was obtained by tilting from the [111] zone axis. Note that ***s*** is slightly negative. The circular patches in the lower left of the image is damage created by the electron beam at higher magnification.

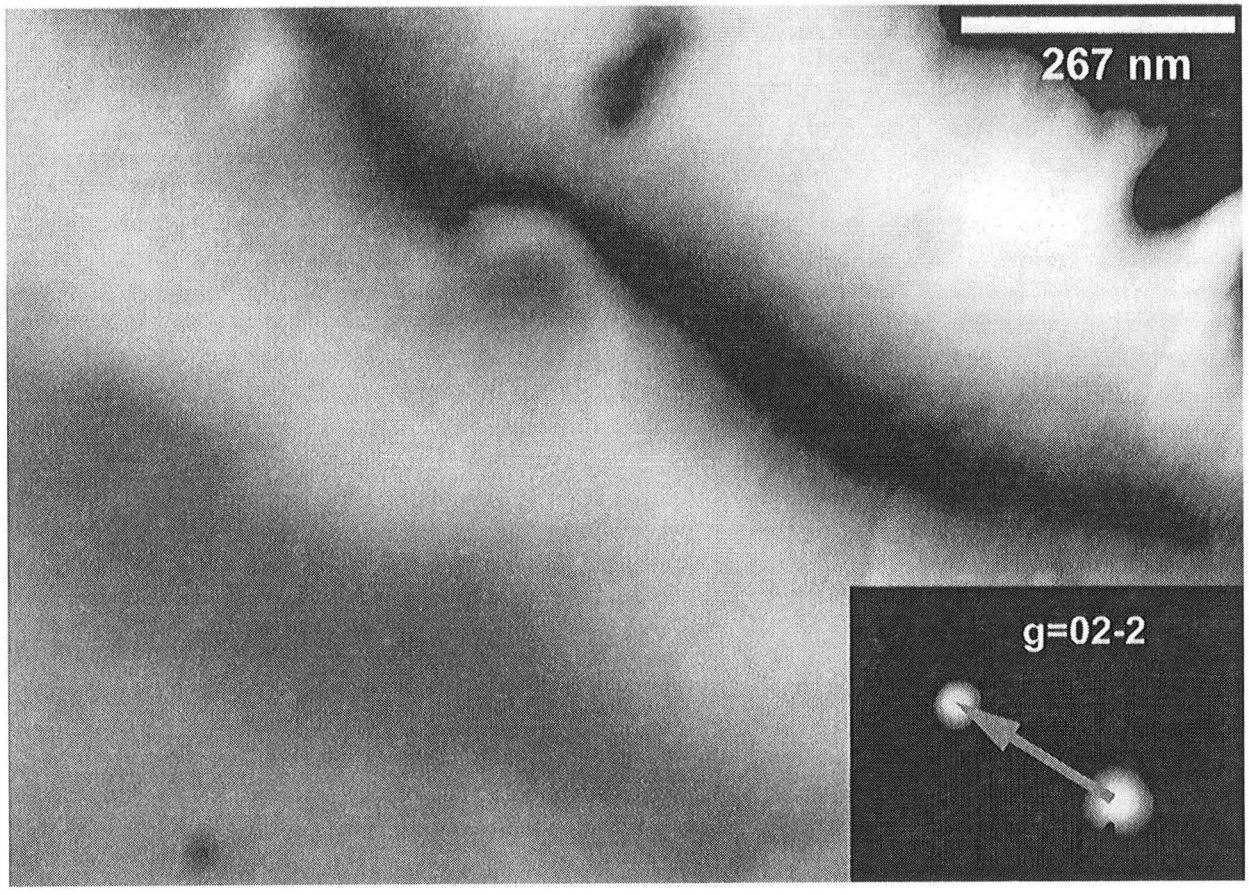

Figure 1.32: The bright field micrograph was obtained for the two-beam condition, ***g***=02-2, shown in the inset. A change in contrast occurs for the precipitates relative to figure 1.31.

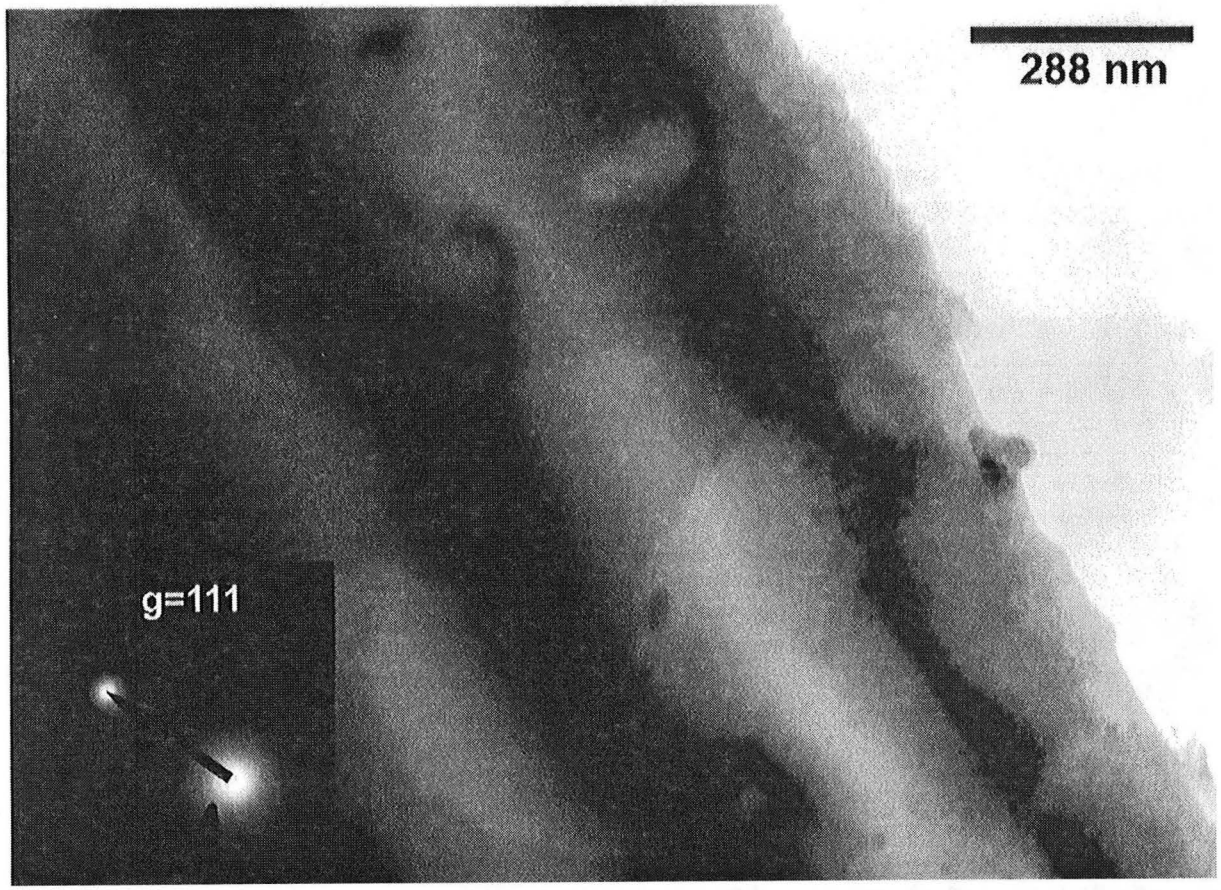

Figure 1.33: A bright field image of the precipitates is shown for the two-beam condition in the inset. A reversal of contrast occurs for the precipitates relative to figure 1.34. The two beam condition was obtained with a slight tilt away from the [110] zone axis.

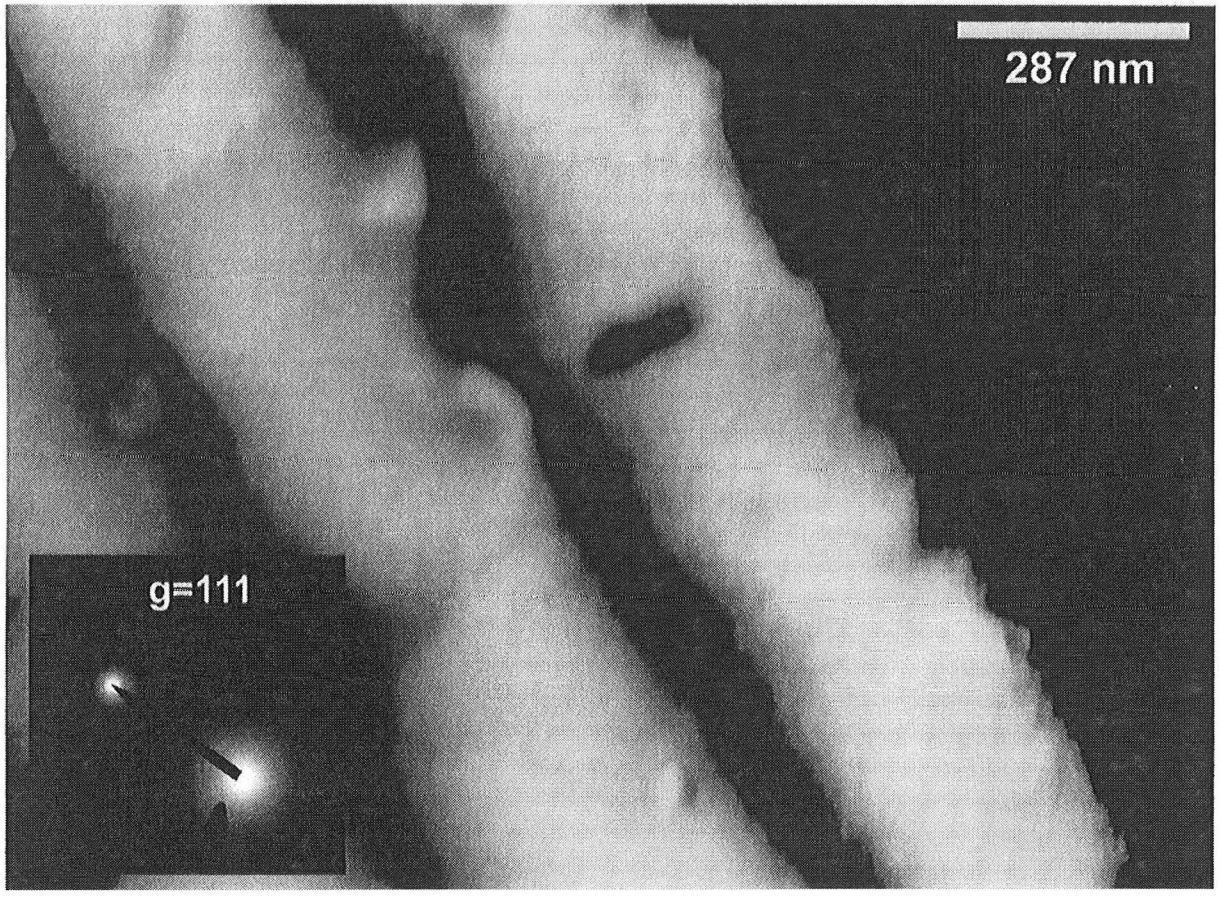

Figure 1.34: For the two-beam condition shown in the inset, the precipitate contrast changes relative to figure 1.33 in this dark field image. The two-beam condition was attained by tilting a few degrees from the [110] zone axis.

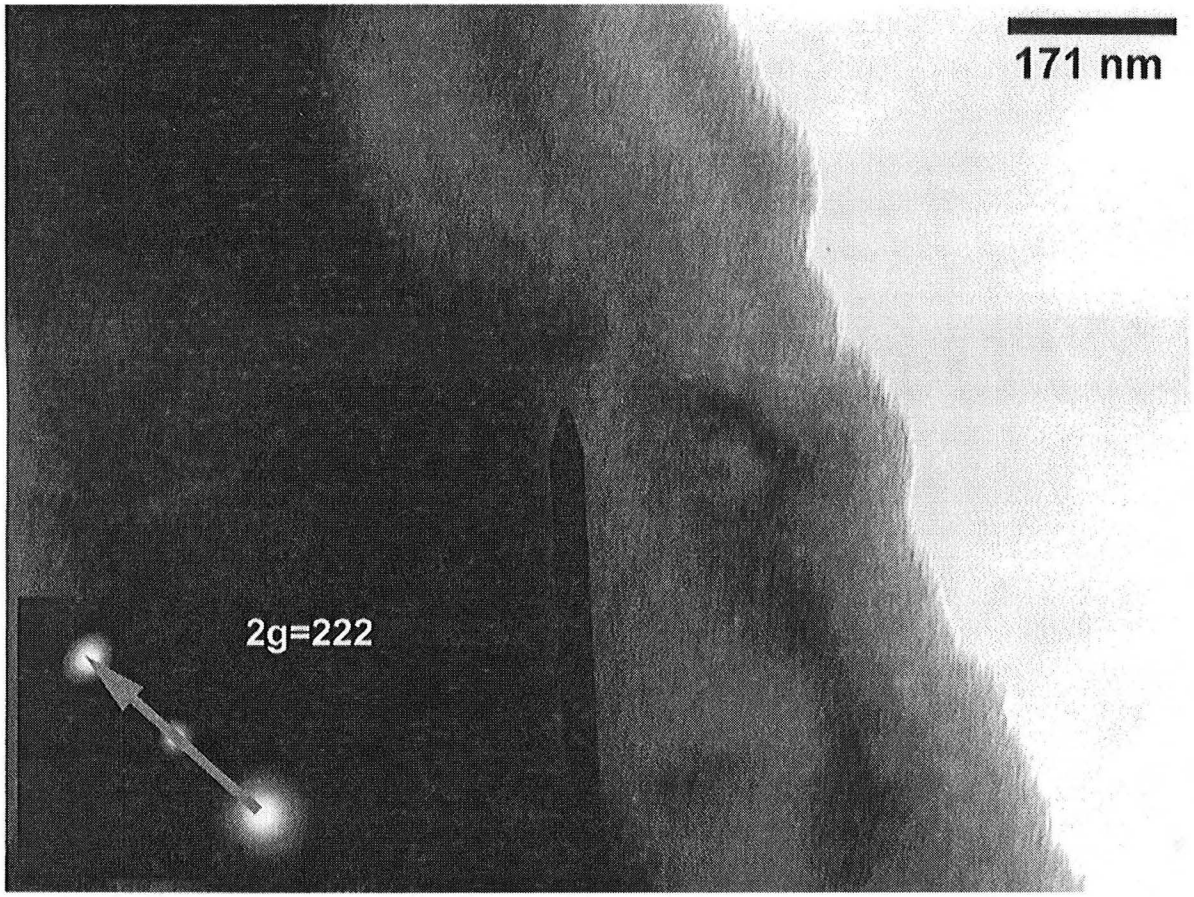

Figure 1.35: A bright field image for the 2***g*** two-beam condition 2***g***=222 shows that a change in contrast occurs with respect to figure 1.36. The two-beam condition was obtained by tilting from the [110] zone axis. The black pointer was inadvertently left in the field of view during the exposure.

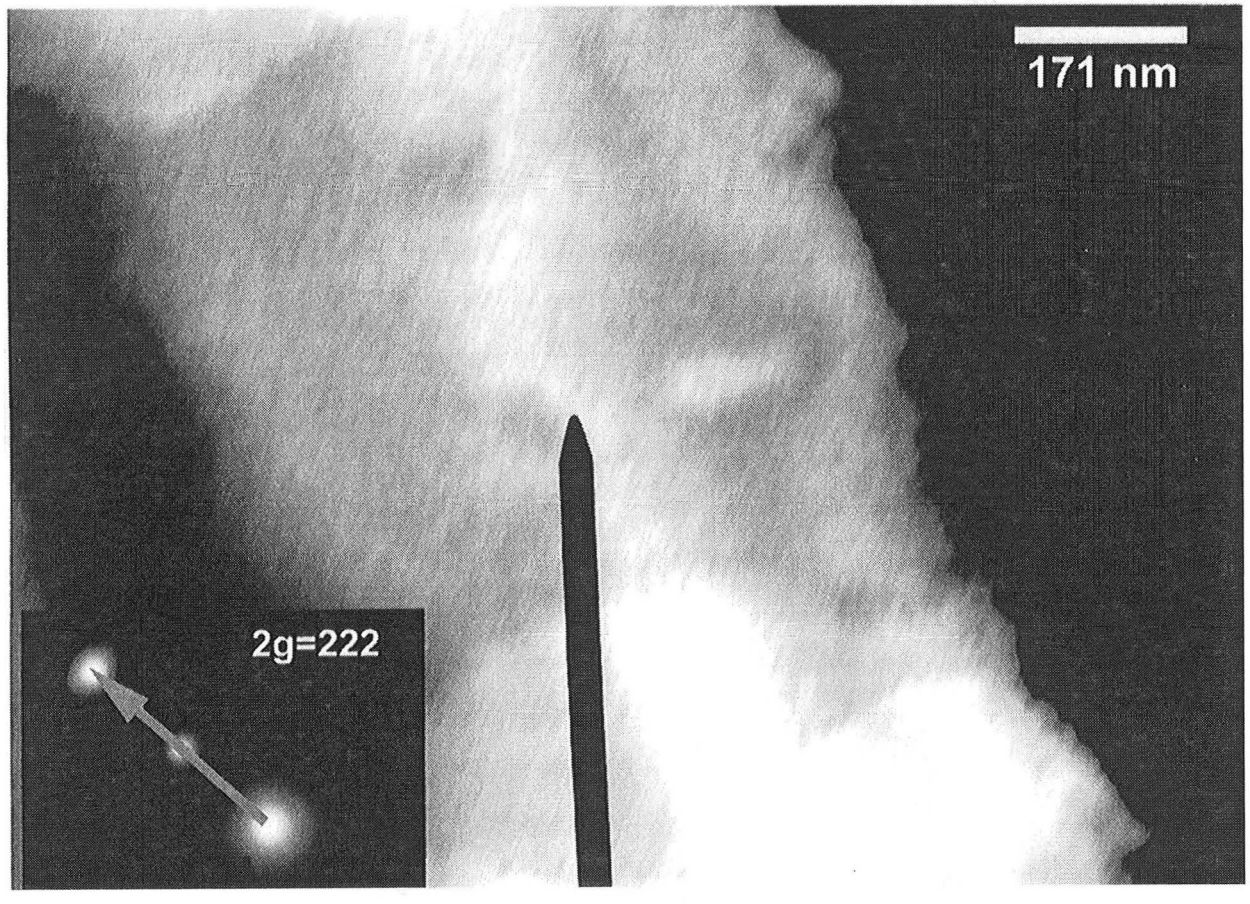

Figure 1.36: The two-beam condition, depicted in the inset, for this dark field image gives rise to the contrast change of the precipitates relative to figure 1.35. The out of focus appearance is due to sample-drift because of the long exposure times necessary for obtaining dark field images at high magnifications. The black pointer was inadvertently left in the field of view during the exposure.

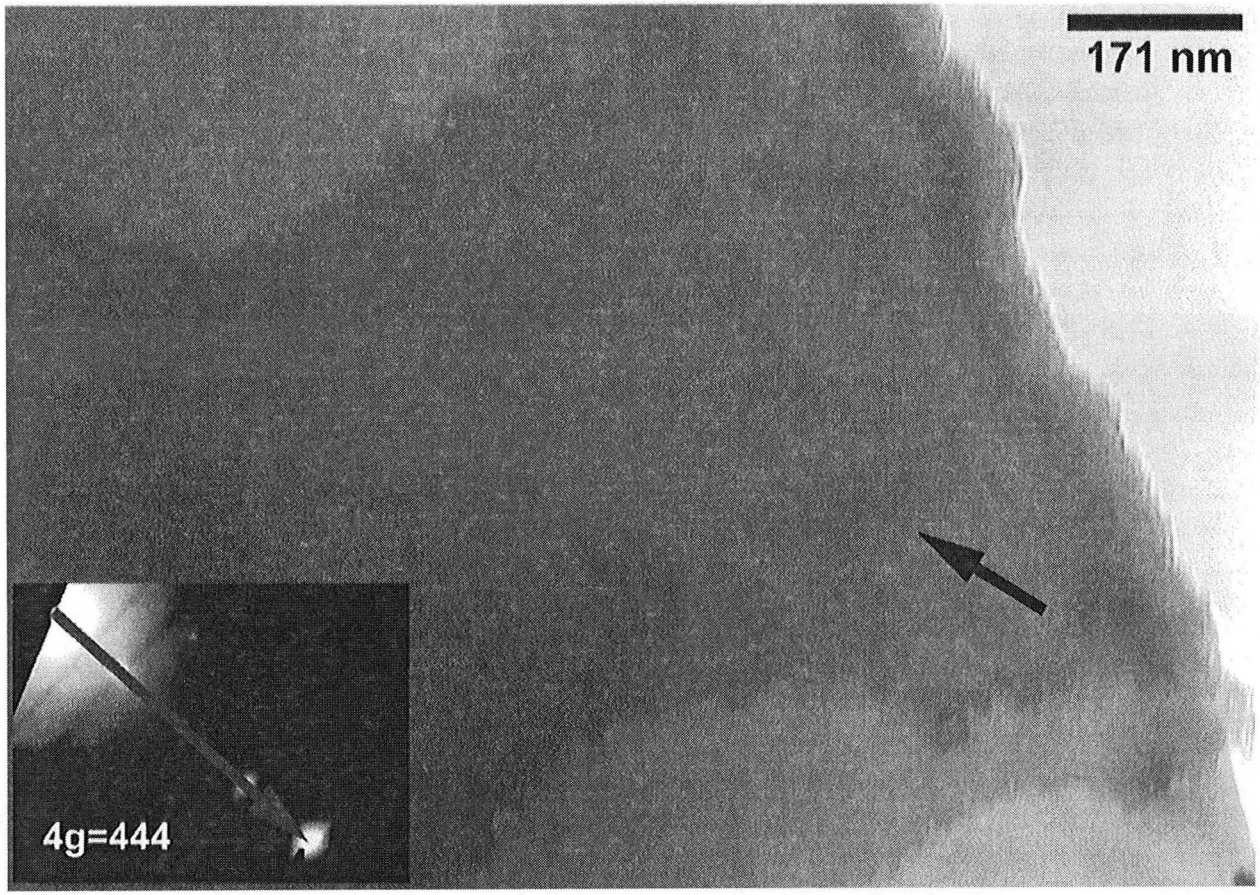

Figure 1.37: The bright field image was obtained using a 4**g** two-beam condition. Large ***g***'s decreases the contrast due to strain thereby maximizing the contrast due to the precipitates. A change in contrast of the precipitates, indicated by the black arrow, continues to be observed relative to the dark field image (figure 1.38) for such a large ***g***. The two-beam condition was obtained by tilting from the [110] zone axis.

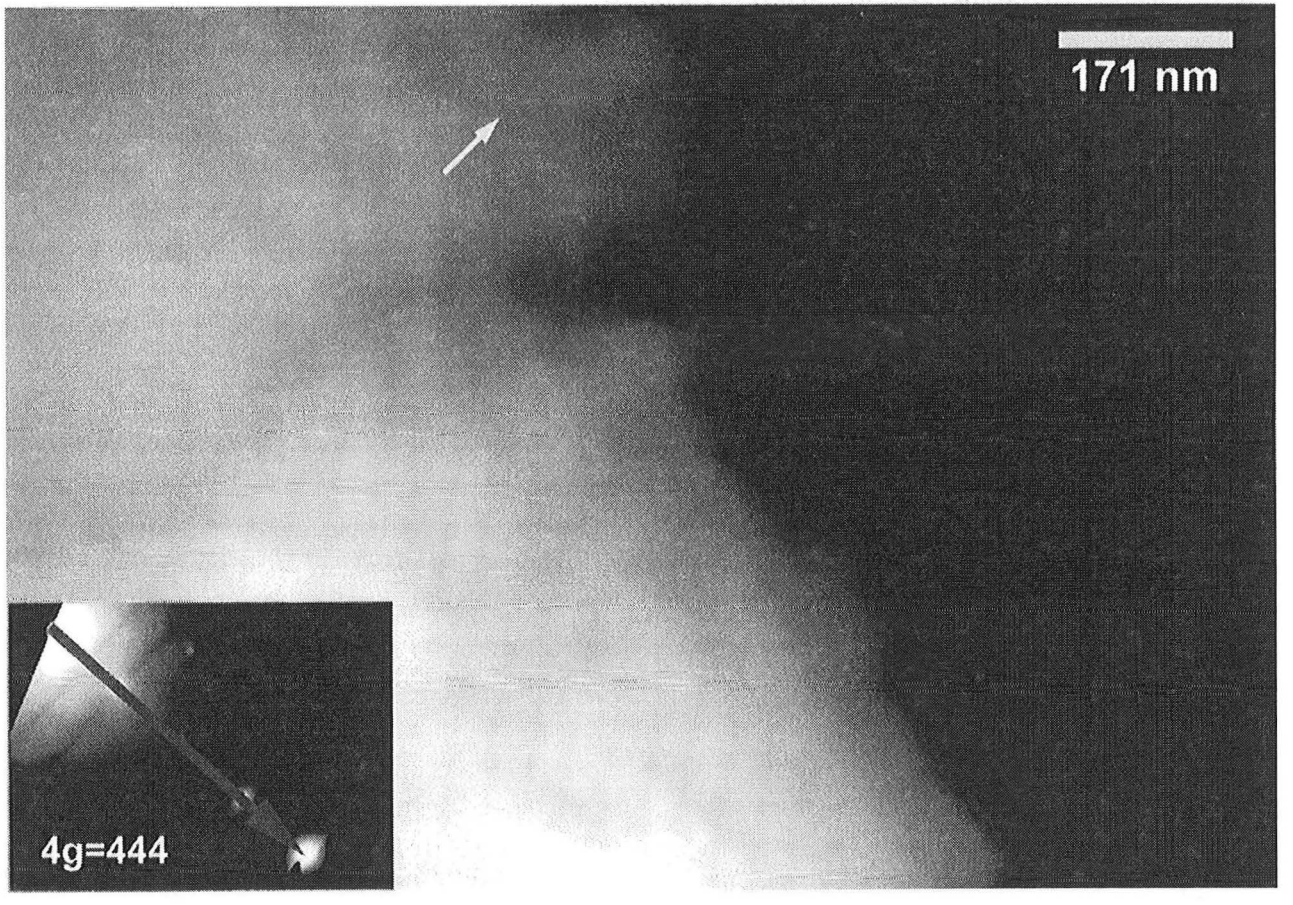

Figure 1.38: For the large ***g*** two-beam condition shown in the inset, the precipitate contrast changes relative to figure 1.37 in this dark field image. The white arrow indicates the location of the precipitate. The two-beam condition was obtained by tilting from the [110] zone axis. The circular patches in the lower left of the image are damage created by the electron beam at higher magnifications. The out of focus appearance is due to sample-drift because of the long exposure times necessary for obtaining dark field images at high magnifications.

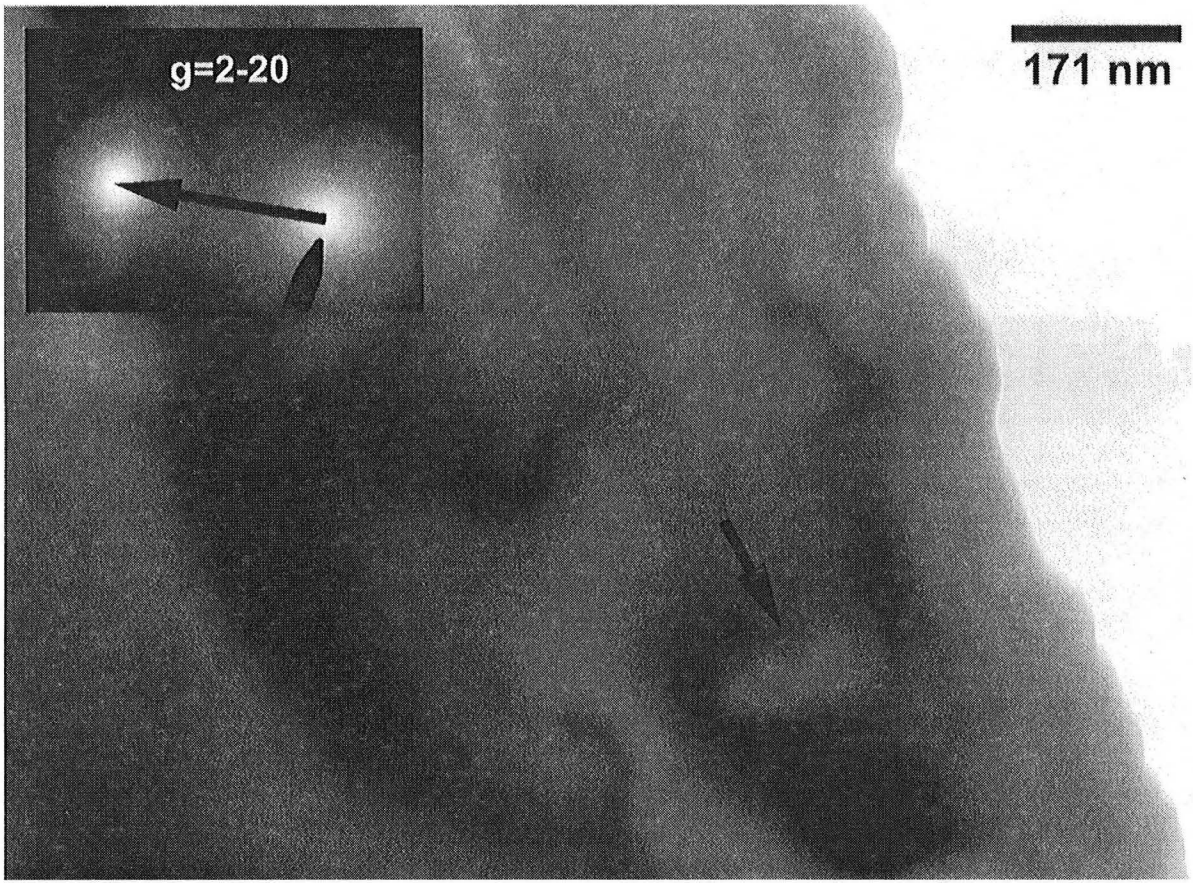

Figure 1.39: For the two-beam condition shown in the inset, the precipitate contrast changes relative to figure 1.40 in this bright field image. The black arrow indicates the location of one precipitate. The two-beam condition was obtained by tilting a few degrees from the [110] zone axis..

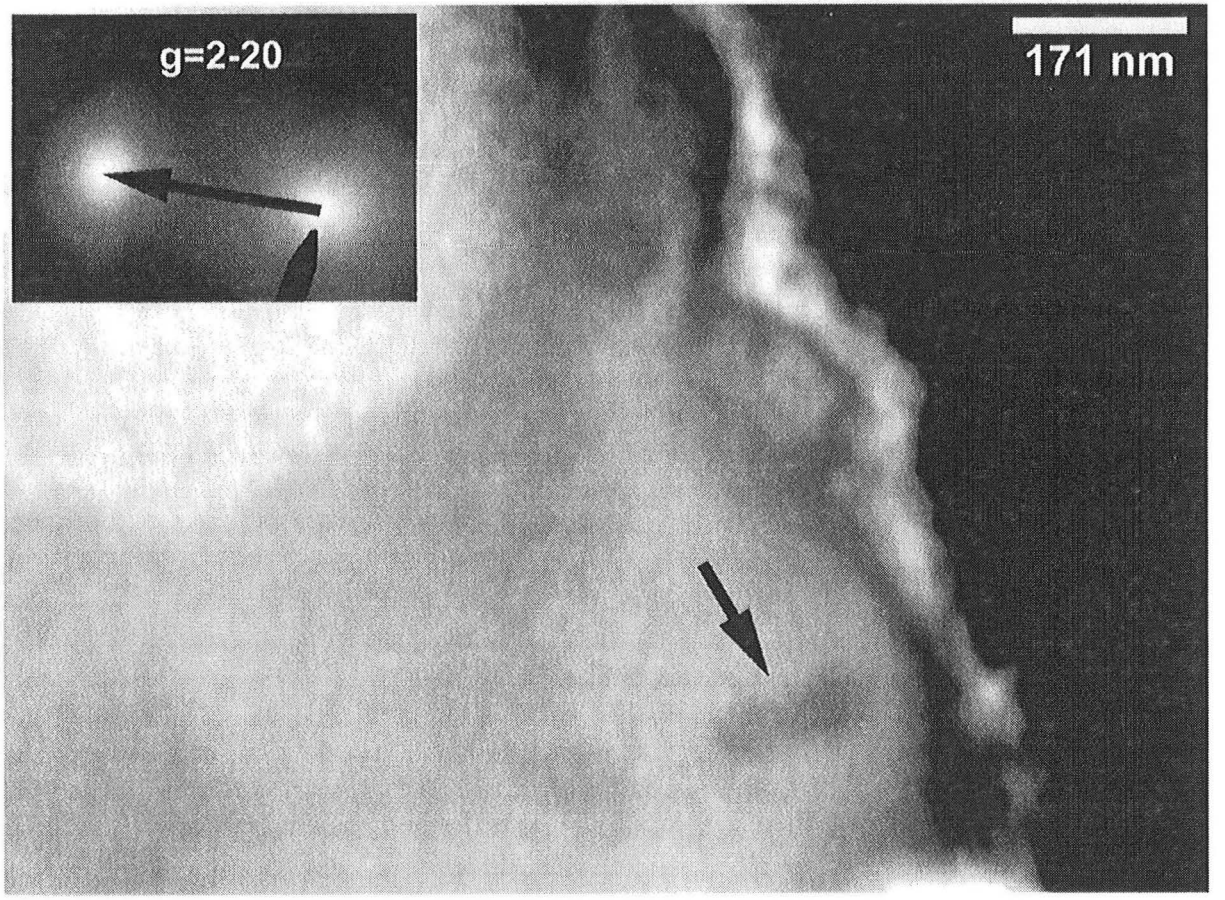

Figure 1.40: The two-beam condition, depicted in the inset, for this dark field image gives rise to the contrast change of the precipitates relative to figure 1.39. The black arrow indicates the location of one precipitate.

1.5 Precipitate Density Study Using TEM and Process Modeling

1.5.1 TEM precipitate density study

Another subject of interest resulting from the study described in this thesis is the manner in which the Li^+ and D-defects interact leading to precipitation. Presuming that the precipitation causes Li^+ drifting to cease, then determining the mechanism behind the precipitation kinetics may lead to more information concerning the D-defect. The mechanism can be studied by the evolution of precipitation. A density distribution of Li precipitates will exist if trapping of Li^+ by D-defects is a transient effect with respect to position. To investigate the depth density distribution of precipitates, a TEM study was performed.

Li ions drift about 1 mm before the process is terminated by D-defects. Within this 1 mm, the precipitate density will vary as a function of Li^+ drift distance from the Li^+ reservoir. For this TEM study, the Li^+ reservoir of most samples was removed by lapping. Chemomechanical polishing was used to remove Si in the 1 mm partially Li^+ drifted region to the desired depth. This technique was used because it is slow and therefore more precise. Electron transparent samples were prepared using dimpling and ion milling techniques.

The results from TEM on all samples indicated that precipitates were present in the three samples that were examined. The precipitates were spherical in geometry. This was determined by examining them in different tilt configurations. For example, figure 1.41 shows precipitates along the <111> zone axis, while figure 1.42 was taken along the <110> zone axis. The two-dimensional shape of the precipitates is nearly the same. The

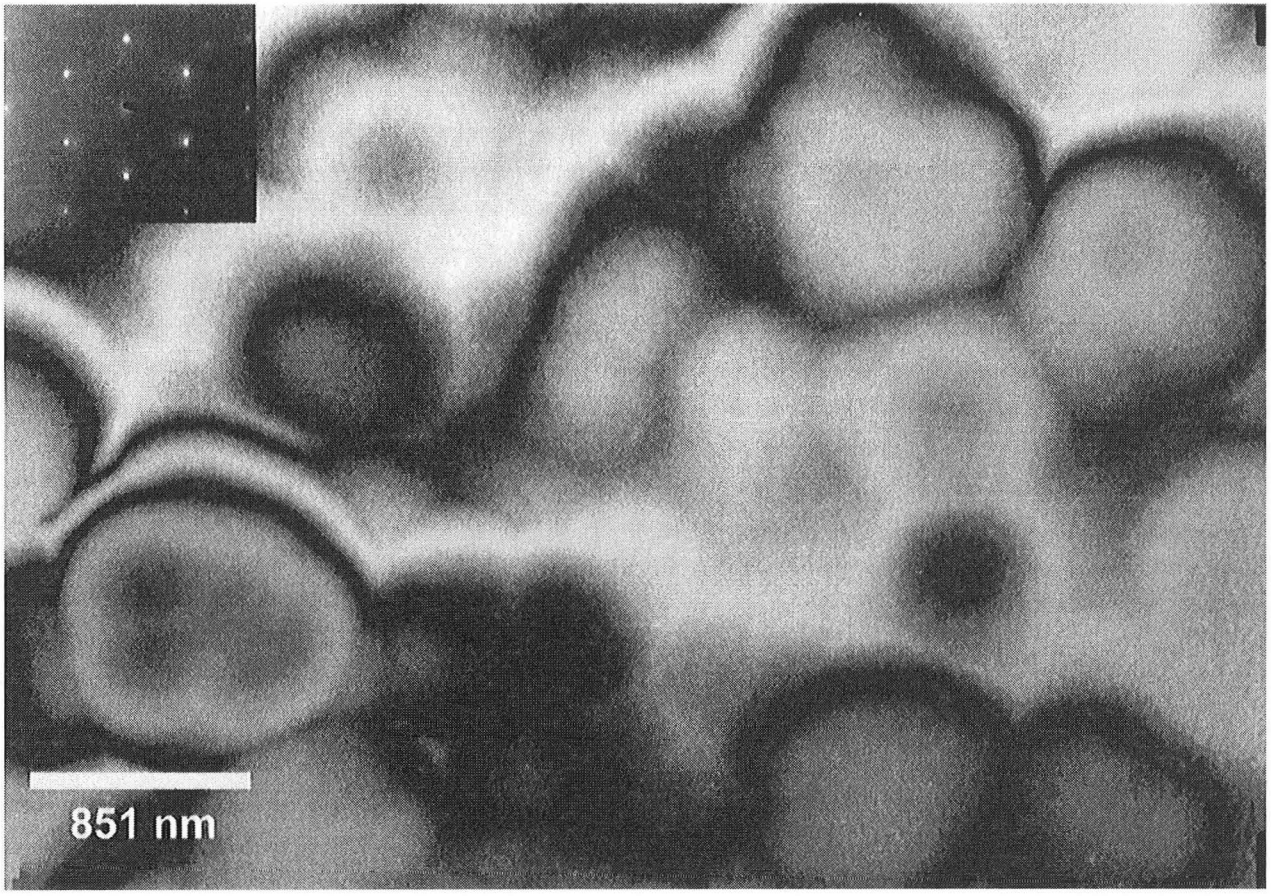

Figure 1.41: The bright field TEM micrograph of precipitates was taken along the [111] zone axis as shown by the diffraction pattern in the inset. Note the similarity to figure 1.42 with regard to the shape and size of the precipitaes.

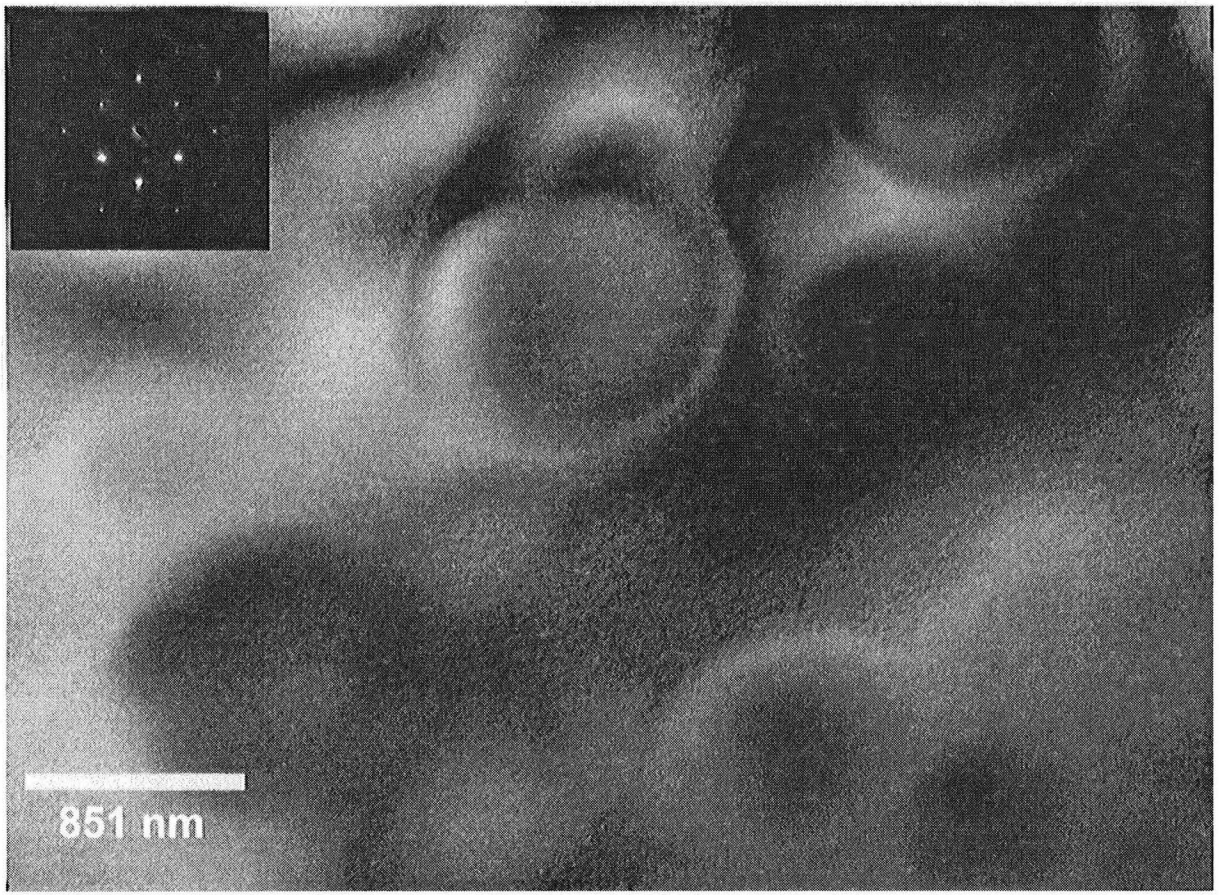

Figure 1.42: The bright field TEM micrograph of precipitates was taken in the same area as in figure 1.41, but along the [110] zone axis as the diffraction pattern in the inset indicates. The shape and size of the precipitates in this orientation is very similar to the shape and size of the precipitates in figure 1.41.

density distribution of the precipitates in the samples examined may be seen in figures 1.43, 1.44 and 1.45. The depths, from the surface on which Li was thermally deposited (i.e., lithiated surface) to where the samples were taken, are 160 μm, 302 μm, and 336 um, with respect to figures 1.43 through 1.45. The areal density is calculated by counting the number of precipitates in a given area. An average distance is determined by averaging the measured distances between the strain fields of neighboring precipitates. This average distance was used to calculate the volume in which the precipitates exist (i.e., product of average length and areal density). The density of the precipitates with respect to depth from the Li reservoir for the three samples is plotted in figure 1.46. As can be seen from the plot, the density of the precipitates does vary with distance from the Li reservoir. A comprehensive list of the data is given in table 1.3.

Table 1.3: Data extracted from TEM micrographs

Data	figure 1.1	figure 1.2	figure 1.3
sample depth (μm)	160	302	336
average distance between precipitates (μm)	0.86	1.2	1.8
areal density (cm^{-2})	$1.2x10^8$	$8.3x10^7$	$4.8x10^7$
volume density (cm^{-3})	$1.4x10^{12}$	$7.0x10^{11}$	$2.7x10^{11}$

Figure 1.43, shows heavy precipitation. The driving force for precipitation of this intensity may be a solubility issue. The depth from which the sample was taken is only 160 μm from the surface into which diffusion of Li occurred. If the sample is within the Li reservoir, then precipitation may simply be due to supersaturation of Li.

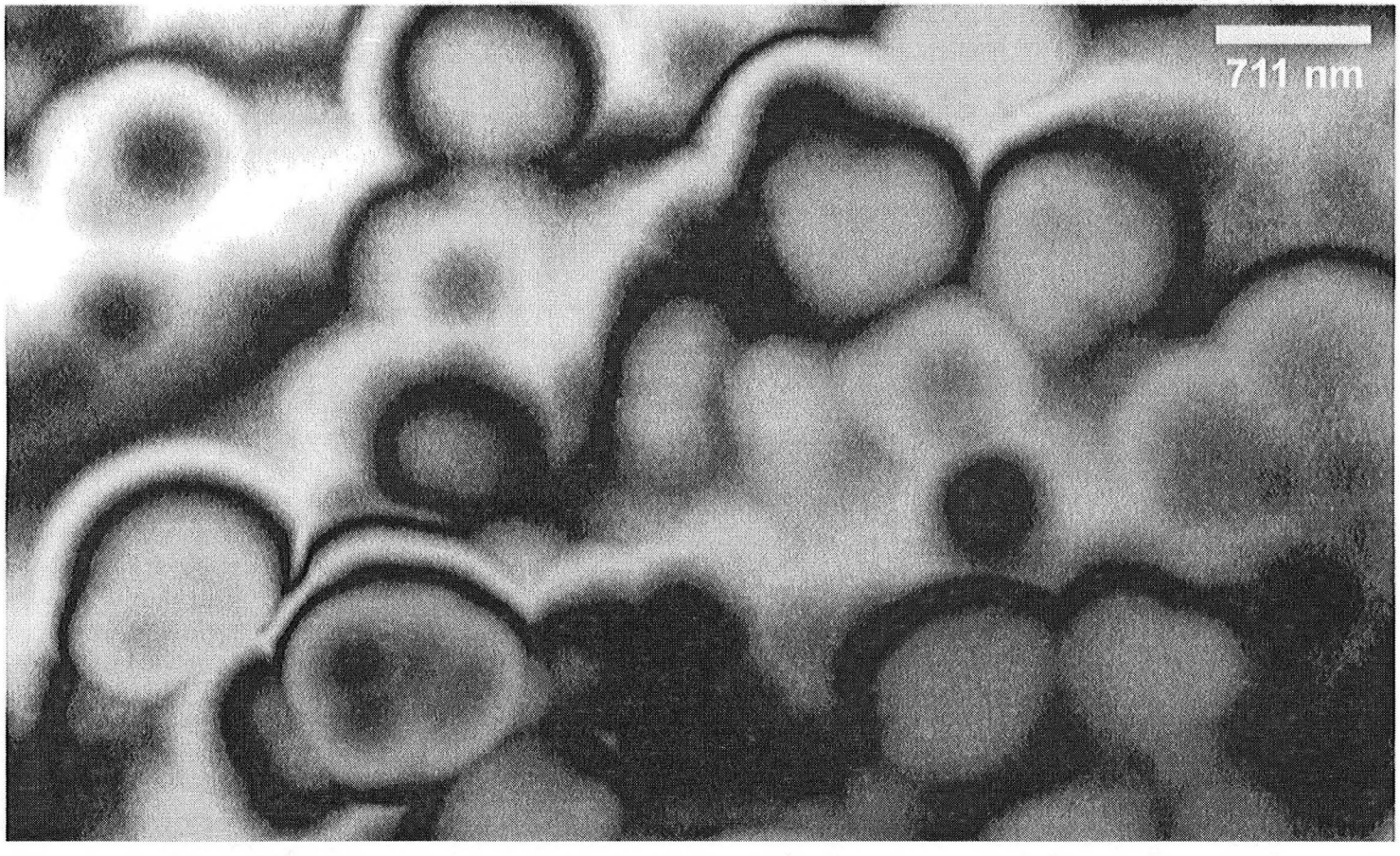

Figure 1.43: A bright field TEM image showing heavy precipitation. The TEM sample was taken from a depth of approximately 160 μm from the lithiated surface (i.e., surface from which Li diffusion occurred).

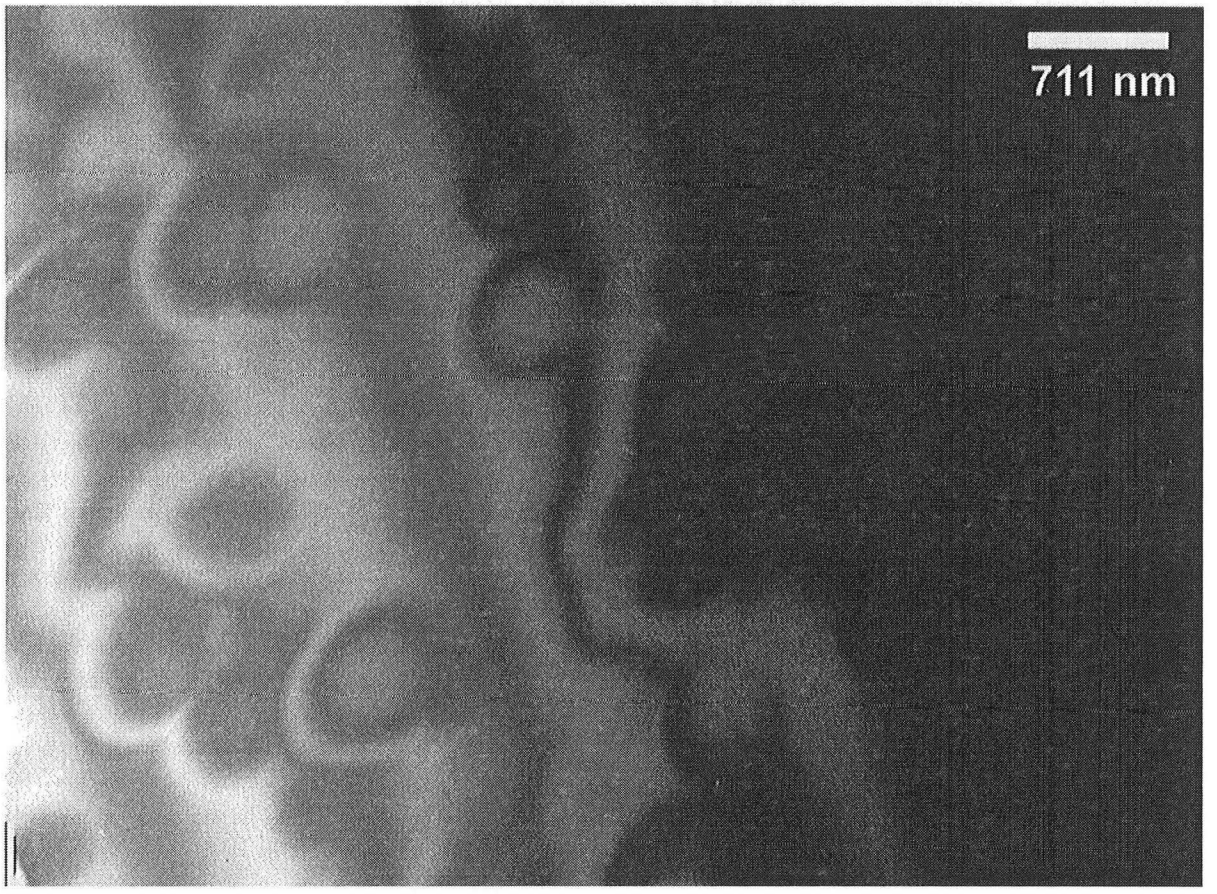

Figure 1.44: A bright field TEM image showing a precipitate density that is lower than the density shown in figure 1.43. The TEM sample was taken from a depth of approximately 302 μm from the lithiated surface (i.e., surface from which Li diffusion occurred).

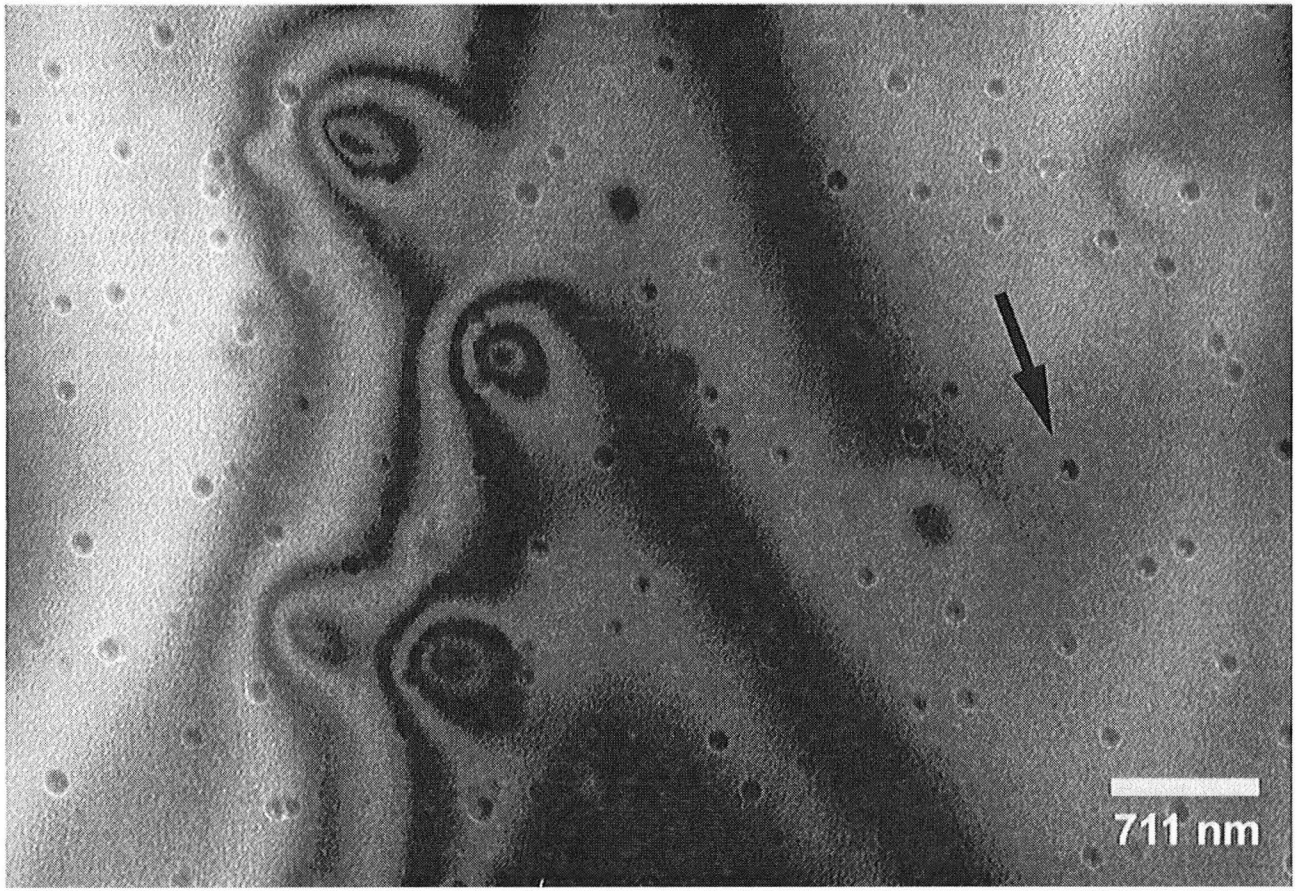

Figure 1.45: A bright field TEM micrograph showing a precipitate density that is lower than the densities shown in figures 1.43 and 1.44. The TEM sample was taken from a depth of approximately 336 μm from the lithiated surface (i.e., surface from which Li diffusion occurred). The smaller and more circular precipitate-like defects are not precipitates. They are caused by residual syton particles (i.e., SiO_2 colloid) that shadow-masked the sample during ion milling.

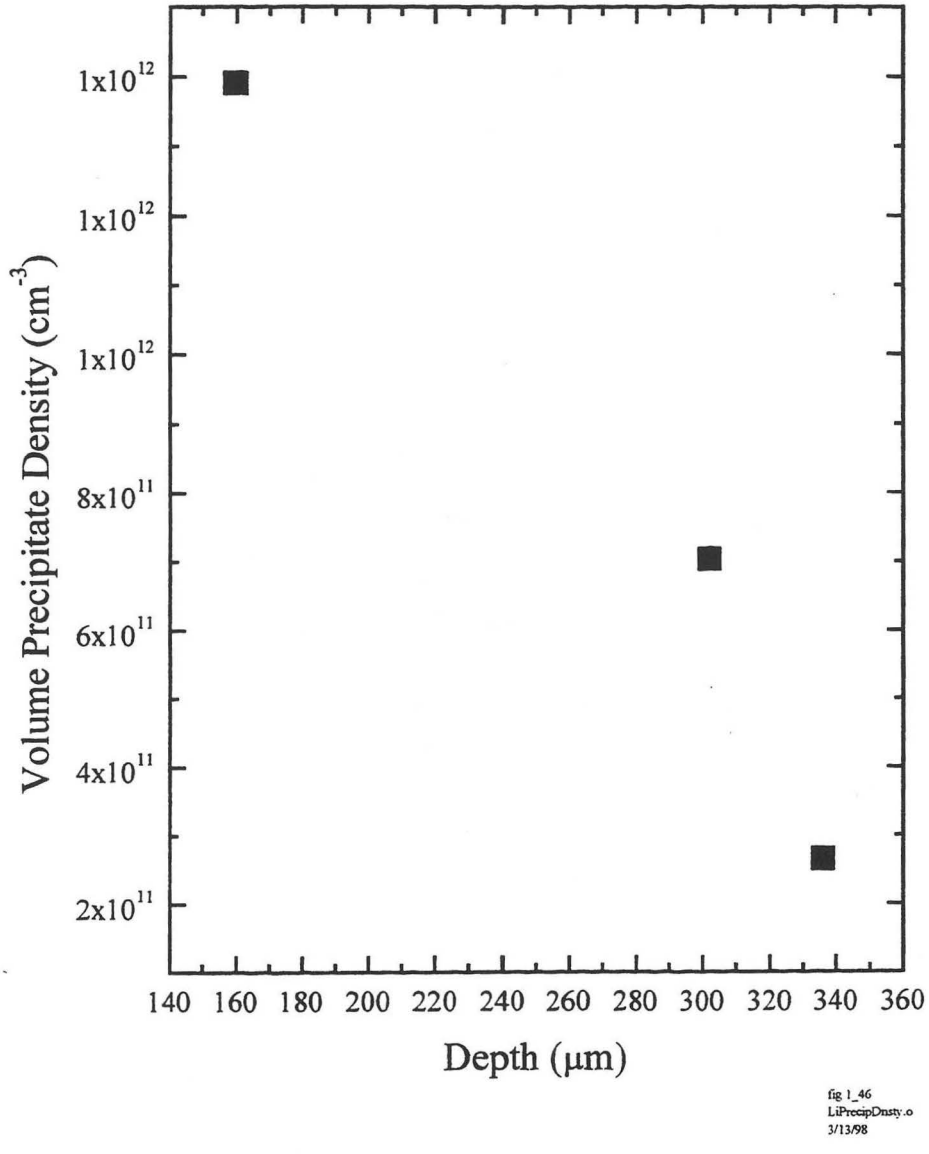

Figure 1.46: A plot of the precipitate density as a function of depth from the lithiated surface.

To determine whether or not the sample was taken from the reservoir region, the depth of the Li reservoir in the bulk Si must be determined. The depth of the boundary between the Li reservoir and the undiffused region is given by one of two conditions. One condition is the depth at which the Li concentration is equal to the solid solubility limit at the Li^+ drift temperature (~ 110°C). The other boundary condition is the depth at which the Li^+ concentration is equal to the B^- concentration. The reaction (i.e., compensation) between the Li^+ and the B^- will easily reduce the unpaired Li concentration to below the solid solubility limit. The depth of the reservoir is the larger value of the two conditions. Hence, the *p*-type Si dopant concentration and the solid solubility at the Li^+ drift temperature must be known.

The dopant concentration in the FZ Si is about $5x10^{13}$ cm^{-3} (see table 1.1). Solubility data for Li in Si do not exist for the temperature range in which the Li diffusion and drift processes are performed. The data was obtained from higher temperature solubility data [Madelung and Schulz, 1989, 69] by extrapolating a "best fit" curve into the temperature range of interest as shown in figure 1.47. The solubility data for 400°C and 100°C are marked on the plot and are approximately $6x10^{17}$ cm^{-3} and $3x10^{14}$ cm^{-3} respectively. Since the solid solubility is larger than the acceptor concentration, it will be used to determine the depth to which the Li reservoir formed. This may be accomplished by using a Li diffusion profile.

A complimentary error function (erfc) was used to determine the distance the Li^+ diffused into the Si bulk to form the Li reservoir. To plot the Li concentration as a function of diffusion depth, both the solid solubility at 400°C and 100°C (i.e., Li^+ drift temperature) and the Li diffusivity needed to be determined. The solid solubility at

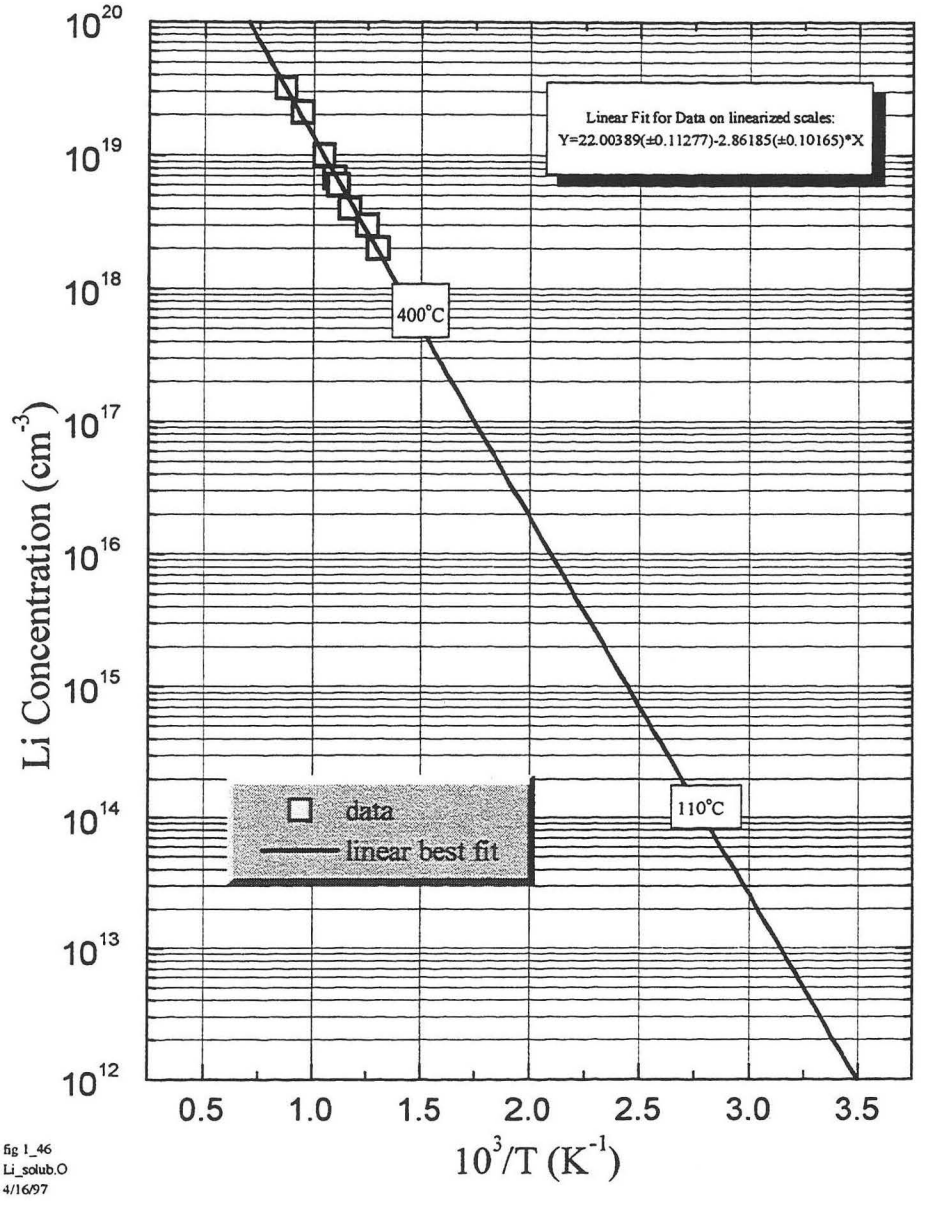

Figure 1.47: Solid solubility of Li in Si as a function of temperature. [Madelung and Schulz, 1989, 69]

400°C, which is used for the initial Li concentration in the erfc plot, is approximately $7x10^{18}$ cm^{-3} as obtained from figure 1.47. The Li diffusivity as a function of temperature was established by Pell in 1960.[Pell, 1960a, 81] The function is plotted in figure 1.48. From figure 1.48, the Li diffusivity at 400°C is about $1x10^{-8}$ cm^2/s. Using these values, the Li diffusion profile is plotted in figure 1.49 for several annealing times at 400°C. Using the solid solubility data at 100°C (~$3x10^{14}$ cm^{-3}), the depth to which the Li reservoir extends is about 200 μm for a diffusion time of 10 minutes.

Since the sample was taken from within the Li rich reservoir (i.e., the n^+ reservoir), supersaturation of Li may have caused the heavy precipitation. To address this issue, a comparison was made between samples taken from areas within the Li reservoir, but free of D-defects, and the sample shown in figure 1.43. If the results are similar, then supersaturation is the probable cause of precipitation – not D-defects.

Samples were taken from areas within the Li reservoir and in the regions free of D-defects. This region can be seen in the Li^+ drift profile shown in figures 1.5, 1.6 and 1.10 of section 1.2. The Li^+ drift profile of each defective wafer shows that the central area of each wafer contains D-defects. Li^+ drifts completely through the wafer in the near periphery region of the wafer indicating the absence of D-defects. It is from this region that the samples were taken. TEM sample preparation, as explained previously, was carried out and TEM was performed.

A representative TEM micrograph is shown in figure 1.50. No precipitates are seen. Hence, precipitation by supersaturation does not occur in this region of the Li reservoir. This result clearly shows that D-defects, not supersaturation, are responsible for the heavy precipitation that is seen in figure 1.43. Therefore, supersaturation is not an

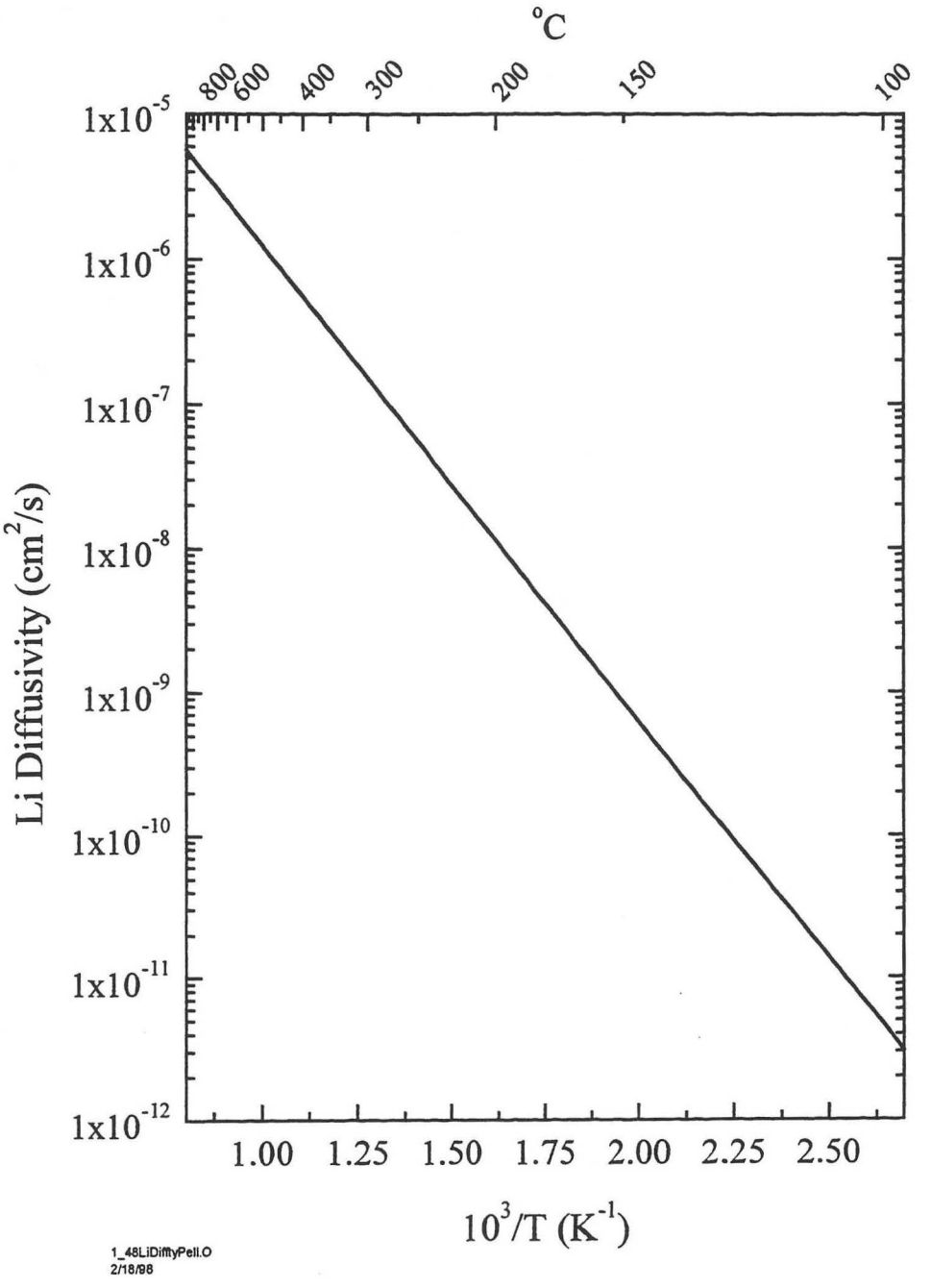

Figure 1.48: Li diffusivity as a function of temperature. [Pell, 1960a, 81]

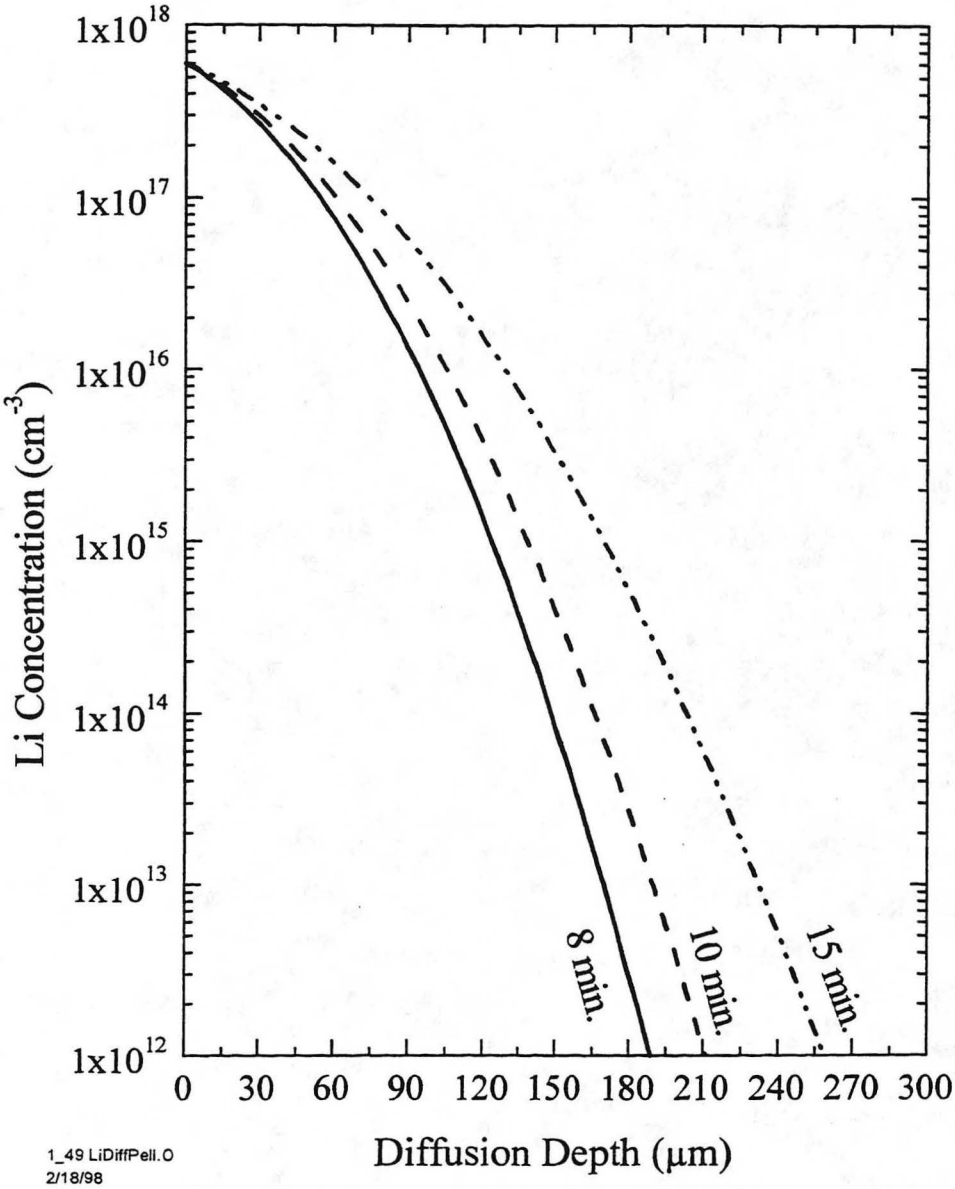

Figure 1.49: A complimentary error function of the Li diffusion profile at 400°C for several diffusion times. The initial Li concentration was obtained from figure 1.47.

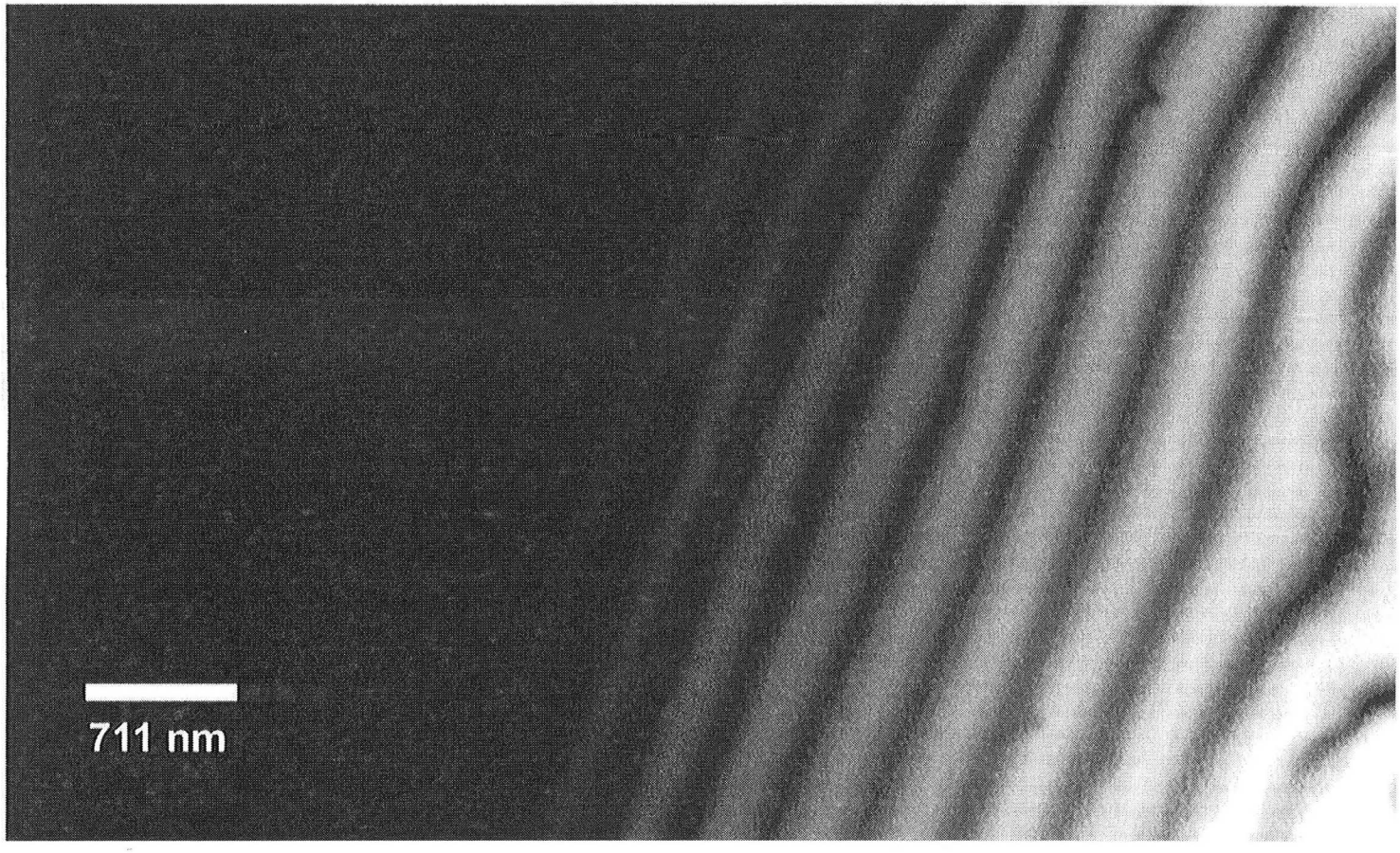

Figure 1.50: A bright field TEM micrograph of a sample taken from a D-defect free region from within the Li reservoir. As can be seen, no precipitation has occurred ruling out the possibility that supersaturation is the driving force for precipitation.

issue. This is supported by studies performed by Haller *et al.* [Haller, 1998, 48] in which resistivity measurements were taken of a Li diffused layer in ultra-pure germanium over a period of time. The maximum Li concentration was larger than 10^{18} cm^{-3}. The resistivity measurements remained constant over time periods of months indicating that the Li donor concentration remained unchanged. This result again suggests that precipitation of the Li does not occur since precipitation would cause a decrease in the donor concentration that would lead to an increase in resistivity. Higher supersaturation is required to initiate precipitation.

1.5.2 Preliminary process modeling of precipitation density results

In order to obtain more information concerning D-defects, the density distribution of the precipitates can be introduced into a model of Li^+ drifting which would simulate precipitation due to D-defects. The size and capture cross-section of the precipitation centers can be determined by adjusting their values to correspond to the experimentally determined Li^+ drift depth. This model is in the process of being developed, but the Li^+ drift model is presented below.[Knowlton, et al., 1998, 64]

The physics of Li^+ drifting was described by Pell [Pell, 1960c, 83]. He begins with Poisson's equation:

$$-\frac{d^2V}{dW^2} = \frac{dE}{dx} = \frac{\rho}{\varepsilon} \tag{1.10}$$

where the charge neutrality, neglecting electrons and holes, is given by:

$$\rho = q\left([Li^+] - [N_A^-]\right) \tag{1.11}$$

The Li^+ concentration before drifting is given by:

$$[Li^+] = [Li^+]_o Erfc\left(\frac{x}{\sqrt{4D_{Li}t}}\right) \tag{1.12}$$

Substituting this expression into Poisson's equation and arranging it such that the derivative of the electric field is proportional to the differential of the intrinsic region width, the following equation is obtained:

$$dE = \frac{q}{\varepsilon}\left([Li^+]_o Erfc\left(\frac{x}{\sqrt{4D_{Li}t}}\right) - [N_A^-]\right)dW \tag{1.13}$$

This is the extent of Pell's model. The model may be further developed by integrating equation 1.13, which yields:

$$E = \frac{q}{\varepsilon}\left\{[Li^+]_o\left(\frac{-1}{\pi}e^{-(x')^2} + x' Erfc(x')\right) - [N_A^-]x\right\}_0^W \tag{1.14}$$

where

$$x' = \frac{x}{\sqrt{4D_{Li}t}} \tag{1.15}$$

Assuming that Li^+ is the only mobile ion (B^- and LiB are immobile), the flux of Li^+ is given by:

$$J = -D_{Li^+}\frac{\partial C_{Li^+}}{\partial x} - \mu C_{Li^+}\frac{\partial V}{\partial x} \tag{1.16}$$

where μ_{Li} is the lithium ion mobility. The first term is the diffusion flux and the second is the drift flux. Since Li^+ drifting occurs at low temperatures, the first term can be ignored. Furthermore, equation 1.14 is just the negative of the derivative in the second term and is substituted into equation 1.16 where:

$$J = \mu C_{Li^+} E \tag{1.17}$$

The continuity equation for the Li^+ is given by:

$$\frac{\partial C_{Li^+}}{\partial t} = -\frac{\partial J}{\partial x} \qquad (1.18).$$

Substituting equation 1.17 into equation 1.18, the continuity equation becomes:

$$\frac{\partial C_{Li^+}}{\partial t} = \frac{\partial}{\partial x}\left(\mu C_{Li^+} E\right) \qquad (1.19).$$

Knowing the applied field, the initial Li^+ profile, and given an initial intrinsic region width, W, E can be determined by solving equation 1.14. Given a short time interval (e.g., 1 sec), equation 1.19 is solved numerically. This gives a new Li^+ profile and intrinsic region width, now equation 1.14 is solved again. This iterative process continues over a given Li^+ drift time and a Li^+ drift profile is derived such as the one shown in figure 1.51. The details of incorporating the Li precipitate density distribution are currently in the stage of development.

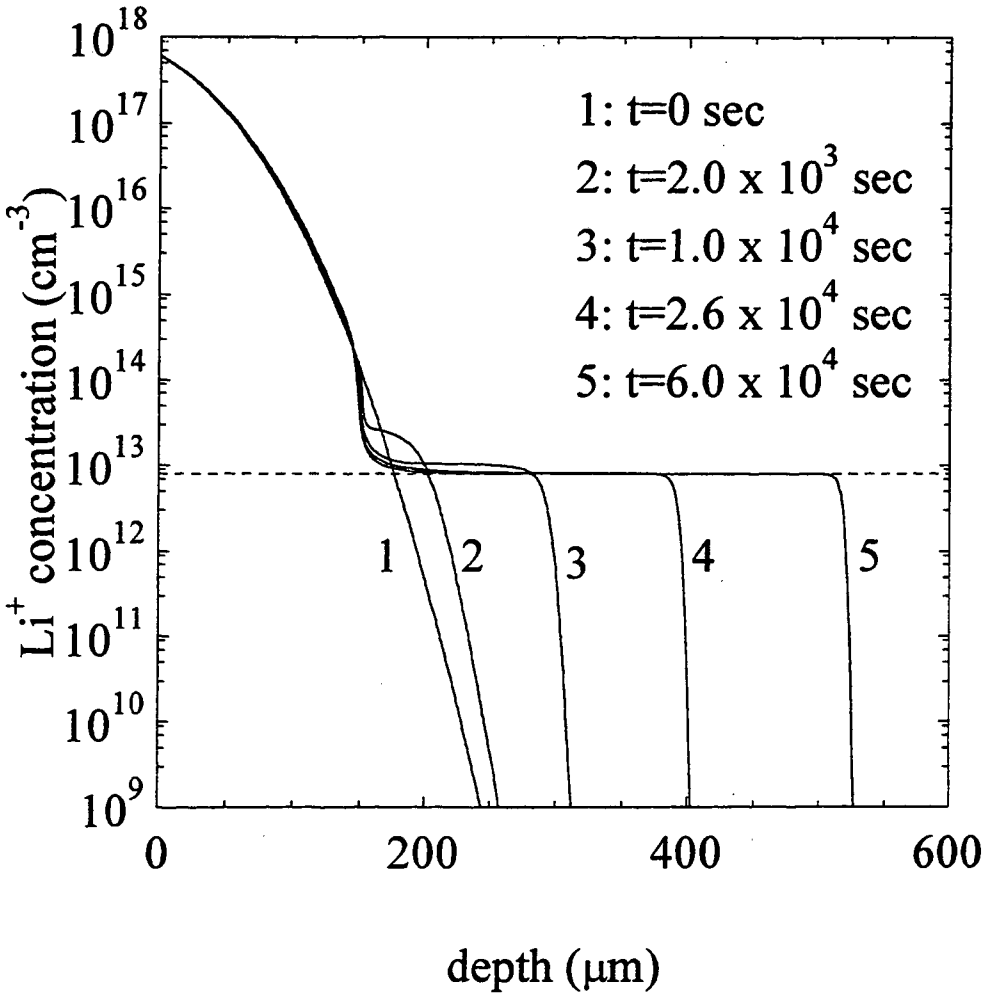

Figure 1.51: Simulated Li^+ drift profiles for given time intervals obtained using the model outlined above. Note the growth of the intrinsic region width and the similarity to the schematic shown in figure 1.3 of section 1.1.1.

2. Self-Interstitial Diffusion in Crystalline Silicon

2.1 Introduction

With the relentless drive to ever smaller device geometries in integrated circuits, reliable values of point defect properties are essential for improving process modeling of these devices. Large differences exist, for example, in the reported values of the diffusivity of silicon self interstitials (D_I).[Zulehner, 1989, 119] The D_I has been determined by several methods including transition metal diffusion [Bracht, et al., 1995, 20; Morehead, 1987, 71; Zimmermann and Ryssel, 1992a, 117] and shallow dopant diffusion experiments.[Bronner and Plummer, 1985, 21; Gossmann, et al., 1993, 44; Griffin, et al., 1985, 46] However, the results vary over nine orders of magnitude as shown in figure 2.1. Furthermore, the D_I data obtained by metal diffusion is somewhat larger than determined by shallow dopant diffusion experiments resulting in a controversy over which experiment produces the more accurate D_I.

In this chapter, experiments using D-defects to study point defect diffusion, and in particular, Si self-interstitial diffusion, are presented. The $POCl_3$ process is used to inject Si self-interstitials into the lattice. The Si self-interstitials migrate to and annihilate D-defects. The absence of D-defects indicates that Si self-interstitials have penetrated at least that distance into the crystal. Si self-interstitial diffusion is studied and values of the D_I for different conditions are determined.

In the first section of this chapter, the general theory of diffusion is discussed and the diffusion equations are derived. In subsequent sections, the role of point defects is

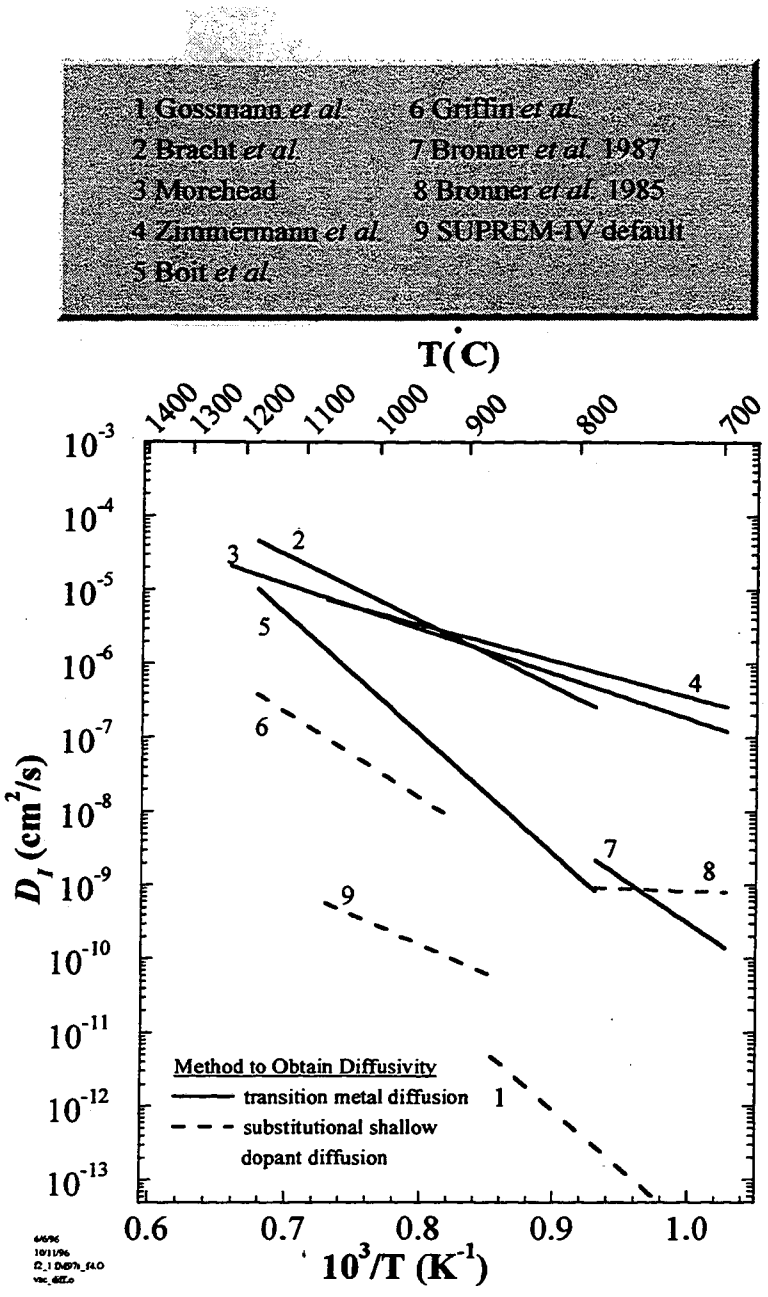

Figure 2.1: Temperature dependence of Si self-interstitial diffusivity deduced from transition metal diffusion experiments (solid) and shallow impurity diffusion (dashed) reported by various authors as indicated.[Boit, et al., 1990, 15; Bracht, et al., 1995, 20; Bronner and Plummer, 1985, 21; Bronner and Plummer, 1987, 22; Gossmann, et al., 1993, 44; Griffin, et al., 1985, 46; Morehead, 1987, 71; SUPREM-IV, 103; Zimmermann and Ryssel, 1992a, 117] Note that the D_I data is spread over nine orders of magnitude. Furthermore, the D_I data deduced by the transition metal diffusion experiments is generally higher than that of the shallow dopant diffusion data.

presented with respect to dopant diffusion in Si and Si self-interstitial diffusion mechanisms are discussed. Then, the experiments used to determine D_I are described. Also, the process modeling program SUPREM-IV is discussed relative to the determination of D_I. Another model is introduced as a possible alternative for SUPREM-IV to describe the experimental results in a manner that incorporates the physics of diffusion in a more intuitive way. Finally, Li^+ drifting, D defects, and Si self-interstitial injection are introduced as another approach to determine D_I.

2.2 Background

2.2.1 The basics of diffusion

Although the emphasis of this section concerns diffusion, a brief review of classical thermodynamics will provide insight to the subject of diffusion. One of the central equations of thermodynamics is the *fundamental equation of thermodynamics*. It describes the change of internal energy of a system that is initially in one state of equilibrium and is perturbed to another state of equilibrium. The perturbation of the system may be due to one or many changes of state and the fundamental equation of thermodynamics considers the possible changes. In its simplest form, the fundamental equation of thermodynamics is given by a change in internal energy of a system as described by sum of the change in heat and work such that:

$$dU = dQ + dW \qquad (2.1).$$

The heat and work of the system are Q and W, respectively. The heat and work differentials are inexact since they are path dependent (depend on past history). Further

details may be found in most textbooks on thermodynamics (see for instance Gaskell [Gaskell, 1981, 38]). The heat differential is described mathematically as:

$$dQ = TdS \tag{2.2}$$

where T and S are the temperature and entropy of the system, respectively. Similarly, the work differential is given by:

$$dW = -PdV_o + \mu dN + \sum YdX \tag{2.3}$$

The first term on the right is hydrostatic work on the system (hence, the negative sign) where P and V_o are the pressure and volume, respectively. The second term, where μ is the chemical potential and N is the number of particles in the system, describes the chemical work done by the system. The last term allows for other forms of work performed on or by the system. Thus, the full fundamental equation of thermodynamics is given by:

$$dU = TdS - PdV_o + \mu dN + \sum YdX \tag{2.4}$$

Two points discussed above directly pertain to the subject of diffusion presented in this thesis. The first point concerns the two types of variables that exist in equation 2.4. The variables that are in differential form are referred to as extensive or state variables. They are called extensive variables because they are directly measurable quantities, and state variables because they describe the state of the system prior to (initial state) and following (final state) the system change. Changes in state variables are path independent. The variables that are pre-factors of the differentials are referred to as field variables and are intensive variables. They are intensive in that they can only be determined by means of the response of an extensive variable to a perturbed system. As alluded to previously, the product of the field variable and differential of the state

variable gives rise to work performed on or by the system. Several examples are given in Table 2.1.

The second point of interest follows from the field variables. The force acting on the system or particles in the system may be described by the negative gradient of a field variable (i.e., field potential) - hence, the term "force field." The force is given by:

$$F = -\nabla V \tag{2.5}$$

where V is the potential field. As shown in table 2.1, the potential field may be a thermal field, a chemical potential, a hydrostatic field, an electrical field, a magnetic field, a stress field, or a gravitational field. Although the superposition principle does not apply to field variables (i.e., intensive), it does to forces. Thus, the gradients of the potential fields are additive; and therefore, the forces driving diffusion processes are additive as well.

Table 2.1: Types of thermodynamic work in differential form

Thermodynamic Work	Work Differential (dW)	Intensive or Field Variable	Extensive or State Variable
thermal	$T \bullet dS$	T = temperature	S = entropy
hydrostatic	$P \bullet dV$	P = pressure	V = volume
chemical	$\mu \bullet dN$	μ = chemical potential	N = number of particles
strain – mechanical	$\sigma \bullet d\varepsilon$	σ = stress	ε = strain
electrical	$E \bullet dP_o$	E = electric field	P_o = polarization
magnetic	$H \bullet dM_g$	H = magnetic field	M_g = magnetization
gravitational	$mg \bullet dr$	mg = mass & gravitational acceleration	r = distance

Consider a force or forces acting on an atom thereby causing atomic motion. The applied force is given by equation 2.5. The motion of the atom is often interrupted by other atoms and collisions occur. Therefore, the velocity of the diffusing atom over a time period larger than the time between collisions is an average velocity. The velocity is proportional to the applied force and can be written as:

$$v = \mu_{mob} F \qquad (2.6).$$

The constant of proportionality, μ_{mob}, is called the mobility and has the units of velocity per unit force or, in more applicable units, the square of the distance per unit time per unit energy.

Consider a flux of atoms, A, diffusing at an average velocity, v, through a homogeneous distribution of B atoms. The flux of A atoms through B is equal to the product of the number of A atoms per unit volume (i.e., concentration) and the average velocity of the A atoms. This is given by:

$$J_A = C_A v_A \qquad (2.7)$$

where C_A and v_A are the concentration and velocity of A atoms, respectively. By comparing equation 2.6 and 2.7, it can be seen that the flux is proportional to the force such that:

$$J_A = C_A \mu_{mob}^A F_A \qquad (2.8).$$

By substituting equation 2.5 into equation 2.8, the following equation:

$$J_A = -C_A \mu_{mob}^A \nabla V_A \qquad (2.9)$$

is obtained which is a general form of Fick's first law. That is, the flux of A atoms through a homogeneous distribution of B atoms is due to the gradient of some potential field. This potential field can be any of the ones mentioned previously (e.g., see table

2.1). Because the gradient of a potential field follows the superposition principle, the more general form of equation 2.9 is given by:

$$J_A = -C_A \mu_{mob}^A \sum_i \nabla V_{i,A} \tag{2.10}$$

where the sum indicates the superposition of potential field gradients.

The potential field for the diffusion described in this thesis is the gradient in the concentration of atoms. Hence, the driving force for diffusion is proportional to the flux of diffusing atoms. This is evident upon examination of the following form of Fick's first law:

$$J_A = -D_A \nabla C_A \tag{2.11}$$

where D_A is the diffusivity of A atoms. The concentration gradient is derived from the gradient of the chemical potential. To this author's knowledge, the derivation of Fick's first law in which the concentration gradient is derived from the chemical potential field has not been performed in full. It has been done in part by P. Shewman.[Shewmon, 1963, 95] Most diffusion is described (in this thesis as well) as driven by a concentration gradient implicitly derived from a chemical potential gradient. In the following paragraphs, Fick's first law, in which the concentration gradient is obtained from the chemical potential, is explicitly derived. Diffusion in solids is based on this delineation.

The chemical potential of atoms A is given by:

$$\mu_A = \left(\frac{\partial \mathrm{E}_A}{\partial N_A} \right)_{T,P,N_{*A}} \tag{2.12}$$

where E_A is a free energy of the A atoms in B. Substituting equation 2.11 into equation 2.9, the flux with respect to the chemical potential gradient is obtain:

$$J_A = -C_A \mu_{mob}^A \nabla \mu_A \tag{2.13}$$

Assuming one-dimensional diffusion (which is assumed throughout the thesis), equation 2.12 simplifies to:

$$J_A = -C_A \mu_{mob}^A \frac{\partial \mu_A}{\partial x} \qquad (2.14).$$

The chemical potential of the A atoms may be written as a function to the activity (i.e., a_A) of A in a distribution of B:

$$\mu_A = \mu_A^\phi + kT \ln a_A \qquad (2.15)$$

where a_A is the activity of A among B, k is Boltmann's constant and μ_A^ϕ is the chemical potential of A in the pure state. The a_A may be described as the amount that the chemical potential of A deviates from the ideal or pure state (i.e., ideality). The ideality can be interpreted as the absence of A-A interaction upon adding an extra A atom to the system. Therefore, the enthalpy change of the system is zero. The mathematical description of the activity is given by:

$$a_A = \gamma_A C_A \qquad (2.16)$$

where γ_A is the activity coefficient and C_A is the concentration of the A atoms. For a range of C_A much smaller than the concentration of B atoms (C_B), γ_A becomes constant. The chance of interaction between A and B atoms is small since A is so dilute in B. The primary interaction of A is with B. This phenomenon is known as Henry's law. Mathematically, as C_A approaches zero, the activity coefficient of A is given by:

$$\gamma_A = \frac{a_A}{C_A} \cong \text{constant} \qquad (2.17).$$

In the case where $C_A >> C_B$ (i.e., B atoms follow Henry's law), the activity coefficient of A is 1. The A atoms have a small probability of interacting with B atoms.

The primary interaction of A atoms is with other A atoms. Hence, the solution of A is effectively pure and the activity coefficient is given by:

$$\gamma_A = \frac{a_A}{C_A} \cong 1 \qquad (2.18).$$

This condition is known as Rault's law. In this thesis, Rault's law is predominant for Si self-interstitial diffusion.

For either Henry's or Rault's law, Fick's first and second law may still be derived from the chemical potential. This eventually can be seen by combining equations 2.14, 2.15, and 2.16 into the following form:

$$J_A = -C_A \mu_{mob}^A \frac{\partial(\mu_A^\phi + kT \ln \gamma_A C_A)}{\partial x} \qquad (2.19).$$

Since the chemical potential of a pure substance is constant, the derivative of μ_A^ϕ is zero. Also, k and T are constant. Under these circumstances and taking the derivative of the natural logarithm, equation 2.19 becomes:

$$J_A = -C_A \mu_{mob}^A \frac{kT}{\gamma_A C_A} \frac{\partial(\gamma_A C_A)}{\partial x} \qquad (2.20).$$

For Henry's law and Rauolt's law, γ_A is a constant or one, respectively. In either case, γ_A may be taken out of the differential. Noting that ratios of both γ_A and C_A factor to 1, equation 2.20 reduces to:

$$J_A = -\mu_{mob}^A kT \frac{\partial C_A}{\partial x} \qquad (2.21).$$

Einstein's relation states that the diffusivity, D, of an atom is proportional to its mobility where the constant of proportionality is kT. Mathematically and in terms of A atoms, this is written as:

$$D_A = kT\mu_{mob}^A \qquad (2.22).$$

Since μ_{mob}^A has the units of the square of the distance per unit time per unit energy and kT has the units of energy, it follows that D_A has the units of the square of the distance per unit time. Invoking Einstein's relation with respect to equation 2.21, Fick's first law is obtained:

$$J_A = -D_A \frac{\partial C_A}{\partial x} \qquad (2.23).$$

It is quite clear that equation 2.23 is equivalent to equation 2.11.

It has been found that as the concentration of A atoms in B changes with time, the concentration changes with position.(e.g., see[Shewmon, 1963, 95]) Known as Fick's second law, it has the following form:

$$\frac{\partial C_A}{\partial t} = -\frac{\partial J_A}{\partial x} \qquad (2.24).$$

Assume that D_A is concentration independent. In the context of this thesis where the concentration of silicon self-interstitials is very small, this assumption may be comfortably made. Substituting equation 2.23 into equation 2.24, Fick's second law, as it pertains to the diffusion discussed in this thesis, is given by:

$$\frac{\partial C_A}{\partial t} = D_A \frac{\partial^2 C_A}{\partial x^2} \qquad (2.25).$$

2.2.2 Diffusion in silicon – the role of point defects

Having presented a general overview of diffusion in solids, the issue of diffusion of self-interstitials in Si can now be addressed. Diffusion in Si has been experimentally studied in several different ways. The most common methods are shallow dopant

diffusion and transition metal diffusion. In both cases, the interstitial diffusivity is determined indirectly. Published results from both of these methods will be presented in a following section. Self-diffusion, as a means to examine Si self-interstitial diffusion, is discussed in the subsequent section.

Silicon self-diffusion

Self-diffusion in Si is governed by intrinsic point defects: Si self-interstitials and vacancies. The self-diffusion coefficient (i.e., diffusivity) (e.g., [Fahey, et al., 1989, 32; Frank, et al., 1984, 34]):

$$D^{SD} = f_I C_I^{eq} D_I + f_V C_V^{eq} D_V + D_{exchange} \qquad (2.26).$$

The last term represents the component of diffusivity resulting in a direct exchange of nearest neighbor Si atoms. The first and second terms denote the contribution from the interstitialcy and vacancy diffusion mechanism, respectively, which will be discussed shortly. $C_{I,V}^{eq}$ and $D_{I,V}$ are the equilibrium concentration and the diffusivity of Si self-interstitials and vacancies, respectively. The product between the equilibrium concentration and diffusivity is known as the *transport capacity*. The correlation factors for the Si self-interstitial and vacancy diffusion components are $f_{I,V}$, respectively. In order to describe $f_{I,V}$, consider a point defect inducing a successful jump of a Si tracer atom deliberately introduced into the lattice. In its new position, the tracer atom continues to be perturbed by the point defect. The correlation factor is the probability that the tracer atom will return to its original position due to the effect of the point defect. Both of their values have been determined.[Fahey, et al., 1989, 32]

Unfortunately, the contribution of each term in equation 2.26 to the self-diffusion of silicon cannot be determined directly (e.g., [Gösele and Tan, 1991b, 42]). This has to do with the limitations of the experimental methods used to study silicon self-diffusion. Self-diffusion in Si can also be studied using naturally occurring and radioactive isotopes of Si. Radio tracer experiments using ^{31}Si have been performed. However, ^{31}Si has a half-life of only 2.6 hours limiting its usefulness in these types of studies. In order to induce diffusion in such a short amount of time, high temperatures near the melting point (~1412°C) must be used. It turns out that the Si self-interstitial transport capacity dominates in the high temperature regime (>1000°C) and this value is well established. Since the equilibrium concentration of Si self-interstitials is not known, D_I cannot be extracted from the Si self-interstitial transport capacity.

A new method of using isotope engineering circumvents these limitations and yields values for the transport factors for Si self-interstitial and vacancy. Isotopically controlled Si heterostructures have been grown and the self-diffusion studied at various temperatures.[Bracht, et al., 1998, 17] However, the D_I cannot be determined directly in any of the silicon steady state self-diffusion studies. Injection of Si self-interstitials from the surface through oxidation or Si implantation can lead to transient enhanced diffusion.[Bronner and Plummer, 1985, 21; Eaglesham, et al., 1994, 29; Gossmann, et al., 1993, 44] Analysis of transient enhanced diffusion profiles can indirectly provide D_I and C_I separately.[Stolk, et al., 1995b, 99]

Impurity atom diffusion in silicon

Many impurity atoms in silicon incorporate interstitially into the lattice. These foreign atoms include Li, Fe, Ni, Cu, and O. Impurity atoms that diffuse without the aid of point defects do so by *direct interstitial diffusion.*

The majority of the substitutional shallow dopants in silicon diffuse via the *indirect method.* That is, they diffuse from substitutional site to substitutional site with the aid of point defects rather then interstitially through the lattice. The primary indirect diffusion mechanisms for these dopants are listed below.[Bracht, et al., 1995, 20; Fahey, et al., 1989, 32]

$$X_i \rightleftharpoons X_s + I \tag{2.27}$$

$$XI \rightleftharpoons X_s + I \tag{2.28}$$

$$XV \rightleftharpoons X_s + V \tag{2.29}$$

$$X_i + V \rightleftharpoons X_s \tag{2.30}$$

The X denotes the dopant atom and the subscripts s and i denote substitutional and interstitial positions, respectively. The first indirect diffusion mechanism is called the *kick-out* mechanism.[Gösele, et al., 1980, 40] Equations 2.28 and 2.29 are the *interstitialcy* and *vacancy* mechanism, respectively. The complexes XI and XV represent an interaction between the dopant and Si self-interstitial and vacancy, respectively, forming a dopant - intrinsic point defect pair (e.g., A-center: phosphorus-vacancy; E-center: oxygen-vacancy). The pairing may be due to lattice distortion or coulomb attraction.[Bracht, et al., 1995, 20] The kick-out and interstitialcy mechanisms are essentially the same in that the substitutional atom is "kicked–out" of its substitutional

site. The vacancy and interstitialcy mechanisms are the same mechanistically. Both mechanisms involve substitutional atoms being evicted from their site by and coupled to an intrinsic point defect. The last equation is the *dissociative* or *Frank-Turnbull* mechanism. Upon examination of the diffusion mechanisms, it becomes obvious that point defects are directly responsible for the diffusion of substitutional shallow dopant atoms.

Knowledge of the paths by which Si self-interstitials and vacancies diffuse through the Si lattice may seem necessary to the discussion at hand; however, they do not need to be known in the subsequent discussions. The interested reader is referred to the articles by Watkins.[Watkins, 1991, 111; Watkins, 1994, 112]

In order to obtain information about Si self-interstitials and vacancies from the above reactions, the reaction rate must be reaction limited. Under equilibrium conditions, the reaction itself does not need to be considered when determining such physical quantities as D_I. However, under nonequilibrium conditions, when the point defect concentrations deviate from their equilibrium values, the reaction rate is controlled by the concentrations of Si self-interstitials and vacancies. Nonequilibrium conditions are established during rapid thermal annealing, particle or ion bombardment, or point defect injection from the surface such as oxidation (see appendix 4.1), nitridation (see section 2.4.5), some silicide formation, and impurity doping at large concentrations (see section 1.2).[Gösele and Tan, 1991a, 41; Hu, 1994, 54]

For the latter case, nonequilibrium exists when the equilibrium concentration of the substitutional impurity is much greater than the equilibrium concentrations of either intrinsic point defect. That is, when the following inequality condition is met:

$$C_{X_s}^{eq} >> C_I^{eq}, C_V^{eq} \quad (2.31).$$

Furthermore, the transport capacities of the diffusing impurity atoms or complexes must be larger than the transport capacities of Si self-interstitials and vacancies. Otherwise, the nonequilibrium concentrations of Si self-interstitials and vacancies produced by X_s will decrease more rapidly than X_s is supplied from the surface. For transition metals such as Au, Pt and Zn, the transport capacities are indeed larger than those of Si self-interstitials and vacancies and are given by:

$$C_{X_i}^{eq} D_{X_i}, C_{XV}^{eq} D_{XV}, C_{XI}^{eq} D_{XI} >> C_I^{eq} D_I, C_V^{eq} D_V \quad (2.32)$$

where the commas denote and/or. Hence, transition metal diffusion has been used extensively to provide information concerning D_I.

However, the transport capacities of substitutional shallow dopants are less than those of Si self-interstitials and vacancies leading to the following inequalities:

$$C_{X_i}^{eq} D_{X_i}, C_{XV}^{eq} D_{XV}, C_{XI}^{eq} D_{XI} << C_I^{eq} D_I, C_V^{eq} D_V \quad (2.33).$$

Therefore, dopant diffusion will not provide any direct information concerning the transport capacities of Si self-interstitials or vacancies. Yet, Si self-interstitials and vacancies are very much involved in the substitutional shallow dopant diffusion process. This is apparent when examining the effective diffusivities of many substitutional shallow dopants in silicon under both equilibrium and nonequilibrium conditions. The intrinsic point defect - substitutional shallow dopant interaction is quite evident. Under equilibrium conditions, where $C_{I,V} = C_{I,V}^{eq}$, the effective diffusivity of substitutional impurities in silicon is given by:

$$D_{X_s}^{eff,eq} = \frac{C_{XI}^{eq} D_{XI}}{C_{X_s}^{eq}} + \frac{C_{XV}^{eq} D_{XV}}{C_{X_s}^{eq}} = D_{XI}^{eff} + D_{XV}^{eff} \quad (2.34).$$

As apparent from equation 2.34, Si self-interstitials and vacancies play a significant role in the equilibrium diffusion of substitutional shallow dopants.

Under nonequilibrium conditions, where $C_{I,V} \neq C_{I,V}^{eq}$, the change in concentration from equilibrium, must be considered. This is apparent upon inspection of the substitutional shallow dopant's effective diffusivity, which is given by:

$$D_{X_s}^{eff} = \frac{C_{XI}^{eq} D_{XI}}{C_{X_s}^{eq}} \frac{C_I}{C_I^{eq}} + \frac{C_{XV}^{eq} D_{XV}}{C_{X_s}^{eq}} \frac{C_V}{C_V^{eq}} = D_{XI}^{eff} \frac{C_I}{C_I^{eq}} + D_{XV}^{eff} \frac{C_V}{C_V^{eq}} \qquad (2.35).$$

Hence, the effective diffusivity under nonequilibrium conditions increases with an increase in concentration above the equilibrium concentration. An interesting manner in which to view the equation above is by dividing through by equation 2.34. This form is given by:

$$\frac{D_{X_s}^{eff}}{D_{X_s}^{eff,eq}} = \frac{D_{XI}^{eff}}{D_{XI}^{eff} + D_{XV}^{eff}} \frac{C_I}{C_I^{eq}} + \frac{D_{XV}^{eff}}{D_{XI}^{eff} + D_{XV}^{eff}} \frac{C_V}{C_V^{eq}} = s_I \frac{C_I}{C_I^{eq}} + s_V \frac{C_V}{C_V^{eq}} \qquad (2.36)$$

The $s_{I,V}$ terms are the fractional diffusivities of the substitutional shallow dopant – intrinsic point defect pairs pertaining to the interstitialcy and vacancy mechanisms, respectively. The plot shown in figure 2.2 shows the fractional interstitialcy component of the effective diffusivity for several of the main substitutional dopant atoms in silicon.[Gösele and Tan, 1991a, 41] Since the dopant atoms are incorporated substitutionally into the lattice, figure 2.2 is plotted relative to the ratio of the dopant radius to the silicon atom radius. The tendency shown is that the smaller substitutional dopant atoms diffuse mainly via the interstitialcy or kick-out mechanisms while the larger substitutional shallow dopant atoms diffuse by the vacancy diffusion mechanism.

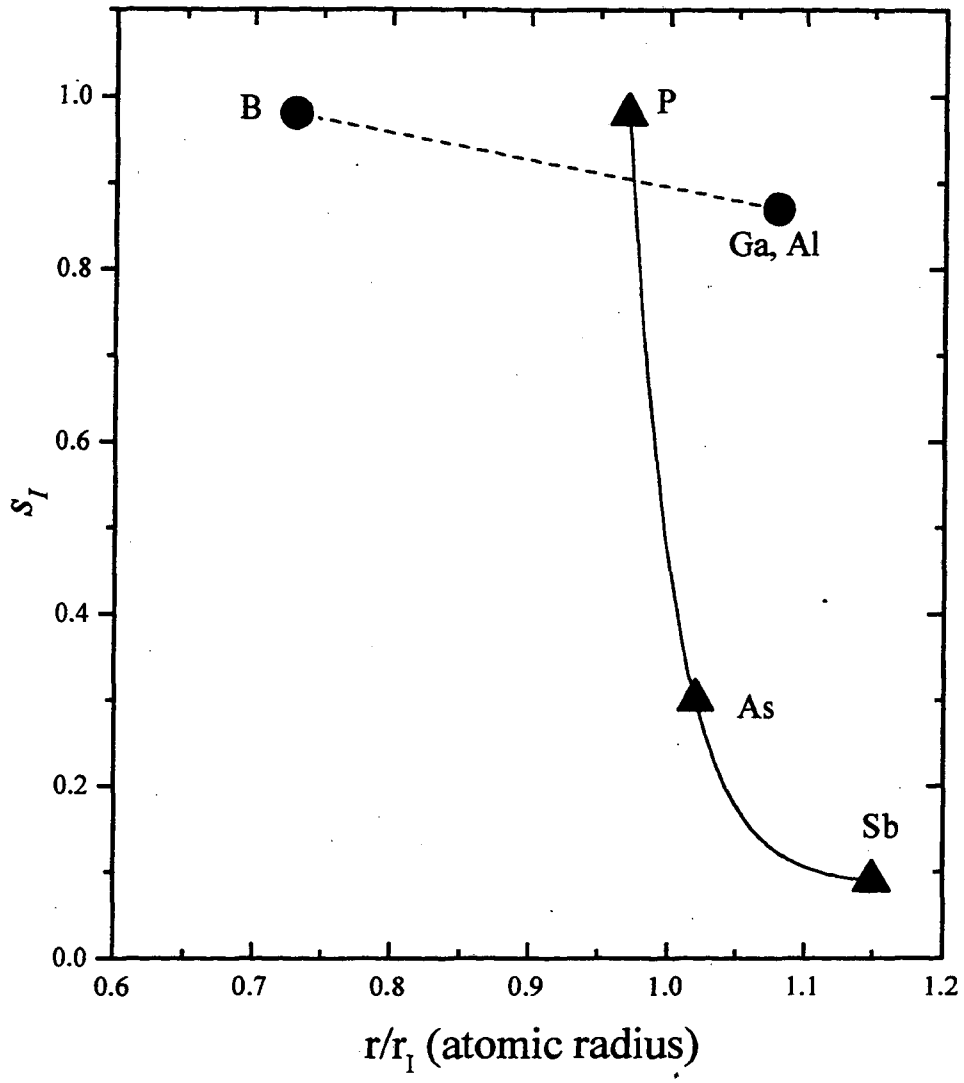

f2.1 interstitial
vs radius.o
5/98

Figure 2.2: The fraction of interstitialcy diffusion with respect to the atomic radii of substitutional shallow dopant normalized to the atomic radius of Si. Notice that B and P diffuse primarily by the interstitialcy mechanism while Sb diffuses mainly by the vacancy mechanism.

From the above discussion, it is clear that intrinsic point defects are intimately involved in the diffusion of substitutional shallow dopants and transition metals. However, steady state substitutional shallow dopant and transition metal diffusion experiments cannot directly yield the diffusivities of Si self-interstitials or vacancies. In the subsequent section, this will become evident for D_I when reviewing the two main experimental methods used to determine the D_I.

2.2.3 Experiments used to determine D_I

In the preceding sections, discussion concerning intrinsic and extrinsic point defect diffusion has indicated that the D_I cannot be obtained explicitly. In the following paragraphs, both substitutional shallow dopant diffusion studies and transition metal diffusion studies will be briefly reviewed to illustrate this point.

D_I determined by transient enhanced substitutional shallow dopant diffusion

A group at Lucent Technologies pioneered the use of delta doping of substitutional shallow dopants in order to determined the D_I.[Eaglesham, et al., 1994, 29; Gossmann, et al., 1995, 43; Gossmann, et al., 1993, 44; Stolk, et al., 1995a, 98; Stolk, et al., 1995b, 99] They developed a superlattice structure of epitaxially grown single crystal silicon with periodic delta doping structures of boron using molecular beam epitaxy (MBE). The 10 nm wide boron spikes, beginning 55 nm from the surface, were about 100 nm apart. One structure was left as-grown. Dry thermal oxidation of the surface of another structure at about 800°C was performed to inject Si self-interstitials. Secondary

ion mass spectroscopy (SIMS) was performed on each structure to determine the boron distribution. The as-grown structure was used to minimize depth resolution errors from SIMS for the oxidized structure. The effective diffusivity of boron in the oxidized structure was determined by fitting the boron distribution of each spike of boron using the equation:

$$D_B^{eff} = D_{B,x}\left[1+\beta\frac{C_B(x)}{n_i}\right] \tag{2.37}$$

where is $D_{B,x}$ is the fitting parameter, β is an enhancement factor, and n_i is the intrinsic carrier concentration. The effective diffusivity of boron in the oxidized structure is proportional to the Si self-interstitial concentration:

$$D_B^{eff} \propto C_I(x,t) \tag{2.38}$$

where C_I is the Si self-interstitial concentration. The effective boron diffusivity of each spike is plotted with respect to the depth, as shown in figure 2.3. A best fit to the curve is performed using the C_I. Assuming that the C_I injected at the surface remains constant during oxidation, then C_I is given, at any time t, by:

$$C_I(x,t) = erfc\left[\frac{x^2}{D_I^{avg}t}\right] \tag{2.39}$$

where D_I^{avg} is the average D_I. The complimentary error function can be expanded such that:

$$erfc(a_o) = erfc(a) + 2a^2 erfc(a) - 2a\pi^{-1/2}\exp(-a^2) \tag{2.40a}$$

where

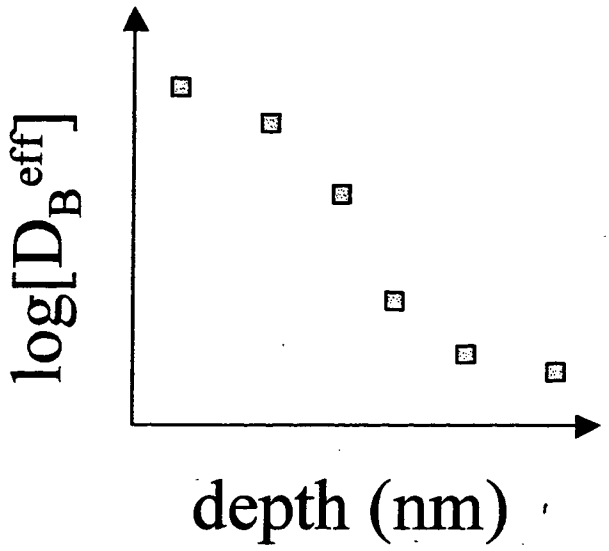

Figure 2.3: Plot of the effective boron diffusivity. Each data point corresponds to one boron spike. The data is proportional to a complimentary error function distribution of C_I where an average D_I is used as a fitting parameter.

$$a = \frac{x}{\sqrt{\frac{1}{4D_I^{avg}t_{ox}}}} \tag{2.40b}$$

and

$$a_o = x\sqrt{\frac{1}{4D_I^{avg}t_{ox}}} \tag{2.40c}$$

The oxide thickness is t_{ox}. In this whole approach, the D_I is by no means obtained directly.

D_I determined by transition metal diffusion

As mentioned in section 2.2.2, transition metal diffusion in silicon may be used to determine properties of intrinsic point. This has been done for Au, Pt and Zn. One point defect property extracted from transition metal diffusion experiments is the D_I.[Boit, et al., 1990, 15; Bracht, et al., 1991, 18; Bracht, et al., 1994, 19; Bracht, et al., 1995, 20; Bronner and Plummer, 1987, 22; Morehead, 1987, 71; Stolwijk, et al., 1983, 100; Zimmermann and Ryssel, 1992a, 117; Zimmermann and Ryssel, 1992b, 118] Although the D_I extraction methods may slightly differ with respect to each experiment, one method [Bracht, et al., 1995, 20] is discussed to give an indication of the procedure involved to obtain the D_I.

A transition metal is diffused into a Si wafer (i.e., both wafer faces) of thickness d at several different temperatures for various times. Spreading resistance measurements with respect to depth are performed to obtain the distribution of the substitutional transition metal concentration, C_{X_s}. It has been determined [Frank, et al., 1984, 34] that the C_{X_s}, at $x=\frac{d}{2}$, normalized to equilibrium solubility concentration, $C_{X_s}(x=0)$, is given by:

$$\tilde{C}_{X_s}\left(x=\frac{d}{2},t\right)=\frac{C_{X_s}\left(x=\frac{d}{2},t\right)}{C_{X_s}(x=0)}=\left(\frac{4\pi}{d^2}\frac{C_{eq}^{I}D_I}{C_{X_s}^{eq}}\right)^{\frac{1}{2}} \qquad (2.41a).$$

Therefore, equation 2.43 is proportional to the square root of the Si self-interstitial transport capacity. $\tilde{C}_{X_s}$, at $x=\frac{d}{2}$, is plotted for each temperature as a function of time as shown in figure 2.4. Since figure 2.4 is plotted log-log, then the slope of the isotherms is given by:

$$slope = \log\left(\sqrt{\frac{C_{eq}^{I} D_I}{C_{X_s}^{eq}}}\right) \qquad (2.41b).$$

Solving for the D_I in terms of the slope, it is given by:

$$D_I = \frac{10^{2 \cdot slope}}{\frac{C_I^{eq}}{C_{X_s}^{eq}}} \qquad (2.41c).$$

The term in the denominator is used as a fitting parameter to obtain the D_I for each temperature. The manner in which D_I is obtained using transition metal diffusion experiments is much more elegant than if it is extracted using substitutional shallow dopant diffusion experiments. However, it remains an indirect method.

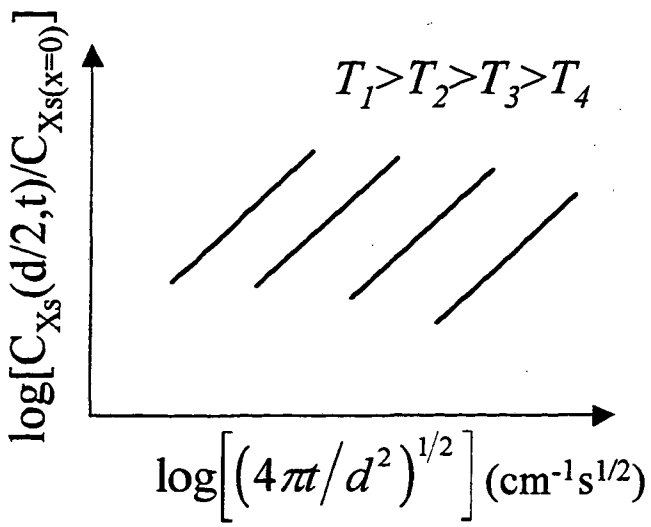

Figure 2.4: The log of $\tilde{C}_{x_s}$ is plotted as a function of time for several different temperatures.

2.3 Modeling D_I

2.3.1 Simulation of D_I using SUPREM-IV

Created at Stanford and further developed at TMA, Inc. and Silvaco Inc., the process modeling program SUPREM-IV is used to simulate such processes as diffusion, ion implantation, oxidation and other processes performed in the silicon industry. The modeling performed in this thesis was done with SUPREM-IV, which was used to obtain D_I. In this section, the equations and approach used in SUPREM-IV are described.

Due to the proprietary agreement between the purchaser and seller of SUPREM-IV, the equations used in SUPREM-IV cannot be divulged. In general, SUPREM-IV models intrinsic point defect kinetics by developing and numerically solving the continuity equations (modified Fick's second law) for the Si self-interstitial and vacancy. The development of the continuity equation for Si self-interstitials, which is analogous for vacancies, focuses on including a plethora of Si self-interstitial diffusion sources that may be present during silicon processing. This is apparent when examining the continuity equation for Si self-interstitials given by:

$$\frac{\partial C_I}{\partial t} + \sum \frac{\partial M}{\partial t} = -\bar{\nabla} \cdot \left[D_I C_I^{eq} \bar{\nabla} \frac{C_I}{C_I^{eq}} + \sum \bar{J}_m \right] + G_p - R_b - R_t \qquad (2.42).$$

where J_m is the flux of dopant - Si self-interstitials complex pairs, M is the concentration of dopant - Si self-interstitials complex pairs, G_p is the reaction equation for dopant-intrinsic point defect pairs, R_b is the net recombination rate of Si self-interstitials with vacancies in bulk Si, and R_t is the Si self-interstitial absorption rate by immobile traps.

The D_I, C_I^{eq} and the Si self-interstitial - vacancy recombination constant, K, are referred to as *point defect parameters* and are described by Arrhenius expressions given by:

$$D_{I,V} = D_o^{I,V} \exp\left(\frac{-E_D^{I,V}}{k_B T}\right) \text{ cm}^2/\text{s} \tag{2.43}$$

$$C_{I,V}^{eq} = C_o^{I,V} \exp\left(\frac{-E_C^{I,V}}{k_B T}\right) \text{ cm}^{-3} \tag{2.44}$$

$$K = K_o \exp\left(\frac{-E_K}{k_B T}\right) \text{cm}^3/\text{s} \tag{2.45}$$

The diffusivity enthalpy term, $E_D^{I,V}$, is the sum of the enthalpy of formation and migration, and $E_C^{I,V}$ is the activation enthalpy for equilibrium, while $E_K^{I,V}$ is the enthalpy barrier of Si self-interstitial – vacancy recombination [Fahey, et al., 1989, 32; Kump and Dutton, 1988, 66]. The pre-exponential factor $D_o^{I,V}$ contains a number of physical constants and properties including the entropy of formation of the defect, the attempt frequency for jumps into available neighboring sites, the lattice constant, and a crystal structure dependence.[Porter and Easterling, 1981, 86] The pre-exponential factor $K_o^{I,V}$ depends on the unit cell volume of silicon, the lattice site density, the capture radius for recombination, and the sum of D_I and D_V [Fahey, et al., 1989, 32]. Lastly, k_B is Boltzmann's constant. Each variable in equation 2.42, other than the point defect parameters, contains anywhere from five to thirteen variables.

The model in SUPREM-IV used for the injection of Si self-interstitials is nearly as complicated. Due to the lack of a $POCl_3$ process model, a wet oxidation model was used to simulate the $POCl_3$ process of Si self-interstitial injection used in this thesis. In the wet oxidation model, a local interface velocity is utilized to show the consumption of

Si during oxidation. The velocity is normalized with a factor that varies with time and oxidation conditions. Unfortunately, this assumption does not allow the peak recombination velocity to vary with the oxidation rate. However, the modeling of experimental observations in this study may not require a variable recombination velocity.

In several cases, the factors used by SUPREM-IV to model Si self-interstitial diffusion do not impact Si self-interstitial diffusion in the experiments presented in this thesis. As will be elucidated in subsequent sections, Si self-interstitial diffusion occurs deep in the bulk well away from the surface. Thus, Si self-interstitial - vacancy recombination at surface does not need to be considered. Furthermore, the actual process of injection can be omitted from the model; only the net flux created during oxidation or the $POCl_3$ process should not be neglected. Other factors considered by SUPREM-IV that are excessive relative to this study are point defect charge states and pair complexes. They can be deferred because the dopant concentration of the Si crystals used is very low (N_A-N_D~$5x10^{13}$ cm^{-3}) and the Si self-interstitial diffusion occurs well away from the surface where the $POCl_3$ process (i.e., high P concentration) occurs.

SUPREM-IV is well suited for process modeling in industry. However, the complexity of the equations and unnecessary factors used in SUPREM-IV inhibits a fundamental understanding of the physics and materials science of diffusion. Therefore, a more innate and elementary model has been developed using lessons acquired in the SUPREM-IV modeling exercise. The model is currently in the preliminary stages of development. The following section outlines the model.

2.3.2 The Bracht-Knowlton Si self-interstitial diffusion model

As has been shown in the previous section, the process simulation program SUPREM-IV is complicated and empirical in many of the models that it incorporates. It is difficult to ascertain which specific materials parameters are associated with SUPREM-IV's parameters. Deconvolving SUPREM-IV's code to determine these parameters would be a difficult and ardent task. The physics of the Si self-interstitial transport and interaction of point defects may be better understood by using a more elementary model that would simulate the experimental results in an intuitive manner. In this section, a model is presented that incorporates the physics of diffusion in a more perceptive way.

The B-K model (Bracht-Knowlton) follows the model that Bracht *et al.* [Bracht *et al.*, 1994, 19] used to describe Zn diffusion in highly dislocated Si. In this work, Bracht *et al.*'s model is revised to incorporate D-defects rather than dislocations. The purpose of this model is two-fold. First, it is designed to be simple and certain rational assumptions, which are subsequently described, are made to make it so. If the experimental results cannot be explained, then the assumptions will be eliminated until the experimental results can be explained. Second, physical parameters important to this study, such as the D-defect concentration and diffusivity, are included in the model so that they may be determined quantitatively.

The purpose of the B-K model is to simulate Si self-interstitial transport from the surface into the bulk of D-defect containing crystalline Si. To do so, several assumptions are made in the B-K model. One-dimensional diffusion is assumed, because lateral diffusion is insignificant. The concentration of Si self-interstitials injected at the surface

is considered to be constant. The D-defects are presumed to be Si self-interstitial traps and their total concentration remains constant (i.e., the number of total sites equals the number of annihilated and remaining traps). Furthermore, only one Si self-interstitial can recombine with one trap site and both annihilate one another. Lastly, assuming an infinite source of Si self-interstitials, the surface concentration of Si self-interstitials at any time, t, $C_I(0,t)$ is constant. As the time becomes very large (i.e., $t \to \infty$) and equilibrium is essentially reached, then the bulk Si self-interstitial concentration, C_I^*, approaches that of the surface concentration, $C_I(0,t \to \infty)$. It is assumed that the C_I^* is greater than the thermal equilibrium Si self-interstitial concentration, C_I^{eq}. Thus, for long time periods where equilibrium has been established, it is found:

$$C_I(t \to \infty) \to C_I^* \qquad (2.46).$$

The reaction equation for the interaction between the Si self-interstitials and the D-defect traps is given by:

$$I + T_e \underset{k_r}{\overset{k_f}{\rightleftharpoons}} T_o + L \qquad (2.47)$$

where T_e, T_o and L are the concentrations of the empty traps, occupied traps and interstitial lattice sites, respectively. The change in the concentration of Si self-interstitials during the reaction with respect to time is described by the differential equation:

$$\frac{\partial C_I^{reac}}{\partial t} = k_r C_{T_o} C_L - k_f C_I C_{T_e} \qquad (2.48).$$

The variables k_f and k_r are the forward and reverse coefficients of reaction, respectively. At equilibrium, the equilibrium constant for the reaction 2.47 is equal to the ratio of the products over reactants:

$$K_{eq} = \frac{C_{T_o}^{eq} C_L}{C_I^* C_{T_e}^{eq}} \tag{2.49}$$

The next assumption presumes that local equilibrium is attained. That is, shortly after the reaction begins, the net Si self-interstitial concentration does not change with small changes in position or time. The system has reached a steady state. This is written mathematically as:

$$\frac{\partial C_I^{reac}}{\partial t} = 0 \tag{2.50}$$

Solving for the ratio of reaction coefficients, equation 2.51 results:

$$\frac{k_f}{k_r} = \frac{C_{T_o} C_L}{C_I^* C_{T_e}} \tag{2.51}$$

By the law of mass action, equation 2.48 and equation 2.51 may be combined giving rise to the equality:

$$\frac{C_I^* C_{T_e}^{eq}}{C_{T_o}^{eq} C_L} = \frac{C_{T_o}^{eq} C_L}{C_I^* C_{T_e}^{eq}} \tag{2.52}$$

Equation 2.52 may be rewritten in terms of the reaction coefficients:

$$\frac{k_f}{k_r} = \frac{C_{T_o} C_L}{C_I^* C_{T_e}} \tag{2.53}$$

Solving for k_r in terms of k_f results in:

$$k_r = k_f \frac{C_I^* C_{T_e}^{eq}}{C_{T_o}^{eq} C_L} \tag{2.54}$$

Leaving the reaction section of the diffusion model momentarily, the diffusion aspect of this diffusion model will be further expanded. The total D-defect trap concentration in this model is described by:

$$C_n = C_{T_e} + C_{T_o} = C_{T_o}^{eq} + C_{T_e}^{eq} \qquad (2.55).$$

As the injected Si self-interstitials diffuse into the bulk, the Si self-interstitial concentration changes at each position as time progresses (neglecting the reaction component of the Si self-interstitial). The change in the Si self-interstitial concentration with respect to time as a result of diffusion may be described by the partial differential equation:

$$\frac{\partial C_I^{dif}}{\partial t} = D_I \frac{\partial^2 C_I}{\partial x^2} \qquad (2.56).$$

In order to determine the total change in the Si self-interstitial concentration with respect to time, both the reaction and diffusion equations must be combined. This is done by combining equations 2.47 and 2.56 which results in the complete form of the diffusion equation describing both the transient reaction and diffusion nature of Si self-interstitials:

$$\frac{\partial C_I}{\partial t} = \frac{\partial C_I^{dif}}{\partial t} + \frac{\partial C_I^{reac}}{\partial t} = D_I \frac{\partial^2 C_I}{\partial x^2} + k_r C_{T_o} C_L - k_f C_I C_{T_e} \qquad (2.57).$$

In mathematical descriptions of diffusion ,such as equation 2.57, an important parameter is the D_I. Because it appears only in the first term of equation 2.57, it is embedded in the solution and difficult to extract. This complicated equation needs to be manipulated such that an effective Si self-interstitial diffusivity is obtained. This is done using substitutions, algebra and calculus that can be found in the appendix. The mathematical manipulations of equation 2.57 result in the following form of the partial differential equation and effective diffusivity of Si self-interstitial:

$$\frac{\partial C_I}{\partial t} = D_I^{eff} \frac{\partial^2 C_I}{\partial x^2} \tag{2.58}$$

where D_I^{eff} is the Si self-interstitial effective diffusivity. As derived in the appendix, D_I^{eff} is given by:

$$D_I^{eff} = \frac{C_I^* D_I}{C_I^* + \dfrac{C_{tt} C_{T_e}^{eq} C_{T_o}^{eq}}{\left(C_{T_o}^{eq} \tilde{C}_I + C_{T_e}^{eq}\right)^2}} \tag{2.59}$$

The variables used in equation 2.59 are defined in the appendix 4.5.

The D-defect concentration and the degree of D-defect - Si self-interstitial interaction are not known at this point in the study. Thus, various cases of Si self-interstitial trapping will be considered to better understand possible ways in which Si self-interstitial trapping may occur. For each case, the D_I^{eff} will vary and result in different solutions for equation 2.58. Hence, the distribution of Si self-interstitials with respect to position will change as well. For each case of Si self-interstitial trapping, the D_I^{eff} for that case will be determined and a general graphical representation of the normalized Si self-interstitial concentration, $\tilde{C}_I$, will be presented.

The first case considered is the case in which an insignificant amount of Si self-interstitial trapping occurs. Therefore, the equilibrium occupied trap concentration, $C_{T_o}^{eq}$, is essentially zero. Thus, the normalized total trap concentration, $\tilde{C}_{tt}$, is much less than $\tilde{C}_I$. Substituting zero for $C_{T_o}^{eq}$ into equation 2.59, D_I^{eff} simplifies to just D_I. The normalized Si self-interstitial concentration, $\tilde{C}_I$, is given by a complementary error function distribution of which a general graphical representation is shown in figure 2.5.

As previously mentioned, the normalized trap concentration, C_{tt}, is negligible relative to $\widetilde{C}_I^{eq}$.

The next case considered is moderate trapping of Si self-interstitials. In this case, the following inequality is met:

$$\frac{C_{T_o}^{eq}}{C_{tt}} \langle\langle 1 \qquad (2.60).$$

Upon substitution into equation 2.59 D_I^{eff} is reduced to:

$$D_I^{eff} \approx \frac{C_I^* D_I}{C_I^* + C_{T_o}^{eq}} = \frac{D_I}{1 + \frac{C_{T_o}^{eq}}{C_I^*}} \qquad (2.61).$$

The mathematics performed to obtain equation 2.61 are given in appendix 4.5. The resulting numerically determined distribution of $\widetilde{C}_I$ is a slightly retarded complementary error function as shown in figure 2.6.

The third case of Si self-interstitial trapping considers a strong D-defect - Si self-interstitial interaction in which Si self-interstitials are readily trapped. Two conditions of strong Si self-interstitial trapping may exist. The first condition is one in which the equilibrium occupied trap concentration is very large, yet not as large as the injected Si self-interstitials concentration. In this case, the equilibrium occupied trap concentration is nearly that of the total trap concentration is given by:

$$C_{tt} \approx C_{T_o}^{eq} \qquad (2.62).$$

Thus, for a large Si self-interstitial concentration, it follows that:

$$\widetilde{C}_I \rangle\rangle \frac{C_{T_o}^{eq}}{C_{T_o}^{eq}} \qquad (2.63).$$

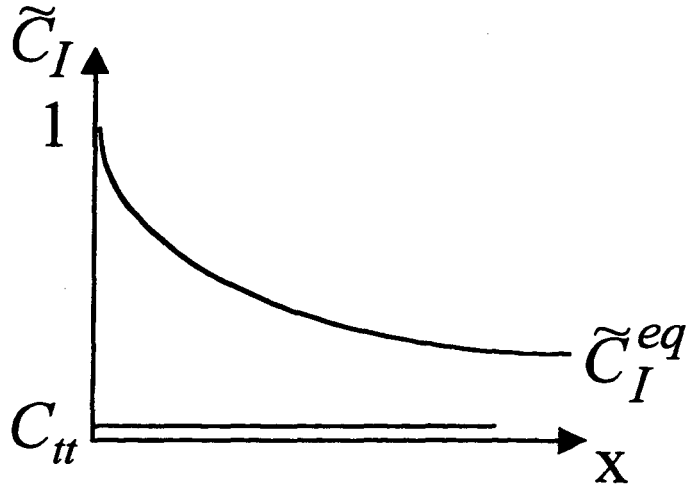

Figure 2.5: A complementary error function distribution of $\tilde{C}_I$ for the case of insignificant trapping. C_{tt} represents the total normalized concentration of traps with respect to the total concentration of Si self-interstitials.

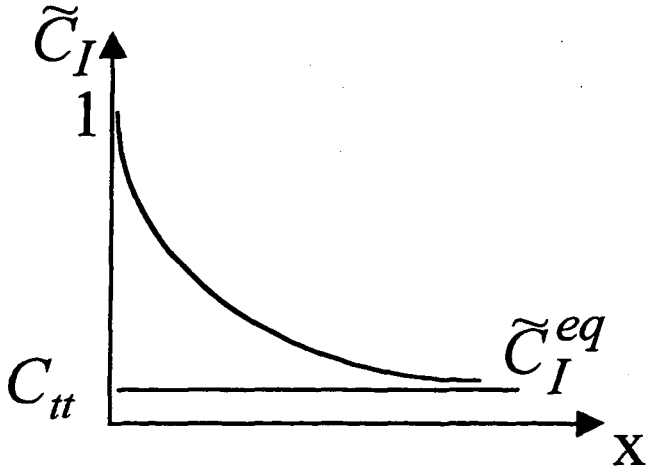

Figure 2.6: A slightly retarded complementary error function distribution of $\tilde{C}_I$ for the case of moderate Si self-interstitial trapping. C_{tt} is somewhat larger than in the first case.

By considering equations 2.62 and 2.63, equation 2.59 reduces to equation 2.64 as derived in the appendix 4.5:

$$D_I^{eff} \approx \frac{D_I}{1+\frac{C_{T_e}^{eq}}{C_I^*}\tilde{C}_I^{-2}} \qquad (2.64).$$

The Si self-interstitial concentration profile which results from the strong trapping is illustrated in figure 2.7. Note that the numerically derived distribution is a truncated complementary error function where the injected Si self-interstitial concentration is severely reduced by the slightly smaller total trap concentration.

Another possible case of strong trapping is similar to the previous case for which equation 2.62 holds. However, in this scenario, the injected Si self-interstitial concentration is smaller than the total trap concentration. Therefore, the subsequent inequality may be expressed by:

$$\tilde{C}_I \langle\langle \frac{C_{T_e}^{eq}}{C_{T_o}^{eq}} \qquad (2.65).$$

Substituting equations 2.60 and 2.61 into equation 2.55 leads to equation 2.62 as shown in the appendix 4.5:

$$D_I^{eff} \approx \frac{D_I}{1+\frac{C_{ii}^2}{C_I^* C_{T_e}^{eq}}} \qquad (2.66).$$

The concentration distribution of Si self-interstitials is also a truncated complementary error function similar to figure 2.8. Notice that, in this case, the total trap concentration is larger than the injected Si self-interstitial concentration.

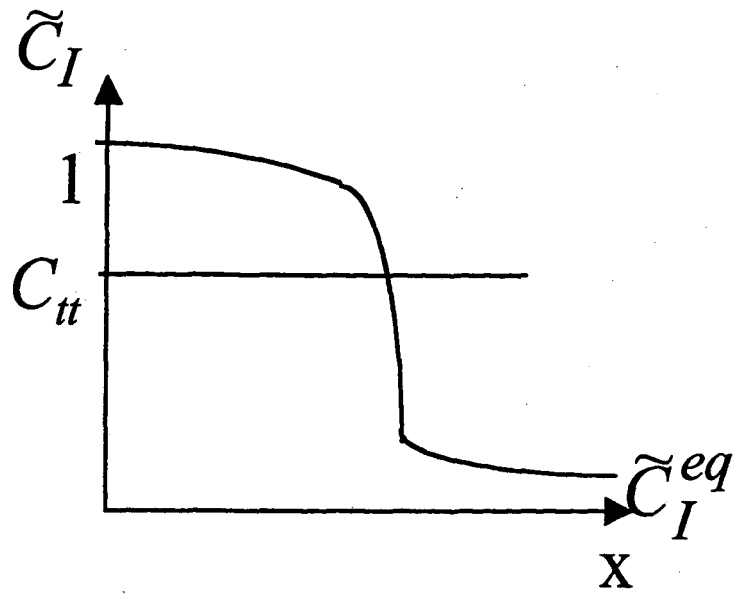

Figure 2.7: A strongly truncated complementary error function distribution of $\tilde{C}_I$ for the case of moderate Si self-interstitial trapping. C_{tt} is somewhat smaller the Si self-interstitial concentration near the surface.

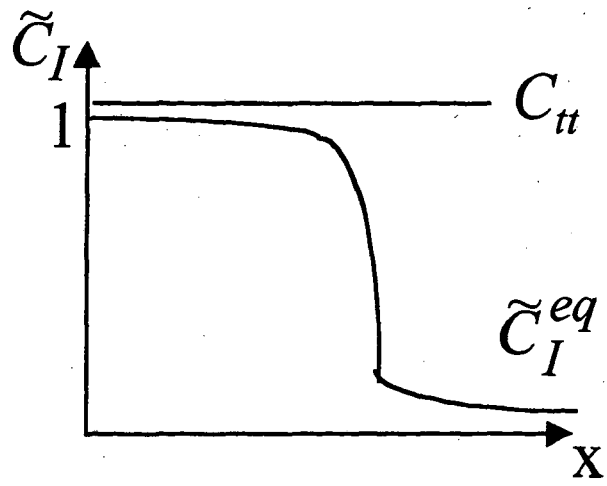

Figure 2.8: A strongly truncated complementary error function distribution of $\tilde{C}_I$ for the case of moderate Si self-interstitial trapping. C_{tt} is larger the Si self-interstitial concentration near the surface.

2.4 D_I as Revealed by Li^+ Drifting

2.4.1 Experiment 1: D-defect study yielding D_I

It was shown previously that the concentration of D-defects was reduced by injection of Si self-interstitials during the $POCl_3$ process. Following the $POCl_3$ process and Li^+ drifting, Cu staining of the cross-sectioned wafer revealed that the Li^+ completely drifted through the entire 3 mm thick wafer. The results are shown in the Li^+ drift profile in figure 1.6. For Li^+ to drift unimpeded, the D-defect concentration must be significantly reduced throughout the wafer. D-defects are eliminated by the recombination of Si self-interstitials and vacancies. During the $POCl_3$ process, Si self-interstitials were injected from both sides of the wafer. The absence of D-defects indicates that Si self-interstitials diffused at least 1.5 mm to the center of the wafer. In this way, $POCl_3$ processing followed by Li^+ drifting can determine the diffusion distance of Si self-interstitials.

Si self-interstitial diffusion can now be studied using Li^+ drifting, D-defects and the $POCl_3$ process. That is, Si self-interstitials can be injected into Si containing D-defects, diffuse through the bulk and annihilate D-defects. In this way, the D-defects are employed as markers. Li^+ drifting can be used to delineate the remaining D-defects thereby revealing the diffusion distance of Si self-interstitials. Using process simulation, the D_I can be determined. Hence, this method to study Si self-interstitial diffusion may resolve the controversy between the published values of D_I as determine by shallow dopant diffusion [Bronner and Plummer, 1985, 21; Gossmann, et al., 1993, 44; SUPREM-IV, 103] and transition metal diffusion [Boit, et al., 1990, 15; Bracht, et al.,

1995, 20; Bronner and Plummer, 1987, 22; Griffin, et al., 1985, 46; Morehead, 1987, 71; Zimmermann and Ryssel, 1992a, 117].

Using SUPREM-IV [SUPREM-IV, 103], Si self-interstitial diffusion distances were simulated based on the point defect default values listed in column 2 of tables 2.2 and 2.3. It was found that the Li^+ drifting and $POCl_3$ results disagree with the results computed with SUPREM-IV. Using the default point defect values, the simulated Si self-interstitial injection depth is only on the order of 50 μm. Figure 2.10 shows the normalized concentration (i.e., C/C_{eq}) of vacancies and interstitials as a function of sample depth. The simulation indicates that the injected Si self-interstitial have reduced the vacancy concentration well below the equilibrium concentration up to 50 μm. This result is clearly inconsistent with the 1.5 mm diffusion distance using Li^+ drifting of the $POCl_3$ processed D-defect containing FZ Si wafers.

Although simulations with SUPREM-IV using the default point defect parameters do not agree with the experimental results, the use of other published point defect parameters with some modifications give experimentally consistent results. For example, using the point defect activation enthalpy values $E_D^{I,V}$ and $E_C^{I,V}$ from Bracht *et al.* [Bracht, et al., 1994, 19] listed in column 3 of table 2.2 and 2.3 and varying the pre-exponential terms for diffusivity and equilibrium concentration, results were obtained that are compatible with those of SUPREM-IV. The simulation results are shown in figure 2.11. As can be seen, the Si self-interstitial injection depth is approximately 1.5 mm agreeing well with the Si self-interstitial injection depths observed experimentally (~1.5 mm). Similar simulations may be obtained by altering other published point defect parameters. This was accomplished using the point defect activation energy values $E_D^{I,V}$

Table 2.2: Selected Si self-interstitial parameters

Point Defect Parameter	SUPREM-IV-IV Default Values	Bracht et al. [Bracht, et al., 1994, 19]	This Work E_D^I & E_C^I taken from ref. [Bracht, et al., 1994, 19]	This Work E_D^I & E_C^I taken from ref. [Park and Law, 1992, 78]
D_O^I (cm^2/s)	3.65x10^{-4}	5.1x10^{1}	~0.9	~9x10^{2}
E_D^I (eV)	1.58	1.77	1.77	2.44
C_O^I (cm^{-3})	1.25x10^{29}	2.9x10^{24}	~3x10^{25}	~8x10^{21}
E_C^I (eV)	3.26	3.18	3.18	2.36
K_O^I (cm^3/s)	10^{-21}	—	~7x10^{-17}	5.1x10^{-3}
E_K^I (eV)	-1	—	0	3.19

Table 2.3: Selected Si vacancy parameters

Point Defect Parameter	SUPREM-IV-IV Default Values	Bracht et al. [Bracht, et al., 1994, 19]	This Work E_D^V & E_C^V taken from ref. [Bracht, et al., 1994, 19]	This Work E_D^V & E_C^V taken from ref. [Park and Law, 1992, 78]
D_O^V (cm^2/s)	3.65x10^{-4}	3x10^{-2}	~0.9	~9x10^{4}
E_D^V (eV)	1.58	1.8	1.8	2.92
C_O^V (cm^{-3})	1.25x10^{29}	1.4x10^{23}	~1.4x10^{20}	~10^{17}
E_C^V (eV)	3.26	2.0	2.0	1.08
K_O^V (cm^3/s)	10^{-21}	—	~7x10^{-17}	5.1x10^{-3}
E_K^V (eV)	-1	—	0	3.19

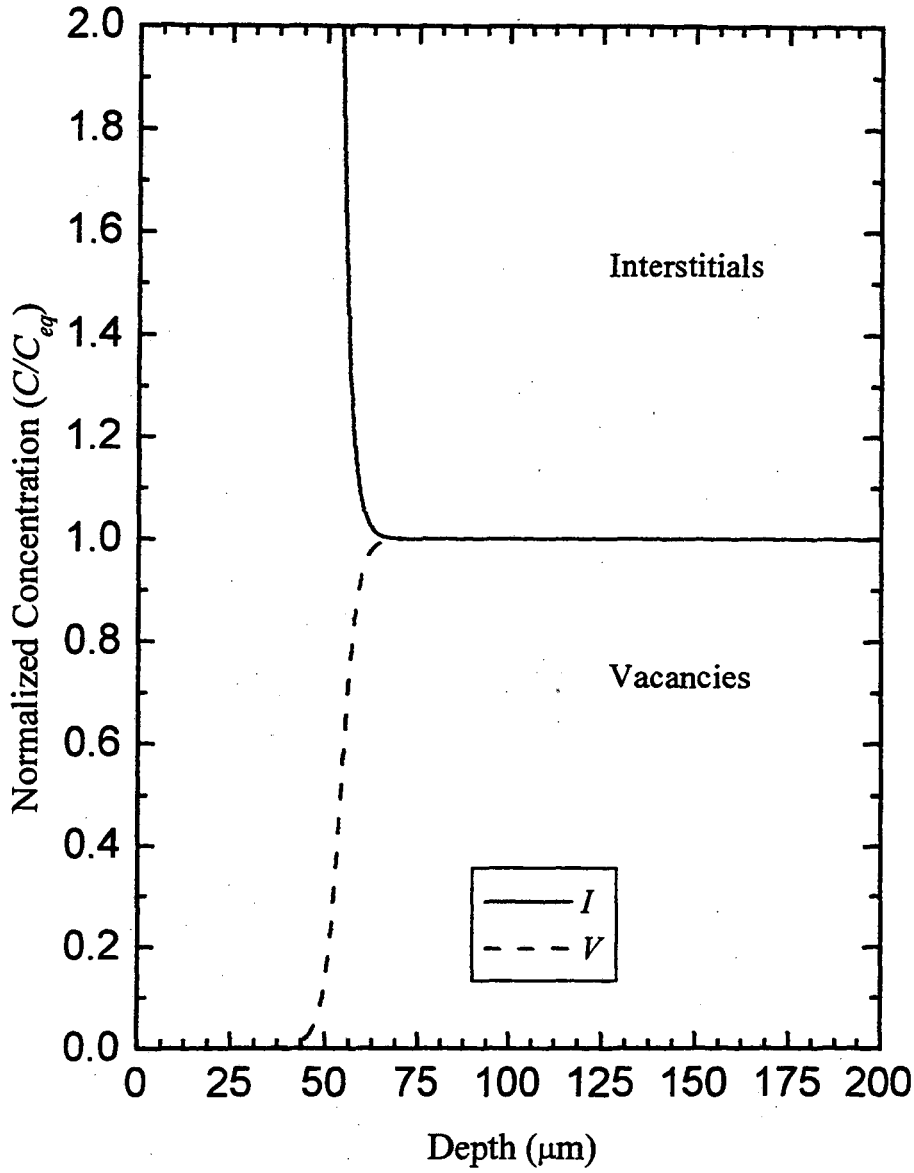

Figure 2.10: The Si self-interstitial diffusion (i.e., injection) depth is simulated using SUPREM-IV's default point defect parameter values. The solid line shows that the Si self-interstitial and vacancy concentrations equilibrate at 50 μm. The simulation shows that Si self-interstitials have diffused and significantly reduced the vacancy concentration up to 50 μm into the bulk. This is not consistent with our results showing that Si self-interstitials diffuse at least 1.5 mm into the bulk.

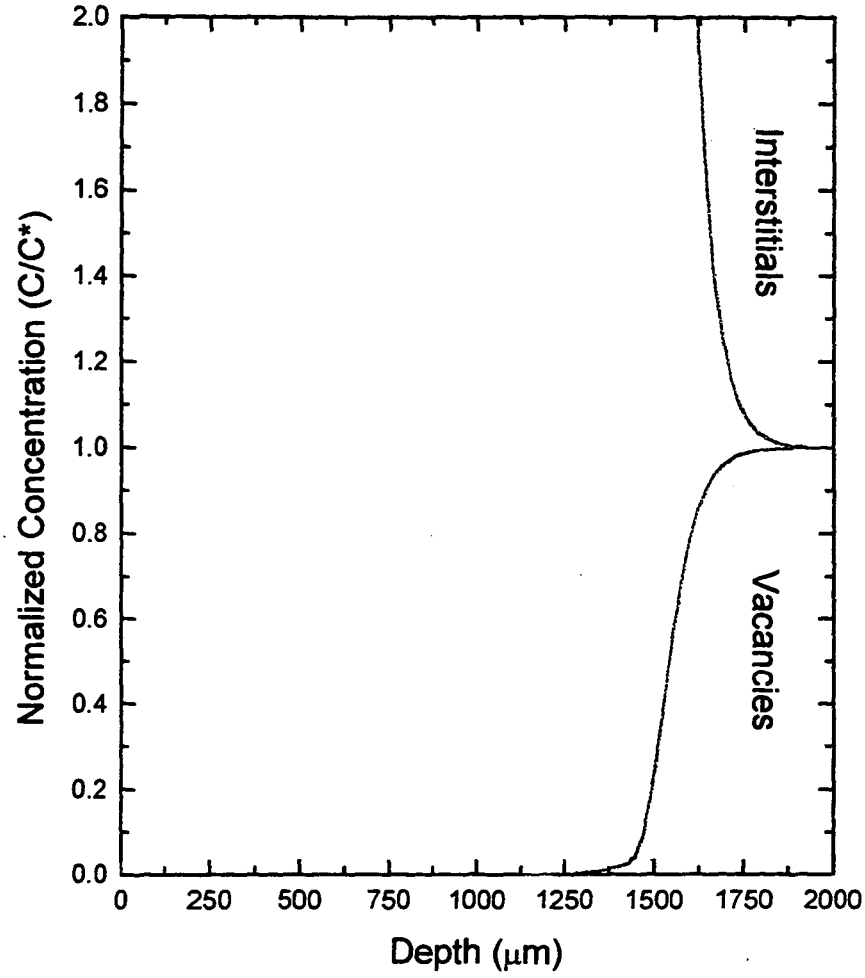

Figure 2.11: The Si self-interstitial diffusion (i.e., injection) depth is simulated using SUPREM-IV. The Si self-interstitial injection depth is consistent with the results using Bracht *et al.* [Bracht, et al., 1994, 19] $E_D^{I,V}$ and $E_C^{I,V}$ values and modifying their other point defect parameter as shown in tables 2.2 and 2.3 . The solid line shows that the Si self-interstitial and vacancy concentrations equilibrate at 1.5 mm. Hence, the simulation shows that Si self-interstitials have diffused and significantly reduced the vacancy concentration up to 1.5 mm into the bulk which is consistent with the observed experimental results.

and $E_C^{I,V}$ published by Park and Law.[Park and Law, 1992, 78] By changing their pre-exponential terms for diffusivity and equilibrium concentration, simulations using SUPREM-IV are obtained describing the experimental results. The modifications are shown in Tables 2.2 and 2.3. The results of the simulation are shown in figure 2.12, which illustrate that Si self-interstitials are injected to a depth of about 1.5 mm.

Modifying as few point defect parameters as possible simplifies the SUPREM-IV simulations. The best approach is minimizing the modifications by using only one variable point defect parameter. This approach was used to determine the experimental diffusion distance based on Park and Law's [Park and Law, 1992, 78] work. The alteration required that the D_I pre-exponential value change by only a factor of 3. Table 2.4 lists Park and Law's modified and unmodified point defect parameters as well as the default values used in SUPREM-IV. The new simulation is shown in figure 2.13 and pertains to the results using the default point defect parameters of SUPREM-IV and the modified D_I pre-exponential value of Park and Law. It is interesting to note that Park and Law's values give rise to a simulation inconsistent with the simulation based on the default point defect parameters used in SUPREM-IV. Based on the simulation shown in figure 2.13, the D_I was calculated and found to be 1.6×10^{-7} cm^2/s. This data point is plotted with other reported ranges of D_I in figure 2.14. Upon examination of the data, the D_I determined in this experiment is in closer agreement with the D_I determined by transition metal diffusion experiments than with the substitutional shallow dopant diffusion experiments.

The results presented here indicate a minimum diffusion distance for the Si self-interstitials. Since D-defects were reduced throughout the whole wafer, a lower bound

diffusion depth of 1.5 mm is established. To better determine the Si self-interstitial diffusion distance, the same experiment could be performed with a thicker wafer. Alternatively, another physical process or phenomenon may be responsible for the reduction of D-defects. One possibility is an interaction between Si self-interstitials and Li^+. In the following sections, these possibilities are examined.

Table 2.4: Selected Si self-interstitial parameters

Point Defect Parameter	**SUPREM-IV Default Values (1982)**	**Park & Law** [Park and Law, 1992, 78] **(1992)**	**Park & Law Modified**†
D_O^I (cm^2/s)	3.65x10^{-4}	6x10^2	~18x10^2
E_D^I (eV)	1.58	2.44	2.44
C_O^I (cm^{-3})	1.25x10^{29}	5.0x10^{22}	5.0x10^{22}
E_C^I (eV)	3.26	2.36	2.36
K_O^I (cm^3/s)	10^{-21}	8.2x10^{-4}	8.2x10^{-4}
E_K^I (eV)	-1	3.19	3.19
D^I (cm^2/s)	1.13x10^{-10}	5.3x10^{-8}	~1.6x10^{-7}

†We chose to change D_O^I, but could have changed another pre-exponential.

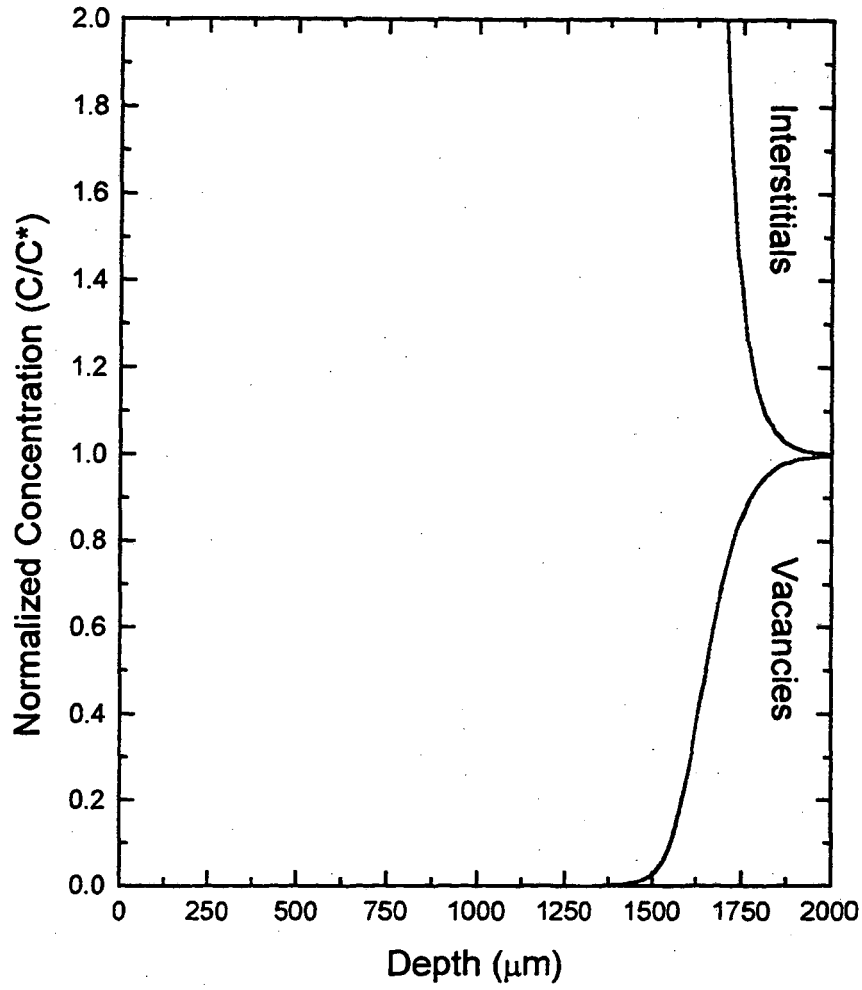

Figure 2.12: The Si self-interstitial diffusion (i.e., injection) depth is simulated using SUPREM-IV. The Si self-interstitial injection depth is consistent with the results using Park and Law's [Law, 1994 #347] $E_D^{I,V}$ and $E_C^{I,V}$ values and modifying their other point defect parameter as shown in tables 2.2 and 2.3 . The solid line shows that the Si self-interstitial and vacancy concentrations equilibrate at 1.5 mm. Hence, the simulation shows that Si self-interstitial have diffused and significantly reduced the vacancy concentration up to 1.5 mm into the bulk which is consistent with the observed experimental results.

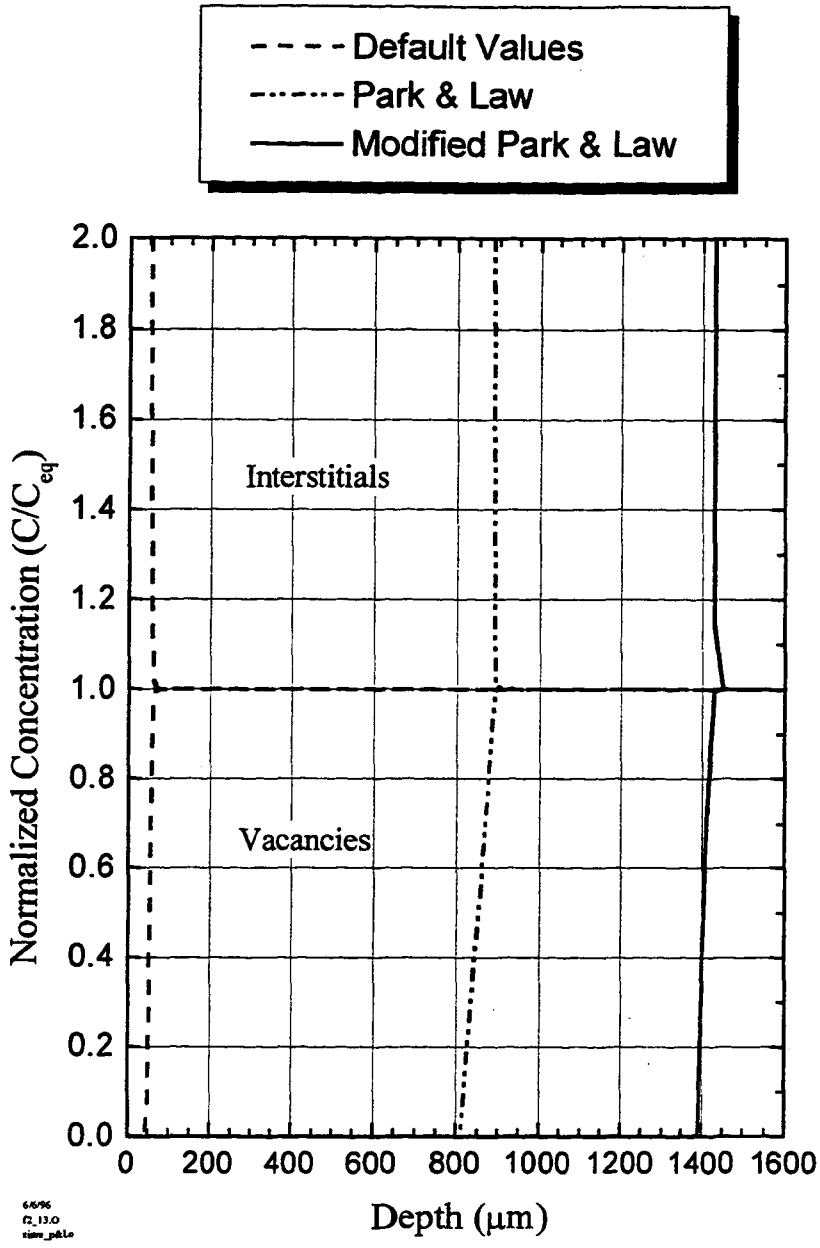

Figure 2.13: The solid line shows a Si self-interstitials diffusion (i.e., injection) depth of about 1.5 mm into the bulk which is consistent with the observed experimental results. This simulation was achieved by modifying only D_I of Park and Law's published point defect parameters. [Park and Law, 1992, 78] For comparison, the dotted-dashed line represents a simulation using the unmodified Park and Law point defect values. The dashed line is the same simulation shown in figure 2.10 and is added for comparison.

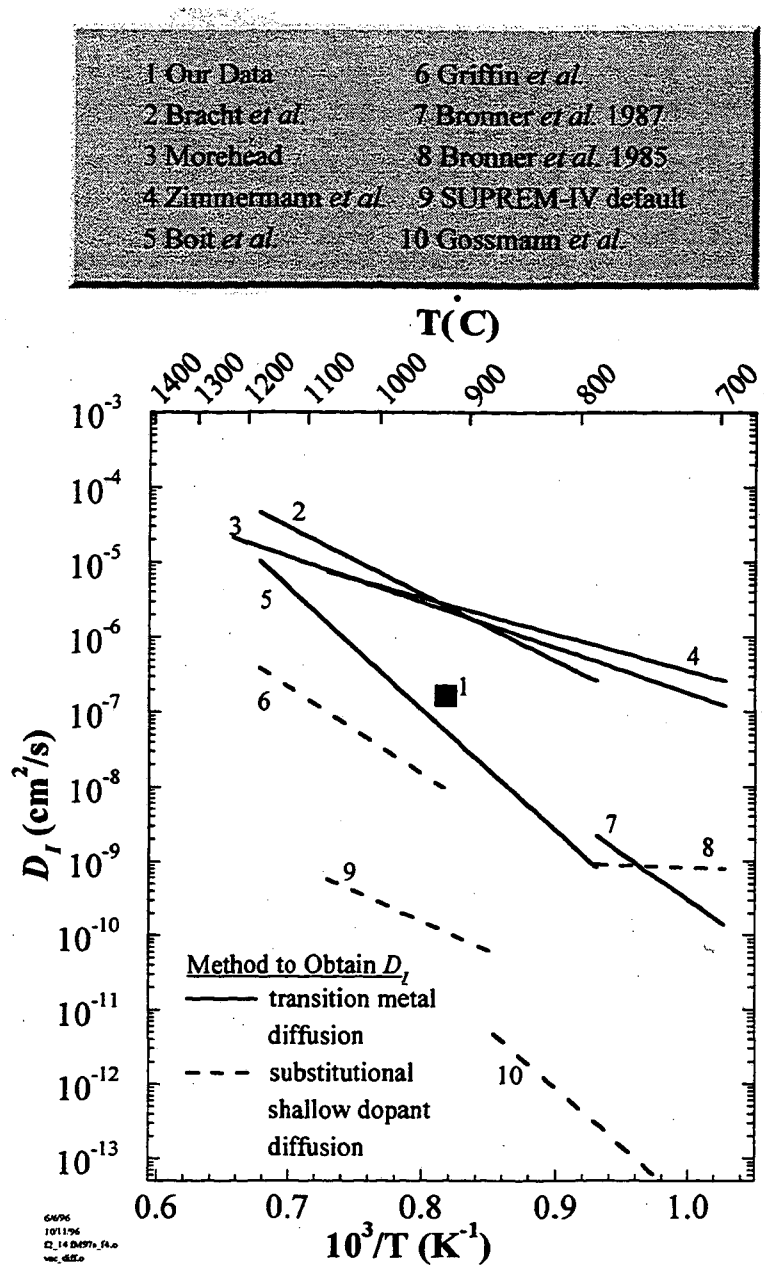

Figure 2.14: Temperature dependence of Si self-interstitial diffusivity deduced from transition metal diffusion experiments (solid) and shallow impurity diffusion (dashed) reported by various authors as indicated.[Boit, et al., 1990, 15; Bracht, et al., 1995, 20; Bronner and Plummer, 1985, 21; Bronner and Plummer, 1987, 22; Gossmann, et al., 1993, 44; Griffin, et al., 1985, 46; Morehead, 1987, 71; SUPREM-IV, 103; Zimmermann and Ryssel, 1992a, 117] The D_I data point represented by square shows this work's lower bound which results from the analysis of the Li^+ drift experiments. The diffusivity data below this data point are inconsistent with this work. However, the D_I of this work, since it is a lower bound, is not in disagreement with the D_I data above it.

2.4.2 Experiment 2: Possibility of Li^+ drifting assisting the transport of Si self-interstitials

In this section, the possibility is examined that Li^+ drifting may assist the transport of Si self-interstitials previously injected into the wafer during the $POCl_3$ process. Suppose, for the moment, that the SUPREM-IV simulations, using the default point defect parameters, are correct. That is, assume that Si self-interstitials are injected 50 μm into the bulk from either face of the wafer as simulated by SUPREM-IV and shown in figure 2.10. The following argument can then be forwarded. After the injection of Si self-interstitials during the $POCl_3$ process and during Li^+ drifting, perhaps Li ions interact with Si self-interstitials. Presume that due to this interaction and the ion-drifting field, transport of Si self-interstitials occurs throughout the bulk of the wafer (i.e., at least 1.5 mm). During the transport, Si self-interstitials would eliminate D-defects and allow Li^+ to drift completely though the wafer. If proven, this argument would explain the completion of Li^+ drifting and the apparent discrepancy of the SUPREM-IV simulations presented in the previous section. It would also suggest that the SUPREM-IV default point defect parameters do not need to be altered.

An experiment was designed to test the validity of this argument. Assume that the Si self-interstitial diffusion distance is indeed 50 μm. Therefore, following the $POCl_3$ process, the injected Si self-interstitials should be within 50 μm from the wafer faces. If 50 μm of material were removed from the wafer face, then all the injected Si self-interstitials would be removed as well. Upon Li^+ drifting this wafer, Si self-interstitials would not be present to interact with Li^+ and would not be transported during Li^+ drifting. Thus, the D-defects would not be eliminated and would be present to curtail Li^+ drifting.

The following experiment was performed to show that Li^+ drifting does not assist the transport of Si self-interstitials. From a *p*-type <111> FZ 7 cm diameter boule of silicon known to have D-defects, three sets of samples were taken and processed in the following manner. The first set of samples were $POCl_3$ treated and then their surfaces were removed by lapping to a depth of either 50 μm or 100 μm. The second and third sets of samples were used as control samples. The second set of samples was $POCl_3$ treated but the surfaces were not removed. The third set of samples was neither $POCl_3$ treated nor were their surfaces removed. Li^+ drifting was performed on all three sets of samples. Following Li^+ drifting, all sample sets were analyzed for drift depth using Cu staining as previously described.

The results of the experiment showed unambiguously that no Li^+ drift-assisted Si self-interstitial transport is taking place. The first and second set of samples were completely Li^+ drifted, whereas the third set of samples did not Li^+ drift completely. The Li^+ drift profiles of the first and second sample sets and the third sample set are analogous to the Li^+ drift profiles of the untreated and $POCl_3$ processed Si samples shown in figure 1.6 in chapter 1. As the simulation illustrates in figure 2.10, Si self-interstitials are injected to a depth of several tens of micrometers during the $POCl_3$ process. This issue is further examined in the following sections where experiments using thicker wafer are discussed.

2.4.3 Experiment 3: The $POCl_3$ process of 2 cm thick wafers

In section 2.4.1, a lower bound Si self-interstitial diffusion distance and D_I were determined. In this section, an experiment is described in which a 2 cm thick wafer,

nearly six times thicker than in the previous experiments, is employed to determine the Si self-interstitial diffusion distance. By using a thicker wafer, the extent of the Si self-interstitial diffusion should become measurable since it is expected to be less than half the wafer thickness. Thus, not all the D-defects would be eliminated. The remaining D-defects would curtail Li^+ drifting and thereby reveal the extent of Si self-interstitial diffusion. From this data, a Si self-interstitial diffusion distance could be determined. Additionally, this experiment allows the further examination of Li^+ drifting assisted Si self-interstitial transport.

Several wafers were cut from a 10 cm diameter boule of *p*-type <111> FZ Si containing D-defects. One wafer was used as a control while the other wafer, following lapping, cleaning and processing, was subjected to the $POCl_3$ process. Post annealing was performed at a temperature of 950°C for 100 min to diffuse the P from both faces causing Si self-interstitial injection to occur from both wafer faces into the bulk.

To keep the Li^+ drifting processing steps consistent with previous experiments, several 3 mm thick slabs were cut from each of the $POCl_3$ treated wafers, perpendicular to the wafer faces (vertical slabs with respect to the wafer). The width of the slab is the diameter of the wafer (10 cm) and the height of the slab is the thickness of the wafer. This is shown in figure 2.14.

Each slab was cut into 8 samples (~ 1.1 cm x 2 cm x 3 mm thick) to simplify the processing. The samples were lapped, processed and Li^+ drifted as described in chapter 1. In this geometry, Li^+ drifting was performed perpendicular to the Si self-interstitial injection direction to enhance the resolution of the drift profile.

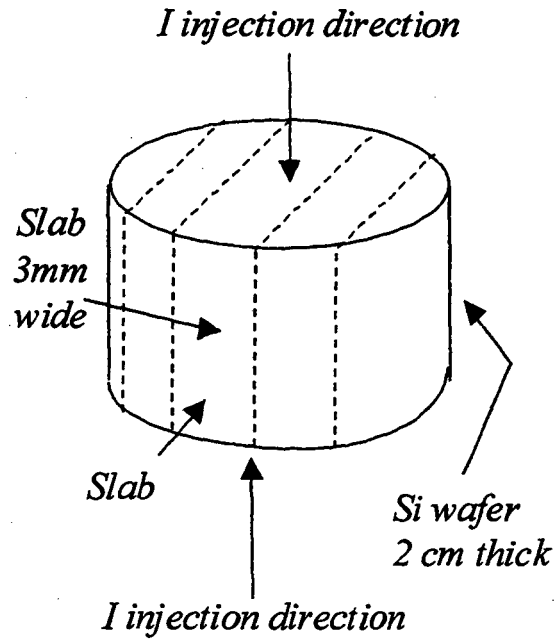

Figure 2.14: A schematic of the 2 cm thick wafer shows the Si self-interstitial injection into both wafer faces during the $POCl_3$ process. Subsequently, the wafer was cut into 3 mm wide slabs and Li^+ drifted perpendicular to the Si self-interstitial injection direction.

As was previously mentioned, the control wafer did not undergo the $POCl_3$ process. This wafer was cut into samples, processed and Li^+ drifted in the same manner as described for the $POCl_3$ treated wafer (see section 1.2.2).

In order to determine if the samples were fully or partially Li^+ drifted, Li^+ drift profiles were established by Cu staining the cross-sectioned samples. The Cu staining results on the samples from the slab of the 2 cm thick control wafer revealed that the wafer periphery fully Li^+ drifted while the inner central region of the wafer did not. This

result is illustrated by the data points given by circles in Li^+ drift profile shown in figure 2.15. As expected, the control wafer has a large concentration of D-defects in the central region.

Cu staining was also performed on the cross-sectioned slabs (i.e., 8 samples per slab) which were taken from the 2 cm thick $POCl_3$ processed Si wafer. The stain profiles of each sample showed that each sample fully Li^+ drifted. Therefore, it is concluded that the 2 cm thick wafer also fully Li^+ drifted. The Li^+ drift data points from the samples is depicted in figure 2.15 as triangles.

The Li^+ drifted samples taken from the wafer, which did not undergo the $POCl_3$ process, were cross-sectioned and Cu stained as well. The Cu staining of the samples showed that only partial Li^+ drifting had occurred within the central region of the crystal as shown in figure 2.15. This proves that D-defects are present in the central region of the crystal. Both results establish that the reduction of D-defects throughout the entire volume of the wafer is a consequence of injected Si self-interstitials during the $POCl_3$ process. Since reduction of D-defects occurs throughout the entire volume, two statements can be made. First, due to this very pronounced effect of Si self-interstitial injection and Li^+ drifting and because Si self-interstitials most likely recombine with vacancies, it is concluded that D-defects are vacancy-related. Second, the injection of Si self-interstitials occurs on both wafer faces and reduces the D-defect concentration throughout the entire volume such that complete Li^+ drifting occurs. Hence, Si self-interstitial diffusion is occurring at least half way through the wafer from each wafer face. This result strongly suggests that Si self-interstitial diffuse to a depth of at least 1 cm into the bulk of the Si wafer.

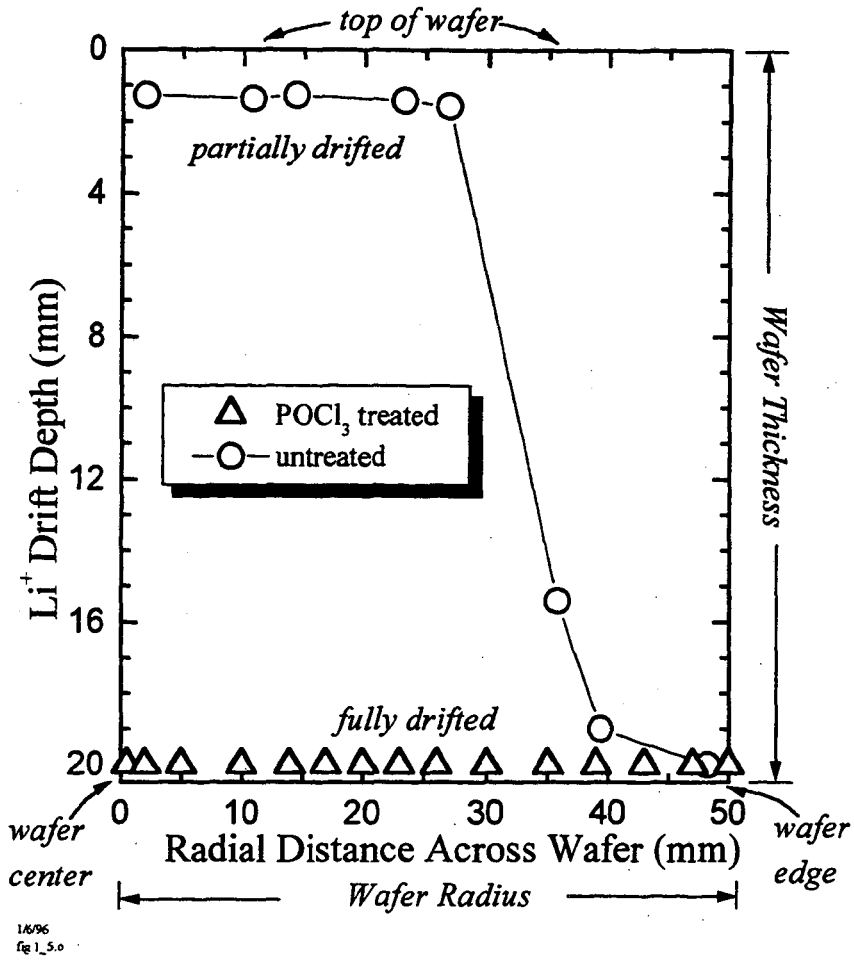

Figure 2.15: Li^+ drift profile of the 2 cm thick control wafer (-o-) and the $POCl_3$ treated wafer (Δ). The profile is shown from the center to the edge of the wafer. The central region of the control sample is only partially drifted which indicates the existence of D-defects. The $POCl_3$ treated wafer is completely Li^+ drifted indicating that Si self-interstitial injection eliminates D-defects throughout the 2 cm thick wafer. This result indicates that Si self-interstitials diffused at least 1 cm.

Reproducibility

In order to confirm this experiment, it was repeated with a slight modification. Another 2 cm thick wafer was $POCl_3$ treated. Rather than slicing the wafer vertical slabs, as shown in figure 2.14, the 2 cm thick wafer was sliced parallel to the wafer faces into five 4 mm thick wafers. This configuration also provides a way to further establish the possibility that Li^+ drifting-assisted Si self-interstitial transport occurs as will become clear later.

The five 4 mm wafers were lapped and etched to remove damage, reducing their thickness to approximately 3.5 mm. The five 3.5 mm thick wafers were processed and Li^+ drifted as illustrated in figure 2.16. Following Li^+ drifting, the drift profiles were obtained by Cu staining the cross-sectioned wafers in the usual way.

All the Li^+ drift results of the five 3.5 mm thick wafers were identical. Cu staining of the cross-sectioned wafers showed that Li^+ drifting proceeded completely through each wafer volume. These results are compared to the results of the control wafer and shown in figure 2.17. The dashed lines in figure 2.17 denote where the cuts were made from the 2 cm thick $POCl_3$ processed wafer forming the 3.5 mm thick wafers.

The semiconductor process simulation program, SUPREM-IV, was used to model the experimental results. Using SUPREM-IV to simulate Si self-interstitial injection and varying only one of the point defect parameters, the experimentally determined diffusion distance of the Si self-interstitials was simulated. Modeling of this Si self-interstitial injection depth with the help of SUPREM-IV requires a diffusivity of Si self-interstitials of at least 3.5×10^{-6} cm^2s^{-1} at 950°C. The results of the simulation are listed in the last column of table 2.5. The other columns are presented for comparison. The dashed lines in

EXPERIMENT

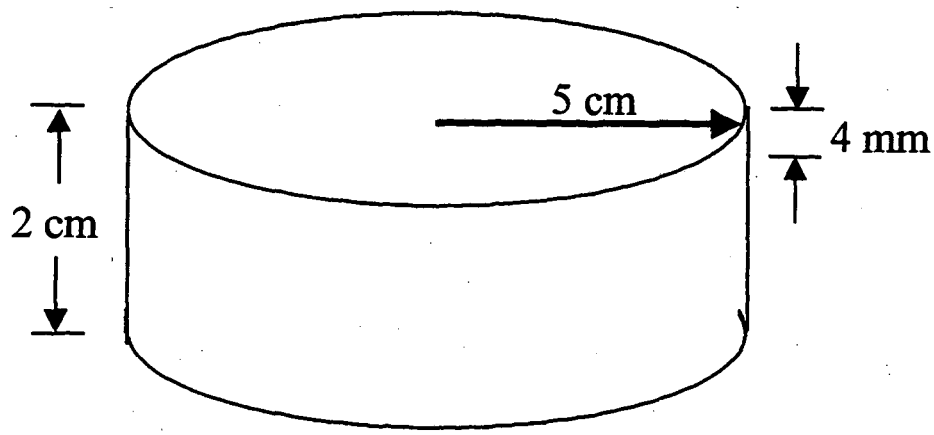

Processed Wafer

1. $POCl_3$ process: 950°C, 100 min
2. cut into 5-4 mm wafers
2. Li^+ drift @ ~100°C
3. obtain Li^+ drift profile

Figure 2.16: Five 4 mm thick wafers were cut from a wafer as depicted by the dashed lines. The wafer processing involved is outlined. Lapping and polish etching actually reduces the width of the five wafers to 3.5 mm.

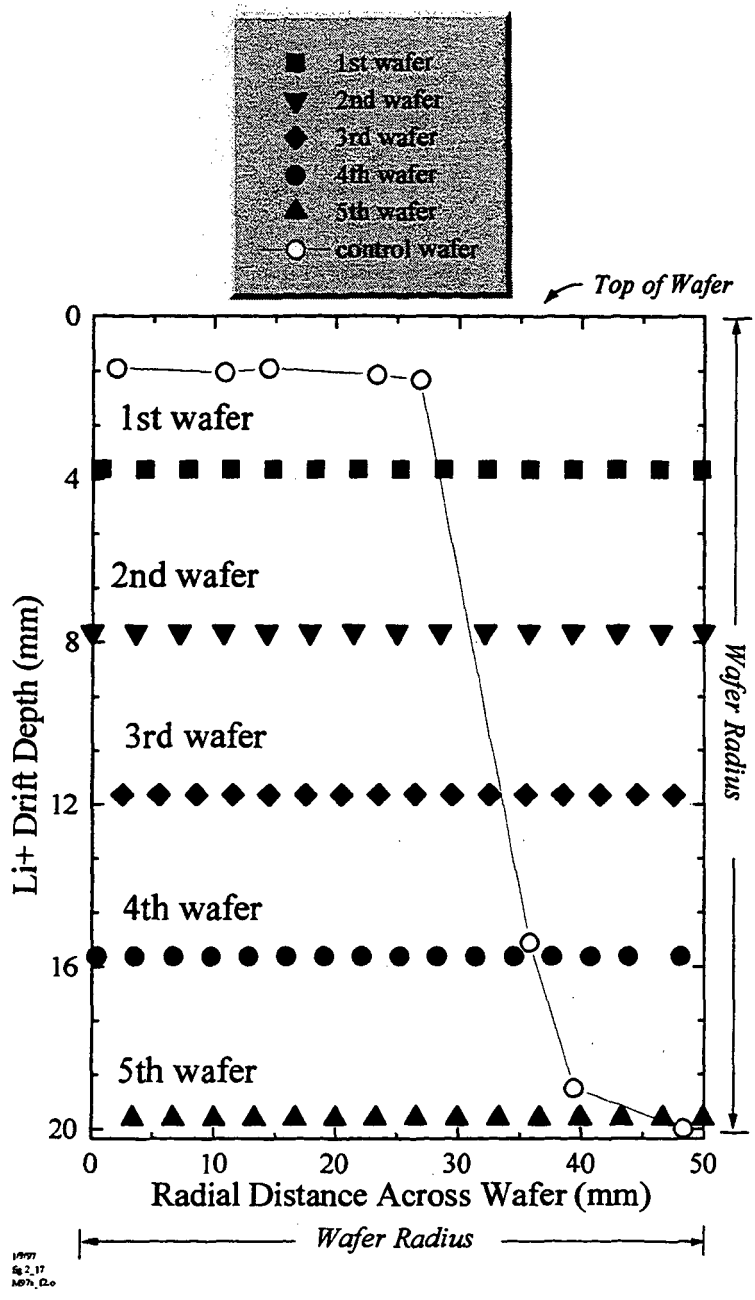

Figure 2.17: Li^+ drift profile, from the center to the periphery of each of the five 3.5 mm thick cross sectioned wafers cut from a 2 cm thick $POCl_3$ treated wafer. The horizontal dashed lines depict where the five 3.5 mm wafers were cut from the 2 cm wafer. Li^+ drifting occurred completely through all five wafers. The control wafer (-o-) is also plotted for comparison.

Table 2.5: Last column are parameters used in Figure 2.10

Point Defect Parameter	SUPREM-IV Default Values (1982)	Park & Law[1] (1992)	Gösele *et al.*[2] (1996)	Describes 1 cm Si self-interstitial diffusion
D_o^I (cm^2/s)	3.65x10^{-4}	6x10^2	3x10^{-4}	~150x10^{-4}
E_D^I (eV)	1.58	2.44	0.88	0.88
C_o^I (cm^{-3})	1.25x10^{29}	5.0x10^{22}	1.87x10^{26}	1.87x10^{26}
E_C^I (eV)	3.26	2.36	3.96	3.96
K_o^I (cm^3/s)	10^{-21}	8.16x10^{-1}	8.16x10^{-1}	8.16x10^{-1}
E_K^I (eV)	-1	3.19	3.19	3.19
D^I(cm^2/s)	1.13x10^{-10}	5.3x10^{-8}	~7.1x10^{-8}	3.5x10^{-6}

[1][Park and Law, 1992, 78]; [2][Gösele, et al., 1996, 39]

figure 2.18 show calculated concentration profiles of Si self-interstitials and vacancies based on this D_I value. The solid lines represent corresponding concentration profiles that were obtained using the default point defect parameters for D_I provided by SUPREM-IV. They show an injection depth of only 50 μm.

Figure 2.19 shows the D_I data of this work (square) in comparison to the temperature dependence of D_I deduced from transition metal diffusion and substitutional shallow dopant experiments in Si. Data mainly from shallow dopant diffusion experiments for 950°C shown by the dashed lines in figure 2.19, which is lower than the

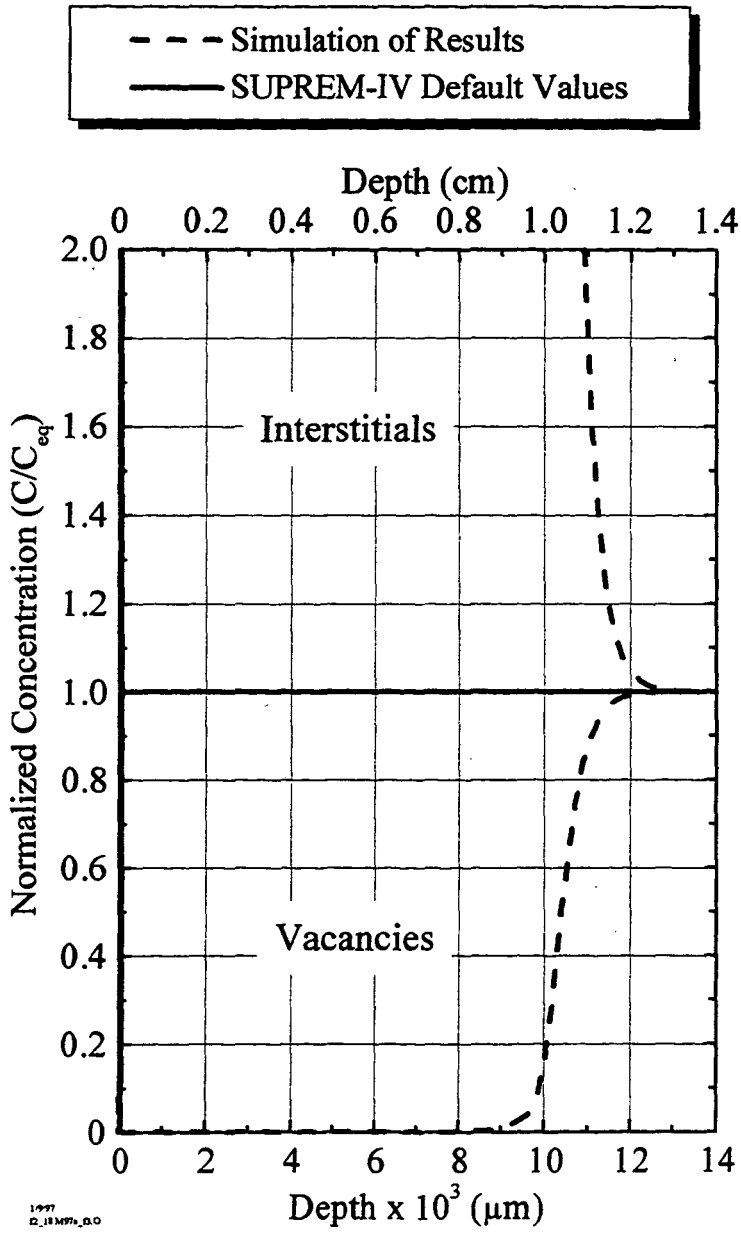

Figure 2.18: The dashed curves show the simulation of the results of this work using SUPREM IV and illustrates Si self-interstitial injection from the surface by the $POCl_3$ process which annihilate vacancies to a depth of at least 1 cm into the bulk. Note that the simulation of the oxidation process using the default point defect parameters essentially coincides with the y-axis. The Si self-interstitial injection depth is ~50 μm.

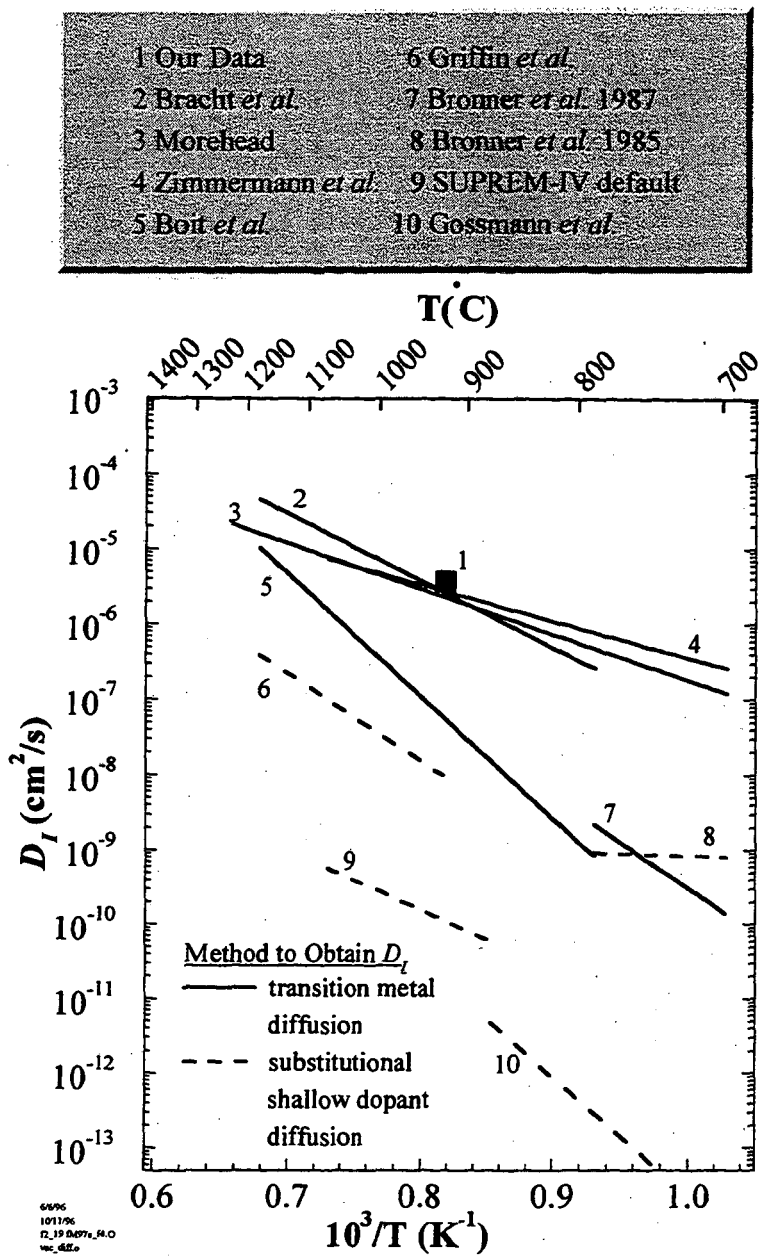

Figure 2.19: Temperature dependence of Si self-interstitial diffusivity deduced from transition metal diffusion experiments (solid) and shallow impurity diffusion (dashed) reported by various authors as indicated.[Boit, et al., 1990, 15; Bracht, et al., 1995, 20; Bronner and Plummer, 1985, 21; Bronner and Plummer, 1987, 22; Gossmann, et al., 1993, 44; Griffin, et al., 1985, 46; Morehead, 1987, 71; SUPREM-IV, 103; Zimmermann and Ryssel, 1992a, 117] The D_I data point represented by square shows this work's lower bound, which results from the analysis of the Li+, drift experiments. The diffusivity data below this data point are inconsistent with this work. However, the D_I of this work is in agreement with the D_I data of Morehead, Zimmerman *et al.* and Bracht *et al.* at 950°C.

D_I data of this work, are inconsistent with the results deduced from Li^+ drift experiments. However, the D_I value of this work determined at 950°C is in agreement with the corresponding data of Bracht *et al.*,[Bracht, et al., 1995, 20] Zimmermann *et al.*,[Zimmermann and Ryssel, 1992a, 117] and Morehead *et al.*[Morehead, 1987, 71] Furthermore, the analysis of transition metal diffusion of Zn in Si distinctly shows that D_I values lower by a factor of 5 or more conflict with the Zn-diffusion results.[Bracht, et al., 1995, 20]

The data in figure 2.17 indicate that the injected Si self-interstitials reduced the D-defect concentration such that Li^+ drifting was no longer hindered. Moreover, the D-defect concentration was reduced throughout the entire volume of the wafer. Several mechanisms may explain these results. For instance, thermal processing involved during the $POCl_3$ treatment may reduce the D-defect concentration. However, Walton *et al.* experimentally [Walton, et al., 1993, 109] dismissed thermal dissolution of D-defects. Another mechanism that may be responsible is thermally assisted Si self-interstitial transport during Li^+ drifting. However, this mechanism is improbable due to the low Li^+ drift process temperature (~100°C). One mechanism that may be culpable and that has been only preliminarily examined (see section 2.4.2) is Li^+ drifting assisted Si self-interstitial transport.

Li^+ drifting-assisted transport of Si self-interstitials – revisited

In section 2.4.2, it was determined that Li^+ drifting assisted transport does not occur assuming that Si self-interstitials are injected to 100 μm depth or less during the $POCl_3$ process. However, if Si self-interstitials are injected further (e.g., millimeters),

then that particular experiment does not yield information on Li^+ drifting and thus is inconclusive. In addition to ascertaining the Si self-interstitial diffusion distance, the experiment discussed in this section also provides a means to examine Li^+ drifting assisted Si self-interstitial transport.

The results presented in figure 2.17 unambiguously demonstrate that the Li^+ drifting process does not assist Si self-interstitial transport into the bulk. The $POCl_3$ process, as modeled by SUPREM-IV using the default point defect parameters, simulates the diffusion distance of the Si self-interstitials to be approximately 50 μm (shown in figure 2.10). If this is true, then only the first and fifth 3.5 mm wafers (i.e., the ends of the original 2 cm thick wafer) contain the injected Si self-interstitials, and consequently, would be the only wafers to fully Li^+ drift. This can also be argued for interstitial injection up to 8 mm (i.e., when considering the second and fourth 3.5 mm wafers). However, all five wafers Li^+ drifted completely! Therefore, Si self-interstitial transport must have occurred in all the 3.5 mm wafers <u>prior</u> to Li^+ drifting, and therefore throughout the 2 cm thick parent wafer during the $POCl_3$ process. These results rigorously eliminate the possibility that Li^+ drifting assists the transport of Si self-interstitials.

2.4.4 Experiment 4: A time reduction in the $POCl_3$ process of 2 cm thick wafers

At this juncture in the study, the parameter space of the previous experiments had to be further refined in order to provide additional information on Si self-interstitial diffusion. Increasing the wafer thickness is the most apparent parameter to alter.

However, limitations in the availability of the material make this approach difficult. A decrease in temperature or a decrease in time may provide the same information. These latter two variations provide the most viable means to obtain the Si self-interstitial diffusion distance.

Simulations were performed using SUPREM-IV to determine by how much a decrease in drive-in time or temperature during the P-diffusion post anneal (during the $POCl_3$ process) would reduce the diffusion distance. The point defect parameters used were those derived from the experiment discussed in section 2.4.3. They are listed in table 2.5. The simulations performed included a reduction in temperature to 850°C, from the original 950°C, for the same length of diffusion time (i.e., 100 min). A simulation was also performed in which the diffusion time was decreased from 100 minutes to 10 minutes at 950°C. The results of these simulations are compared to the simulation of the original $POCl_3$ process (i.e., 950°C for 100 min diffusion time) in figure 2.20.

A decrease in either the diffusion temperature or diffusion time leads to a decrease in the Si self-interstitial diffusion depth relative to the initial parameter values. The greatest decrease of the Si self-interstitial diffusion distance was due to the reduction of the diffusion time from 100 minutes to 10 minutes as shown in figure 2.20. Based on these simulations, the decision was made to decrease the diffusion drive-in time rather than the temperature in order to establish the Si self-interstitial diffusion distance. A diffusion time of 15 minutes was chosen while continuing to keep the temperature constant. Furthermore, it was advantageous to keep the temperature constant because of the constraints of the $POCl_3$ process.

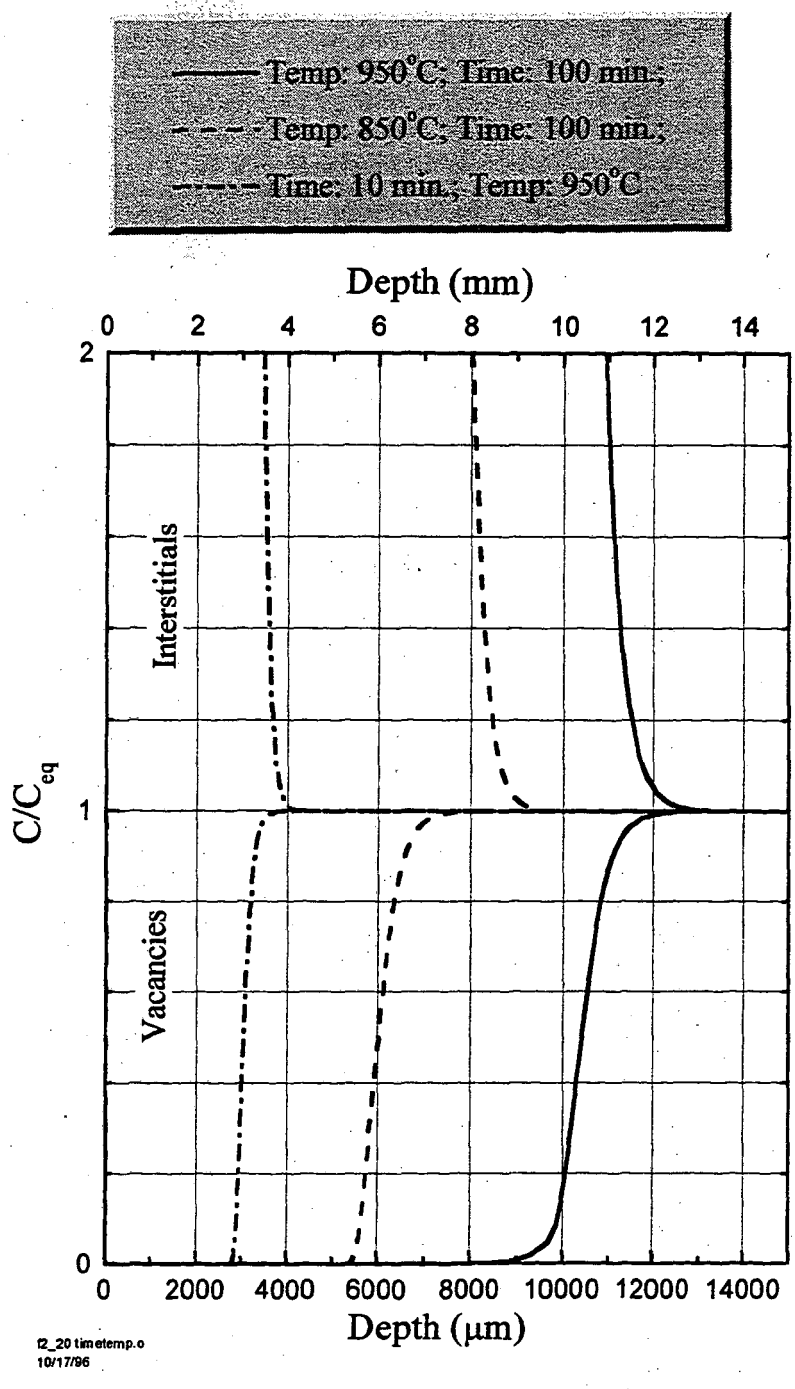

Figure 2.20: Three simulations of Si self-interstitial injection are shown for a decrease in temperature and a decrease in diffusion time, respectively. The point defect parameters used in the simulation were derived from the experiment in section 2.4.3 and are listed in the last column of table 2.5.

One potential problem for this approach pertains to the length of time necessary for a 2 cm thick 10 cm in diameter Si wafer to reach thermal equilibrium when placed into a furnace at 950°C. To insure that the Si wafer can attain thermal equilibrium in a time that is considered short relative to the anneal time, heat transfer calculations were performed.

A brief digression is necessary here to discuss the manner in which the heat transfer calculations were performed and the results they provided. The heat transferred during the initial annealing stage is position dependent and time dependent. For the size and cylindrical geometry of the wafer, it can be assumed that heat is transferred both axially and radially. Hence, the position dependence is assumed to be two-dimensional. The heat transfer equation, which describes the change of temperature in a system with respect to time, is related to the second derivative of the temperature with respect to position in that system. Since the geometry of the wafer (i.e., the system) may be considered cylindrical, then the heat transfer equation is expressed in cylindrical coordinates:

$$\frac{1}{r}\frac{\partial}{\partial r}\left(r\frac{\partial T}{\partial r}\right)+\frac{\partial^2 T}{\partial x^2}=\frac{1}{D_T}\frac{\partial T}{\partial t} \tag{2.67}$$

where x is parallel to the growth direction of the wafer, T is the temperature, t is the time and a D_T is the thermal diffusivity. In this form, it is assumed that the D_T does not change with time or position, and therefore temperature. By examining data of D_T [Incropera and DeWitt, 1990, 56] plotted as a function of temperature in figure 2.21, one can see this is not entirely true. However, D_T only changes significantly at low temperatures and saturates at medium to high temperatures as shown by the exponential fit in figure 2.21. To solve equation 2.67 in a closed form, the lower temperature regime is assumed to be

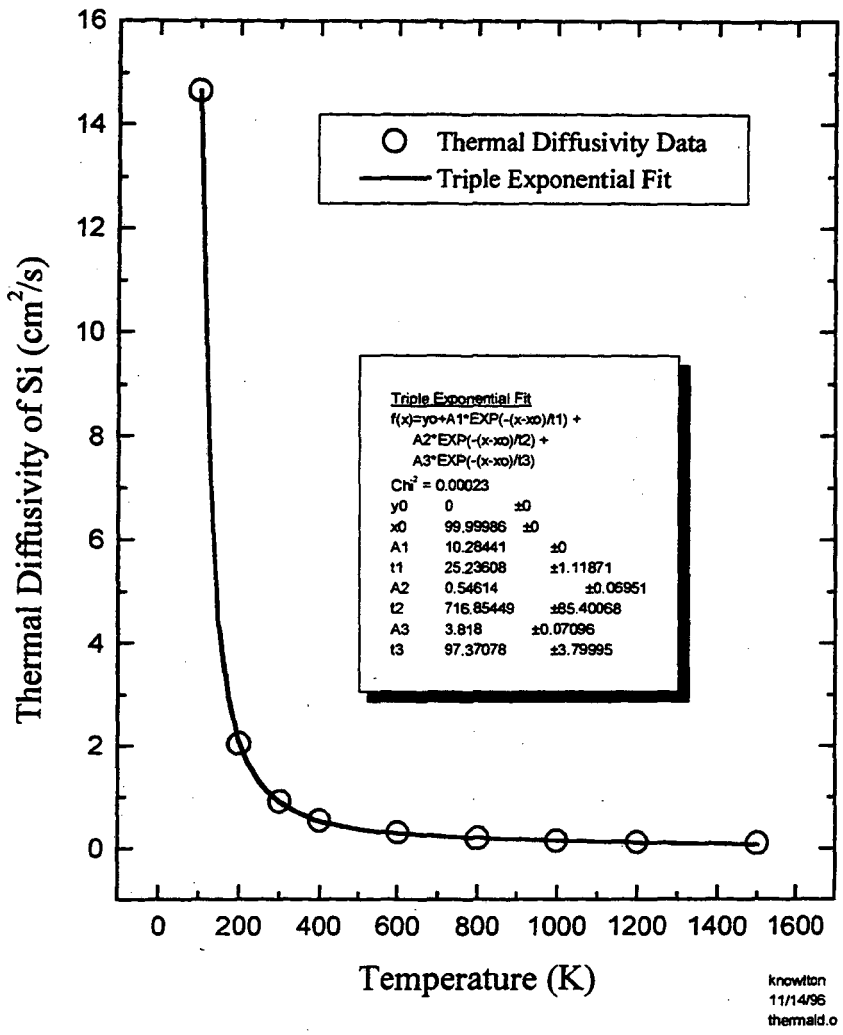

Figure 2.21: D_T versus temperature shown by the data points. The line is a triple exponential decay fit depicting the rapid manner in which the D_T saturates.

transiently insignificant. If the solution shows that the Si wafer does not quickly reach thermal equilibrium, then D_T may not be considered position independent. Given this assumption, the solution may be determined by the method of separation of variables. The solution, which is two-dimensional (neglecting time), may be expressed as a product of two one-dimensional solutions. In this case, they are a radial solution with respect to time and an axial solution with respect to time. This is shown in the following equation:

$$\frac{T(r,x,t)-T_\infty}{T_i-T_\infty}=\left.\frac{T(x,t)-T_\infty}{T_i-T_\infty}\right|_{\substack{\text{plane}\\ \text{wall}}}\cdot\left.\frac{T(r,t)-T_\infty}{T_i-T_\infty}\right|_{\substack{\text{infinite}\\ \text{cylinder}}} \tag{2.68}$$

where $T(x,t)$ and $T(r,t)$ are graphically solved for their respective geometry (see for instance [Incropera and DeWitt, 1990, 56]).

The temperature was calculated at the center of the 2 cm thick and 10 cm diameter Si cylinder for various times. By the end of the first minute, the calculated temperature in the center of the wafer is about 577°C. Further computation shows that the temperature reaches 947°C after 5 minutes. The calculations show that the temperature asymptotically approaches 950°C within several minutes. Although the method used to solve the heat transfer equation does not seem to provide the perfect solution, it does seem to furnish a suitable approximation to the problem. With this approximation, the calculations indicate that the 2 cm thick and 10 cm diameter Si wafer reaches thermal equilibrium within several minutes. Hence, performing the $POCl_3$ process at a diffusion time of 15 minutes should not lead to anomalous results.

Preparation of the 2 cm thick and 10 cm in diameter Si wafer was accomplished as described in section 2.4.3. The $POCl_3$ process was performed at 950°C with a P-diffusion drive-in time of 15 minutes. The Si cylinder was removed from the furnace

after this time. The effect of the cooling rate on the D_I was examined and found to be negligible. The 2 cm thick Si wafer was sectioned in 5 - 3.5 mm thick wafers as described in section 2.4.3 and further processed for Li^+ drifting. Each wafer was then Li^+ drifted. Following Li^+ drifting, the 5 - 3.5 mm thick Si wafers were cut in cross-section and copper stained to determine the Li^+ drift profile, which in turn, would reveal the Si self-interstitial – microdefect interaction. From this data, a Si self-interstitial diffusion distance was derived.

Copper staining of the 5 – 3.5 mm thick cross-sectioned wafers showed that Li^+ had drifted completely through the central region of all 5 wafers. Therefore, Si self-interstitials had diffused throughout the bulk and reduced the microdefect concentration in each of the 5 wafers. Hence, during the $POCl_3$ process, Si self-interstitials had diffused throughout the bulk of the 2 cm thick 10 cm in diameter Si wafer. Since Si self-interstitials were injected from both wafer faces, then the maximum distance that the Si self-interstitials diffused was 1 cm during the 15 minute diffusion time.

Although SUPREM-IV simulations of this Si self-interstitial diffusion distance at 950°C for 15 minutes have not yet been performed, the D_I can be estimated using an equation taken from the Gaussian solution of the diffusion equation. The equation is given by:

$$x = 2\sqrt{D_I t} \tag{2.69}$$

where x and t are the distance and time of Si self-interstitial diffusion, respectively. This equation is based on the assumption that, at a certain distance x, the concentration equals half the surface concentration. Solving for the D_I, the equation has the form:

$$D_I = \frac{x^2}{4t} \tag{2.70}$$

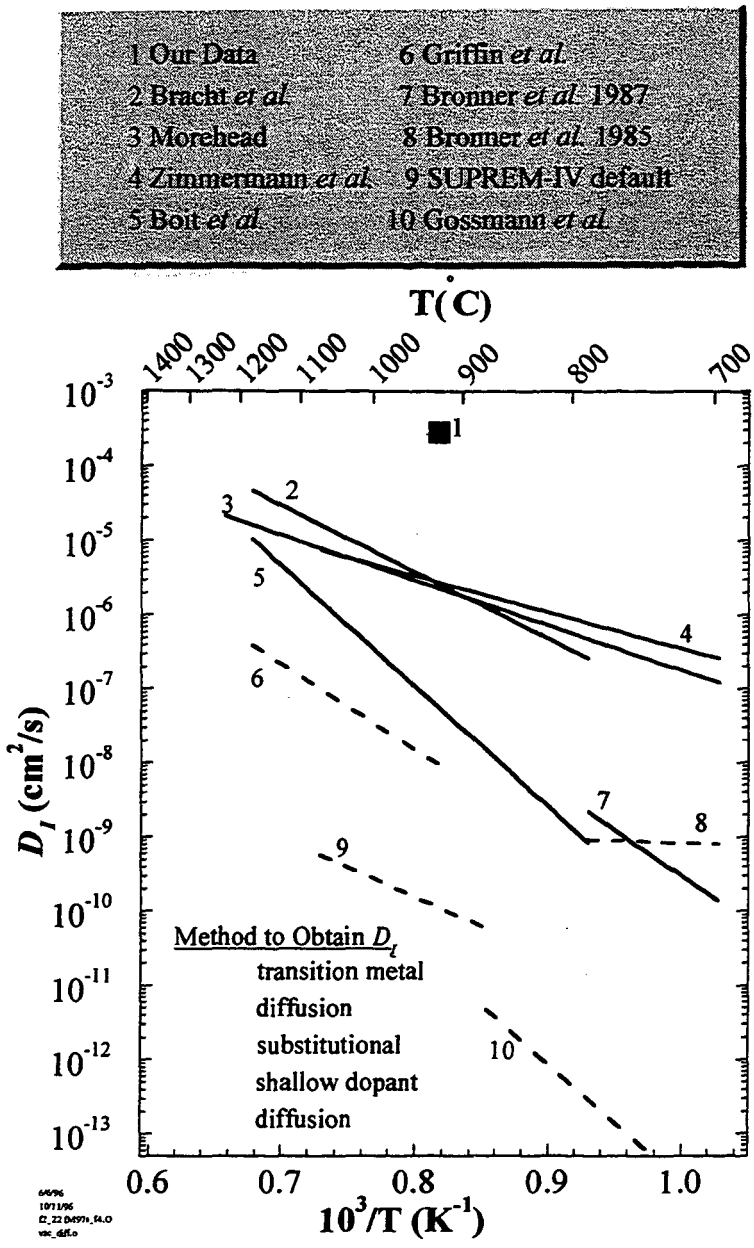

Figure 2.22: The D_I, calculated by equation 2.3, is compared to D_I determine by transition metal (solid lines) and substitutional shallow dopant diffusion studies (dashed lines) as reported by various authors as indicated.[Boit, et al., 1990, 15; Bracht, et al., 1995, 20; Bronner and Plummer, 1985, 21; Bronner and Plummer, 1987, 22; Gossmann, et al., 1993, 44; Griffin, et al., 1985, 46; Morehead, 1987, 71; SUPREM-IV, 103; Zimmermann and Ryssel, 1992a, 117] From the comparison, the calculated D_I from the experimental results is significantly above the other diffusivities.

Given the diffusion condition of x and t equaling 1 cm and 100 seconds, respectively, the calculated D_I is approximately 2.8×10^{-4} cm^2/s. This diffusivity is on the order of the diffusivity of an atom in a liquid. Clearly, some aspect of the experiment or the interpretation of the results appears to be in error. This is evident when comparing the calculated D_I to the D_I data obtained by transition metal diffusion and substitutional shallow dopant diffusion experiments as shown in figure 2.22. The calculated D_I is well above the other D_I data. Since it has already been shown that Li^+ drifting does not interact with Si self-interstitial diffusion, then the next assumption to consider is a possible thermal effect. Walton *et al.* [Walton, et al., 1994, 110] published results that indicated that thermal effects did not reduce the number of D-defects. These results will be further examined in the following sections.

2.4.5 Nitridation

Performed in parallel to the experiments described in the foregoing sections, an experiment was performed that would further establish the identity of the D-defects located in the central region of the defective Si wafers. The reduction of the D-defects by Si self-interstitial injection into the bulk using the $POCl_3$ process strongly suggested that the D-defects were vacancy-related defects. This implication can be further substantiated if the D-defect concentration could be increased by the introduction of vacancies thereby more severely abating Li^+ drifting. This section describes an experiment performed in order to further establish that the microdefects in the central region of the defective Si wafers are vacancy-related. But more importantly, this section discusses the results that

led the author to further question Si self-interstitial diffusion as the mechanism believed to eliminate D-defects and reduce their overall concentration.

The process of thermal nitridation has been shown to inject vacancies into the bulk single crystal Si. It is believed that the formation of Si_3N_4 creates compressional stress in the Si at the Si_3N_4/Si interface that is relieved by the formation of excess vacancies and thus leads to vacancy injection into the Si bulk. [Ahn, et al., 1988, 7; Baumvol, et al., 1995, 13; Fahey, et al., 1983, 31; Hayafuji, et al., 1982, 49; Kang and Schroder, 1989, 61; Mizuo, et al., 1983, 70] Nitridation by chemical vapor deposition (CVD) has also been shown to induce the same effect.[Osada, et al., 1995, 74] In order to both reduce the processing temperature and the possible introduction of unwanted impurities into the defective Si wafers, CVD nitridation was chosen over thermal nitridation.

The process of Si nitridation is performed using primarily the following reaction:

$$4NH_3 + 3SiH_4 \rightarrow Si_3N_4 + 6H_2 \qquad (2.71).$$

The Si-Si bond is longer than the Si-N bond. Hence, the lattice constant of the Si_3N_4 film is less than that of Si. This difference causes a tensional stress in the Si_3N_4 film and a compressional stress in the near surface region of the Si adjacent to the Si/Si_3N_4 interface. To relieve the compression in the Si, Si atoms from the Si lattice near the interface jump to the Si_3N_4 film leaving excess vacancies in the Si lattice.[Osada, et al., 1995, 74] The vacancies diffuse into the bulk. This mechanism is supported by studies performed by Hayafuji *et al.* [Hayafuji, et al., 1982, 49] that show extrinsically dislocated Si that has undergone nitridation becomes extrinsic dislocation free due to dislocation annihilation by the injected vacancies. Moreover, the diffusion of phosphorus, boron, gallium, carbon,

and oxygen into Si is inhibited by nitridation, while the diffusion of antimony is enhanced by nitridation. Because the former impurities diffuse via the interstitialcy diffusion mechanism shown by equation 2.28, their diffusion is inhibited by excess vacancies. Conversely, antimony is assisted by vacancies during diffusion. The vacancy diffusion mechanism is described by equation 2.29.

CVD nitridation experiments were performed on dummy Si wafers to establish that vacancies were indeed injected during the nitridation process. The procedures employed were those established by researchers at Keio University.[Osada, et al., 1995, 74] Using shallow substitutional dopant diffusion, they show that vacancies are the predominant point defects introduced into bulk Si during nitridation. Boron diffuses via the *kick-out* mechanism with the predominant intrinsic point defect being the Si self-interstitial. Hence, if the predominant point defects present are vacancies, then B diffusion will be retarded. Contrarily, if the concentration of Si self-interstitials is beyond the C_I^{eq}, then the B diffusivity will be enhanced. The Keio University researchers implanted B into three Si wafers. One wafer underwent CVD nitridation and a subsequent six hour anneal. Another wafer did not undergo the nitridation and was only thermally annealed for six hours. The remaining wafer did not undergo any further processing following implantation. Secondary ion mass spectroscopy (SIMS) was performed on all three wafers and compared. The results showed that CVD nitridation retarded the diffusion of B strongly suggesting that the equilibrium vacancy concentration had been exceeded and showing the same effect as thermal nitridation.

The following experiment was designed to verify the results of Keio group, since similar studies have not been reported. If the experiment shows that CVD nitridation

injects vacancies into the Si bulk, the concentration of D-defects will be enhanced which should further obstruct Li^+ drifting.

Three *p*-type Si wafers approximately 500 μm thick were implanted with B^- at a dose and energy of $7.5x10^{13}$ cm^2 and 70 keV, respectively. CVD nitridation was performed on one wafer in a silane and NH_3 ambient at 750°C for 50 minutes resulting in an 1150 Å thick Si_3N_4 film. The wafer was annealed at 1015°C for 6 hours to activate and accelerate B diffusion. CVD nitridation was not performed on the next Si wafer, but it was also annealed at 1015°C for 6 hours. No other processing was performed on the remaining B^- implanted wafer. Following the removal of the Si_3N_4 films, secondary ion mass spectroscopy (SIMS) was performed on each wafer in several different areas to confirm reproducibility of the results.

The B concentration depth profiles of the three Si wafers as measured by SIMS are shown in figure 2.23. As expected, the-as implanted Si wafer showed the shallowest B depth profile. A B concentration of 10^{15} cm^{-3} existed at a depth of about 1.1 μm. The profile is what is expected for the given energy and dose of the B^- implantation performed in the experiment. The SIMS results of the annealed-only wafer showed the deepest B depth profile at about 1.7 μm for a B concentration of 10^{15} cm^{-3}. The SIMS results on the wafer which underwent the CVD nitridation followed by 6 hour thermal annealing revealed a B depth profile of about 1.2 μm for a B concentration of 10^{15} cm^{-3}. The nitridized and annealed wafer showed a pronounced retardation of B diffusion relative to the wafer that was annealed only. This result strongly indicates that vacancies were injected into the bulk Si during the nitridation. Another possibility is that the initial Si self-interstitial concentration was reduced during nitridation and retarded B diffusion.

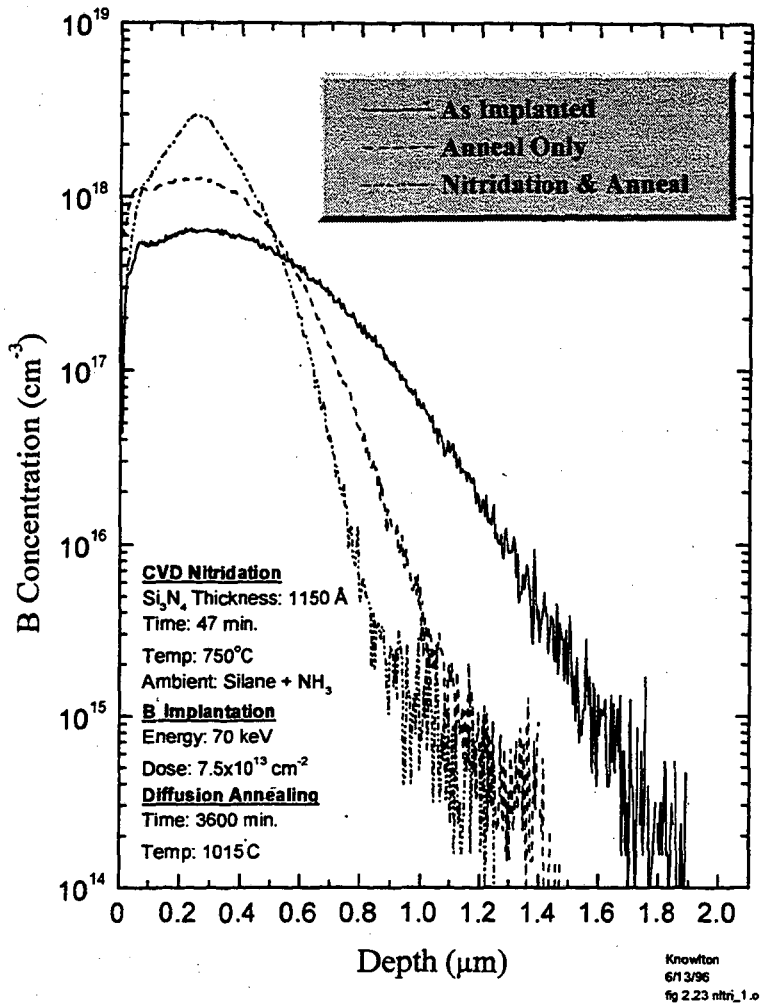

Figure 2.23: As implanted, anneal only, and CVD nitridation with anneal. The CVD nitridation impedes the diffusion of boron relative to the annealed only sample.

In either case, nitridation should enhance the effect of D-defects on Li^+ drifting. In the latter case, the Si self-interstitial – vacancy interaction would decrease thereby increasing the lifetime of the D-defects.

Nitridation was next performed on a D-defect containing Si wafer. Following the nitridation and annealing, the wafer was processed for Li^+ drifting in the usual manner. After Li^+ drifting, the wafer was cross-sectioned and copper stained to determine the Li^+ drift profile. It is expected that Li^+ drifting should be further impeded due to the nitridation further establishing that D-defects are vacancy-related.

The copper staining of the cross-sectioned wafer showed that the wafer completely Li^+ drifted in the central region. Not only did the nitridation fail to further suppress the Li^+ drifting, but it reduced the D-defect concentration such that it enhanced Li^+ drifting. This result contradicts the interpretation of results of the Si self-interstitial injection experiments, which raises further questions about the mechanism responsible for the reduction of D-defects. Comparing the $POCl_3$ process to the nitridation process reveals that the relatively high process temperatures are similar in the two experiments. The $POCl_3$ process is performed at 950°C while the CVD nitridation is performed at 1015°C. Albeit the high temperature process times are considerably different, the temperatures are nearly equivalent.

Previous Li^+ drifting experiments on wafers containing D-defects indicated that thermal dissociation of the D-defects in these wafers did not occur at 950°C.[Walton, et al., 1994, 110] A review of the experiment performed by Walton *et al.* [Walton, et al., 1994, 110] showed that their data came only from one annealing experiment on only one wafer. The wafer used in that annealing experiment was from a completely different

boule of Si than the boules listed in table 1.1. Therefore, thermal dissociation of D-defects is an obvious and consistent explanation for the results furnished in the last two sections.

2.4.6 Experiment 5: Thermal annealing of 3 mm thick Si crystals

Thermal processing during the $POCl_3$ process or the nitridation process may be responsible for the reduction of the D-defect concentration in Si wafers used in this study. In this section, thermal annealing experiments performed on Si used in the experiments for this thesis are described and discussed.

The annealing experiments were carried out with the Si samples sealed under vacuum in quartz ampoules. The use of quartz ampoules eliminates the concern of contamination from the furnace which was also used for $POCl_3$ processing.

Two 14 mm^2 by 3 mm thick samples were cut from the central region of a wafer containing D-defects. The samples were polish-etched and cleaned in the usual manner. After sealing the samples in an evacuated ampoule, the ampoule was placed in the furnace maintained at 950°C. The samples were annealed for 15 minutes and removed from the furnace. Following Li^+ drifting, samples were cross-sectioned and copper stained.

The copper staining revealed that the two samples had completely Li^+ drifted. This result demonstrated that the D-defects were reduced in concentration by thermal effects.

A similar experiment was performed on 3 mm thick Si wafers containing D-defects which were cut from a different boule. Rather than cut them into 14 mm^2

samples, they were sectioned into quarters. The quartered samples were processed and cleaned. Two of the quartered samples were used as control samples and Li^+ drifted without being annealed. The remaining two quarter sections were annealed at 950°C for 15 minute in an Ar ambient. Following removal from the furnace, they were Li^+ drifted. After Li^+ drifting, the four samples were cross-sectioned and stained with a $CuSO_4$ solution.

The results of the copper staining showed that the control samples did not completely drift in the central region of the wafer confirming the presence of D-defects. On the thermally processed sections, the copper staining revealed that Li^+ drifting had occurred through the entire thickness of both quartered sections. These results, as well as the results described above, further support the nitridation and $POCl_3$ findings that thermal dissolution of D-defects may occur.

2.4.7 Re-evaluation of the thermal dissolution of D-defects

The results of several experiments force the reevaluation of the possible mechanisms that reduce the D-defect concentration below the resolution of Li^+ drifting. Furthermore, the reassessment of the D-defect identity is also necessary. The experiments that have revealed a possible flaw in the identification and apparent reduction of the D-defects include experiment 4 (section 2.4.4), experiment 5 (section 2.4.6), and the nitridation study (section 2.4.5).

The processing characteristics shared by these experiments are the high process temperature, the pre-annealing procedures (cutting, lapping, Li deposition and diffusion), and Li^+ drifting. Li^+ drifting following the $POCl_3$ process has been shown not to aid in the

D-defect annihilation. Although the results pertaining to Li^+ drifting assisting Si self-interstitial transport, the experimental results clearly established that the mechanism responsible for the annihilation of the D-defects occurred prior to Li^+ drifting.

The pre-annealing process may introduce undesirable impurities, which may affect the D-defect dissolution kinetics. But the pre-annealing procedures are the same for the control wafers as well as for the processed wafers. Furthermore, the $POCl_3$ process is used by the semiconductor industry to getter many impurities. Based on these observations, it is doubtful that the pre-annealing procedures are responsible for the dissociation of D-defects.

Si self-interstitial injection cannot be ruled out since it occurs to a certain extent during annealing. However, it is highly improbable that Si self-interstitials are injected at least 1.5 mm into the bulk. This would need to occur to support the results of experiment 5.

The above discussion leads to thermal annealing as the most probable candidate for the dissolution of D-defects. Hence, a thorough review of the literature concerning the annealing behavior of D-defects is in order.

Several groups reported that the dissolution of D-defects occurs as a result of annealing in a dry oxygen environment. For instance, Fusegawa *et al.* [Fusegawa, et al., 1995, 37] demonstrated that following dry oxidation at 1200°C for 2hr, GOI tests showed a reduction in the D-defect concentration in CZ Si and a complete elimination in undoped FZ Si.

Also, Furukawa *et al.* [Furukawa, et al., 1995, 36] have shown that D-defects in CZ Si are eliminated 6 μm into the bulk after annealing for 4 hr at 1280°C in an oxygen

ambient. As mentioned in section 1.1.2, several groups have seen a reduction of D-defects when annealing in a dry oxygen environment. However, oxidation occurs which injects Si self-interstitials creating a situation where it is difficult to separate the Si self-interstitial injection effect from the thermal annealing effect.

Several groups studied the annealing behavior of the D-defect region in ambients other than oxygen. For instance, Fusegawa *et al.* [Fusegawa, et al., 1995, 37] have demonstrated that, at 1150°C in hydrogen, the D-defects are entirely removed from the CZ Si. It is not clear that annealing in a hydrogen ambient was performed on FZ Si.

Furthermore, studies by Furukawa *et al.* [Furukawa, et al., 1995, 36] have shown that after annealing at 1180°C for 2 hr in hydrogen ambient, the D-defects in CZ Si are annihilated up to 6 μm deep into the wafer. Similarly, Abe *et al.* [Abe and Kabayashi, 1998, 3] established that rapid thermal annealing in hydrogen at 1200°C for about 20 s reduces the D-defect concentration in 200 mm diameter CZ Si. The depth to which the D-defects were removed was not reported.

According to a study by Kissinger *et al.* [Kissinger, et al., 1998, 62], annealing CZ Si at or above 1100°C in hydrogen improves GOI. Kissinger *et al.* have ascertained that high temperature annealing in the hydrogen environment caused D-defects to completely fill with SiO_2. No annihilation of D-defects was observed. They suggest that this is due to O_i diffusion to the D-defects, which consume silicon from the walls of the defects, and ultimately fills the void with SiO_2. Since Si is consumed, the SiO_2 – filled void is larger than the initial D-defect.

In the studies discussed above, CZ Si was used. Since the O_i concentration in CZ Si is at least 2 orders of magnitude greater than in FZ Si, it is difficult to separate the

effects of oxygen on the dissolution of D-defects during annealing. The presence of oxygen leads to the formation of SiO_2 which injects Si self-interstitials. The formation of SiO_2 can act as internal D-defect gettering agents via Si self-interstitial – vacancy recombination. Or, as Kissinger *et al.* have demonstrated, diffusion of O_i leads to the entire permeation of the D-defects by SiO_2. Since they are of the same material, this would render the D-defects harmless to gate oxides. Whatever may be the mechanism for the malignant to benign transformation of D-defects in CZ Si, it most likely does not occur in FZ Si.

Dornberger *et al.* [Dornberger, et al., 1996, 27] have suggested that D-defects in CZ Si form in the solid Si at a depth from the solid/liquid interface where the temperature range is between1050°C to 900°C. Borionetti *et al.* [Borionetti, et al., 1996, 16] concluded that D-defect nucleation in CZ Si occurs in the temperature range of 1040°C to 1070°C based on a model by Voronkov [Voronkov, 1982, 108] of swirl defect formation in silicon. Hence, it is plausible that the results of experiments 4, 5, and the nitridation study are due to thermal dissolution of D-defects. Yet, the reports of Dornberger *et al.* [Dornberger, et al., 1996, 27] and Borionetti *et al.* [Borionetti, et al., 1996, 16] involve CZ Si. So, it is quite evident that more research on the effects of thermal processing on FZ Si are required to understand the dissolution kinetics of D-defects.

3. Conclusion

This thesis has presented a study of D-defects and self-interstitial diffusion in Si. Li^+ drifting was shown to be a unique technique for delineating D-defects and transmission electron microscopy (TEM) established the nature of the delineation. The presence of D-defects and the detection of these defects by Li^+ drifting were used to study Si self-interstitial diffusion. Several conclusions can be drawn from this work.

A possibility existed that instead of D-defects interstitial oxygen might be responsible for hindering Li^+ drifting. The O_i concentration with respect to the radial position was measured by local vibrational mode Fourier transform infrared spectroscopy. The measured O_i concentration was about $2x10^{15}$ cm^{-3} and did not vary radially across the wafer. Since the O_i concentration in the central region of the wafers is the same as in the wafer periphery, then D-defects and not oxygen are responsible for hindering Li^+ drifting.

Obstruction of Li^+ drifting has been found in wafers from certain but not all FZ *p*-type Si. Incomplete Li^+ drifting always occurs in the central region of the wafers. TEM was performed on a samples from the partially Li^+ drifted area and compared to regions without D-defects. Precipitates were found only in the region containing D-defects that had partially Li^+ drifted. This result strongly indicates D-defects are responsible for the precipitation that halts the Li^+ drift process.

Nitrogen (N) doping has been shown to eliminate D-defects as measured by conventional techniques. However, Li^+ drifting has shown that D-defects are indeed still present. Li^+ drifting appears to be able to detect D-defects at concentrations lower than conventional techniques. Therefore, Li^+ drifting is a more sensitive technique then others

to delineate D-defects. Furthermore, the $POCl_3$ process was found to reduce the D-defect concentration below the limits of Li^+ drifting.

The precipitates were characterized using selected area diffraction (SAD) and image contrast analysis. The selected area diffraction pattern (SADP) taken along the Si [-233] ZA showed extra reflections which are not produced by Si nor by Li. The extra reflections are most likely produced by a material with a lattice constant greater than that of Li. The SADP taken along the Si [111] ZA show extra reflections and may stem from stacking faults produced by the precipitate-like defects. They may also be due to lithium silicides such as $Li_{21}Si_5$ and $Li_{13}Si_4$, which produce g_{220} and g_{440}, respectively, of similar magnitudes. Contrast analysis showed that structure factor contrast dominates, which indicates that the predominant contrast type is precipitate contrast rather than matrix type contrast. This suggests that the precipitate-like defects are precipitates.

TEM was performed to determine whether a depth-density distribution of precipitates exists in the partially Li^+ drifted region of a wafer that contained D-defects. The results showed that a density distribution of precipitates is present. Precipitates were found in high concentrations in the Li^+ reservoir region. Supersaturation was ruled out as a cause for precipitation establishing D-defects as the cause.

To extract information about D-defects from the study of precipitate density distribution with respect to depth, a Li^+ drift model was formulated to simulate precipitation due to D-defects. The use of the density distribution and Li^+ drift depth in the model can obtain the size and capture cross-section of the D-defects.

Li^+ drifting and D-defects provide a useful means to study Si self-interstitial diffusion. SUPREM-IV was used to model the results of Si self-interstitial diffusion

obtained from Li^+ drifting experiments. Anomalous results from the Si self-interstitial diffusion experiments forced a re-examination of the possibility of thermal dissociation of D-defects. Thermal annealing experiments that were performed support this possibility. A review of the current literature illustrates the need for more research on the effects of thermal processing on FZ Si to understand the dissolution kinetics of D-defects.

4. Appendices

4.1 Oxidation of Silicon

The mechanism of *I* injection during thermal oxidation has been studied by several groups.[Hayafuji, et al., 1982, 49; Hu, 1974, 51; Hu, 1985, 52; Strunk, et al., 1979, 101] During oxidation, Si forms SiO_2 when two oxygen atoms replace one Si atom. The main two methods of thermal oxidation are the wet and dry methods and are described by the following reactions:

$$\text{Dry: } Si + O_2 \rightarrow SiO_2 \qquad (4.1)$$

$$\text{Wet: } Si + 2H_2O \rightarrow SiO_2 + 2H_2 \qquad (4.2).$$

The oxidation rate for wet oxidation is much larger than that for dry oxidation. A lattice relaxation occurs because the Si-O bond is longer than the Si-Si bond. Hence, the newly formed SiO_2 takes up more volume than the bulk Si it replaces. Moreover, the volume expansion causes a compressive stress in the SiO_2 film which induces a tensile stress in the Si matrix near the Si/SiO_2 interface.[Abe and Kimura, 1990, 5] On average, there are 1.25 Si atoms released for every O atom consumed by SiO_2.[Hu, 1994, 54] Hence, the excess Si atoms, which are repelled by the compressive stress field, are injected into the Si lattice and diffuse interstitially and are known as *Si self interstitials*. The formation of *extrinsic stacking faults* in oxidized Si wafers proves the existence of extra interstitial Si atoms injected into the bulk during oxidation.[Hu, 1974, 51; Strunk, et al., 1979, 101]

4.2 Local Vibrational Mode Fourier Transform Infrared (FTIR) Spectroscopy

FTIR spectroscopy is an optical absorption technique that is sensitive method by which to measure the vibrational or electronic transitions of defect states. Figure 4.1 shows a simple schematic of the absorption experiment. A defect can absorb a photon and its energy may be transferred into a vibrational or electronic excitation. In this study, FTIR spectroscopy was used to measure the intensity of the local vibrational mode spectrum of O_i. Because the oxygen atom's mass is less than the mass of the matrix Si atoms as depicted in figure 4.2, the localized oxygen atom will vibrate at higher frequencies than the Si atoms upon absorption of photons in that frequency range. Because the oxygen vibrational modes occur at higher frequencies than the Si lattice vibrational modes, they are easily detectable. The area under the oxygen LVM line gives an accurate measure of the O_i concentration.

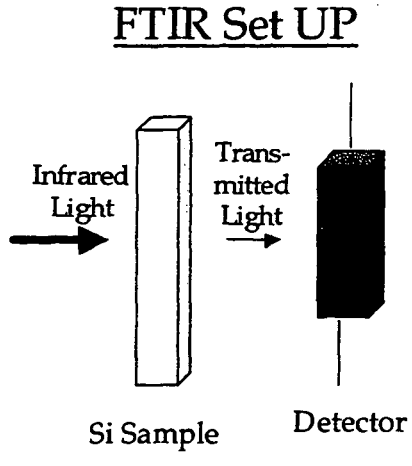

Figure 4.1: A schematic of a basic IR absorption experimental setup in which the transmitted light is measured.

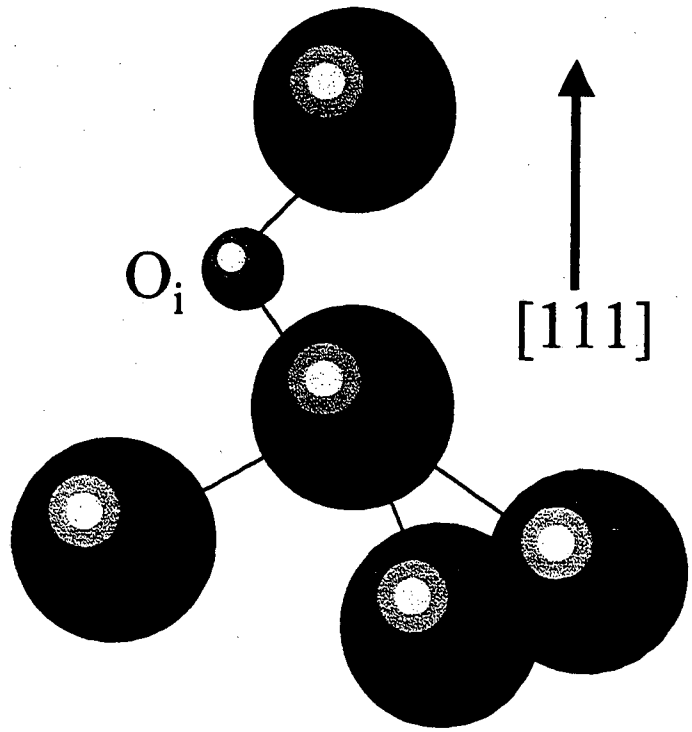

Figure 4.2: Oxygen interstitials are located in the "bond-centered" interstitial position, yet they are slightly off-center. Since the oxygen's mass is less than the mass of the matrix Si atoms, it will vibrate at much higher frequencies than the Si lattice. The arrow depicts the crystallographic direction.

At room temperature, a broad vibrational band (~30cm^{-1}) produced by O_i is located near 1106 cm^{-1}. However, at room temperature, SiO_2 precipitates produce absorption bands which interfere with the O_i vibrational band.[Pajot, 1995, 77] For

accurate O_i concentration determinations, low temperature (~10 K) measurements are required. The peak area of the spectrum is used to calculate the absorption coefficient. Using standardized calibration constants for specific temperatures,[Pajot, 1977, 76; Pajot, 1995, 77] the concentration of O_i may be determined.

4.3 TEM Calibrations

In order to properly interpret the data obtained in the selected area diffraction and precipitate contrast analysis study, both a rotation and camera constant calibration should be performed. In this section, the calibrations are briefly described and calibration data presented.

A rotation calibration is performed to determine the amount of beam rotation and image inversion as a function of the magnification. Both electron focusing and sample image magnification are achieved with electromagnetic lenses. Inducing an electrical current to the lens produces a magnetic field, which imparts a force (Lorentz force) to the electrons in the beam. The magnetic field causes the electrons to travel in a helical path. A change in the magnetic field produces a change in the helical path that causes the image to rotate and magnify (increase or decrease). Focusing the electron beam generates cross over points at which inversion of the image occurs. Because of image rotation and inversions, a rotation calibration is crucial for reliable interpretation of data. The information provided by rotation calibration facilitates such analyses as the determination of reciprocal lattice vectors relative to defect positions.

Typically, and for this calibration, the samples used in the rotation calibration are molybdenum trioxide (MoO_3) crystals. They are formed by evaporating Mo in air (to oxidize) on a carbon film supported by a Cu grid. The MoO_3 crystals grow in platelet form with their edges parallel to <100>.[Thomas and Goringe, 1979, 105] The orientation of the sample relative to the diffraction pattern can then be easily established.

In the actual procedure, a cubic faceted MoO_3 crystallite is chosen and centered in the viewing screen. At low magnification (~5000x = 5kx), the image is recorded on film. In diffraction mode, a diffraction pattern is obtained of the cubic crystallite. The diffraction pattern is recorded on the last film frame used (i.e., double exposure). The image must be recorded before the diffraction pattern or the diffraction pattern will not be seen in the double exposure. This process is repeated for a representative array of magnifications. If an image inversion occurs for a particular magnification, the magnification is noted for an image inversion.

The results of the rotation calibration for both TEMs used in the precipitate diffraction and contrast analysis are shown in figures 4.4 and 4.5. The plots show the rotation angle, ϕ, as a function of magnification. Note that for both TEMs, a crossover occurs at 22kx causing the image to invert.

Analogous to the image of the sample, the diffraction pattern of the sample is magnified. Usually, the lens settings are standardized so that the magnification of the diffraction pattern is constant.[Edington, 1976, 30] However, the amount of magnification that occurs in the diffraction pattern still must be determined for proper analysis of the diffraction patterns. The *camera constant calibration* is used to obtain this information. The camera constant is determined through the use of diffraction patterns of

a known material (usually polycrystalline Au) and the camera constant equation is given by:

$$d_{hkl} = \frac{\lambda L}{r} \tag{4.3}$$

where L is the distance from the sample to the diffraction pattern recording film, λ is the electron's wavelength determined by the beam energy, and r is the distance from the center of the diffraction pattern to a specific diffraction spot. The geometry of the above description is shown in figure 4.3.

The specimen of choice, and that was used for this calibration, is polycrystalline Au. The Au is evaporated on a Cu support grid. The polycrystalline microstructure of the Au consists of multi-oriented grains both parallel and perpendicular to the growth direction. The diffraction patterns result in rings or circles whose radii are given by the camera constant equation. The diffraction patterns are indexed. A ring radius is measured and its corresponding $\boldsymbol{d_{hkl}}$ is calculated using:

$$d_{hkl} = \frac{a}{\sqrt{h^2 + k^2 + l^2}} \tag{4.4}$$

where h, k, and l are the Miller indices. This particular equation is valid for a cubic lattice. This procedure is repeated with several different rings. Using λ, $\boldsymbol{d_{hkl}}$ and $\boldsymbol{r}$, the camera length is determined with equation 4.3. For the calibration of the TEM used in sections 1.3 and 1.4, the camera length, $\boldsymbol{L}$, was calculated to be approximately 931 mm.

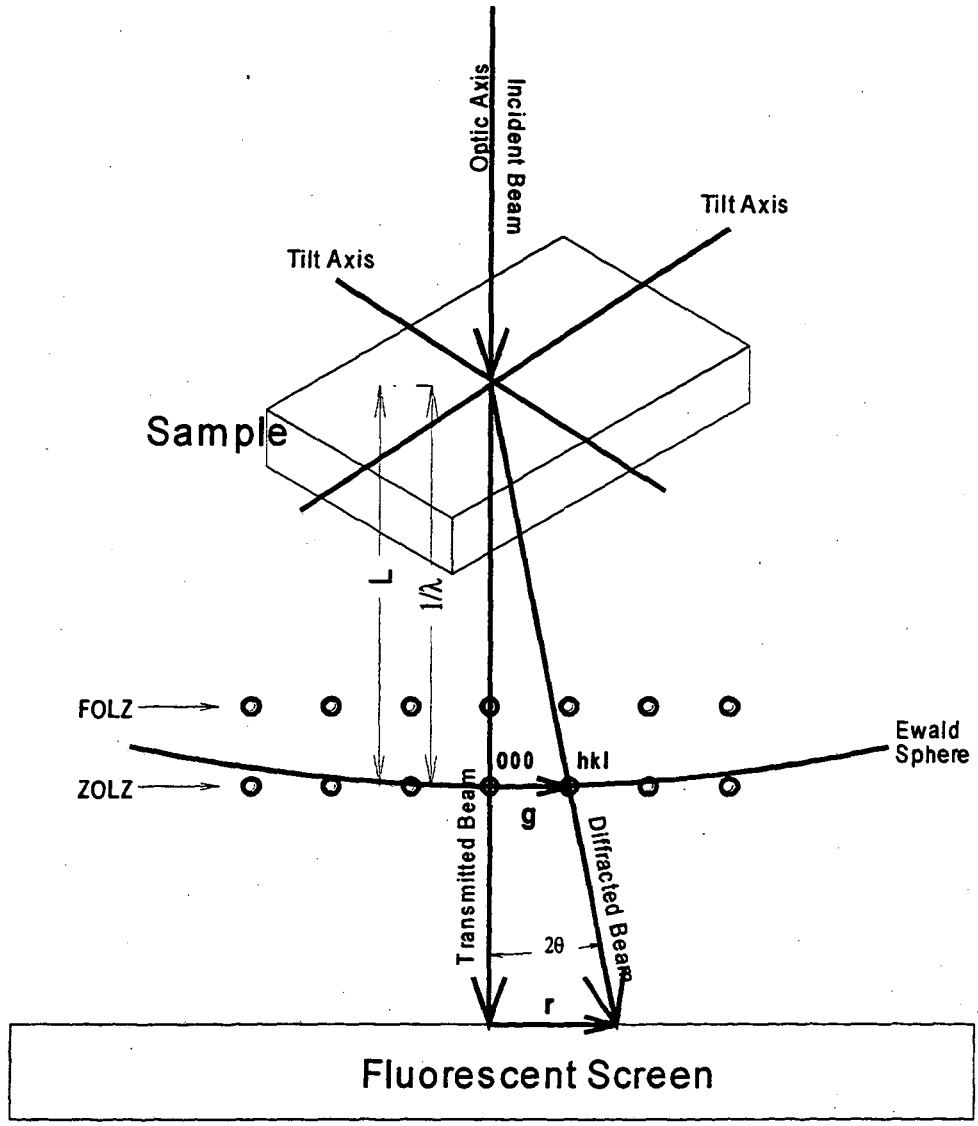

Figure 4.3: The geometric relationship of the camera constant relative to the Ewald sphere.

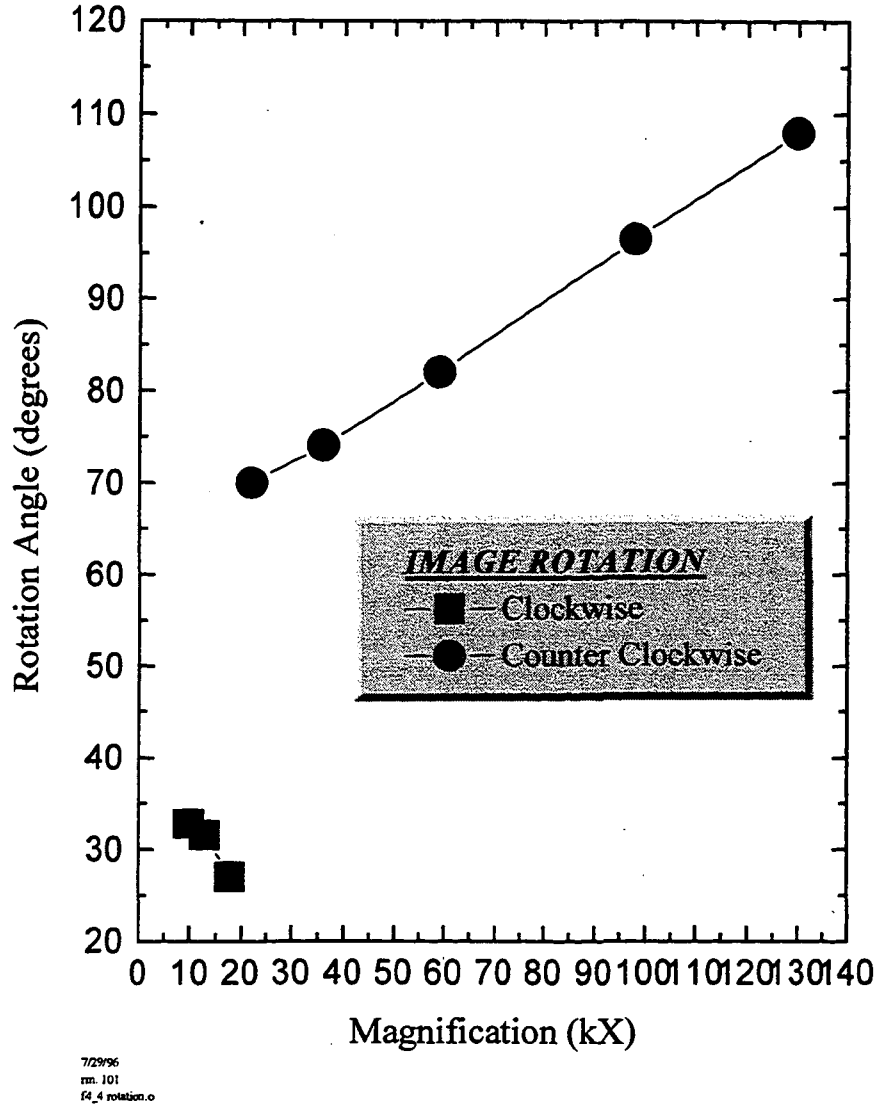

Figure 4.4: Rotation calibrations for one of the two transmission electron microscopes used in the diffraction and contrast analysis of the precipitate-like defects.

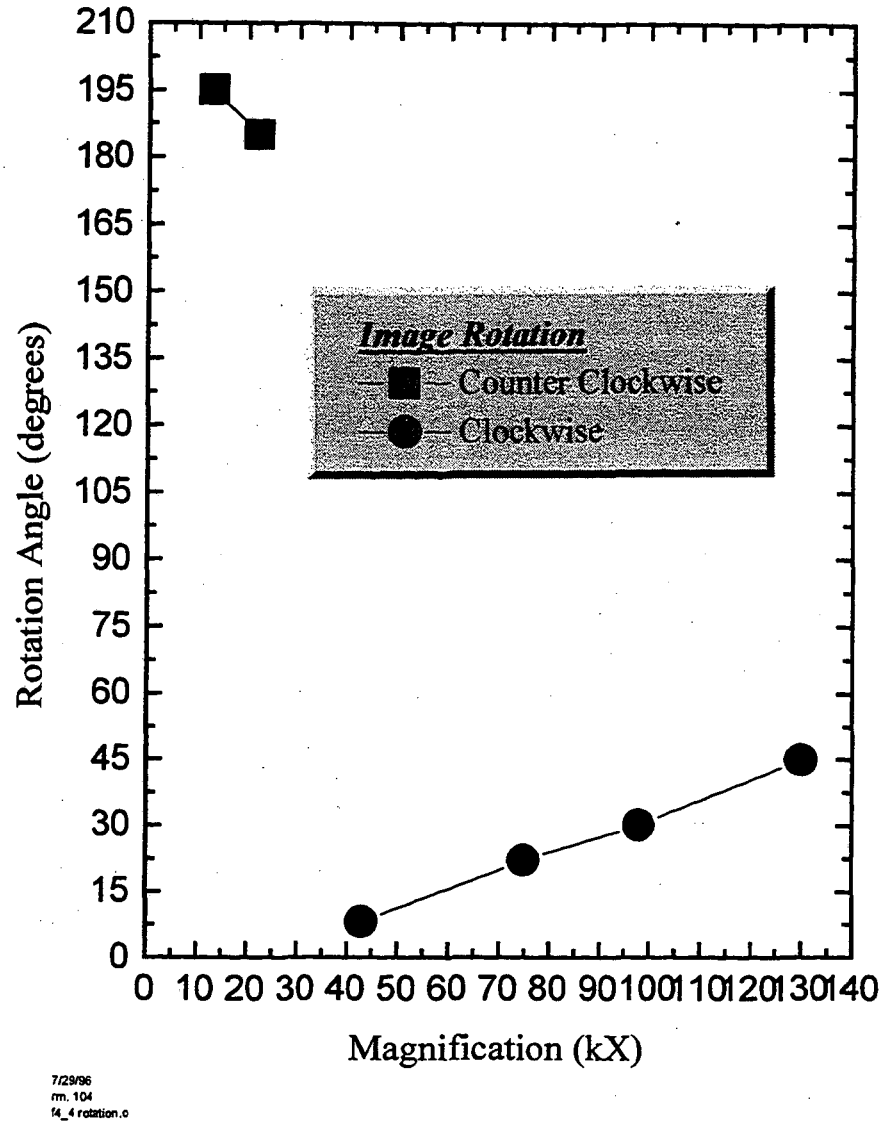

Figure 4.5: Rotation calibrations for the second transmission electron microscopes used in the diffraction and contrast analysis of the precipitate-like defects.

4.4. Background for Selected Area Diffraction and Contrast Analysis

4.4.1 The basis for contrast analysis

In the image mode, intensity variations are seen on the viewing screen which are the result of electron beam intensity fluctuations. This is a near field condition since the electrons exiting the sample surface are relatively "near" the viewing screen. The near field condition can be mathematically modeled. In order to rigorously model the near field scattering distribution, several simplifications are made. The first assumption is that only local scattering occurs. Local scattering is defined by a narrow column within the examined specimen in the direction of a specific diffracted beam containing all contributions to that beam. Known as the *column approximation*, it ignores second order scattering events from other diffracted beams. The wave functions of electrons, both transmitted (i.e., same wave vector as incident electrons) and diffracted, need to be resolved in order to determine the intensity of the exiting electron beam. Another simplification is made by only considering the interaction between two electron beams: the transmitted and a diffracted beam. This two-beam approximation is applicable when the wave function is the linear combination between the transmitted (i.e., same wave vector as incident beam) and diffracted beam in a narrow column and is given by:

$$\psi(r) \sim \phi_o(z)e^{2\pi k\cdot r} + \phi_g(z)e^{2\pi k'\cdot r} \tag{4.5}$$

where $\phi_o(z)$ and $\phi_g(z)$ are the amplitudes, as a function of crystal thickness (i.e., z), of the forward scattered beam and Bragg scattered beam, respectively. Also, k and k' are the wave vector of the forward scattered beam and Bragg scattered beam, respectively.

Because beam interaction is occurring, dynamical theory needs to be used. It should be noted that the forward scattered beam is the transmitted beam. Because multiple scattering is occurring in the sample beam, those electrons that are transmitted are being scattered in the forward direction. Kinematic theory assumes that the transmitted electrons are not scattered. In the two-beam condition, where the amplitudes of the transmitted and diffracted beams are very similar, kinematic theory fails. Thus, the column and two-beam approximations are used to compensate for this failure and dynamical theory is therefore required.[Hirsch, et al., 1977, 50]

Both $\phi_o(z)$ and $\phi_g(z)$ vary with crystal thickness, which is a result of repeated scattering events. This variance or change in amplitude with respect to crystal depth (i.e., incremental thickness dz in a column) is described by the Howie-Whelan equations given by:

$$\frac{d\phi_o(z)}{dz} = \frac{\pi i}{\xi_o}\phi_o(z) + \frac{\pi i}{\xi_g}\phi_g(z)e^{2\pi isz} \tag{4.6}$$

and

$$\frac{d\phi_g(z)}{dz} = \frac{\pi i}{\xi_o}\phi_g(z) + \frac{\pi i}{\xi_g}\phi_o(z)e^{-2\pi isz} \tag{4.7}$$

where s is the magnitude of the deviation parameter (explained later) and ξ is the extinction distance.[Edington, 1976, 30; Gronsky, 1994, 47; Hirsch, et al., 1977, 50] The extinction distance for a particular reciprocal lattice vector (g) is given by:

$$\xi_g = \frac{\pi V_c \cos\theta}{\lambda F_g} \tag{4.8}$$

where V_c is the unit cell volume and F_g is the structure factor. With boundary conditions of $z=0$ and $z=t$ (t=crystal thickness), the solutions of the Howie-Whelan equations are

sinusoidal. Their solutions show that if either s or t vary oscillations in the amplitude will occur and create contrast. The sinusoidal variation is explained by noting that at every integral number and every odd half multiple number of ξ, contrast occurs. The former creates contrast in the forward scattered beam and the latter in the diffracted beam. A notable example of this type of contrast is *thickness fringes* that are seen in many of the TEM micrographs presented in this thesis. They are alternating dark and light bands that occur when a strong two-beam condition exists in a thin region of crystal where absorption is negligible. If t_f is the distance of one period of the alternating bands and M is the magnification, the crystal thickness, t, can be calculated using the equation:

$$t = \xi_g \frac{t_f}{M} \tag{4.9}$$

providing ξ_g is known for the material.[Gronsky, 1994, 47]

For imperfect crystals in which lattice displacement occurs due to defects or strain, the amplitudes of the incident and scattered electron beams change and the Howie-Whelan equations must be modified. This is accomplished by incorporating into equations 4.6 and 4.7 a vector $\boldsymbol{R}$, describing the displacement due to the defect, such that:

$$\frac{d\phi_o(z)}{dz} = \frac{\pi i}{\xi_o}\phi_o(z) + \frac{\pi i}{\xi_g}\phi_g(z)e^{(2\pi isz + 2\pi ig\cdot R)} \tag{4.10}$$

and

$$\frac{d\phi_g(z)}{dz} = \frac{\pi i}{\xi_o}\phi_g(z) + \frac{\pi i}{\xi_g}\phi_o(z)e^{-(2\pi isz + 2\pi ig\cdot R)} \tag{4.11}$$

The addition of a phase factor, given by:

$$\alpha = 2\pi ig \cdot R \tag{4.12}$$

describes the phase shift which occurs as the electron beam passes through the crystal region of imperfection. For values of $\alpha \neq 0$, contrast arises for the crystal imperfection. This condition is called the *visibility criterion.*

The modification of the Howie-Whelan equations (equations 4.10 and 4.11) are valid only when the displacements are constant. For varying lattice displacements (e.g., varying strain fields), the gradient of R must be taken with respect to z. The effect of varying strain field on the amplitude requires further modification of the Howie-Whelan equations:

$$\frac{d\phi_o'(z)}{dz} = \frac{\pi i}{\xi_g}\phi_g'(z) \tag{4.13}$$

and

$$\frac{d\phi_g'(z)}{dz} = \frac{\pi i}{\xi_o}\phi_o'(z) + (2\pi i s + 2\pi i g \cdot \frac{dR}{dz})\phi_g'(z) \tag{4.14}$$

where the $\phi_o'(z)$ and $\phi_g'(z)$ are the modified amplitudes.[Edington, 1976, 30; Gronsky, 1994, 47; Hirsch, et al., 1977, 50] The effect of the strain in the equation is given by $g \cdot dR/dz$. Hence, if the following condition exists:

$$g \cdot \frac{dR}{Dz} = 0 \tag{4.15}$$

(i.e., visibility criterion) then strain contrast is not visible. The essence of the two-beam dynamical approximation, on the basis of which contrast analysis is formulated, is contained in these last Howie-Whelan equations.(equations 4.13 and 4.14) [Thomas and Goringe, 1979, 105]

4.4.2 Types of contrast caused by precipitates

The presence of coherent and partially coherent precipitates cause contrast in the image. The contrast is a result of the lattice mismatch between the precipitates and parent lattice, which causes strain in the material. Electron beam interaction with the precipitate itself may also produce contrast. Hirsch *et al.* [Hirsch, et al., 1977, 50] call the contrast due to lattice mismatch *matrix contrast* and contrast due to electron beam interaction with the precipitate *precipitate contrast.*

Matrix contrast is produced by displacements of the lattice, described by $\boldsymbol{R}$, which induce the electrons to deviate from the Bragg condition of the parent lattice. The resulting contrast can be analyzed to determine information about the precipitates.

Spherical coherency of precipitates is one type of information that may be ascertained by contrast analysis. In this case, the strain field is constant. When imaged in the two-beam condition, a *line of no contrast* will be visible. The line is perpendicular to the $\boldsymbol{g}$ of the two-beam condition. Thus, the visibility criterion is valid in this case and $g \bullet R = 0$.[Edington, 1976, 30; Gronsky, 1994, 47]

The use of bright field (BF) and dark field (DF) imaging can provide useful information about precipitates. For example, Ashby and Brown in their paper *Diffraction Contrast from Spherically Symmetrical Coherency Strain* state that the dependence on the depth of the precipitates below the upper surface is important to the shape and symmetry of both the DF and BF images.[Ashby and Brown, 1963a, 11; Ashby and Brown, 1963b, 12; Gronsky, 1994, 47] Only when the inclusion is in the foil center, is the BF symmetrical. Near the bottom of the surface of the foil, both the dark and bright field images are almost complementary, whereas they are nearly identical near the bottom of

the surface of the foil. This provides a means for determining the location of precipitates relative to the foil surfaces.

Small misfitting precipitates creating strain fields may produce images consisting of lobes of contrast. The precipitates' elastic displacement field, given by:

$$u_r = \frac{\in r_0^3}{r^2} \quad r \geq r_0 \quad \text{or} \quad u_r = \in r \quad r \leq r_0 \tag{4.16}$$

where r_0 is the constrained precipitate radius which is a parameter that describes the strength of the elastic strain field. These equations must be modified when precipitates are near the foil surface because a stress-free boundary condition needs to be considered. When the precipitate distance is within about one extinction distance of the foil surface, free surface effects become apparent. This causes very aberrantly wide, asymmetrical images. Black and white contrast occurs.

Under two-beam condition, two types of images can be formed. One type of image is due to small particles with spherical strain fields arising from volume mismatch. The type of image depends on the parameter:

$$P_s = \frac{g\varepsilon r_0^3}{\xi_g^2} \tag{4.24}$$

which is essentially the product between the fractional change in amplitude caused by the elastic displacements and the constrained precipitate radius, r_o. Two conditions of phase contrast with respect to P_s exist.

Condition 1: If $P_s \leq 0.2$, the image consists of small black/white lobes. The diameter of the image is $\leq 0.3\xi_g$. Between layers in the center of the foil, the BF image is a black dot.

Condition 2: In BF, if $P_s \geq 0.2$, the image consists of small black lobes unless the precipitate lies within the extinction distance of the surface in which case black/white lobes appear.

For BF and DF imaging, precipitates within ξ_g of the surface exhibit like and opposite black/white lobe images at the top and bottom surface, respectively. The diameter of the image is about ξ_g and thus is larger than for ξ_g of condition 1. Also, the line of no contrast is normal to $\boldsymbol{g}$.

As mention earlier, electron beam interaction within precipitates will cause contrast. Several types of contrast may result including structure factor contrast, orientation contrast, displacement fringe contrast, Moiré fringe contrast, and interface contrast.

Structure factor contrast originates from the differences in structure factor between the matrix and coherent precipitates.[Gronsky, 1994, 47; Hirsch, et al., 1977, 50] Ashby and Brown [Ashby and Brown, 1963b, 12], in their paper *On diffraction contrast from inclusions*, state that this causes a maximum intensity variation for thin crystals given by:

$$\Delta I = -\pi t\left(\frac{1}{\xi_g^p} - \frac{1}{\xi_g}\right)\sin\frac{2\pi t_{eff}}{\xi_g} \tag{4.25}$$

where ξ_g^p is the precipitate extinction distance and t_{eff} is the effective crystal thickness. Therefore, maximum visibility for small precipitates occurs for $t/\xi_g=n/4$ where n is an odd integer. Uniform contrast will occur when $t/\xi_g=0$ and $t/\xi_g=m/2$ where m is an

integer.[Hirsch, et al., 1977, 50] Using a matrix two-beam condition, DF imaging will show a sharp reversal of contrast.

When specific precipitate planes are near the Bragg condition while matrix planes are not, *orientation contrast* will occur. Typically, this contrast arises in large precipitates with significant differences between the crystal structures of the precipitate and matrix. DF imaging will show a sharp reversal of contrast only when using a precipitate reflection in the two-beam condition.[Gronsky, 1994, 47; Hirsch, et al., 1977, 50]

Displacement fringe contrast occurs when the precipitates cause the matrix to abruptly displace. Hence, the phase of the incident and diffracted beam change upon entering the precipitate where the phase change is given by equation 4.19. Resembling the appearance and nature of stacking fault fringes, the displacement fringes' visibility criterion is similar to that of stacking fault fringes. Some of the characteristic properties of displacement fringes include:[Hirsch, et al., 1977, 50]

defined regions of constant crystal thickness

fringes from planar precipitates are parallel to the intersection between the crystal surface and precipitate disc

fringes are straight only when the precipitate is flat

strong matrix reflections and minimum precipitate reflections allow for most easily visible fringes

fringe intensity minimum when α is close to an integer

Generally, analysis of fringe intensity for various orders of a specific reflection may give an approximate value of R.

Constructive and destructive interference between excited waves in the matrix and precipitates forming a Moiré pattern is due to *Moiré fringe contrast*. When two or more crystals with different orientation and/or lattice spacings are superimposed, Moiré fringe contrast may occur.[Hirsch, et al., 1977, 50; Williams and Carter, 1996, 113]

Interface contrast is similar in appearance to displacement contrast and matrix contrast. The principal source for interface contrast is the curvature of the interface induced by plate-shaped precipitates. If the precipitates are perpendicular to the electron beam, broad fringes may be observed. The fringes may be circular, elliptical, or highly irregular for smooth lenticular, slightly tilted, or irregularly shaped precipitates, respectively.[Hirsch, et al., 1977, 50]

4.4.3 Two beam condition

The purpose of using the two-beam condition in contrast analysis of defects is to simplify a seemingly complicated system of diffracting planes. By establishing a two-beam condition, only one set of planes is in the Bragg condition and thus diffracting, and so only one ***g*** is excited. Hence, the effect in which one set of planes has on the contrast of a defect can be established.[Gronsky, 1994, 47] For each zone axis orientation, two beam-conditions for every reciprocal lattice vector, ***g***, may be established and its affect on image contrast recorded on film. Analysis of the data may establish information on the defect that was previously discussed. For clarification, a two-beam condition is a condition in which the sample is tilted such that two beams, the transmitted (i.e., same wave vector as incident beam) and the diffracted, are very similar in amplitude. From this simple definition, one can immediately see that the assumptions required for the use of

kinematic theory are invalid. Thus, dynamical theory, which accommodates the similarity in amplitude between the transmitted and diffracted beam, is used to describe the electron-sample interactions.

In some cases, it is beneficial to tilt, and thus deviate, slightly away from an exact two-beam Bragg condition.[Gronsky, 1994, 47] The slight deviation from the two-beam condition enhances the contrast. The deviation parameter, s, is the vector used to signify the magnitude and direction of the deviation. The geometry of s, relative to the Ewald sphere, can be seen in figure 4.6.

4.4.4 Effects of precipitate-matrix coherency on electron diffraction

Precipitates within a matrix can alter a matrix diffraction pattern in several ways. The precipitates may produce their own diffraction pattern that will result in spots from both the precipitate and matrix. Also, depending on the size and shape of the precipitates, they may alter the size and shape of the matrix diffraction spots. When the precipitates are embedded in the matrix, they may induce double diffraction (discussed latter). Finally, effects may arise for small and uniformly shaped precipitates due to finite crystallite size.[Hirsch, et al., 1977, 50] Therefore, it is useful to categorize precipitate diffraction effects by the coherency between the matrix and precipitate (i.e., precipitate coherency).

Incoherent precipitates typically do not have the same or a similar crystal structure as the matrix. In this case, the matrix will not have a template effect on the precipitate. The precipitates' crystal structure is not constrained to bear resemblance to the matrix crystal structure because little or no interaction takes place between the matrix

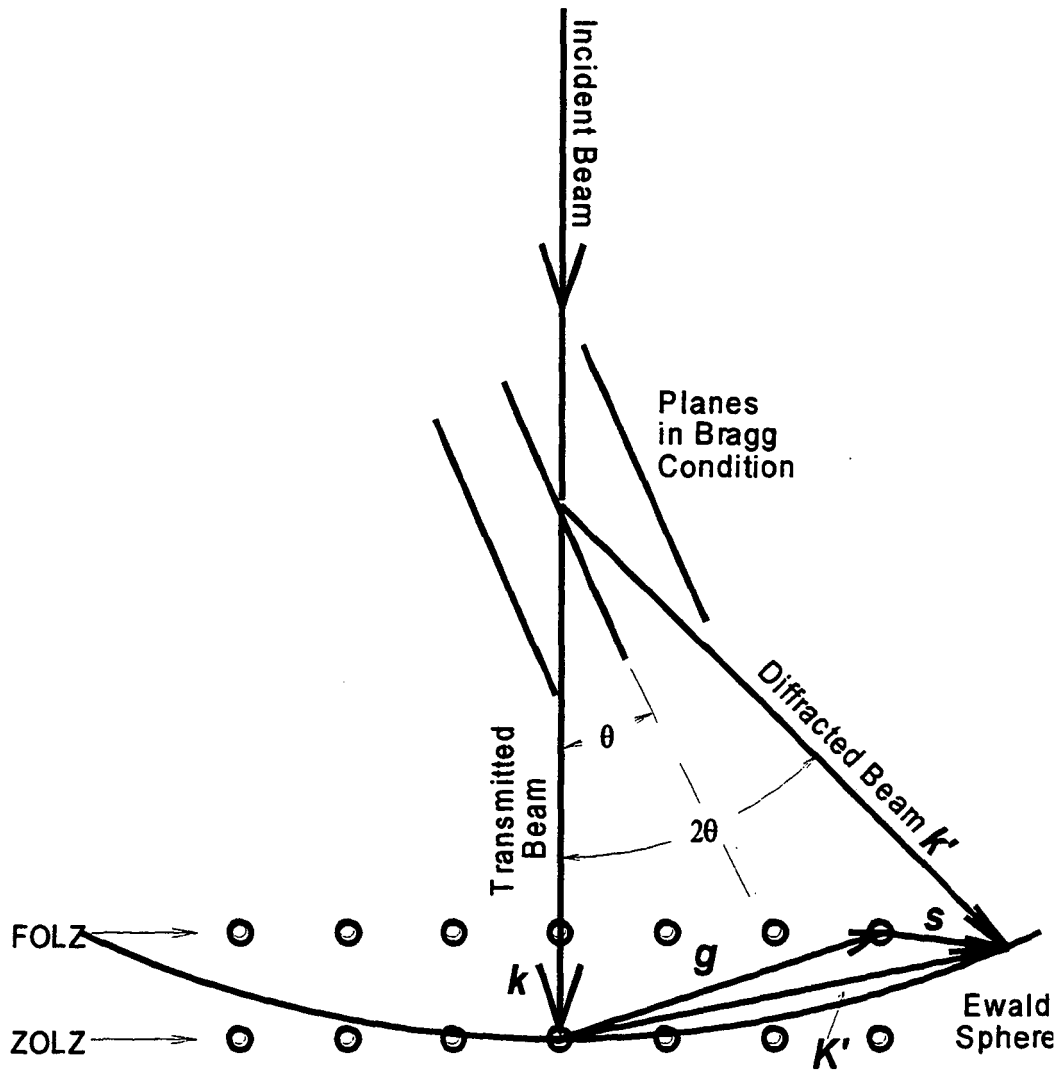

Figure 4.6: The deviation parameter, ***s***, is the deviation from the exact Bragg scattering condition and is given by ***g***+***s***=***K'***. Because the vector, ***s***, is inside the Ewald sphere, it is positive. If the Bragg Condition were met exactly, then ***K'***=***g***.

and precipitate at the interface. Thus, SAD works best when bright field (BF) contrast of the precipitate is the result of Bragg scattering (i.e., precipitates are black). One problem that may occur with incoherent precipitates is double diffraction. The diffracted beam from the matrix above acts as a secondary incident beam in the precipitate.[Hirsch, et al., 1977, 50] This will be discussed in detail later.

Unlike incoherent precipitates, coherent (e.g., pseudomorphic) precipitates are usually structurally related to the matrix. The matrix behaves as a template on which the precipitate coherently forms. Several diffraction effects occur due to coherent precipitates in a matrix. The physical appearance of the diffraction spots depends on the shape of the precipitate. Because the size and shape of a unit cell affect the direction of the diffracted beams, a change in the unit cells by lattice distortion resulting from matrix-precipitate coherency may cause streaking and displacement of diffraction spots parallel to the lattice displacement.[Cullity, 1978, 24; Hirsch, et al., 1977, 50] Furthermore, the magnitude of the diffraction spot displacement increases with higher order reflections. This effect is not seen for changes in precipitate shape. Additionally, curved streaking may occur if the transmitted beam is not parallel to the zone axis. Also, if $s \neq 0$, satellites are formed when the Ewald sphere cuts the precipitate streaks. Macroscopic habit planes of coherent plate precipitates are perpendicular to the streaks and thus their orientation may be determined.[Edington, 1976, 30] Four diffraction patterns are shown in figure 4.7 illustrating the effects of distortion and shape effects by differing precipitate-matrix systems.[Hirsch, et al., 1977, 50]

Like coherent precipitates, the crystal structure of semicoherent (i.e., relaxed) precipitates usually is related to that of the matrix. The difference being that the strain

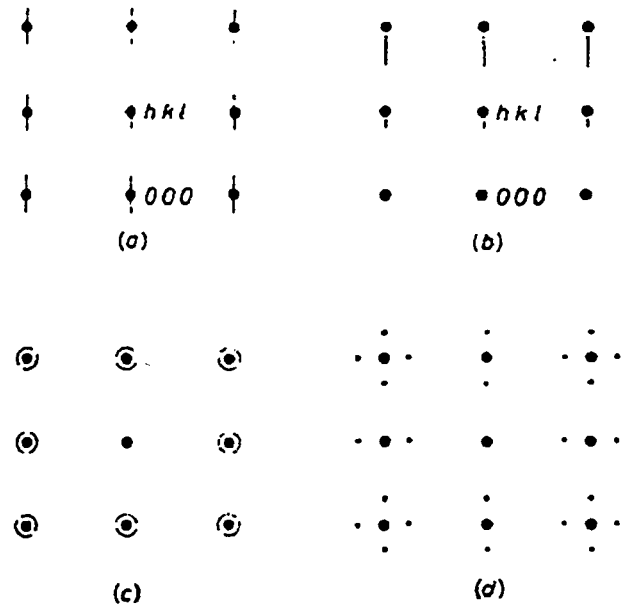

Figure 4.7: Four diffraction patterns illustrating various strain effects. **a)** thin strain free disc on (hkl) with a difference in scattering amplitude between the precipitate and matrix; **b)** distorted disc on (*hkl*) where the atom diameter of the matrix atom is greater than that of the precipitate atom; **c)** distorted sphere; **d)** distorted cuboid with faces parallel to the cube planes.[Hirsch, et al., 1977, 50]

between the precipitate and matrix is considerably less due to relaxation of the matrix-precipitate interface. Thus, diffraction effects are due to the precipitate and not to lattice distortion from the matrix. Diffraction reflections from the precipitates themselves are common. Satellites about matrix spots may occur because of the close relation in crystal structure between the precipitate and matrix. Semicoherent precipitates tend to be small and thin. Because they may exist in several orientations, the effective volume fraction decreases. This results in rather diffuse diffraction spots and complex diffraction patterns.

Typically, the diffraction pattern consists of an array of small spots displaced slightly from a matrix reflection. Therefore, semicoherent precipitates are probably the most difficult to analyze by electron diffraction [Hirsch, et al., 1977, 50] unless the misfit dislocations (causing the strain relaxation between matrix and precipitate) at the interface are discernible.

4.4.5 Diffraction analysis using selected area diffraction

Selected area diffraction (SAD) is a technique in which an aperture is used to select incident and Bragg scattered electrons from a specific area of interest. A field-limiting aperture is used to block all electrons from reaching the fluorescent screen except those transmitted from the area of interest. To insure that all and only those electrons not coming from the area of interest are blocked from forming an image or diffraction pattern on the fluorescent screen, the aperture needs to be placed in the first image plane. The way this is achieved is to separately focus the field limiting aperture and the image so that it can be seen on the fluorescent screen. Now, both the aperture and the first image are coplanar. The field-limiting aperture is focused with the diffraction lens while the image is, as usual, focused with the objective lens.

In addition, during selected area diffraction pattern (SADP) analysis, placement of the back focal plane (diffraction plane) coplanar with the objective aperture is required for proper diffraction analysis. Usually this is accomplished by focusing an objective aperture with the diffraction lens. Performing this operation prior to recording diffraction patterns insures that only the incident and diffracted beams of the area of interest are seen.[Edington, 1976, 30]

A brief introduction to the ideas of the analysis of diffraction patterns is sufficient for an understanding of the data presented in this thesis. Since the materials under investigation are cubic, this will be described only for cubic crystalline materials simplifying the analysis.

Diffraction patterns represent a two dimensional projection of the reciprocal lattice (in reciprocal or $\bar{k}$ -space) of the material. The reciprocal lattice is defined by a *general reciprocal lattice vector* given by:

$$g_{hkl} = h\boldsymbol{a}^* + k\boldsymbol{b}^* + l\boldsymbol{c}^* \tag{4.19}$$

where (*hkl*) represent the Miller indices of the real space lattice planes, and $\boldsymbol{a}^*$, $\boldsymbol{b}^*$, and $\boldsymbol{c}^*$ are the fundamental reciprocal lattice translation vectors given by:

$$\boldsymbol{a}^* = \frac{\boldsymbol{b} \times \boldsymbol{c}}{V_c} \tag{4.20}$$

$$\boldsymbol{b}^* = \frac{\boldsymbol{a} \times \boldsymbol{c}}{V_c} \tag{4.21}$$

$$\boldsymbol{c}^* = \frac{\boldsymbol{a} \times \boldsymbol{b}}{V_c} \tag{4.22}$$

The volume of the real space unit cell, V_c, is given by:

$$V_c = \boldsymbol{a} \cdot \boldsymbol{b} \times \boldsymbol{c} = \boldsymbol{b} \cdot \boldsymbol{c} \times \boldsymbol{a} = \boldsymbol{c} \cdot \boldsymbol{a} \times \boldsymbol{b} \tag{4.23}$$

where $\boldsymbol{a}$, $\boldsymbol{b}$, and $\boldsymbol{c}$ are the real lattice fundamental translation vectors (unit cell basis vectors). Note that the dot product between $\boldsymbol{a}$ and $\boldsymbol{a}^*$, $\boldsymbol{b}$ and $\boldsymbol{b}^*$, and $\boldsymbol{c}$ and $\boldsymbol{c}^*$ is 1 for a cubic lattice. The general reciprocal lattice vector is normal to the planes (hkl) and its magnitude is equal to the reciprocal of the interplanar spacing, d_{hkl}:

$$|g_{hkl}| = \frac{1}{d_{hkl}} \tag{4.24}$$

For cubic crystals, d_{hkl} is given by:

$$d_{hkl} = \frac{a}{\sqrt{h^2 + k^2 + l^2}} \tag{4.25}$$

where a is the lattice constant. The interplanar distance, d_{hkl}, is determined from the diffraction pattern by the *camera constant*, λL:

$$d_{hkl} = \frac{\lambda L}{r} \tag{4.26}$$

where L is the distance from the sample to the diffraction pattern recording film, λ is the electron's wavelength determined by the beam energy, and r is the distance from the center of the diffraction pattern to a specific diffraction spot. The camera constant equation can be derived from the geometry shown in figure 4.3. The intersection of the transmitted and diffracted beams with the Ewald sphere approximately form a right triangle when a reciprocal lattice vector, $\boldsymbol{g}$, is drawn between the two intersection points. This triangle is similar to the triangle consisting of the transmitted and diffracted beams and the real space lattice vector $\boldsymbol{r}$. Since the triangles are similar, the following mathematical relation exists:

$$\tan(2\theta) = \frac{r}{L} = \frac{g}{\frac{1}{\lambda}} \tag{4.27}$$

Substitution of equation 4.22 for $\boldsymbol{g}$ returns equation 4.26. By performing a camera constant calibration, which involves equation 4.26 and a series of diffraction patterns of a known polycrystalline material, the camera constant can be determined.

In TEM, the electron wavelength is small (~ 10^{-2} Å) so the corresponding Bragg angles (θ) for widely spaced planes (a few Angstroms) are less than 1°. It can therefore be assumed that, to a first approximation, the diffraction pattern is a planar section

through the reciprocal lattice. The Bragg angle is defined such that electron scattering in a crystal will occur if the following condition is met:

$$n\lambda = 2d\sin(\theta) \tag{4.28}$$

where n is an integral number.[Cullity, 1978, 24] By simply measuring the distance between two diffraction spots, knowing the camera constant and the electron wavelength (i.e., energy), planar spacing and angles can be determined using equations 4.26, 4.27 and 4.28. From this information, and if either the crystal structure or the material is known, then equation 4.25 may be used to determine the other unknown.

To determine the crystal structure, additional information is necessary. In crystals with more than one atom in the basis, certain lattice planes will not give rise to diffraction maxima. In general, the kinematical *structure factor* (scattering amplitude) of the unit cell, F_g, given by:

$$F_g = \sum_j f_j\left(\frac{\sin\theta}{\lambda}\right)e^{(2\pi \mathbf{g}\cdot \mathbf{r}_j)} \tag{4.29}$$

where $\mathbf{r}_j$ is the general real lattice vector for the jth atom's position. The *atomic scattering factor* for the jth atom is given by:

$$f_j\left(\frac{\sin\theta}{\lambda}\right) \tag{4.37}$$

The summation is over all the atoms in the unit cell. The *general real lattice vector*, $\mathbf{r}$, is given by:

$$\mathbf{r} = x\mathbf{a} + y\mathbf{b} + z\mathbf{c} \tag{4.38}$$

The dot product between $\mathbf{g}$ and $\mathbf{r}$ is an integral value because, as previously mentioned, the dot products between the real and reciprocal fundamental lattice vectors of the same letter are 1. The condition F_g=0 gives the disallowed or forbidden diffracting

planes.[Thomas and Goringe, 1979, 105] Physically, this corresponds to destructive interference between atomic planes with a spacing of less than a projected unit lattice vector. In certain high symmetry directions, disallowed reflections may be present because of multiple diffraction (dynamical theory).

4.4.6 Double diffraction [Hirsch, et al., 1977, 50]

Double diffraction results in the production of diffraction spots not predicted by the structure factor. Double diffraction may be caused by two phenomena: dynamical effects and the presence of a second phase. By kinematic theory, the structure factor predicts allowed reflections. However, for thick crystal when dynamical theory must be used, scattering of the transmitted beam and second order scattering of the diffracted beam may take place. For fcc and bcc crystals, which have 1 basis atom per primitive unit cell, this is not a problem because the vector addition of the indices of any two lattice points results in a multiple of or a fundamental translation vector. However, for diamond cubic (dc) or hcp, the addition of any two lattice points may result in a translation that is disallowed under kinematic theory (i.e., the structure factor). As just suggested, the diffraction spots produced by double diffraction may be determined by adding the allowed reflections using vector addition. Reflections that cannot be indexed in this manner are not caused by double diffraction in a perfect crystal.

Double diffraction may also be caused by a second phase (e.g., precipitates). In this case, a diffracted beam from the matrix above a precipitate acts as an incident beam for a precipitate. Some of the precipitates' planes may diffract the incident beam. Upon

entering the matrix, the diffracted beam from the precipitate may transmit through or diffract again causing the once forbidden reflections.

4.5 The Bracht-Knowlton Si Self-Interstitial Diffusion Model

Derivation of equations 2.58 and 2.59

To obtain equation 2.58 from 2.57, the following mathematics is performed. Note that the reaction part of equation 2.57 is equal to the opposite of the change in occupied trap concentration, T_o, with respect to time. This is given by:

$$\frac{\partial C_{T_o}}{\partial t} = k_f C_I C_{T_e} - k_r C_{T_o} C_L = -\frac{\partial C_I^{reac}}{\partial t} \qquad (4.39).$$

Substituting equation 2.54 and 2.55 into equation 4.39 gives:

$$\frac{\partial C_I}{\partial t} = D_I \frac{\partial^2 C_I}{\partial x^2} + k_f \frac{C_I^* C_{T_e}^{eq}}{C_{T_o}^{eq} C_L} C_{T_o} C_L - k_f C_I (C_{tt} - C_{T_o}) \qquad (4.40).$$

Let:

$$\tilde{C}_{T_o} = \frac{C_{T_o}}{C_{tt}} \qquad (4.41)$$

and

$$\tilde{C}_I = \frac{C_I}{C_I^*} \qquad (4.42).$$

Equation 4.43 is obtained by substituting equation 4.41 and 4.42 into 4.40:

$$\frac{\partial \tilde{C}_I}{\partial t} = D_I \frac{\partial^2 \tilde{C}_I}{\partial x^2} - k_f C_{tt} \left[\tilde{C}_I (1 - \tilde{C}_{T_o}) - k_f \frac{C_{T_e}^{eq}}{C_{T_o}^{eq}} \tilde{C}_{T_o} \right] \qquad (4.43).$$

Substituting equations 2.54, 4.41 and 4.42 into equation 4.39 gives:

$$\frac{\partial \tilde{C}_{T_o}}{\partial t} = k_f C_I^* \left[C_I(1-\tilde{C}_{T_o}) - k_f \frac{C_{T_e}^{eq}}{C_{T_o}^{eq}} \tilde{C}_{T_o} \right] \qquad (4.44).$$

By inspection of and equating the last terms in parenthesis of equations 4.43 and 4.44, it can be seen that equation 4.45 is true.

$$\frac{\partial \tilde{C}_I}{\partial t} + \frac{C_{tt}}{C_I^*} \frac{\partial \tilde{C}_{T_o}}{\partial t} = D_I \frac{\partial^2 \tilde{C}_I}{\partial x^2} \qquad (4.45).$$

Substituting equation 2.54 and 2.55 into the negative of equation 4.39 produces:

$$\frac{\partial C_I}{\partial t} = k_f \frac{C_I^* C_{T_e}^{eq}}{C_{T_o}^{eq} C_L} C_{T_o} C_L - k_f C_I (C_{tt} - C_{T_o}) \qquad (4.46).$$

Assuming local equilibrium for equation 4.46, as given by equation 2.50, generates:

$$\frac{C_{T_o}}{C_I(C_{tt} - C_{T_o})} = \frac{C_{T_o}^{eq}}{C_I^* C_{T_e}^{eq}} \qquad (4.47).$$

From equation 2.55, equation 4.48 is obtained

$$C_{T_e}^{eq} = C_{tt} - C_{T_o}^{eq} \qquad (4.48).$$

Substituting equation 4.48 into equation 4.47 gives:

$$\frac{C_{T_o}}{C_I(C_{tt} - C_{T_o})} = \frac{C_{T_o}^{eq}}{C_I^*\left(C_{tt} - C_{T_o}^{eq}\right)} \qquad (4.49).$$

Multiplying the LHS of equation 4.49 by $\frac{1}{C_{tt}} \Big/ \frac{1}{C_{tt}}$ and substituting equation 4.41 into the LHS of equation 4.49 and equating the result to the RHS of equation 4.49 gives:

$$\frac{\tilde{C}_{T_o}}{C_I(1-\tilde{C}_{T_o})} = \frac{C_{T_o}^{eq}}{C_I^*(C_{tt} - C_{T_o}^{eq})} \qquad (4.50).$$

Solving for $\tilde{C}_{T_o}$ results in:

$$\tilde{C}_{T_o} = \frac{C_I C_{T_o}^{eq}(1-\tilde{C}_{T_o})}{C_I^*(C_{tt} - C_{T_o}^{eq})} \qquad (4.51).$$

Defining equation 4.52 as:

$$\tilde{C}_I = \frac{C_I}{C_I^*} \qquad (4.52)$$

and substituting it and equation 4.48 into equation 4.51 gives:

$$\tilde{C}_{T_o} = \frac{\tilde{C}_I C_{T_o}^{eq}}{C_{T_e}^{eq}} - \frac{\tilde{C}_I C_{T_o}^{eq}}{C_{T_e}^{eq}} \tilde{C}_{T_o} \qquad (4.53).$$

Factoring out and solving for $\tilde{C}_{T_o}$ in equation 4.53 provides:

$$\tilde{C}_{T_o} = \frac{\tilde{C}_I C_{T_o}^{eq}}{C_{T_e}^{eq}\left(1 + \frac{\tilde{C}_I C_{T_o}^{eq}}{C_{T_e}^{eq}}\right)} \qquad (4.54).$$

Multiplying equation 4.54 by $\frac{1}{\tilde{C}_I C_{T_o}^{eq}} \Big/ \frac{1}{\tilde{C}_I C_{T_o}^{eq}}$ gives:

$$\tilde{C}_{T_o} = \frac{1}{\frac{C_{T_e}^{eq}}{C_{T_o}^{eq}} \tilde{C}_I^{-1} + 1} \qquad (4.55).$$

Taking the derivative of equation 4.55 with respect to time gives:

$$\begin{aligned} \frac{\partial \tilde{C}_{T_o}}{\partial t} &= \frac{\partial \left[\frac{C_{T_e}^{eq}}{C_{T_o}^{eq}} \frac{1}{\tilde{C}_I} + 1\right]^{-1}}{\partial t} \\ &= -\left[\frac{C_{T_e}^{eq}}{C_{T_o}^{eq}} \frac{1}{\tilde{C}_I} + 1\right]^{-2} \frac{C_{T_e}^{eq}}{C_{T_o}^{eq}} \frac{\partial (\tilde{C}_I)^{-1}}{\partial t} \\ &= \left[\frac{C_{T_e}^{eq}}{C_{T_o}^{eq}} \frac{1}{\tilde{C}_I} + 1\right]^{-2} \frac{C_{T_e}^{eq}}{C_{T_o}^{eq} \tilde{C}_I^{\,2}} \frac{\partial \tilde{C}_I}{\partial t} \end{aligned} \qquad (4.56).$$

Substituting equation 4.56 into equation 4.45 gives equation 4.57:

$$\frac{\partial \tilde{C}_I}{\partial t}+\frac{C_{tt}}{C_I^*}\left[\frac{C_{T_e}^{eq}}{C_{T_o}^{eq}}\frac{1}{\tilde{C}_I}+1\right]^{-2}\frac{C_{T_e}^{eq}}{C_{T_o}^{eq}\tilde{C}_I^{\,2}}\frac{\partial \tilde{C}_I}{\partial t}=D_I\frac{\partial^2 \tilde{C}_I}{\partial x^2} \qquad (4.57).$$

Factoring out $\frac{\partial \tilde{C}_I}{\partial t}$ gives:

$$\frac{\partial \tilde{C}_I}{\partial t}\left[1+\frac{C_{tt}C_{T_e}^{eq}}{C_I^* C_{T_o}^{eq}\tilde{C}_I^2}\left(\frac{C_{T_e}^{eq}}{C_{T_o}^{eq}}\tilde{C}_I^{-1}+1\right)^{-2}\right]=D_I\frac{\partial^2 \tilde{C}_I}{\partial x^2} \qquad (4.58).$$

Let the prefactor of the time differential be:

$$D=\left[1+\frac{C_{tt}C_{T_e}^{eq}}{C_I^* C_{T_o}^{eq}\tilde{C}_I^2\left(\frac{C_{T_e}^{eq}}{C_{T_o}^{eq}}\tilde{C}_I^{-1}+1\right)^2}\right] \qquad (4.59).$$

Therefore, equation 4.58 becomes

$$\frac{\partial \tilde{C}_I}{\partial t}D=D_I\frac{\partial^2 \tilde{C}_I}{\partial x^2} \qquad (4.60).$$

Dividing though by D gives:

$$\frac{\partial \tilde{C}_I}{\partial t}=\frac{D_I}{D}\frac{\partial^2 \tilde{C}_I}{\partial x^2} \qquad (4.61).$$

In equation 4.59, multiply into the squared term in the denominator by $C_{T_o}^{eq^2}\tilde{C}_I^2$ and the multiply the numerator by $C_{T_o}^{eq}$ to give equation 4.62:

$$D=\left[1+\frac{C_{tt}C_{T_e}^{eq}C_{T_o}^{eq}}{C_I^*\left(C_{T_e}^{eq}+C_{T_o}^{eq}\tilde{C}_I\right)^2}\right] \qquad (4.62).$$

Multiplying equation 4.62 by $1/C_I^*$ results in:

$$D = \frac{1}{C_I^*}\left[C_I^* + \frac{C_{tt}C_{T_e}^{eq}C_{T_o}^{eq}}{\left(C_{T_e}^{eq} + C_{T_o}^{eq}\tilde{C}_I\right)^2}\right] \qquad (4.63).$$

Substituting 4.63 back into equation 4.61 gives:

$$\frac{\partial \tilde{C}_I}{\partial t} = \frac{C_I^* D_I}{C_I^* + \frac{C_{tt}C_{T_e}^{eq}C_{T_o}^{eq}}{\left(C_{T_o}^{eq}\tilde{C}_I + C_{T_e}^{eq}\right)^2}} \frac{\partial^2 \tilde{C}_I}{\partial x^2} \qquad (4.64).$$

Letting D_I^{eff} equal the prefactor of the second order partial differential equation in equation 4.64 gives equation 2.59. Substituting equation 2.59 into equation 4.64 results in equation 2.58.

Derivation of equation 2.61

Let equation 2.59 have the form:

$$D_I^{eff} = \frac{C_I^* D_I}{C_I^* + C} \qquad (4.65)$$

$$C = \frac{C_{tt}C_{T_e}^{eq}C_{T_o}^{eq}}{\left(C_{T_o}^{eq}\tilde{C}_I + C_{T_e}^{eq}\right)^2} \qquad (4.66).$$

From equation 2.55, it can be seen that:

$$C_{T_e}^{eq} = C_{tt} - C_{T_o}^{eq} \qquad (4.67).$$

Substituting equation 4.67 into equation 4.66 factoring out C_{tt} gives:

$$C = \frac{C_{T_o}^{eq}\left(1 - \frac{C_{T_o}^{eq}}{C_{tt}}\right)}{\left[\frac{C_{T_o}^{eq}}{C_{tt}}\tilde{C}_I + \left(1 + \frac{C_{T_o}^{eq}}{C_{tt}}\right)\right]^2} \qquad (4.68).$$

Evoking the inequality of equation 2.60 for equation 4.68 results in:

$$C = \frac{C_{T_o}^{eq}\left(1 - \overbrace{\frac{C_{T_o}^{eq}}{C_{tt}}}^{\ll 1}\right)}{\left[\underbrace{\frac{C_{T_o}^{eq}}{C_{tt}}}_{\ll 1}\widetilde{C}_I + \left(1 + \underbrace{\frac{C_{T_o}^{eq}}{C_{tt}}}_{\ll 1}\right)\right]^2} \approx C_{T_o}^{eq} \qquad (4.69).$$

Substituting equation 4.69 into equation 4.65 gives:

$$D_I^{eff} \approx \frac{C_I^* D_I}{C_I^* + C_{T_o}^{eq}} \qquad (4.70).$$

Factoring out C_I^* from the denominator results in equation 2.61.

Derivation of equation 2.64

Multiplying equation 4.54 by $\frac{1}{(C_{T_o}^{eq})^2} \Big/ \frac{1}{(C_{T_o}^{eq})^2}$ produces equation 4.71:

$$C = \frac{C_{T_o}^{eq}\frac{C_{tt}}{C_{T_o}^{eq}}}{\left(\widetilde{C}_I + \frac{C_{T_o}^{eq}}{C_{T_o}^{eq}}\right)^2} \qquad (4.71).$$

Evoking equation 2.62 and 2.63 results in equation 4.72:

$$C = \frac{C_{T_e}^{eq} \overbrace{\frac{C_{tt}}{C_{T_o}^{eq}}}^{\sim 1}}{\left(\widetilde{C}_I + \underbrace{\frac{C_{T_e}^{eq}}{C_{T_o}^{eq}}}_{\langle\langle 1} \right)^2} \approx \frac{C_{T_e}^{eq}}{\widetilde{C}_I^2} \qquad (4.72).$$

Substituting 4.72 into equation 4.65 gives:

$$D_I^{eff} \approx \frac{C_I^* D_I}{C_I^* + \frac{C_{T_e}^{eq}}{\widetilde{C}_I^{\,2}}} \qquad (4.73).$$

Factoring out C_I^* and multiplying by $\frac{C_I^*}{C_I^*} \Big/ \frac{C_I^*}{C_I^*}$ gives equation 2.64.

Derivation of equation 2.66

The derivation of equation 2.66 follows the derivation of 2.64 through equation 4.71. Evoking equation 2.62 and 2.65 relative to equation 4.71 results in:

$$C = \frac{C_{tt} \frac{C_{T_e}^{eq}}{C_{T_o}^{eq}}}{\left(\widetilde{C}_I + \underbrace{\frac{C_{T_e}^{eq}}{C_{T_o}^{eq}}}_{\rangle\rangle \widetilde{C}_I} \right)^2} \qquad (4.74).$$

The inequality in equation 4.74 gives:

$$C \approx \frac{C_{tt} \frac{C_{T_e}^{eq}}{C_{T_o}^{eq}}}{\left(\frac{C_{T_e}^{eq}}{C_{T_o}^{eq}} \right)^2} = \frac{C_{tt}}{\frac{C_{T_e}^{eq}}{C_{T_o}^{eq}}} \qquad (4.75).$$

Substituting equation 2.62 into equation 4.75 provides equation 4.76:

$$C \approx \frac{C_{tt}^{2}}{C_{T_e}^{eq}} \qquad (4.76).$$

Equation 4.77 is obtained by substituting equation 4.76 into equation 4.65:

$$D_I^{eff} \approx \frac{C_I^{*} D_I}{C_I^{*} + \frac{C_{tt}^{2}}{C_{T_e}^{eq}}} \qquad (4.77).$$

Factoring out C_I^{*} of equation 4.77 gives equation 2.66.

5. References

1. Abe, T., H. Harada and J.-i. Chikawa, *Microdefects and impurities in dislocation-free silicon crystals*, Defects in Semiconductors II, Mat. Res. Soc. Symp. Proc. Vol. **14**, 1 (1982).

2. Abe, T., H. Harada, N. Ozawa and K. Adomi, *Deep level generation-annihilation in nitrogen doped FZ crystals*, Oxygen, Carbon, Hydrogen and Nitrogen in Crystalline Silicon, Mat. Res. Soc. Symp. Proc. Vol. **59**, 537 (1986).

3. Abe, T. and N. Kabayashi, *Defect-free surfaces of bulk wafers by combination of RTA and crystal growth conditions*, Internal Shin-Etsu Report **unknown**, 24 (1998).

4. Abe, T. and Y. Kato, *The effects of polishing damage and oxygen concentration on gate oxide integrity in silicon crystals*, Japanese Journal of Applied Physics **32**, 1879 (1992).

5. Abe, T. and M. Kimura, *Behavior of point defects in FZ silicon crystals*, Semiconductor Silicon/1990, The Electrochemical Society Proceedings Series Vol. **90-7**, 105 (1990).

6. Abe, T. and H. Takeno, *Dynamic behavior of intrinsic point defects in FZ and CZ silicon crystals*, Defect Engineering in Semiconductor Growth, Processing and Device Technology, Mat. Res. Soc. Symp. Proc. Vol. **262**, 3 (1992).

7. Ahn, S.T., H.W. Kennel, J.D. Plummer and W.A. Tiller, *Film stress-related vacancy supersaturation in silicon under low-pressure chemical vapor deposited silicon nitride films*, Journal of Applied Physics **64**, 4914 (1988).

8. Alexander, H., J.C.H. Spence, D. Shindo, H. Gottschalk and N. Long, *Forbidden-reflection lattice imaging for the determination of kink densities on partial dislocations*, Philosophical Magazine A **53**, 627 (1986).

9. Ammon, W.v., P. Dreier, W. Hensel, U. Lambert and L. Köster, *Influence of oxygen and nitrogen on point defect aggregation in silicon single crystals*, Materials Science & Engineering B **B36**, 33 (1996).

10. Ammon, W.v., A. Ehlert, U. Lambert, D. Gräf, M. Brohl and P. Wagner, *Gate oxide related bulk properties of oxygen doped floating zone and Czochralski silicon*, Semiconductor Silicon/1994, Vol. **94-10**, 136 (1994).

11. Ashby, M.F. and L.M. Brown, *Diffraction contrast from spherically symmetrical coherency strains*, Phil. Mag. **8**, 1083 (1963a).

12. Ashby, M.F. and L.M. Brown, *On diffraction contrast from inclusions*, Phil. Mag. **8**, 1649 (1963b).

13. Baumvol, I.J.R., F.C. Stedile, J.-J. Ganem, S. Rigo and I. Trimaille, *Mechanisms of thermal nitridation of silicon*, Journal of the Electrochemical Society **142**, 1205 (1995).

14. Bernewitz, L.I., B.O. Kolbesen, K.R. Mayer and G.E. Schuh, *TEM observation of dislocation loops correlated with individual swirl defects in as-grown silicon*, Applied Physics Letters **25**, 277 (1974).

15. Boit, C., F. Lau and R. Sittig, *Gold diffusion in silicon by rapid optical annealing*, Applied Physics A **50**, 197 (1990).

16. Borionetti, G., P. Godio, M. Porrini and S. Ilic, *Investigation on low density defects in Czochralski silicon crystal: Their detectability, formation kinetics and influence on gate oxide integrity*, High Purity Silicon IV, The Electrochemical Society Proceedings Series Vol. **96-13**, 160 (1996).

17. Bracht, H., E.E. Haller and R. Clark-Phelps, *Silicon self-diffusion in isotope heterostructures*, Physical Review Letters **submitted for publication**, (1998).

18. Bracht, H., N.A. Stolwijk and H. Mehrer, *Diffusion and solubility of copper, silver, and gold in germanium*, Physics Review B **43**, 14 (1991).

19. Bracht, H., N.A. Stolwijk and H. Mehrer, *Equilibrium concentrations of intrinsic point defects in silicon determined by zinc diffusion*, Semiconductor Silicon/1994, The Electrochemical Society Proceedings Series Vol. **94-10**, 593 (1994).

20. Bracht, H., N.A. Stolwijk and H. Mehrer, *Properties of intrinsic point defects in silicon determined by zinc diffusion experiments under nonequilibrium conditions*, Physical Review B **52**, 16542 (1995).

21. Bronner, G.B. and J.D. Plummer, *Silicon interstitial generation by argon implantation*, Applied Physics Letters **46**, March 1985 (1985).

22. Bronner, G.B. and J.D. Plummer, *Gettering of gold in silicon: a tool for understanding the properties of silicon interstitials*, Journal of Applied Physics **61**, 5286 (1987).

23. Chikawa, J., T. Abe and H. Harada, *Impurity effect on formation of microdefects during silicon crystal growth*, Semiconductor Silicon/1986, The Electrochemical Society Proceedings Series Vol. **86-4**, 61 (1986).

24. Cullity, B.D., Elements of X-Ray Diffraction, (Addison-Wesley Publishing Co., Inc., Reading, 1978), p. 555.

25. d'Aragona, F.S., *Dislocation etch for (100) planes in silicon*, Journal of the Electrochemical Society **119**, 948 (1972).

26. DiMaria, D.J., E. Cartier and D. Arnold, *Impact ionization, trap creation, degradation, and breakdown in silicon dioxide films on silicon*, Journal of Applied Physics **73**, 3367 (1993).

27. Dornberger, E., W.v. Ammon, D. Gräf, U. Lambert, A. Miller, H. Oelkrug and A. Ehlert, *The impact of dwell time above 900°C during crystal growth on the gate oxide integrity of silicon wafers*, High Purity Silicon IV, The Electrochemical Society Proceedings Series Vol. **96-13**, 140 (1996).

28. Dumin, D.J., *Wearout and breakdown in thin silicon oxide*, Journal of the Electrochemical Society **142**, 1272 (1995).

29. Eaglesham, D.J., P.A. Stolk, H.-J. Gossmann and J.M. Poate, *Implantation and transient B diffusion in Si: the of the interstitials*, Applied Physics Letters **65**, 2305 (1994).

30. Edington, J.W., *Monographs in Practical Electron Microscopy in Materials Science*, (Philips Technical Library/Van Nostrand Reinhold Co., Eindhoven, 1976), p. 400.

31. Fahey, P., R.W. Dutton and M. Moslehi, *Effect of thermal nitridation processes on boron and phoshporus diffusion in <100> silicon*, Applied Physics Letters **43**, 683 (1983).

32. Fahey, P.M., P.B. Griffin and J.D. Plummer, *Point defects and dopant diffusion in silicon*, Reviews of Modern Physics **61**, 289 (1989).

33. Föll, H. and B.O. Kolbesen, *Formation and nature of swirl defects in silicon*, Applied Physics **8**, 319 (1975).

34. Frank, W., U. Gösele and H. Mehrer, *Diffusion in silicon and germanium*, in Diffusion in crystalline solids, edited by Murch, G.E. and A.S. Nowick (Academic Press, Inc., Orlando, 1984), p. 63.

35. Fuller, C.S., *Diffusion of donor and acceptor elements into germanium*, Physical Review **86**, 136 (1952).

36. Furukawa, J., N. Iwaoka and H. Furuya, *Annealing behaviour of a light scattering tomography of detected defect near the surface of Si wafers*, Proc. 18th Intl. Conf. on Defects in Semicon./1995, Vol. 1725 (1995).

37. Fusegawa, I., K. Takano, M. Kimura and N. Fujimaki, *Review of the influence of micro defects in silicon crystals on gate oxide integrity*, Proc. 18th Intl. Conf. on Defects in Semicon./1995, Vol. 1683 (1995).

38. Gaskell, D.R., Introduction to Metallurgical Thermodynamics, (Hemisphere Publishing Corp., New York, 1981), p. 611.

39. Gösele, U., A. Plöbl and T.Y. Tan, *The influence of carbon on the effective diffusivities of intrinsic point defects in silicon*, Process Physics and Modeling in Semiconductor Technology, The Electrochemical Society Proceedings Series Vol. **96-4**, 324 (1996).

40. Gösele, U.M., W. Frank and A. Seeger, *Mechanism and kinetics of diffusion of gold in silicon*, Applied Physics **23**, 361 (1980).

41. Gösele, U.M. and T.Y. Tan, *Equilibria, nonequilibria, diffusion, and precipitation*, in Electronic Structure and Properties of Semiconductors, edited by Cahn, R.W., P. Haasen and E.J. Kramer (VCH, Weinheim, 1991a), p. 197.

42. Gösele, U.M. and T.Y. Tan, *Point defects and diffusion in semiconductors*, MRS Bulletin **XVI**, 42 (1991b).

43. Gossmann, H.-J., *et al.*, *Determination of Si self-interstitial diffusivities from the oxidation-enhanced diffusion in B doping-superlattices: The influence of the marker layers*, Journal of Applied Physics **77**, 1948 (1995).

44. Gossmann, H.-J., C.S. Rafferty, H.S. Luftman, F.C. Unterwald, T. Boone and J.M. Poate, *Oxidation enhanced diffusion in Si B-doping superlattices and Si self interstitial diffusivities*, Applied Physics Letters **63**, 639 (1993).

45. Gräf, D., M. Suhren, U. Lambert, R. Schmolke, A. Ehlert, W.v. Ammon and P. Wagner, *Characterization of crystal quality by delineation of COP and the impact on the silicon wafer surface*, High Purity Silicon IV, The Electrochemical Society Proceedings Series Vol. **96-13**, 117 (1996).

46. Griffin, P.B., P.M. Fahey, J.D. Plummer and R.W. Dutton, *Measurement of Silicon interstitial diffusivity*, Applied Physics Letters **47**, 319 (1985).

47. Gronsky, R., *MSE 204 Lecture Notes*, MSE 204 (1994).

48. Haller, E.E., *Personal Communication*, 1998.

49. Hayafuji, Y., K. Kajiwara and S. Usui, *Shrinkage and growth of oxidation stacking faults during thermal nitridation of silicon and oxidized silicon*, Journal of Applied Physics **53**, 8639 (1982).

50. Hirsch, P., A. Howie, R. Nicholson, D.W. Pashley and M.J. Whelan, Electron Microscopy of Thin Crystals, (Robert E. Krieger Publishing Co., Inc., Malabar, Florida, 1977), p. 563.

51. Hu, S.M., *Formation of stacking faults and enhanced diffusion in the oxidation of silicon*, Journal of Applied Physics **45**, 1567 (1974).

52. Hu, S.M., *Kinetics of interstitial supersaturation and enhanced diffusion in short-time/low-temperature oxidation of silicon*, Journal of Applied Physics **57**, 4527 (1985).

53. Hu, S.M., *Vacancies and self-interstitials in silicon*, Defects in Silicon II, The Electrochemical Society Proceedings Series Vol. **91-9**, 211 (1991).

54. Hu, S.M., *Nonequilibrium point defects and diffusion in silicon*, Materials Science and Engineering **R13**, 105 (1994).

55. Hull, D. and D.J. Bacon, Introduction to Dislocations, (Pergamon Press, Oxford, 1984), p. 257.

56. Incropera, F.P. and D.P. DeWitt, Introduction to Heat Transfer, (John Wiley & Sons, New York, 1990), p. 263.

57. Itsumi, M., H. Akiya and T. Ueki, *The composition of octahedron structures that act as an origin of defects in thermal SiO_2 on Czochralski silicon*, Journal of Applied Physics **78**, 5984 (1995a).

58. Itsumi, M. and F. Kiyosumi, *Origin and elimination of defects in SiO_2 thermally grown on Czochralski silicon substrates*, Applied Physics Letters **40**, 496 (1982).

59. Itsumi, M., M. Tomita and M. Yamawaki, *The origin of defects in SiO_2 thermally grown on Czochralski silicon substrates*, Journal of Applied Physics **78**, 1940 (1995b).

60. Jones, R., C. Ewels, J. Goss, J. Miro, P. Deák, S. Öberg and F.B. Rasmussen, *Theoretical and isotopic infrared absorption investigations of nitrogen-oxygen defects in silicon*, Semiconductor Science Technology **9**, 2145 (1994).

61. Kang, J.S. and D.K. Schroder, *Gettering in silicon*, Journal of Applied Physics **65**, 2974 (1989).

62. Kissinger, G., G. Morgenstern, J. Vanhellemont, D. Gräf, U. Lambert, R. Schmolke and H. Richter, *Internal oxidation of vacancy agglomerates in Czochralski silicon wafers during high-temperature anneals*, Applied Physics Letters **72**, 223 (1998).

63. Kitano, T., *Identification of vacancy clusters in FZ-Si crystals*, Physica Status Solidi **127**, 341 (1991).

64. Knowlton, W.B., H. Bracht, J.T. Walton, Y.K. Wong and E.E. Haller, *Microdefects in floating zone silicon studied by Li^+ drifting, transmission electron microscopy and process modeling*, Fall ECS Meeting/1998, The Electrochemical Society Proceedings Series Vol. **submitted for presentation**, (1998).

65. Knowlton, W.B., J.T. Walton, J.S. Lee, Y.K. Wong, E.E. Haller, W.v. Ammon and W. Zulehner, *Microdefects in nitrogen doped FZ silicon revealed by Li^+ drifting*, Proc. 18th Intl. Conf. on Defects in Semicon./1995, Materials Science Forum Vol. **196-201**, 1761 (1995).

66. Kump, M.R. and R.W. Dutton, *The efficient simulation of coupled point defect and impurity diffusion*, IEEE Transactions on Computer-Aided Design **7**, 191 (1988).

67. Ling, C.H., *Trap generation at Si/SiO_2 interface in submicrometer metal-oxide-semiconductor transistors by 4.9eV ultraviolet irradiation*, Journal of Applied Physics **76**, 581 (1994).

68. Loretto, M.H., Electron Beam Analysis of Materials, (Chapman and Hall, London, 1984), p. 272.

69. Madelung, O. and M. Schulz, Landolt-Bornstein: Numerical Data and Functional Relationships in Science and Technology - Group III: Crystal and Solid State Physics - Semiconductors - Impurities and Defects in Group IV Elements and III-V Compounds, (Springer-Verlag, Berlin, 1989), **22b**, p. 207.

70. Mizuo, S., T. Kusaka, A. Shintani, M. Nanba and H. Higuchi, *Effect of Si and SiO_2 thermal nitridation on impurity diffusion and oxidation induced stacking fault size in Si*, Journal of Applied Physics **54**, 3860 (1983).

71. Morehead, F.F., *The diffusivity of self-interstitials in silicon*, Defect Electronic Materials, Mat. Res. Soc. Symp. Proc. Vol. **104**, 99 (1987).

72. Muller, R.S. and T.I. Kamins, Device Electronics for Integrated Circuits, (John Wiley & Sons, New York, 1986), p. 524.

73. Ono, H., T. Ikarashi, S. Kimura and A. Tanikawa, *Anomalous ring-shaped distribution of oxygen precipitates in Czochralski-grown silicon crystal*, Journal of Applied Physics **78**, 4395 (1995).

74. Osada, K., Y. Zaitsu, S. Matsumoto, M. Arai and T. Abe, *Effect of stress in the deposited silicon nitride films on boron diffusion of silicon*, Journal of the Electrochemical Society **142**, 202 (1995).

75. Ourmazd, A. and W. Schröter, *Phosphorus gettering and intrinsic gettering of nickel in silicon*, Applied Physics Letters **45**, 781 (1984).

76. Pajot, B., *Characterization of oxygen in silicon by infrared absorption*, Analusis **5**, 293 (1977).

77. Pajot, B., *Evaluation of the concentration of interstitial oxygen in silicon*, 1995.

78. Park, H. and M.E. Law, *Point defect based modeling of low dose silicon implant damage and oxidation effects on phosphorus and boron diffusion in silicon*, Journal of Applied Physics **72**, 3431 (1992).

79. Park, J.-G., J.-K. Jung, K.-C. Cho and G.A. Rozgonyi, *Nature of D-defect in CZ silicon: D-defect dissolution and D-defect related T.D.D.B.*, Proc. 18th Intl. Conf. on Defects in Semicon./1995, Materials Science Forum Vol. **196-201**, 1697 (1995).

80. Park, J.-G., H. Kirk, K.-C. Cho, H.-K. Lee, C.-S. Lee and G.A. Rozgonyi, *Structure and morphology of "D-defects" in CZ Si*, Semiconductor Silicon/1994, The Electrochemical Society Proceedings Series Vol. **94-10**, 370 (1994).

81. Pell, E.M., *Diffusion rate of Li in Si at low temperatures*, Physical Review **119**, 1222 (1960a).

82. Pell, E.M., *Effect of Li-B Ion Pairing on Li^+ Ion Drift in Si*, Journal of Applied Physics **31**, 1675 (1960b).

83. Pell, E.M., *Ion drift in an n-p junction*, Journal of Applied Physics **31**, 291 (1960c).

84. Pell, E.M., *Study of Li-O interaction in Si by ion drift*, Journal of Applied Physics **32**, 1048 (1961).

85. Pell, E.M. and F.S. Ham, *Recombination kinetics for thermally dissociated Li-B ion pairs in Si*, Journal of Applied Physics **32**, 1052 (1961).

86. Porter, D.A. and K.E. Easterling, Phase Transformations in Metals and Alloys, (Chapman & Hall, London, 1981), p. 67.

87. Rasmussen, F.B., S. Öberg, R. Jones, C. Ewels, J. Goss, J. Miro and P. Deak, *The NNO defect in silicon*, Proc. 18th Intl. Conf. on Defects in Semicon./1995, Materials Science Forum Vol. **196-201**, 791 (1995).

88. Ravi, J. and W. Wijaranakula, *Dependence of the gate oxide integrity on the crystal originated defects in Czochralski silicon*, High Purity Silicon IV, Vol. **96-13**, 151 (1996).

89. Reiss, H., C.S. Fuller and F.J. Morin, *Chemical interactions among defects in germanium and silicon*, The Bell System Technical Journal **XXXV**, 535 (1956).

90. Roksnoer, P.J., *The mechanism of formation of microdefects in silicon*, Journal of Crystal Growth **68**, 596 (1984).

91. Roksnoer, P.J. and M.M.B. van den Boom, *Microdefects in a non-striated distribution in floating-zone silicon crystals*, Journal of Crystal Growth **53**, 563 (1981).

92. Ryuta, J., E. Morita and T. Tanaka, *Crystal-originated singularities on Si wafer surface after SC1 cleaning*, Japanese Journal of Applied Physics **29**, L1947 (1990).

93. Severiens, J.C. and C.S. Fuller, *Mobility of impurity ions in germanium and silicon*, Physical Review **92**, 1322 (1953).

94. Sher, A.H. and J.A. Coleman, *Lithium driftability in detector-grade germanium*, IEEE Transaction on Nuclear Science **NS-17**, 125 (1970).

95. Shewmon, P.G., Diffusion in Solids, (McGraw-Hill Book Co., New York, 1963), p. 125.

96. Spence, J., *Personal Communication*, 1996.

97. Stein, H.J., *Nitrogen in crystalline Si*, Oxygen, Carbon, Hydrogen and Nitrogen in Crystalline Silicon, Mat. Res. Soc. Symp. Proc. Vol. Vol. **1985**, 523 (1985).

98. Stolk, P.A., H.H. Gossmann, D.J. Eaglesham, D.C. Jacobson and J.M. Poate, *Trap-limited interstitial diffusion and enhanced boron clustering is silicon*, Applied Physics Letters **66**, 568 (1995a).

99. Stolk, P.A., H.H. Gossmann, D.J. Eaglesham and J.M. Poate, *Implantation and transient boron diffusion: the role of the silicon self-interstitial*, Nuclear Instruments and Methods in Physics Research B **96**, 187 (1995b).

100. Stolwijk, N.Z., B. Schuster, J. Hölzl, H. Mehrer and W. Frank, *Diffusion and solubility of gold in silicon*, Physica **116B**, 335 (1983).

101. Strunk, H., U. Gösele and B.O. Kolbesen, *Interstitial supersaturation near phosphorus-diffused emitter zones in silicon*, Applied Physics Letters **34**, 530 (1979).

102. Suga, H., H. Abe, H. Koya, T. Yoshimi, I. Suzuki, H. Yoshioka and N. Kagawa, *Effects of solidification induced defects in CZ silicon upon thin gate oxide integrity*, Physics and Chemistry of SiO_2 and Si-SiO_2 Interface 2, Proceedings of the Second Symposium on the Physics and Chemistry of SiO_2 and Si-SiO_2 interface Vol. **2**, 279 (1993).

103. SUPREM-IV, Stanford University, Office of Technology Licensing **Stanford CA.**

104. Takeno, H., S. Ushio and T. Takenaka, *Evaluation of microdefects in as-grown silicon crystals*, Defect Engineering in Semiconductor Growth, Processing and Device Technology, Mat. Res. Soc. Symp. Proc. Vol. Vol. **1992**, 51 (1992).

105. Thomas, G. and M.J. Goringe, Transmission Electron Microscopy of Materials, (John Wiley & Sons, New York, 1979), p. 388.

106. Triplett, B.B., *The limitation of extrinsic defect density on thin gate oxide scaling in VLSI devices*, Semiconductor Silicon/1994, The Electrochemical Society Proceedings Series Vol. **94-10**, 333 (1994).

107. Ueki, T., M. Itsumi and T. Takeda, *Octahedron void defects in the bulk of Czochralski silicon*, Applied Physics Letters **70**, 1248 (1997).

108. Voronkov, V.V., *The mechanism of swirl defects formation in silicon*, Journal of Crystal Growth **59**, 625 (1982).

109. Walton, J.T., Y.K. Wong, N. Derhocobian and E.E. Haller, *Lithium-ion mobility improvement in floating-zone silicon by external gettering*, Applied Physics Letters **63**, 343 (1993).

110. Walton, J.T., Y.K. Wong, N. Derhocobian and E.E. Haller, *Lithium drifted silicon detector fabrication on gettered floating-zone silicon*, IEEE Transaction on Nuclear Science **41**, 1031 (1994).

111. Watkins, G.D., *Intrinsic point defects in semiconductors*, in Electronic Structure and Properties of Semiconductors, edited by Cahn, R.W., P. Haasen and E.J. Kramer (VCH, Weinheim, 1991), p. 105.

112. Watkins, G.D., *35 years of defects in semiconductors: what next?*, The 17th International Conference on Defects in Semiconductors, Materials Science Forum Vol. **196-201**, 9 (1994).

113. Williams, D.B. and C.B. Carter, Transmission Electron Microscopy: a Textbook for Materials Science, (Plenum Press, New York, 1996), p. 729.

114. Yamagishi, H., I. Fusegawa, N. Fujimaki and M. Katayama, *Recognition of D defects in silicon single crystals by preferential etching and effect on gate oxide integrity*, Semiconductor Science Technology **7**, A135 (1992).

115. Yamagishi, H., I. Fusegawa, K. Takano, E. Iino, N. Fujimaki, T. Ohta and M. Skurada, *Evaluation of FPDS and COPS in silicon single-crystals*, Semiconductor Silicon/1994, The Electrochemical Society Proceedings Series Vol. **94-10**, 125 (1994).

116. Young, R.C., J.W. Westhead and J.C. Corelli, *Interaction of Li and O with radiation-produced defects in Si*, Journal of Applied Physics **40**, 271 (1969).

117. Zimmermann, H. and H. Ryssel, *Gold and platinum diffusion: The key to understanding of intrinsic point defect behavior in silicon*, Applied Physics A **55**, 121 (1992a).

118. Zimmermann, H. and H. Ryssel, *The modeling of platinum diffusion in silicon under non-equilibrium conditions*, Journal of the Electrochemical Society **139**, 256 (1992b).

119. Zulehner, W., *Defects in CZ silicon*, in Semiconductor Silicon, edited by Harbeke, G. and M.J. Schulz (Springer-Verlag, Berlin, 1989), p. 127.

Ernest Orlando Lawrence Berkeley National Laboratory
One Cyclotron Road | Berkeley, California 94720

Prepared for the U.S. Department of Energy under Contract No. DE-AC03-76SF00098